University of Glasgow

From Sonotrode to Tube Transducer for Flow-Based Sonoprocessing: Ultrasonically-Enhanced Metal Recovery from Electronic Waste

Shida Li

Submitted in fulfilment of the requirements for the Degree of Doctor of Philosophy

College of Science and Engineering
University of Glasgow
June 2026

Abstract

Electronic waste (E-waste) generation reached 62 Mt in 2022, with the total value of technology critical metals (TCMs) amounting to $91 billion. Printed circuit boards (PCBs) and lithium-ion batteries (LiBs), account for 3-5% and 3-4% of the total mass, respectively, and represent two of the most important targets for resource recovery. Traditional recycling routes generally suffer from high energy consumption, limited selectively, and environmental risks. Power ultrasound offers a promising pathway for improving E-waste recycling processes. Improved mass transport and acoustic cavitation mediated effects have demonstrated the ability to enhance material delamination, thereby providing significant potential for green recycling applications.

Deep eutectic solvent (DES)-based ionometallurgical methods offer several advantages, including low-temperature operation, reduced toxicity, and the potential for selective metal recovery. However, their high viscosity leads to limited mass transfer and slow dissolution/delamination kinetics, making it difficult to meet high-throughput processing requirements. Using the delamination of TCM-containing layers from PCB surfaces in Ethaline-DES as a case study, this thesis first demonstrates the intensification effect of power ultrasound on green-solvent recycling processes. By combining sonotrode-induced acoustic cavitation with Ethaline-DES, the delamination rate of TCM was increased by more than thirtyfold compared with passive treatment without sonication.

However, the development of high-throughput applications for sonochemistry and sonoprocessing remains one of the major challenges in ultrasonic engineering. Conventional power-ultrasound devices are typically based on Langevin transducers and are commonly implemented as sonotrodes or ultrasonic baths. This creates an inherent trade-off between cavitation intensity and spatial distribution, limiting the scalability of conventional ultrasonic configurations for high-load and continuous-flow processing.

This thesis presents the first comprehensive study of the development, testing, optimisation and application of a novel tube transducer comprising a single, element radially poled tubular piezoceramic element. The transducer is designed to generate an intense, inward-focused cavitation field within the tube bore. Acoustic measurements, high-speed imaging (HSI), and sonochemiluminescence (SCL) demonstrated that the tube transducer can produce high-intensity cavitation throughout the entire bore, with peak activity concentrated along the central axis. Compared with the highly localised cavitation field generated by a conventional

sonotrode, this geometry is inherently more suitable for flow-through processing applications.

Graphite delamination from LIB anodes was employed as the primary application case study to evaluate the practical sonoprocessing capability of the tube transducer. Under geometrically comparable conditions, the static tube-transducer configuration achieved higher graphite-delamination efficiencies than a sonotrode for both sheet and flake samples, demonstrating that its broader cavitation field can be translated into improved materials-processing performance.

To investigate flow-based processing, a recirculation system containing three tube transducers in series was designed and constructed. Pulsed excitation was introduced under flow conditions, and the effects of operation duration, processing load, and flow rate on graphite delamination efficiency were systematically investigated. Complete graphite delamination of flake samples was achieved within an operation duration of 2 min. The processable load per unit reactor volume was increased to approximately three times that of the static configuration. Furthermore, the principal limitation at high processing loads was identified as blockage caused by abrupt pipe contractions within the circulation loop, providing a clear direction for future system optimisation and scale-up.

Overall, this thesis demonstrates that transitioning from localised sonotrode-based processing to a modular tube-transducer configuration can effectively mitigate the structural limitations of conventional power-ultrasound systems associated with the trade-off between cavitation intensity and spatial coverage. Through modular integration and series connection, the tube-transducer concept provides a route towards a future continuous-flow sonoprocessing platform. These findings indicate that tube transducer-based sonoprocessing represents a promising and scalable approach for LiB anode recycling and, more broadly, for the sustainable recovery of valuable materials from electronic waste.

Table of Contents

List of figures

List of tables

Acknowledgements

The PhD has been a long and intensive journey of research and writing. As I complete my thesis, I would like to express my heartfelt gratitude to the many people who have supported, guided and assisted me at different stages of this work.

First and foremost, I would like to thank my supervisor, Dr. Paul Prentice. Thank you for your consistent oversight of my research direction and high standards throughout my PhD, and for your meticulous and patient guidance in refining scientific questions, iterating experimental protocols, interpreting results and writing the thesis. Your commitment to research quality and rigorous training in academic expression have enabled me to achieve systematic improvement in my research capabilities, academic perspective and independent thinking. These gains will have a lasting impact on my academic path and professional development.

I am also sincerely grateful to my second supervisor, Dr Andrew Feeney. I also sincerely thank my co-supervisor, Andrew Feeney. During period of heightened stress and low morale, your understanding, comfort and encouragement meant a great deal to me. Your support helped me regain confidence, adjust my pace, and continue moving forward. I will always remember your kindness and trust.

My special thanks go to Dr. Ben Jacobson for his substantial support in advancing the research and in thesis preparation. You reviewed and revised my writing on multiple occasions, offering highly specific and valuable suggestions regarding logical structure, precision of expression and rigour of argumentation. Many key sections became clearer and more professional through your careful scrutiny, and I have benefited greatly from this training in academic writing and expression.

I would also like to thank Paul Daly for working closely with me throughout the PhD. We designed and conducted experiments together, repeatedly discussed the interpretation of results and the structure of the manuscripts, and published a paper as co-first authors. You devoted a great deal of time and effort to the execution of experiments, data analysis and manuscript revisions; your rigorous approach and efficient collaboration were crucial to my completion of this research.

I am grateful to PhD students Faraz Amini Boroujeni and Yikai Zhang for their help and companionship in daily scientific discussions, experimental collaboration and technical problem-solving. Your willingness to share expertise and provide timely feedback often offered new perspectives for problem-solving, making the research environment in the laboratory more supportive and cohesive. I also thank Dr. Hilde Mezger for her support and insights in research discussions and teamwork. Your attention to detail and commitment to academic quality consistently influence my understanding and practice of ‘rigorous research’.

Finally, I would like to thank my family and friends. The understanding, tolerance and support you have shown me in the face of pressure and uncertainty have been a vital source of strength that enabled me to persevere and complete my doctoral studies.

To everyone who has supported me in any way, I offer my heartfelt thanks.

Declaration

All work in this thesis was carried out by the author unless explicitly stated otherwise.

List of Abbreviations

- Cavitation Research Laboratory (CavLab)
- Centre for Medical and Industrial Ultrasound (C-MIU)
- Deep eutectic solvent (DES)
- Electronic waste (E-waste)
- Field of view (FOV)
- Frames per second (fps)
- Hydrogen-bond acceptor (HBA)
- Hydrogen-bond donor (HBD)
- High-intensity focused ultrasound (HIFU)
- High-speed imaging (HSI)
- Lithium-ion batteries (LiBs)
- Millivolts (mV)
- Printed circuit boards (PCBs)
- Passive cavitation detectors (PCDs)
- Periodic shockwaves (PSWs)
- Polyvinylidene fluoride (PVDF)
- Pulse-width modulation (PWM)
- Scanning electron microscopy (SEM)
- Sonoluminescence (SL)
- Sonochemiluminescence (SCL)
- Technology critical metals (TCMs)
- Polyfluoroalkyl substances (PFAS)

List of Symbols

V_{rms} Time average shockwave content

f Resonant frequency

f_0 Frequency of driving signal

f_c Cut-off frequency

V Voltage

N_p Number of primary coil turns of the impedance matching transformer

N_s Number of secondary coil turns of the impedance matching transformer

a Turns ratio of the impedance matching transformer

I Current

R Resistance

L Dynamic inductance

L_s Equivalent inductance

C Dynamic capacitance

C_0 Static capacitance

t_{on} Pulse duration

t_{off} Pulse interval

K Duty cycle

Re Reynold number

Q Flow rate

u flow velocity

ρ Density

D Diameter

μ Dynamic viscosity

N Number of circulation cycles for the LiB flakes

t_r Residence time of a sample during a single pass through the three tube transducers

t_c Time required for one complete circulation through the re-circulation system

T_{SD} Cumulative sonication duration of the sample over the full operation duration

Thesis Overview & Dissemination

The following will detail how this thesis is structured and outline the relevant chapters within it. This study was carried out in the Cavitation Research Laboratory (CavLab) at the Centre for Medical and Industrial Ultrasound (C-MIU). The main research theme of the CavLab is the fundamental understanding of acoustic cavitation, with the aim of advancing and improving applications. The laboratory is based on high-speed cameras (see Chapter 3), which are used to image the rapid dynamics of cavitating bubbles with high temporal and spatial resolution. A number of commercially available hydrophones, as well as passive cavitation detectors (PCDs) of in-house design and fabrication, are available for simultaneous acoustic detection. Previous research at CavLab has been biased towards medical therapeutic applications of cavitation, such as the cavitation of microbubbles driven by focused ultrasound at several hundred kilohertz (kHz), for the application of disruption of the blood-brain barrier, for drug delivery. More recent research has focussed on industrial applications of cavitation, such as characterising cavitation activity generated by commercial ultrasonic horns and designing novel tube transducers for applications such as technology critical metal recycling.

This thesis is the first doctoral research project aimed at designing a novel ultrasonic tube transducer for the recovery of technology critical metals (TCMs) from electronic waste (E-waste). The ultrasonic sources used in this study were a commercial sonotrode and a newly designed tube transducer, as shown in the results chapters 4-7. Deionised water and a variety of liquids with different properties used in this study, in particular variations in viscosity, which have a significant effect on the cavitation behaviour. The categories of liquids used in this study are deionised water, deep eutectic solvent (DES), and citric acid solution. DESs are green and customisable solvents that show great potential for metal leaching, are sustainable and environmentally friendly, and can help to reduce the use of traditional pyrometallurgy and hydrometallurgy, which are associated with high energy consumption and significant environmental impact, respectively - as discussed in thesis chapter 2.

Chapter 1 provides an overview of the acoustic cavitation and reviews the literature on the fundamental principles and representative applications of sonochemistry and sonoprocessing. It summarises commonly used methods for cavitation monitoring and characterisation. Commercial high-power ultrasonic devices are then classified and evaluated in terms of the inherent structural trade-off between cavitation intensity and spatial

coverage, as well as overall system complexity. On this basis, this chapter further introduces the novel tube transducer developed in this study and outlines the motivation for its development.

Chapter 2 reviews the global scale of E-waste generation and its resource recovery value, with a particular focus on printed circuit boards (PCBs) and lithium-ion batteries (LiBs). This chapter provides a structured review of the mainstream recycling routes for PCBs and LiBs, and critically analyses the advantages and limitations of different recycling methods in terms of energy consumption, and the feasibility of pollution control. §2.4 then introduces the green solvent used in chapter 4 - DESs. Their formulations, advantages, and key physical properties are summarised, together with the current state of research and application potential in the recovery of TCMs.

Chapter 3 describes the technical details of the main equipment, solutions and key data processing approaches used in the project, as outlined below:

- Commercial sonotrode: used to generate a reference field and perform sonication experiments on E-waste.

- Sonication tank: used to accommodate solvent containers and to support the corresponding control conditions.

- High-speed imaging system and illumination: comprising a high-speed camera and associated light sources for visualisation and recording of cavitation structures.

- Static tube transducer configuration developed by CavLab: providing the structural design, fabrication process and the basis for selecting the operating frequency.

- Tube transducer excitation chain: including the signal generator, power amplifier, and impedance-matching transformer, enabling stable transducer excitation.

- Shockwave passive cavitation detector (swPCD) and signal-processing workflow: including the swPCD design and fabrication procedure, together with the filtering protocol applied to the acoustic data.

- Preparation and storage of chemical reagents: including the preparation processes and storage methods for the various DESs, sonochemiluminescence (SCL) reagents, and citric acid solutions used in this thesis.

Chapter 4 is focuses on the Ethaline-DES ionometallurgical system (the other two DESs are described in Appendix B), systematically characterising sonotrode-induced cavitation at different input powers, with particular emphasis on the periodic collapse behaviour of the primary bubble cluster and its associated shockwave emissions, which are then used to identify favourable operating parameters. Subsequently, dual-perspective high-speed imaging was employed to investigate the process by which the sonotrode achieves TCM delamination on the PCB surface in Ethaline-DES, with the aim of identifying specific cavitation phenomena that underpin the ultrasound-enhanced delamination/etching rate. Camera 1 records the delamination behaviour at the PCB surface in real time. Camera 2 simultaneously captures high spatio-temporal resolution shadowgraph images of cavitation activity during sonication, with particular attention to cavitation events associated with metal etching. The results of this section have been published in Ultrasonic Sonochemistry and Faraday Disicussions, both papers were led by Dr Ben Jacobson, with the second author contributing.

Journal Paper
A mechanistic study identifying improved technology critical metal delamination from printed circuit boards at lower power sonications in a deep eutectic solvent. Ben Jacobson, **Shida Li**, Rodolfo Marin Rivera, Paul Daly, Christopher E. Elgar, Daniel M. Mulvihill, Andrew P. Abbott, Andrew Feeney and Paul Prentice.
Ultrasonic Sonochemistry, vol. 101, p. 106701, 2023.
Journal Paper
Observation of cavitation dynamics in viscous deep eutectic solvents during power ultrasound sonication. Ben Jacobson, **Shida Li**, Paul Daly, Christopher E. Elgar, Andrew P. Abbott, Andrew Feeney and Paul Prentice.
Faraday Discussions, vol. 253, p. 10.1039, 2024.

Chapter 5 addresses the limitation that the high viscosity of Ethaline-DES imposes on delamination efficiency by reducing viscosity through dilution with de-ionised water. The delamination performance of TCM from PCB surface was compared across Ethaline-deionised water mixtures with different volume fractions at a fixed transducer amplitude.

The impact of adjusting the solvent properties on cavitation output and delamination efficiency was evaluated. This work was presented at an international conference.

Conference Paper
Acoustic Cavitation Enhanced Delamination of Technology Critical Metals from Electronic Waste Using Green Solvents **Shida Li**, Ben Jacobson, Andrew Feeney; Christopher E Elgar; Andrew P Abbott and Paul Prentice
2024 IEEE Ultrasonics, Ferroelectrics, and Frequency Control Joint Symposium (UFFC-JS), Taipei, Taiwan, 22-26 September 2024, ISBN 9798350371901

Chapter 6 conducts multi-scale cavitation characterisation of the newly developed static tube transducer configuration. First, acoustic emission signals were acquired using the swPCD to compare shockwave intensity within the tube bore under air and water-backed conditions, thereby identifying the more favourable backing arrangement in terms of cavitation intensity. Second, high-speed imaging (HSI) and SCL were used to compare the cavitation activity and spatial coverage of the tube transducer versus the sonotrode under geometrically comparable configurations. The advantages of the tube transducer in terms of 'coverage range and activity distribution' are verified. Finally, based on the time-dependent evolution of cavitation structures revealed by HSI, the cavitation intensity response under different excitation durations was examined to identify more effective excitation durations and to provide a basis for subsequent operating-condition optimisation. Parts of this chapter have already been published as a journal paper.

Journal paper
The tube transducer as a novel source for power ultrasound: A case study in delamination of graphite coating from lithium-ion battery anode **Shida Li**, Paul Daly, Ben Jacobson, Joshua Cooke, Chunhong Lei, Andrew P. Abbott, Andrew Feeney, Paul Prentice Chemical Engineering and Processing - Process Intensification, vol. 225, p. 110813, 2026

Chapter 7 aims to verify whether the cavitation coverage and intensity advantages of the tube transducer characterised in chapter 5 can be translated into processing performance for practical recycling tasks, using delamination of the graphite coating on LiB anodes as an example. Firstly, the delamination performance of the tube transducer is evaluated on intact anode production waste, and compared with sonotrode results obtained at two different tip-to-sheet distances. Subsequently, to simulate future flow processing scenarios, the

delamination of anode flakes is further investigated under static conditions, with comparative results against various sonotrode exposure configurations provided. Additionally, to better approximate industrial disassembly conditions at end-of-life, a combined process of "citric acid pre-soaking + sonication" was introduced, systematically comparing the effects of different citric acid concentrations and soaking times on the graphite delamination efficiency of aged LiB anodes. Finally, considering that the introduction of flakes may alter the availability of cavitation nuclei and consequently affect the cavitation output at a given power, this chapter supplements the study with acoustic characterisation of the cavitation intensity in flake-containing aqueous systems, using swPCD measurements to support subsequent comparisons and parameter selection. Parts of this chapter feature in Li *et al* CEPPI **225**, 110813 (2026), with other findings disseminated at a conference.

Conference Paper
Pretreatment of aged lithium-ion battery anode to enable high-throughput sonoprocessing **Shida Li**, Paul Daly, Ben Jacobson, Andrew Feeney and Paul Prentice
1st International REACT Conference, Glasgow, November 2025

Chapter 8 builds upon the static studies conducted in chapters 5 and 6, with a focus on engineering route towards continuous and scalable processing. This chapter marks the first advancement of the tube transducer from a static configuration to a flow configuration. A re-circulating flow system comprising three tube transducers connected in series was constructed, enabling aged LiB anode flakes suspended in citric acid solution to pass repeatedly through the three-tube module under pump action, whilst undergoing multi-stage acoustic treatment. This was done to evaluate the feasibility and performance limits of the system as a high-throughput sonoprocessing prototype.

Chapter 1

Acoustic cavitation and power ultrasound for sonoprocessing

1.1 Introduction to acoustic cavitation

Acoustic cavitation refers to the formation of bubbles within a liquid under a periodic ultrasonic field, followed by a series of dynamic processes including growth, oscillation, and collapse [1]. As ultrasound propagates through the liquid, the acoustic pressure alternates between two phases: rarefaction and compression (fig. 1.1) [2]. During rarefaction, the ultrasonic field imposes a negative pressure and the liquid experiences tensile stress, allowing pre-existing cavitation nuclei to expand into bubbles. Conversely, during compression, the liquid experiences positive pressure, causing the bubbles to contract and potentially undergo violent collapse.

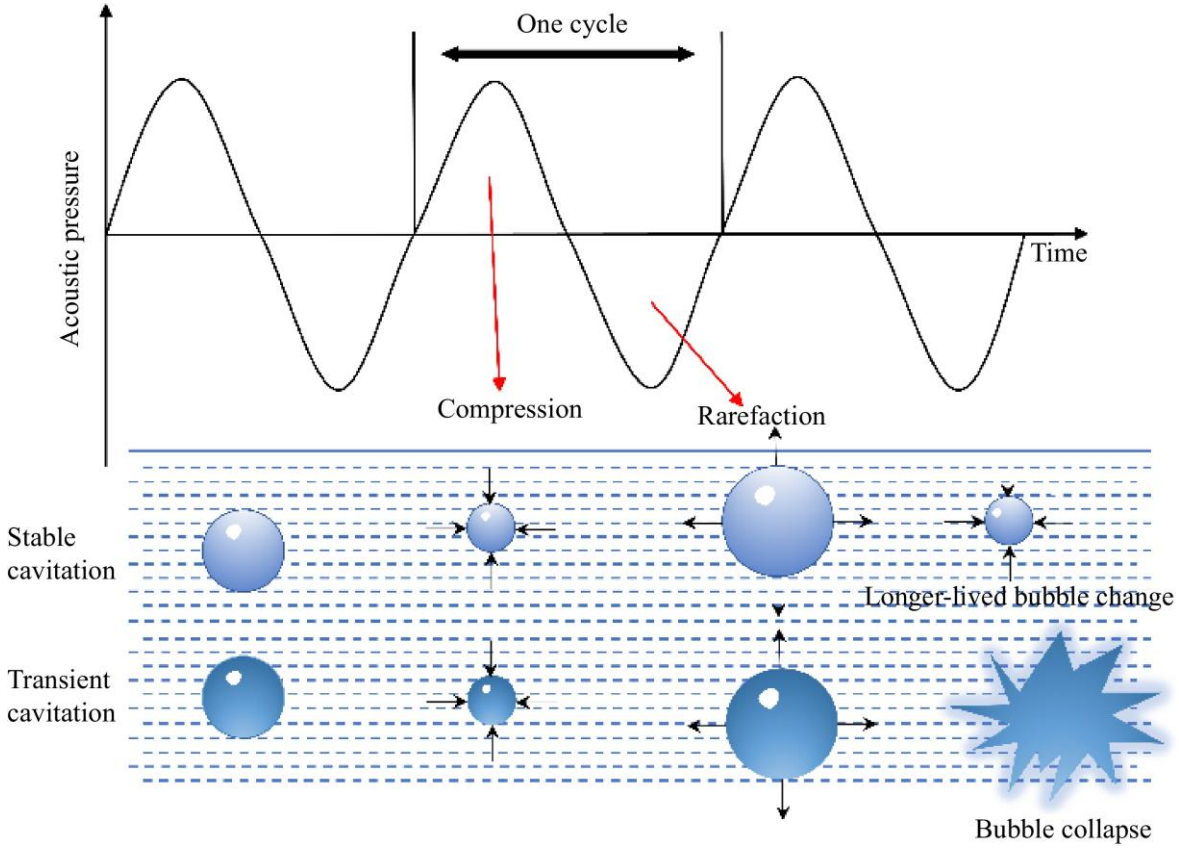

Fig. 1.1: General classification of acoustic cavitation, (a) stable (non-inertial) cavitation, (b) inertial (or transient) cavitation. Taken from [3].

As demonstrated above, a negative pressure must develop to break the cohesion of the liquid molecules and form a cavity. The pressure amplitude value at which this occurs is referred to as the 'cavitation threshold' [4]. The magnitude of the cavitation threshold is influenced by a range of factors. As the ultrasonic frequency increases, the time available for bubble growth within each rarefaction phase becomes increasingly limited, rendering cavitation more difficult to initiate [5], [6]. Increased dissolved gas content [7] and elevated liquid temperature [6] typically lower the cavitation threshold by reducing the tensile strength and surface tension of the liquid. Conversely, a higher ambient pressure and greater liquid viscosity will elevate the threshold. Furthermore, suspended solid particles [8] can serve as nucleation substrates, lowering the threshold. Consequently, the cavitation threshold can be adjusted in experiments by modifying these influencing factors.

Acoustic forcing and bubble dynamics For an ideal sinusoidal acoustic field, the far-field liquid pressure acting as the forcing term on a bubble may be expressed as [4]

$$p_\infty(t) = p_0 - p_A \sin(2\pi f t) \tag{1.1}$$

where $p_\infty(t)$ is the instantaneous far-field liquid pressure, p_0 is the static ambient pressure, p_A is the peak acoustic-pressure amplitude, f is the excitation frequency, and t is time. During the rarefactional phase of the acoustic cycle, $p_\infty(t)$ falls below p_0, allowing pre-existing gas or vapour nuclei to expand when the pressure reduction is sufficiently large. The subsequent compression phase drives bubble contraction and, following sufficiently nonlinear expansion, may result in inertial collapse. It should be noted that p_A is an acoustic-pressure parameter and should not be directly equated with the electrical input power supplied to an ultrasonic transducer.

To a first approximation, the radial motion of an isolated spherical bubble can be described by the Rayleigh-Plesset equation [4]:

$$\rho_l \left(R\ddot{R} + \frac{3}{2}\dot{R}^2 \right) = p_B(t) - p_\infty(t) - \frac{2\sigma}{R} - \frac{4\mu_l \dot{R}}{R} \tag{1.2}$$

Where R, $\dot{R}$, and $\ddot{R}$ are the instantaneous bubble radius, bubble-wall velocity, and bubble-wall acceleration, respectively; ρ_l and μ_l are the liquid density and dynamic viscosity; σ is the surface tension; and $p_B(t)$ is the total pressure inside the bubble, including contributions from non-condensable gas and vapour. The pressure difference $p_B(t) - p_\infty(t)$ drives

bubble-wall motion, whereas surface tension particularly resists the expansion of small nuclei and viscous stress opposes bubble-wall motion. The excitation frequency influences the response through $p_\infty(t)$, because it determines the duration of each rarefactional and compressional phase.

Equation (1.2) provides a qualitative basis for interpreting how liquid density, viscosity, and surface tension influence cavitation-bubble dynamics. It is therefore relevant to the Ethaline–water mixtures investigated in Chapter 4. Increasing viscosity generally increases viscous damping and restricts rapid bubble-wall motion. However, water dilution also changes other liquid characteristics, including vapour pressure, acoustic attenuation, dissolved-gas behaviour, and chemical speciation, which are not represented explicitly by the Rayleigh–Plesset equation. The experimental comparison should therefore be interpreted as a coupled liquid-property and chemical-system investigation rather than as a viscosity-only study.

The classical Rayleigh-Plesset equation assumes a single spherical bubble in an infinite, incompressible Newtonian liquid. It neglects liquid compressibility, nearby boundaries, bubble–bubble interactions, acoustic shielding, and reactor-scale wave propagation. It is therefore used in this thesis as a conceptual framework rather than as a quantitative model of the multibubble cavitation fields produced by the sonotrode and tube transducer. Experimental characterisation using high-speed imaging, sonochemiluminescence, and passive cavitation detection remains necessary to determine the actual cavitation behaviour within these reactor configurations.

Existing research commonly classifies acoustic cavitation into two categories: (1) Stable (or non-inertial) cavitation, characterised by the bubble exhibiting stable, multicycle oscillations driven by low amplitude acoustic waves, fig. 1.1 (a). (2) Inertial cavitation, defined by the bubble undergoing several cycles of unstable oscillation under high amplitude acoustic waves and then collapsing during the next compression phase, fig. 1.1 (b). This binary classification, however, fails to provide a sufficient explanation for the complex features observed in the acoustic cavitation emission spectrum. Song *et al* [9] therefore proposed a third category “stable-inertial cavitation”, detailed in §1.5.1.

Notably, bubble collapse can generate mechanical effects such as jets [10], bubble collapse shockwaves [11] and localised hotspots [12] characterised by extremely high temperatures and pressures that can reach or even exceed 5000 K and 500 atm, respectively [13]. These physical and chemical effects serve a key role in sonochemistry [14] and sonoprocessing

[15], discussed in detail in §1.2. The following paragraphs will briefly describe these cavitation phenomena.

Jetting The characteristic feature of a cavitation jet is the non-spherical collapse of a bubble, in which one side of the bubble involutes to form a high-speed liquid jet. This jet ultimately pierces through the bubble and can impact on nearby surfaces [16]. Such behaviour typically occurs when a single bubble or a bubble cluster collapses under the influence of an external boundary causing an external pressure gradient. The pressure gradient can be introduced by local flow and boundary conditions, such as when the bubble is close to a rigid wall [17] or a free surface [18], near other bubbles [19], perturbed by shockwaves [20], or exposure to an ultrasonic field [21]. Cavitation jets are prevalent in sonochemistry [22] and sonoprocessing [23] within ultrasonic reactors, recognised as a key mechanism promoting effects such as surface erosion [24] and decontamination [25], as detailed in §1.2.2. As shown in fig. 1.2 (a), the surface (at the bottom of the images) disrupts the symmetry required for spherical oscillation, resulting in the bubble surface furthest from the wall inverting and thereby generating a jet directed toward the solid boundary. Fig. 1.2 (b) demonstrates jetting from asymmetrical bubble collapse due to the ultrasonic pressure field propagating within the vessel after 38 μs, such that the jet direction aligns with the direction of acoustic wave propagation (arrowed in white), [26].

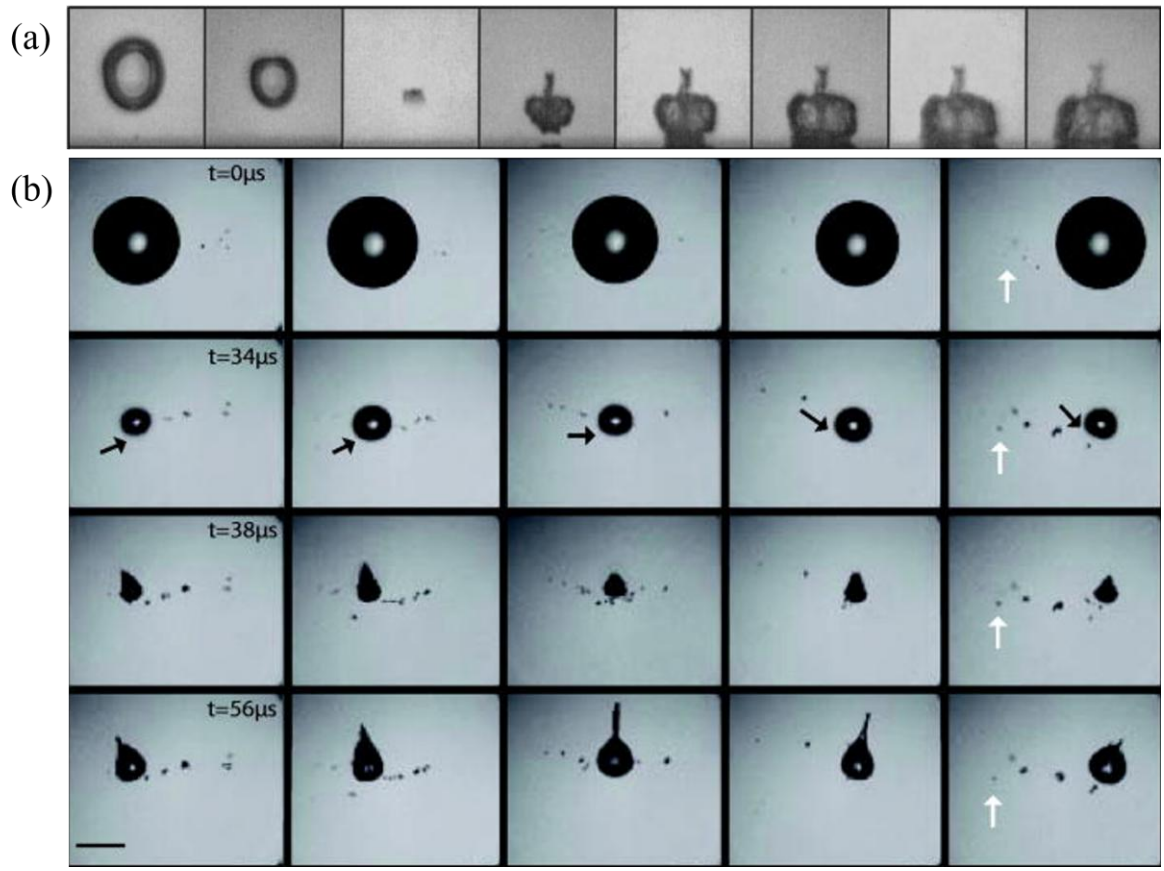

Fig. 1.2: (a) High-speed imaging (HSI) of jet towards the solid wall formed by asymmetric bubble collapse. Taken from [16]. (b) Jet generated by bubble collapse in a 1.47 MHz focused ultrasound field (3.3 MPa peak-negative-pressure amplitude), the white arrow indicates the direction of ultrasonic propagation. Taken from [26].

Shockwaves Cavitation shockwaves refer to high-pressure pulses radiated outward during the collapse of an inertially cavitating bubble. The bubble then rebounds and grows to a maximum radius followed by a subsequent collapse during successive compression phases of oscillation. These shockwaves are regarded as one of the key physical origins of material damage observed in bubble-mediated processes [27], [28]. In experimental characterisation, the direct visualisation of shockwave can be achieved by combining shadowgraphic illumination with high-speed imaging. Fig. 1.3 shows shockwaves radiating outward during repeated bubble cloud collapses within an ultrasonic field operating at 220 kHz and 682.9 ± 62.0 kPa peak-pressure amplitude [9].

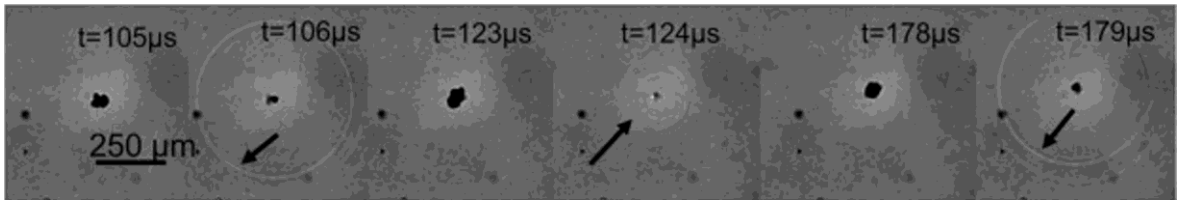

Fig. 1.3: High-speed shadowgraph imaging of shockwaves radiated during the collapse of cavitation bubble cloud in a 220 kHz and 682.9 ±62.0 kPa peak-pressure amplitude acoustic field. Taken from [29].

Hotspots Cavitation hotspots describe the transient extreme environments locally formed during the final stage of bubble collapse as a result of rapid compression [12], characterised by extremely high temperatures and pressures [13]. Although the extreme conditions are highly transient, only persisting for durations in the scale of a few microseconds [12], they are widely regarded as the principal origin of many sonochemical reactions. Liquid molecules undergo pyrolysis in high temperature and pressure environments, in turn generating highly reactive species such as hydroxyl radicals (•OH), hydrogen radicals (•H), hydroperoxyl radicals (OOH•), and hydrogen peroxide (H_2O_2). There are, consequently, promoters of a wide range of redox reactions [13], [30].

1.2 Previous CavLab research

CavLab is dedicated to fundamental research on acoustic cavitation and the refinement and optimisation of related applications. The laboratory is equipped with advanced high-speed imaging facilities and a range of acoustic detection devices, enabling characterisation of cavitation structural evolution and the associated acoustic emissions, fig 1.3. Early investigations primarily focused on cavitation applications within the medical field, such as inducing cavitation by driving microbubbles with focused ultrasound transducers [9], [31]. Industrial applications of acoustic cavitation have also become an increasing research focus, leading to a series of contributions [32], [33]. These studies provide important reference points for this thesis and are therefore briefly outlined in this section.

1.2.1 Stable-inertial cavitation: periodic shockwaves

An analysis of the acoustic cavitation noise spectrum: The role of periodic shock waves.

Jae Hee Song, Kristoffer Johansen, and Paul Prentice. The Journal of the Acoustical Society of America. vol. 140, pp 2494-2505, 2016

To investigate the 'stable-inertial cavitation' described in §1.1, Song *et al* established an acoustic field in degassed de-ionised water using a high-intensity focused ultrasound (HIFU) transducer operating at 692 kHz. Laser-induced single cavitation bubble was employed, with the nucleation point positioned at the focal point of the transducer. Acoustic emissions were recorded using a 1.0 mm diameter needle hydrophone (Precision Acoustics, Dorchester, UK), with amplitude and phase calibrated over a bandwidth of 125 kHz to 20 MHz.

Fig. 1.4 (a) & (b) presents the cavitation bubble acoustic emission time-domain signal (after filtering out the fundamental drive frequency, f_0 = 692 kHz) and its corresponding spectrum at the ultrasonic pressure amplitude of 1.63 ± 0.12 MPa, respectively. The results show that the bubble collapses once every two acoustic cycles, with the shockwave peaks repeating with a period of $2T_0$. This phenomenon is referred to as a period-doubling response, in which liquid inertia prevents collapse during every compression phase. The synthesised spectrum of the periodic shockwaves (PSWs) further confirms their contribution to the measured emission spectrum. A series of pronounced peaks appears at nf_0/m (where m and n are integers and m=2) when the shockwave repetition period is $2T_0$, fig. 1.4 (d). The nonlinear response of the bubble is further strengthened and the PSW period shifts to $3T_0$ and consequently relocating the spectral peak to $nf_0/3$ when the driving pressure amplitude is increased to 2.42±0.09 MPa. This study indicates that PSW are responsible for the subharmonic and ultraharmonic components observed in the acoustic emission signal. The collapse periodicity m exhibits a progressive increase with rising driving acoustic pressure (i.e., m = 2, 3, 4, ...).

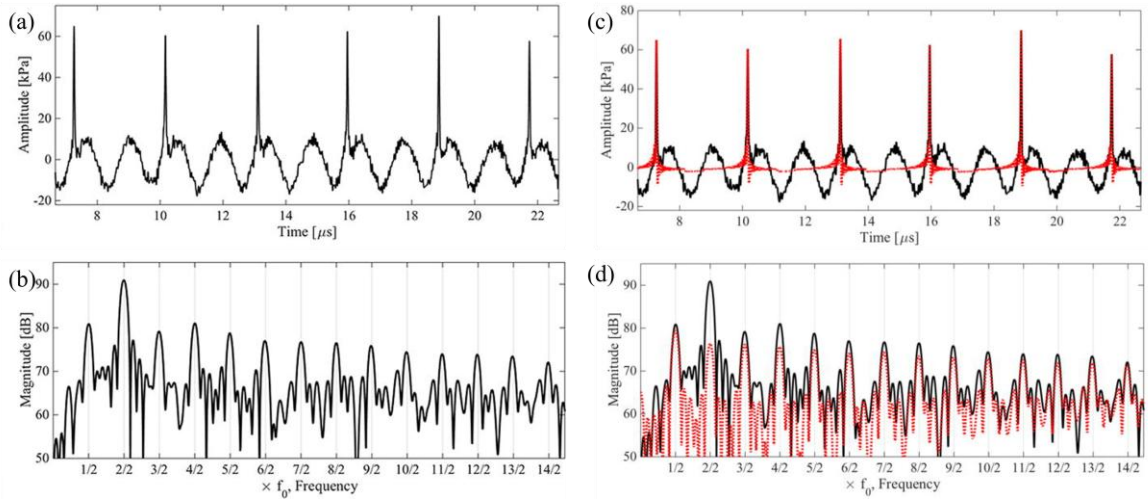

Fig. 1.4：(a) Acoustic emission signals from laser-induced cavitation bubbles detected by hydrophone in ultrasound field, after subtraction of the background signal acquired with no bubble. (b) Acoustic emission spectrum of (a). (c) Synthetic PSW signal (red) overlaid on

hydrophone detected signals. (d) The synthetic PSW spectrum overlaid to the hydrophone measured cavitation emission spectrum. Taken from [9].

1.2.2 Characterising the cavitation activity generated by an ultrasonic horn at varying tip-vibration amplitudes

Characterising the cavitation activity generated by an ultrasonic horn at varying tip-vibration amplitudes.

Lukman Yusuf, Mark D. Symes, Paul Prentice. Ultrasonics Sonochemistry, vol. 43, pp 146-155, 2018

Yusuf *et al* [34] investigated the cavitation generated by a vibrating 20 kHz sonotrode whose tip immersed in water. Observations and measurements were undertaken at 25 input powers. Experiments employed dual perspective high-speed imaging (HSI), observing cavitation activity under different fame rates and imaging durations to fully analyse its dynamic evolution. Parallel acoustic monitoring was conducted using a 15 mm diameter swPCD acoustic emission detection system.

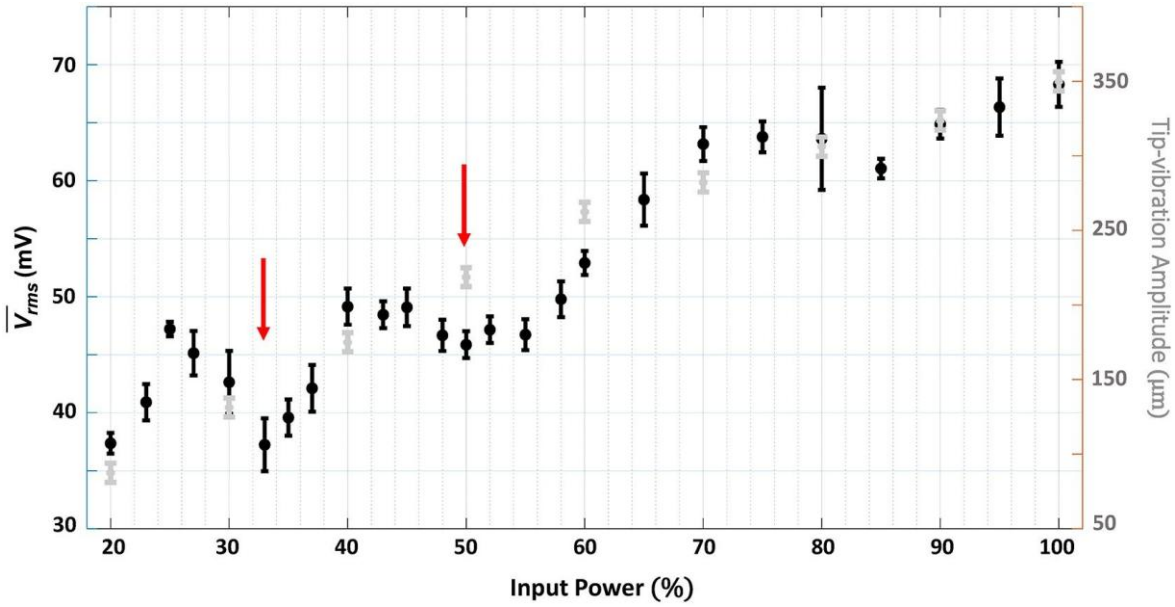

Fig. 1.5: Mean Vrms of the signals collected by swPCD after five 2 s sonications at each of the 25 input powers. Error bars represent standard deviations within five datasets. The peak-to-peak amplitude of the tip vibration is also shown. Taken from [34].

Cavitation was systematically examined across 25 input power settings, with particular emphasis on quantifying the time-averaged shockwave content in the acoustic emission through dense sampling during power ramping. The objective was to evaluate the functional relationship between cavitation intensity and sonotrode input power, thereby a basis for energy optimisation of cavitation-mediated processes. Fig. 1.5 summarises the key findings. The root mean square voltage (V_{rms}) of the emission signals recorded by the swPCD, served as a measure for the overall bubble collapse shock wave content detected during each sonication, and indicator for cavitation intensity

The results show that, cavitation intensity (as determined by time-averaged bubble collapse shock wave amplitudes, detected during the sonication) does not increase linearly with increasing input power, as measured by the average shockwave content within the emitted signals. Multiple local minima in V_{rms} are observable in fig. 1.5, arrowed red. Analysis of the acoustic emission and corresponding spectra, corroborated by HSI, reveals a pronounced non-linear elevating response within the primary cavitation cluster beneath the sonotrode tip. The collapse frequency of the cluster sequentially transitions from $f_0/2$ to $f_0/3$ and $f_0/4$, corresponding to double-period, triple-period, and quadruple-period behaviours, and ultimately increases to $f_0/6$ at higher input powers. However, the cavitation intensity exhibits a marked decrease within the power range indicated by the red arrows. This reduction occurs because the primary cavitation cluster is undergoing a transition between periodic collapse states (e.g., from a collapse repetition frequency of $f_0/3$ to $f_0/4$), preventing regular collapses from locking onto a single resonant frequency. The proportion of non-collapsing bubbles increases at the transitional input powers, thereby reducing the shockwave content within the acoustic emission signal. The findings highlight the importance of performing accurate acoustic characterisation of cavitation intensity for any ultrasonic source, as this has direct implications for optimising energy utilisation efficiency in industrial sonoprocessing.

1.3 Sonochemistry and sonoprocessing applications of acoustic cavitation

Research on acoustic cavitation for industrial processes can generally be segregated into two primary categories. The first focuses on the initiation and intensification of chemical reactions through hotspots generated by cavitation collapse, and is known as sonochemistry. The second targets process intensification in material treatment through mechanical effects such as cavitation jets and shockwaves, and is termed sonoprocessing. Although these two

categories focus on different outcomes, both rely on cavitation as the central enabling mechanism. This section will introduce these two approaches separately.

1.3.1 Sonochemistry

The acoustic wavelength is related to excitation frequency by [2]

$$\lambda = \frac{c}{f} \tag{1.3}$$

where λ is the acoustic wavelength, c is the speed of sound in the liquid, and f is the excitation frequency. Taking the speed of sound in water is approximately 1500 $m \cdot s^{-1}$. For the ultrasonic frequency range of 15 kHz to 10 MHz, the corresponding wavelengths are between 10 to 0.01 cm, markedly larger than the molecular scale [12]. The influence of ultrasound on chemical reactions therefore does not act directly upon molecules, but rather through acoustic cavitation. The localised transient hotspots generated by bubble collapse in the ultrasonic field promote the formation of highly reactive radical species from liquid molecules, thereby initiating or accelerating chemical reactions in solution [13]. Sonochemistry can therefore be understood fundamentally as a cavitation-mediated process of chemical intensification, rather than a direct effect of the ultrasonic wave.

Existing research typically classifies sonochemical reactions as highly heterogeneous processes, dividing the reaction zone into three distinct regions as shown in fig. 1.6: the cavity interior, the gas-liquid interface, and the bulk liquid [13], [30], [35]. Radical-mediated reactions may occur within all the three regions [36], [37].

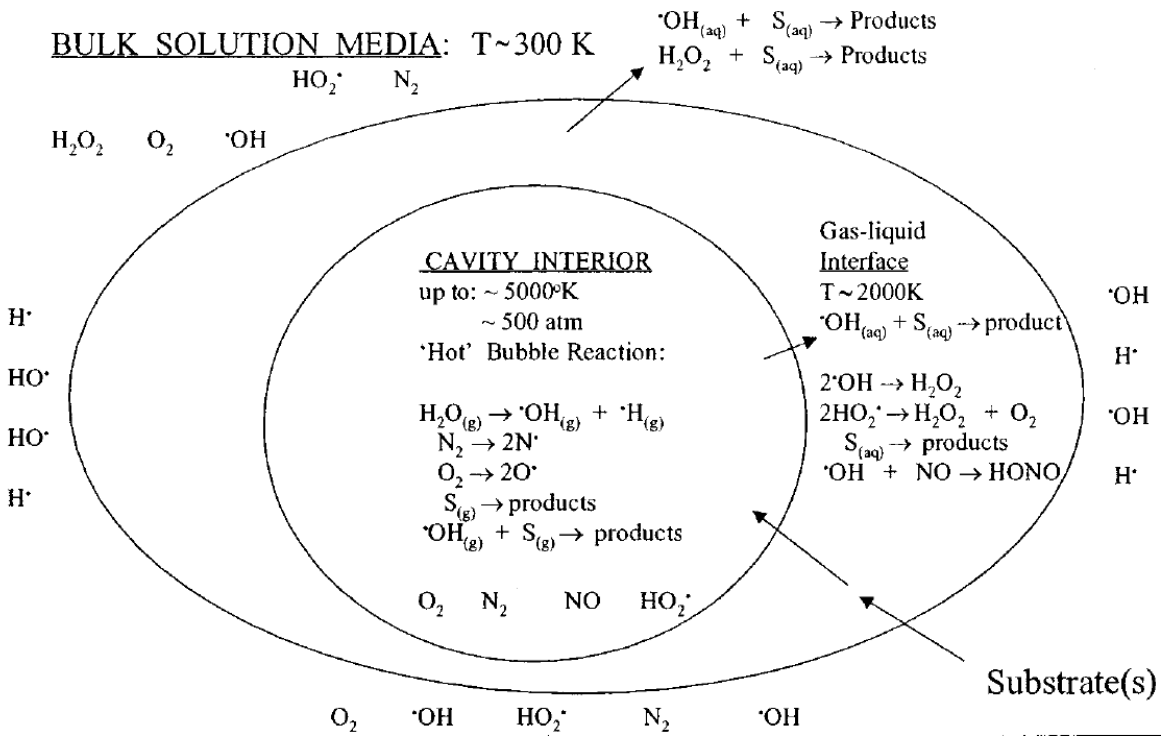

Fig. 1.6: Three reaction zones in the acoustic cavitation process. Taken from [13].

Cavity interior The rapid contraction of the bubble radius during the final stage of collapse causes a sharp, transient increase in internal temperature and pressure [12]. These extreme conditions cause bond breakage and the dissociation of water and other vapour and gases, producing radicals or electronically excited states. Solvent and substate molecules entering the bubble are also exposed to bond breakage, producing highly reactive intermediates [30]. The radicals may recombine to form new molecules and additional radicals, or diffuse into the bulk liquid to function as oxidants [13].

Gas-liquid interface The temperature at the gas-liquid interface can reach as high as 2000 K, making it possible for pyrolytic reactions and radical-mediated reactions to take place simultaneously [38]. The reaction mechanism is dominant by pyrolytic reactions at higher solute concentration and by radical-mediated reactions at lower concentration [13], [39]. The preferential enrichment of surface-active reactants at the interface enhances the contact probability between bulk liquid chemicals and bubble generated species. As a result, reactions such as degradation processes often initiate preferentially in the interfacial region [38], [40].

Bulk liquid Sonochemical reactions in the bulk liquid are mainly induced by the outward diffusion of radicals generated in the bubble interior and at the gas-liquid interface. The

effective reaction zone is confined to a region only 200 nm thick from the gas-liquid interface and the timescale for radical-mediated reactions following bubble collapse is less than 2 μs [41]. Moreover, the temperature of the bulk liquid is near ambient, about 300 K, making it incapable of supporting primary reactions similar to those in hotspots. Therefore, sonochemical reactions in the bulk liquid are mainly secondary reactions, in which a few radicals diffusing out of the bubble or interface react with the substrates in the liquid to form new products [13], [42].

Sonochemistry has now been applied in a wide range of chemical processing applications. Taking water purification as an example, organic pollutants such as toxic azo dyes, per- and polyfluoroalkyl substances (PFAS) can be degraded either through reaction with radicals generated at hotspots or via direct pyrolysis [35], [43]. Tezcanli-Guyer *et al* [44] sonicated 1 L Basic Brown 4 solution (BBr4, $C_{21}H_{26}Cl_2N_8$, 20 $mg \cdot L^{-1}$) using a 520 kHz plate-type piezoelectric transducer with a 22.05 cm^{-2} emission area at 40 W input power. Results indicate that 49% of aromatic/olefinic carbon was disrupted after 4 h continuous sonication. Furthermore, the colour of BBr4 removal reached 99.8% within 2 h, and its toxicity was completely eliminated. Wood *et al* [45] coupled a 6.6 cm diameter piezoceramic transducer to a 10 cm diameter vibrating plate. A 10 $mg \cdot L^{-1}$ solution of potassium salt of perfluorooctane sulfonic acid (K-PFOS) with a liquid height of 58 mm was sonicated for 4 h at 400, 500, and 1000 kHz. The reported PFOS degradation percentages after 4 h (loss relative to the initial concentration) were 96.9%, 93.8%, and 91.2%, respectively, at an input power of 40 W.

In nanomaterial synthesis, volatile organometallic carbonyl compounds such as $Fe(CO)_5$, $Mo(CO)_6$ and $W(CO)_6$ undergo complete dissociation within cavitation bubbles, with the resulting metal atoms subsequently aggregate to form nanostructured materials with diverse morphologies [46]. For example, Bang *et al* [47] dissolved 0.5 mL $Fe(CO)_5$ and 0.1 g carbon nanoparticles (4 - 12 nm diameter) in 40 mL hexadecane ($C_{16}H_{34}$). Under argon atmosphere, continuous sonication was performed for 3 h using a VCX-505 sonotrode (Sonics & Materials，20 kHz, 1 cm^2 Ti horn) at 50 W input power. This process successfully produced iron oxide with nanosized hollow cores.

Overall, sonochemistry demonstrates advantages in reducing processing times and lowering energy and chemical consumption by introducing hotspot environments and reactive species into liquids, effectively advancing more sustainable chemical reactions and processes [35].

1.3.2 Sonoprocessing

Chemical and mechanical effects commonly occur in parallel during acoustic cavitation. Where sonochemistry focuses on enhancing chemical reactions through cavitation hotspots, sonoprocessing is generally driven by the mechanical effects of cavitation as described in §1.1 to enhance multiphase systems and material processing. The process intensification can generally be classified into three types:

Enhanced mass and heat transfer As the ultrasound waves propagate through a liquid, part of the acoustic energy is dissipated, establishing momentum gradients that drive a bulk flow known as acoustic streaming [48]. In addition, the nonlinear oscillations and collapse of cavitation bubbles induce intense microscale disturbances locally, triggering the onset of acoustic microstreaming and turbulence [49], [50], [51]. These combined flow effects accelerate liquid renewal and mixing, enhancing local convective transport, resulting in an overall intensification of heat and mass transfer performance.

Setareh *et al* [49] experimentally investigated the enhancement of heat transfer performance in a double-pipe heat exchanger using power ultrasound. The inner diameter, outer diameter and length of the inner pipe are 8 mm, 10 mm, and 1200 mm, respectively. The inner diameter and length of the outer pipe are 25 mm, and 892 mm, respectively. A 3 kW Langevin transducer was employed to apply ultrasonic vibration to the inner tube, with water at 60 ℃ and 20 ℃ flowing through the inner and outer pipe, respectively. The results demonstrated that the acoustic power raised the outlet temperature of the cold water and lowered the outlet temperature of the hot water, indicating enhanced heat transfer. When the flow rates on both sides were set to 0.5 $L \cdot min^{-1,}$ the heat transfer efficiency increased by 60% compared with the case without sonication.

Dispersion and deagglomeration The shockwave, shear forces, and jetting induced by bubble collapse can disrupt the weak Van der Waals - dominated bonds within agglomerates, thus promoting deagglomeration and dispersion, and shifting the particle size distribution towards smaller scales [52]. In immiscible liquid systems, larger droplets can also be fragmented by the same mechanical perturbations into finer droplet clusters, leading to emulsification [53].

In dispersion and deagglomeration, ultrasonic melt processing can fracture and refine larger intermetallic grains in molten metals, thereby improving the mechanical and electrochemical

performance [54], [55], [56]. EI-Hadad *et al* [54] sonicated an Al-10 wt% Ce alloy melt for 100 s using a 21.4 kHz, 4 kW sonotrode. Scanning electron microscopy (SEM) results showed that sonication at 655 ℃ disrupted the original elongated particle morphology in the alloy, reducing the size from 30 μm to 3 μm.

Sonoprocessing can be utilised for emulsion preparation through the production of nanoemulsions (a metastable micrometre-scale oil-in-water dispersion), which can be used in the pharmaceuticals as drug delivery carriers [57], [58]. Laxmi *et al* [59] prepared artemether nanoemulsions by sonicating artemether and coconut oil using a sonotrode (D.P. 120, Lark USA) at 40% amplitude with a 6 s/3 s on/off pulse cycle for 3 min. The resulting nanoemulsion exhibited an average particle size of 79 nm with a drug content of 98.42 ± 0.87%. In vitro drug release experiments using simulated intestinal fluid, the nanoemulsion exhibited a 2.5-fold increase in drug-release rate compared with artemether (plain drug), indicating its potential as an effective alternative for improving artemether bioavailability.

Delamination and erosion Under power ultrasound conditions, sustained inertial cavitation continuously generates jets and shockwaves, subjecting solid surfaces to repetitive high-intensity pulsed loading. This can accumulate fatigue damage and promote microcrack initiation and growth, eventually causing coating debonding, delamination of layered structures, or surface erosion [60].

In delamination and erosion, ultrasonic cleaning is a mature technique in precision manufacturing and instrument maintenance, capable of removing contaminants from crevices that are inaccessible by traditional methods while minimising damage to material surfaces [61], [62]. Huang *et al* [63] experimentally compared the cleaning performance of chemical cleaning (soft-bristle toothbrush with fluoride toothpaste), chemical cleaning (denture cleaning tablets), and ultrasonic cleaning (KQ3200E, Kunshan Ultrasonic Instruments Co., China) using a coffee-stained orthodontic retainer model (PET-G, 0.040” × 5”, FDA-approved; JBC and Company, USA). The results showed that ultrasonic cleaning was the most effective at restoring the optical transmittance of the retainer while maintaining its transparency. Compared with the localised surface roughening caused by mechanical cleaning, ultrasonic cleaning better preserved surface integrity and minimised abrasion.

In the field of electronic-waste (E-waste) processing and metal recovery, Xie *et al* [64] developed an ultrasonic-leaching technology for separating copper and iron from printed circuit board (PCB) residues (Patent Title: Ultrasonic assisted heavy metal recovery. US

Application No.: 12/388,948; International Application No.: PCT/US2009/002063). This study employed a 160 W ultrasonic generator to sonicate 1 L of PCB sludge for 60 min at 25 ℃. Results demonstrated 97.83% copper dissolution into solution, whilst 98.77% iron was retained in the sludge in the form of precipitates. This process was subsequently implemented at an industrial heavy metal recovery plant in China. Using PCB residues containing 3.14%-4.85% copper and 3.71%-4.23% iron as feedstock, conventional hydrometallurgical processing achieved copper extraction efficiency of 80%-85%. With the ultrasound-assisted leaching technology, the recovery efficiencies of copper and iron increased to 95.2%-97.5% and 97.1%-98.5%, respectively.

1.4 Monitoring acoustic cavitation

As discussed in §1.3, acoustic cavitation gives rise to a wide range of bubble-mediated physical and chemical effects. The selection of appropriate methods for monitoring cavitation is therefore crucial for research into sonochemistry and sonoprocessing. Several commonly employed detection methods are outlined below.

1.4.1 Aluminium foil erosion test

The aluminium (Al) foil erosion test is widely used to evaluate cavitation distribution and relative intensity under sonotrode tip and within ultrasonic bath [65], [66]. When Al foil is placed within the ultrasonic field, shockwaves and jets produce pitting, erosion and mass loss. The erosion patterns or mass loss consequently serve as qualitative indicators for cavitation intensity [67], [68]. Observing Al foil erosion morphology within an ultrasonic bath allows simple assessment of the optimal cavitation region within the vessel. Although this method is highly sensitive to factors such as temperature, foil positioning and ultrasound frequency, and debris released during erosion may contaminate the reagent rendering subsequent measurements incomparable, it remains advantageous in its simplicity, low cost, and the permanent preservation of results [69].

1.4.2 Sonochemiluminescence

As described in §1.1, water molecules can dissociate into ·OH and ·H radicals under the extreme conditions within cavitation hotspots. The combination of these radicals can yield H_2O_2 as an intermediate product. Luminol ($C_8H_7N_3O_2$) can be oxidised in the presence of ·OH, emitting blue light at a wavelength of 430 nm under alkaline conditions. This phenomenon is referred as sonochemiluminescence (SCL) [70], [71]. As the luminescence

of the luminol system is closely related to the generation of cavitation-induced reactive species, the luminescent region can be taken as a proxy for the sonochemically active zone. The distribution of luminescence thus characterises the coverage and activity intensity of the cavitation field [72], [73]. Long exposure imaging with an optical camera can capture the SCL phenomenon in a darkened environment, enabling visual monitoring of cavitation active regions within the sonoreactor [74]. SCL is employed in Chapter 5 to enable the visual monitoring of the cavitation fields generated by a sonotrode and tube transducer. The method for preparing the solution is described in §3.9.

1.4.3 Acoustic detection

Detecting acoustic emissions generated by cavitation bubbles represent one of the simplest methods currently available. Devices commonly employed for acquiring acoustic signals include passive cavitation detectors (PCDs) and hydrophones. Both operate on the piezoelectric effect, converting pressure fluctuations in liquids into electrical signals. Acoustic emissions in liquids containing cavitation bubbles typically comprise a broad range of frequency spectral components. Applying a fast Fourier transforms to the time-domain acoustic signal yields a frequency-domain spectrum, enabling the identification of various acoustic components [34], [75].

Fig. 1.7 (a) and (b) displays representative emission spectra from a 20 kHz sonotrode with a 3.2 mm tip, operated at input power of 52 mW and 180 mW, respectively [76]. At 52 mW input power (fig. 1.5 (a)), the spectrum reveals the driving (or fundamental) frequency f_0 and its integer harmonics ($2f_0$, $3f_0$,$4f_0$, etc.), which originate from the periodic non-linear oscillations of cavitation bubbles [77], [78]. Subharmonic f_0/m, where m is an integer, are observed (at $f_0/2$) when the input power increases to 180 mW as shown in fig. 1.7 (b). This subharmonic peak has come to identify the beginning of stable-inertial cavitation, with the value of m incrementally increasing as input power rises[34]. The spectrum also contains ultraharmonic components at nf_0/m (where n and m are integers, and $n > m$), generated by the same group of cavitation bubbles producing the subharmonics [77], [78]. Moreover, broadband noise is observable in the spectrum, exhibiting a marked intensification in fig. 1.7 (b) compared to fig. 1.7 (a). This broadband enhancement is considered associated with inertial cavitation, and is attributed to mechanism such as chaotic oscillations of bubble or shockwaves produced during bubble collapse [78], [79].

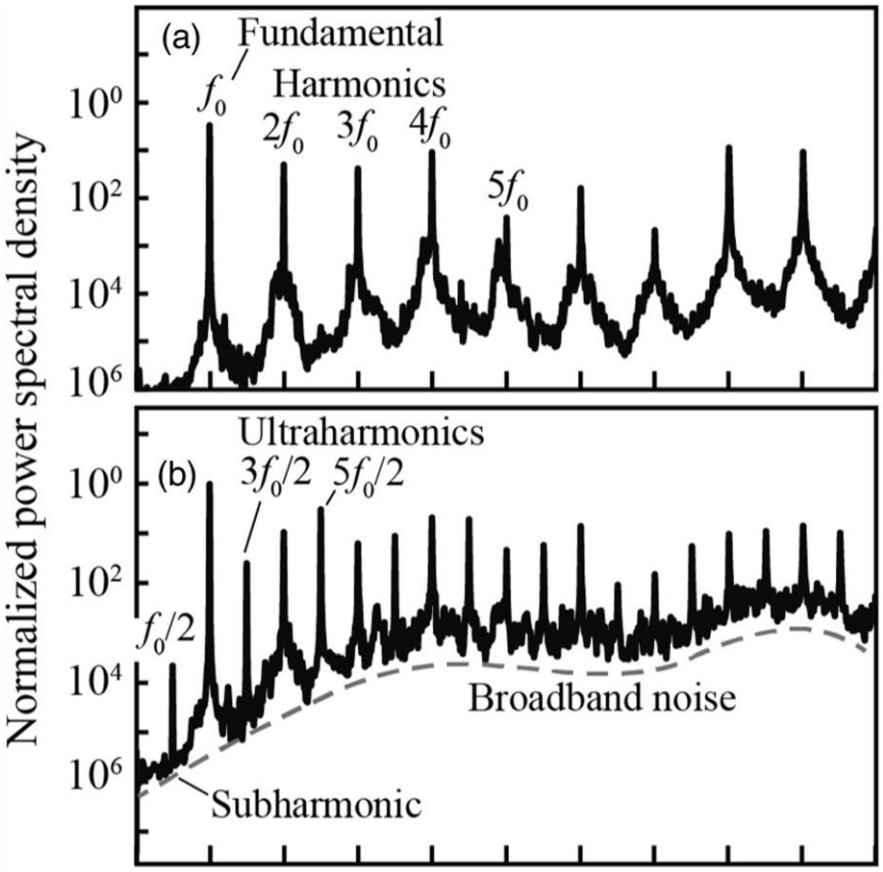

Fig. 1.7: Cavitation noise spectrum generated by cavitation bubble clusters under a 20 kHz sonotrode with a 3.2 mm tip diameter, at input powers of (a) 52 mW and (b) 180 mW. Taken from [76].

According to the technical standard for measuring cavitation noise in sonotrodes and ultrasonic baths published by the International Electrotechnical Commission (IEC), the acoustic emission spectrum of power ultrasonic devices with a fundamental frequency in the range of 20-150 kHz is classified into three components: direct field, stable cavitation, and inertial cavitation [80]. The dominant peak at f_0 is attributed to the direct field; harmonics, subharmonics and ultraharmonics are attributed to stable cavitation, while the broadband noise between spectral peaks is taken to represent inertial cavitation. This classification, however, is insufficient to fully describe the acoustic characteristics of cavitation noise. For instance, stable cavitation bubbles can also oscillate at the f_0 frequency and contribute to the fundamental peak [79], [80]. Nonlinear distortion during ultrasonic propagation in liquid can also generate harmonics [81]. Research in CavLab further indicates that subharmonic and ultraharmonic can arise when cavitation bubbles undergo periodic collapse [9]. Consequently, the simple binary division into stable and inertial cavitation fails to adequately summarise acoustic emission features, and it is necessary to introduce a third type, ‘stable-inertial cavitation’, detailed in §1.2.1.

Because the cavitation emission spectrum are highly nonlinear and broadband, an appropriate detector with a suitable frequency-response range should be selected for the target band prior to signal acquisition [75], [82]. Commercial PCDs are widely adopted in experiments, with models typically selected based on experimental requirements and operational bandwidth [29]. However, details of the internal structure and material parameters (including active elements) are proprietary and are generally not disclosed [29]. Commercial needle [83] or capsule hydrophones [84] as an alternative are also a common choice for cavitation emission monitoring. In-house fabricated PCDs are another common option, with active sensing elements typically composed of polyvinylidene fluoride (PVDF). Here, selection of element thickness, matching and backing layer materials enables customisation of bandwidth and sensitivity according to requirements [29].

1.4.3.1 Shockwave passive cavitation detector

Performance characterisation of a passive cavitation detector optimised for subharmonic periodic shock waves from acoustic cavitation in MHz and subMHz ultrasound.

Kristoffer Johansen, Jae Hee Song, Paul Prentice. Ultrasonics Sonochemistry, vol. 43, pp 146-155, 2018

To enhance detection sensitivity to the low-frequency components within periodic shockwaves, Johansen *et al* [29] independently designed and constructed a shockwave passive cavitation detector (swPCD).

As shown in fig. 1.8, (a) presents the fabricated swPCD, while (b) shows the cross-sectional structure, comprising the active element, backing layer, and electrical connections. The active element comprises a PVDF film with a diameter of 15 mm, thickness of 110 μm, and acoustic impedance of 4.56 MRayl. A high acoustic impedance Tungsten-Epoxy backing layer (>10 MRayl) was used to shift the resonant frequency of the PVDF film into the MHz and sub-MHz sensitivity bandwidth. The choice of the bandwidth was guided by the bubble collapse shockwave spectrum reported by Johansen *et al* [82].

The HIFU transducer described in §1.2.1 was used as the acoustic excitation source in the experiment, with a geometric focal length of 68 mm. The driving frequency was set to 220 kHz. A 20 mm aperture was positioned at the transducer centre, within which the swPCD could be positioned for acoustic emission acquisition. A laser-induced single cavitation bubble was nucleated at the ultrasound focus. A commercial Y-107 hydrophone (Sonic

Concepts Inc, WA, USA) was currently employed to comparatively evaluate the performance of swPCD. The Y-107 features a claimed bandwidth of 10 kHz - 15 MHz. The active element comprises a PVDF stack with a thickness of 0.2 mm and a diameter of 1 mm, backed by a high acoustic impedance backing material (>4 MRayl). Y-107 was positioned 68 mm from the focus during experiments to ensure a fair comparison with the swPCD.

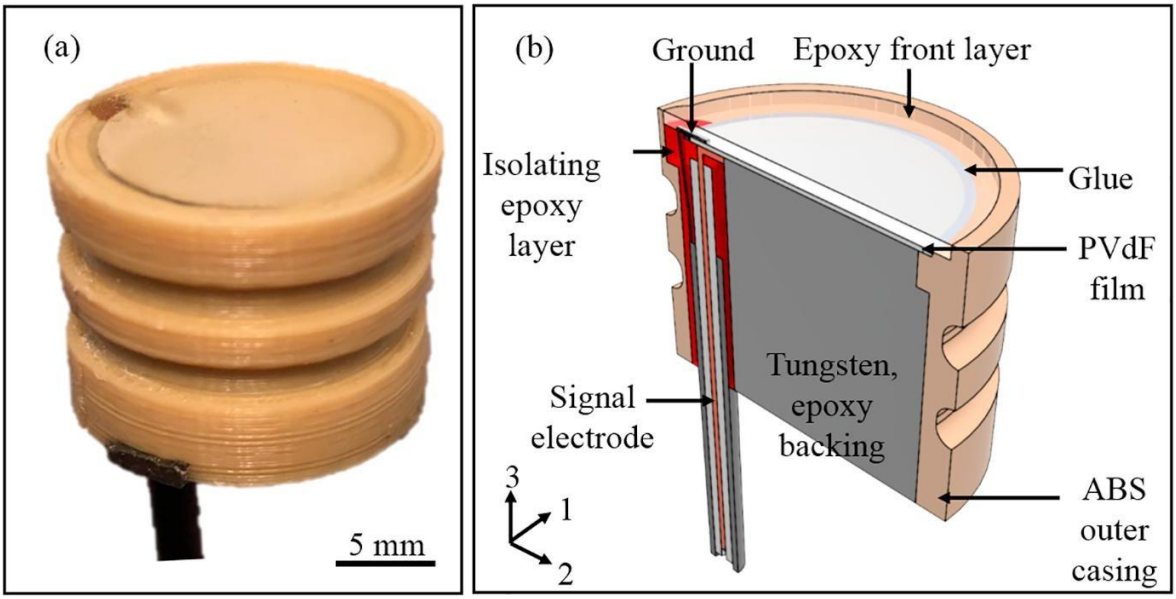

Fig. 1.8: (a) Final stage swPCD, (b) schematic cross-section of the swPCD. Taken from [29].

The time-domain waveforms in fig. 1.9 (a), obtained from a laser-induced single cavitation bubble, demonstrate that the swPCD offers higher sensitivity, with a measured shockwave amplitude approximately four times than recorded by the Y-107. In the frequency-domain comparison, the swPCD exhibits an approximately 30 dB higher signal to noise ratio (SNR) than Y-107 at 2 MHz and maintains superior sensitivity over the frequency range up to 3 MHz, fig. 1.9 (b). This increased sensitivity, however, is achieved at the expense of reduced temporal resolution. Moreover, the larger active element area of the swPCD leads to poorer spatial directivity.

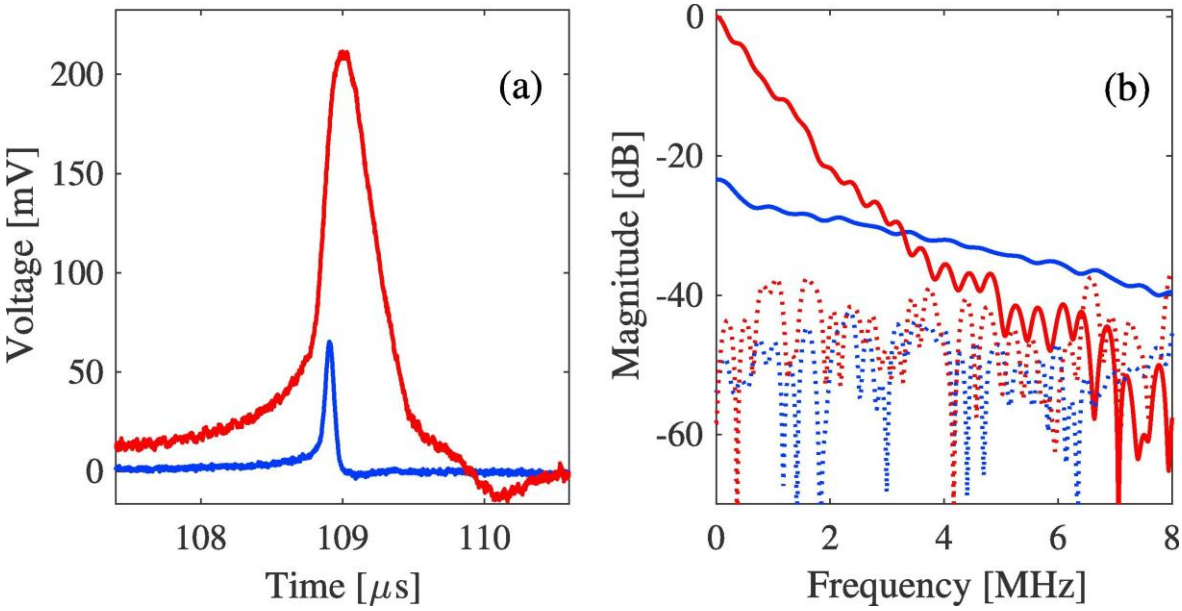

Fig 1.9: (a) Voltage trace comparing swPCD (solid red) and Y-107 (solid blue) for detection of a laser-induced bubble collapse shockwave. (b) Spectra of shockwaves in (a), and stapled data represents the noise floor. Taken from [29].

To address the issues outlined above, Jacobson [33] further optimised the swPCD design by reducing the diameter of the active element to 10 mm. This swPCD was selected as the primary acoustic signal detector for subsequent experiments. The fabrication process for the improved swPCD is detailed in §3.7.

1.5 Power ultrasound reactor configurations for liquid phase sonoprocessing

Power ultrasonic reactors used in both laboratory and industrial applications predominantly employ Langevin transducers as the core acoustic source. A typical Langevin transducer, as shown in fig. 1.10, comprises a head (or front) mass, piezoelectric elements and a tail (or back) mass [85]. The piezoelectric elements are constructed from stacked piezoelectric ceramic rings, converting electrical energy into longitudinal mechanical vibration. The tail mass is fabricated from a high-density metal with high-acoustic-impedance, which reflects the longitudinal waves generated by the piezoelectric elements forward. The head mass is manufactured from a metal with both lower acoustic impedance and density than the tail mass, facilitating the forward transmission of acoustic energy. These three components are clamped through a central high-strength bolt to provide overall pre-stress and structural constraint. This process prevents fracture of the piezoelectric elements during expansion and

ensures longitudinal pressure is transmitted throughout the transducer with minimal mechanical loss [86], [87], [88].

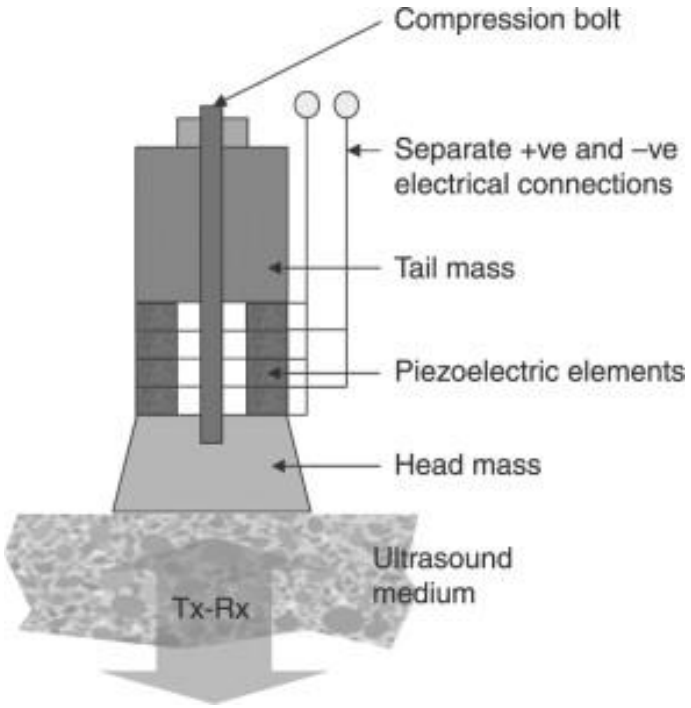

Fig. 1.10: Diagram of Langevin transducer structure. Taken from [85].

Power ultrasonic reactors almost exclusively utilise the Langevin transducer. Whilst their design and manufacture may have evolved to suit specific applications, these reactors fundamentally operate with the Langevin transducer as the actuator of ultrasound generation. These reactors are commonly categorised as batch or flow-based systems according to the operational perspective [89], [90]. Significant variations exist within each category however, concerning transducer quantity, reactor geometry, sonication mode, flow conditions, and the cavitation structure. The following sections therefore introduce batch and flow-based reactors in turn.

1.5.1 Batch sonoreactors

1.5.1.1 Sonotrode-based batch sonoreactors

The fundamental frequency of sonotrodes generally operate between 20-30 kHz [91], with a structure composed of a Langevin transducer, booster and horn as shown in fig. 1.11 (a) [92]. Since the vibration amplitude of the transducer is typically only a few micrometres, whereas the amplitude at the horn tip commonly requires tens to hundreds of micrometres, a booster is placed between the transducer and horn to amplify the displacement and achieve

mechanical impedance matching. The booster typically employs an inverted trapezoidal or stepped geometry, whose gradient interface not only enhances displacement gain but also concentrates vibrational energy [92].

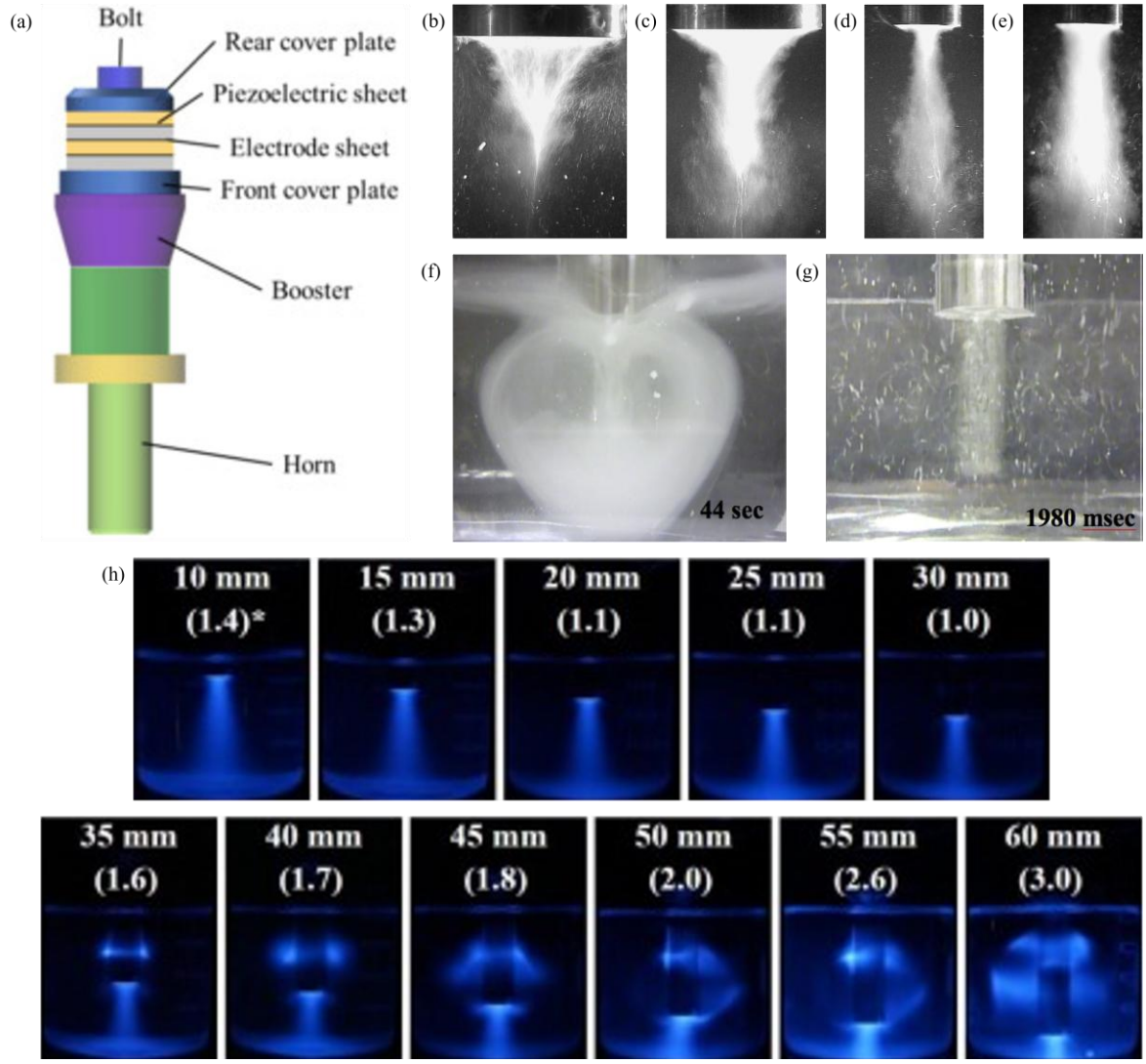

Fig. 1.11: (a) Diagram of sonotrode structure. Taken from [92]. Cavitation structures in water at average acoustic intensity at the radiating surface of 8.2 W·cm^{-2} for sonotrode tip diameters of (b) 120 mm, (c) 80 mm, and (d) 20 mm. (e) Cavitation structure in water at 80 W·cm^{-2} using a 20 mm sonotrode tip. Taken from [93]. Cavitation structures at 100% input power with a 40 mm tip in (f) glycerine and (g) ethanol. Taken from [94]. (h) SCL images at 50% input power and 10-60 mm probe immersion depth. Taken from [95].

The horn connects to the front of the booster, with the tip directly immersed in the liquid, where the amplified vibrations are directly coupled into the liquid to induce high-intensity cavitation [91], [96]. This configuration also allows the transducer and booster to be

positioned above the liquid, reducing corrosion and contamination risks for critical components [89]. Horn modules are typically designed in multiple shapes and sizes to accommodate varying liquid volumes, tip power densities, and radiation areas [89].

Cavitation induced by a sonotrode is typically confined to a limited region beneath the tip, with the structure of the cavitation bubble cluster varying according to liquid properties (such as viscosity), tip geometry, the power density and the probe immersion depth. Moussatov *et al* [93] compared cavitation structure in water at 20.7 kHz with tip diameters of 120, 80, and 20 mm, fig. 1.11 (b)-(d). At identical average acoustic intensity at the radiating surface of 8.2 $W \cdot cm^{-2}$, the 120 mm diameter tip more easily formed a cone-like cavitation structure. Turbulence in the liquid near the tip surface significantly intensified with the diameter decreased, making the cone structure more susceptible to disturbance and exhibiting unsteady characteristics. When the power density was further increased to 80 $W \cdot cm^{-2}$ with the 20 mm tip, the pronounced coupling between turbulence and cavitation further intensified the disordered behaviour, causing disappearance of the cone structure, fig. 1.11 (e). In addition to tip geometric effects, liquid properties equally alter the structure of cavitation bubble clusters. Tzanakis *et al* [94] observed vortex-like cavitation structures with distinct recirculation trajectory in glycerol at 100% input power using a 40 mm tip diameter sonotrode, fig. 1.11 (f). Cavitation bubble clusters formed beneath the tip and migrated downward, redirecting at the base before ascending along both sides and ultimately reaching the tip edge. Conversely, cone or vortex-like structures struggle to form beneath the tip in ethanol. Bubbles predominantly generate, oscillate, and float in a dispersed manner throughout the active zone, fig. 1.11 (g). Son *et al* [95] investigated the influence of sonotrode immersion depth on cavitation structures. The 13 mm diameter tip of a 20 kHz sonotrode (VCX-750, Sonics & Materials Inc., USA) was immersed in a 500 mL beaker filled with water and operated at 50% input power. SCL results revealed that a highly active cavitation bubble cluster could be observed near the mid-section of the immersed probe when the immersion depth exceeded 35 mm, fig. 1.11 (h). With further increases in immersion depth, the cavitation zone surrounding the probe continued to expand. The overall cavitation zone could be divided into two parts: (i) the region between the tip and the bottom of the vessel; (ii) the lateral cavitation zone formed around the immersed probe.

Sonotrodes are primarily employed in sonochemical research and sonoprocessing applications where high-intensity cavitation effects are required, including disintegration [97], melting processing [55] and food processing [98]. From the perspective of industrial scale-up and long-term stable operation however, it presents several limitations. Firstly, the

high-intensity cavitation zone is concentrated in the localised region beneath the tip, making it difficult to achieve cavitation coverage over larger volumes. Secondly, high-intensity cavitation accelerates erosion of the tip, shortening the service life of the horn [99]. Wear debris contaminates the treating liquid and compromises the experiment results, while frequent maintenance and replacements increase operational costs [89], [100]. Some horns employ replaceable tip designs to reduce expenses however, their use in organic solvents or low surface tension liquids should be avoided. Such liquids may infiltrate the joint gap between the probe and the replaceable tip, cause isolation and preventing the tip from vibrating at resonance frequency, eventually leading to damage [89]. Thirdly, acoustic energy dissipation and cavitation collapse convert substantial energy into thermal energy absorbed by the liquid, particularly in small volume treatment applications. Liquid temperature may consequently rise uncontrollably, adversely affecting cavitation efficiency. Consequently, external cooling systems are commonly implemented to maintain a stable operating temperatures, albeit with increased system complexity [101], [102].

1.5.1.2 Ultrasonic cup-horn reactors

The ultrasonic cup-horn reacors are similar to sonotrodes in both structure and operating principles, distinguished as an inverted sonotrode arrangement and the attachment of a cup-shaped reaction vessel externally to the horn [103], fig. 1.12 (a). Ultrasound transmitted upwards from the vessel base radiates into the liquid. Cup-horn reactors possess a larger transducer radiation area compared to sonotrodes, resulting in a power density reduction of approximately 50-fold and diminished cavitation intensity. This configuration partially mitigates the risk of erosion at the radiation surface [96].

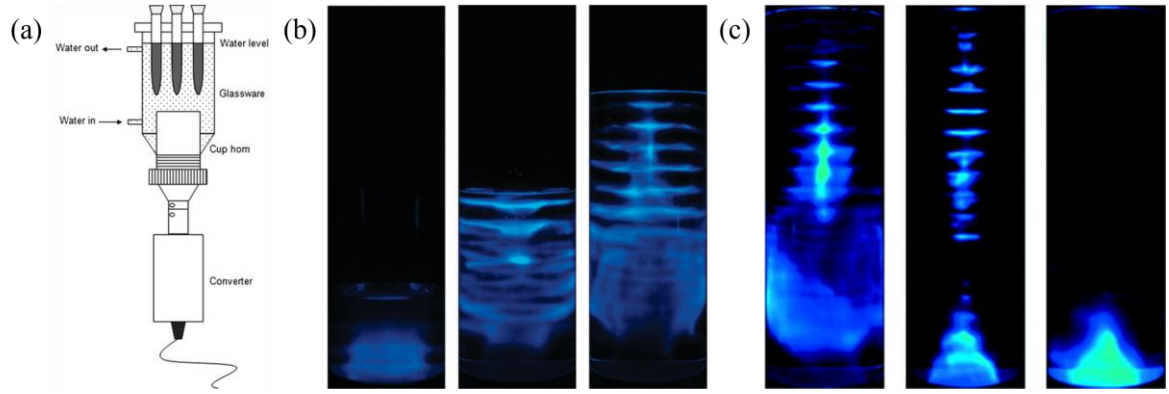

Fig. 1.12: (a) Diagram of ultrasonic cup structure. Taken from [103]. (b) SCL images of cavitation structure in a 110 mm diameter cup-horn reactor at 36 kHz and 74 W input power, for water height of 10, 20, and 30 cm. Taken from [104]. (c) SCL images of cavitation structure at 40 cm water height under 30, 40, and 90 W input powers. Taken from [105].

SCL is widely used to visualise cavitation field within a cup-horn reactor. Son *et al* [104] investigated the effected of 10, 20, and 30 cm water height on the cavitation structure in a 110 mm diameter cup-horn reactor operated at 36 kHz and 74 W input power, as shown in fig. 1.12 (b). At 10 cm water height, the SCL was dominated by travelling waves extending upwards from the transducer. When the water height increased to 20-30 cm, SCL structures induced by travelling waves appeared in the lower part of the reactor, while the upper exhibited a striped standing wave pattern. The author speculates that the overall SCL morphology was governed by the travelling waves when travelling and standing waves components coexisted within the same region. Strip-like structure was more readily activated and maintained when the travelling and standing waves became spatially separated.

Fig. 1.12 (c) further illustrates the evolution of cavitation structure at 40 cm water height for 30, 40, and 90 W input powers [105]. The lower half of the reactor exhibits travelling wave SCL structure, while striped standing-wave bands were visible in the upper half at 30 W input power. As the input power increased, the travelling wave SCL region contracted towards the transducer surface and adopted a cone shape, while the striped standing wave structure progressively narrowed towards the central axis until vanishing. This phenomenon was attributed to enhanced acoustic attenuation associated with the aggregation of cavitation bubbles into larger bubbles within the travelling wave dominated region. The bubble density was lower and attenuation was weaker at lower input power, allowing acoustic energy to reach the upper liquid and sustain the striped structure. However, increased power causes a proliferation of bubbles near the transducer, forming a dense bubble cloud that acts as a

shielding layer. Acoustic energy struggles to penetrate this barrier, suppressing or even eliminating the upper standing wave stripe structure.

Cup-horn reactors, in contrast to sontorodes, can operate not only in a direct mode but also in an indirect mode. The cup is filled with acoustic coupling medium in the indirect configuration, while the target liquid is contained in a separate vessel (e.g., a test tube) and immmersed into the cup for sonication [103], [106]. This configuration both prevents direct chemical attack of the transducer surface by corrosive media and helps mitigate the risk of contamination. Cup-horn reactors are widely used in applications such as acid leaching of heavy metals [103], organic synthesis [107], nanoparticle preparation [108], and the degradation of aqueous contaminants [109]. The design also enables multiple samples (up to eight) to be sonicated in parallel yet independently, eliminating cross-contamination, an advantage that is difficult to achieve with sonotrodes. Consequently, the reactors are frequently employed for cell disruption, liposome preparation, and protein shearing [89].

1.5.1.3 Ultrasonic bath reactors

Ultrasonic baths are commonly used in laboratories owing to their simple construction and low cost. A typical unit comprises a rectangular stainless steel tank with multiple Langevin transducers bonded to the base and/or side walls [96]. The number and spatial arrangement of the transducers are selected according to the tank volume and the target operating conditions (e.g., frequency, input power, or multi-frequency operation), to meet diverse application requirements for cavitation intensity and spatial coverage [91]. Ultrasonic baths can incorporate heating/cooling systems and power regulation modules for controlled operation, with parameter adjustment achieved via external electronic controller [89].

Conventional ultrasonic baths employ epoxy resin to affix transducers externally to the tank [91], [96]. Constrained by enclosure packaging, details of the transducer mounting are inaccessible for direct observation [89], as shown in fig. 1.13 (a). an alternative configuration employs immersible transducer modules, where multiple Langevin transducers are sealed within a rectangular metal enclosure. This module is then positioned at the bottom, aide, or top of the tank, fig. 1.13 (b). This immersible module offers greater design flexibility compared to externally mounted setups, enabling adjustment of the ultrasonic radiation direction and coverage area by altering installation position, orientation and quantity, thereby providing additional design freedom for enhancing cavitation activity within a target region [89], [91]. The third, more novel reference vessel was developed by the National Physical

Laboratory (NPL), fig. 1.13 (c). This apparatus employs a cylindrical vessel measuring 330 mm in height, with an internal diameter of 312 mm and a volume of 25 L. Thirty 25 kHz PZT transducers are affixed to the outer surface of the vessel and distributed axially in three horizontal rows (ten transducers per row). The system operates with three generators driving each respective row of transducers, with each row capable of receiving a maximum input power of 600 W, corresponding to a maximum power density of 27 $W \cdot L^{-1}$.

Ultrasonic baths can be operated in both direct and indirect modes [110]. Direct sonication involves immersing the sample directly into the bath liquid. Indirect sonication requires placing the sample in a secondary vessel (e.g., beaker or test tube) filled with reagents, which is then submerged into the bath containing the coupling liquid for sonication. Direct sonication exposes the tank to chemical reagents over prolonged periods, increasing corrosion and contamination risks while shortening device lifespan. Indirect sonication is therefore predominantly employed in practical applications involving highly corrosive solvents or where cross-contamination of systems must be avoided [111].

Ultrasonic baths are capable of establishing an acoustic treatment zone over a large volume of liquid, the acoustic field and cavitation activity however, exhibit pronounced spatial non-uniformity [112]. Jenderka *et al* [113] characterised the acoustic field in a 4 L ultrasonic bath (Elmasonic S150, Elma, Germany) which full with 128 mm height water using a hydrophone (B&K 8103). The result revealed a standing wave dominated field, fig. 1.13 (d). The erosion result obtained using the Al foil erosion method, as shown in fig. 1.13 (e), further indicates that cavitation activity does not uniformly cover the whole tank but corresponds to the spatial distribution of the standing wave field. The SCL image of fig. 1.13 (f) by using NPL reference vessel acquired at an input power of 350 W and 25 kHz indicates that cavitation forming concentric annular structures centred on the reactor axis. It exhibits higher SCL intensity in the central region compared to surrounding areas, corresponding to a more pronounced ultrasonic focal zone.

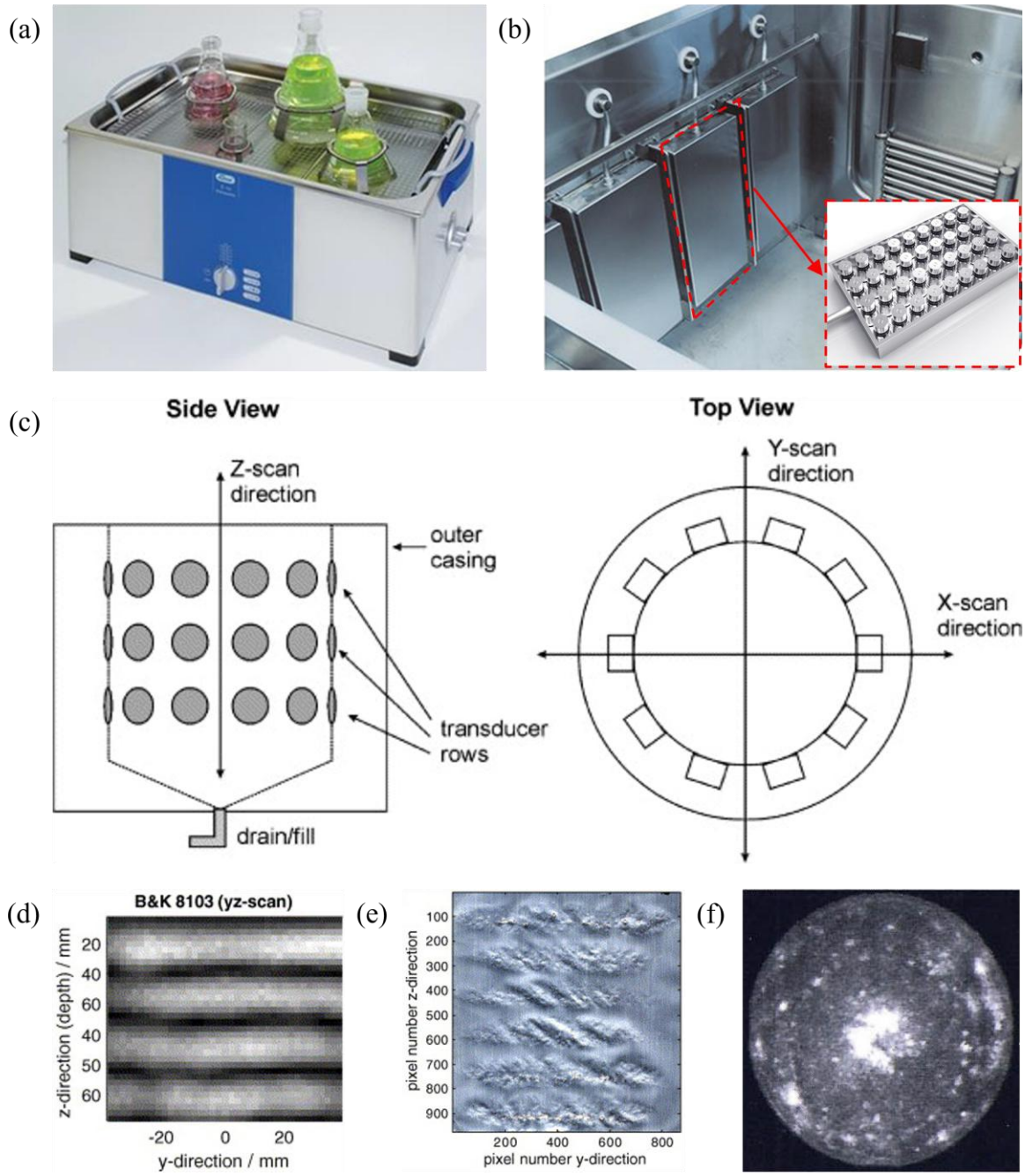

Fig. 1.13: (a) Diagram of Elmasonic S150 ultrasonic bath. (b) Diagram of industrial ultrasonic bath (CTG Asia), the enlarged view of the rectangular metal box fitted with multiple transducers is indicated by the red arrow. Taken from [89]. (c) Schematic of NPL reference vessel. Taken from [114]. (d) Pressure amplitude diagram obtained from hydrophone scanning of the y-z plane. (e) Image of Al foil erosion after sonication. Taken from [113]. (f) SCL image of NPL reference vessel at 350 W input power and 25 kHz. Taken from [115].

The application of ultrasonic baths spans a wide range of fields, including extraction [116], cleaning [117], electrodeposition [118], water treatment [119], and synthesis [120]. As the sonication volume within the bath reaches several litres or more, the acoustic power density

(per unit volume) falls at least 100 times lower than sonotrode, resulting in comparatively weak cavitation intensity [89], [96]. Ultrasonic baths are primarily suited for applications such as cleaning and synthesis, where large processing volumes are required but high cavitation intensity is not essential [89].

1.5.2 Flow-based sonoreactors

Continuous reactors offer greater flexibility in reactor design compared to batch reactors and are increasingly being adopted for industrial applications.

1.5.2.1 Flow-based sonoreactors with transmitting walls

Flow-based reactors with transmitting walls adopt polyhedral and cylindrical geometries. Both configurations achieve cavitation enhancement within large liquid volumes by superimposing acoustic fields via multiple Langevin transducers mounted on the outer surface of the vessel. However, differences in boundary geometry and ultrasonic reflection conditions lead to distinct cavitation structures.

Polygonal flow-based reactors (primarily quadrilateral, hexagonal, and octagonal) employ transducer arrays affixed to the exterior of the polygonal vessel, fig. 1.14 (a). Multi-face radiation enables constructive superposition of the acoustic field within the chamber. Such apparatus permits multi-frequency radiation by arranging transducers of different operating frequencies across distinct walls. Gogate *et al* [121] developed a hexagonal flow cell with a total volume of 7.5 L, in which three 150 W transducers were installed on each wall and driven at 20, 30, and 50 kHz, enabling continuous flow operation under tri-frequency excitation. As shown in fig. 1.14 (b), the SCL image for the 24-40-70 kHz tri-frequency hexagonal reactor at 657 W input power reveals a hexagonal annular pattern of bright and dark cavitation structures concentrating around the reactor centre [122].

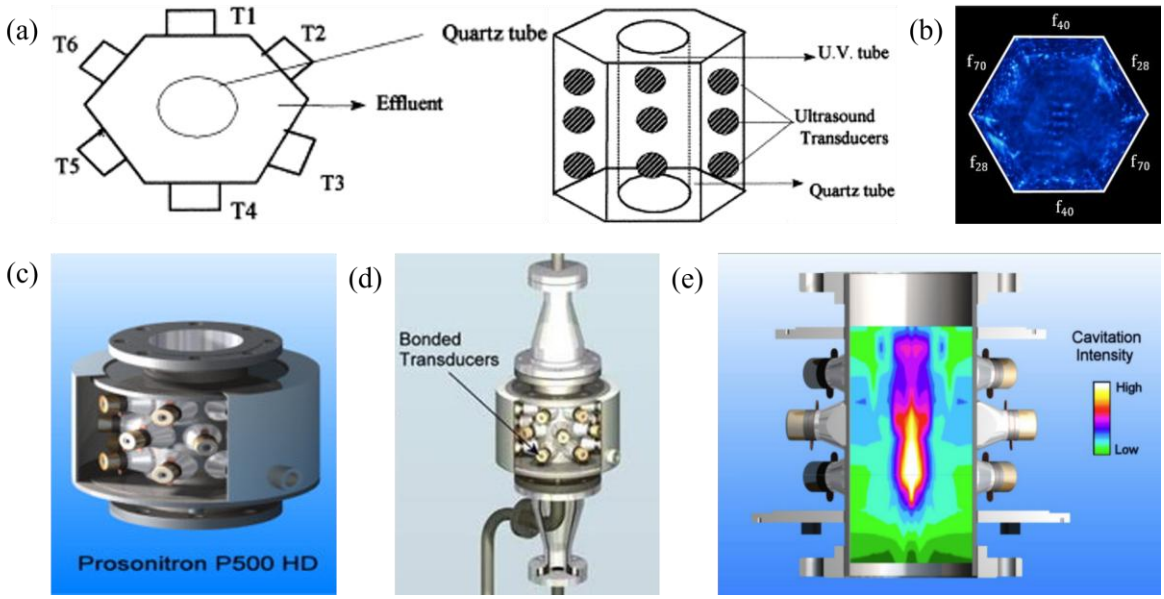

Fig. 1.14: (a) Diagram of tri-frequency hexagonal flow cell with 21 transducers. Taken from [121]. (b) SCL image taken for 28-40-70 kHz tri-frequency hexagonal sonoreactor at 657 W input power. Taken from [122]. (c) Prosonitron P500 HD 20 kHz flow cell. Taken from [123]. (d) Schematic of the Prosonitron P500 HD pipeline connection. (e) P500 HD cavitation intensity map acquired using an NPL acoustic sensor. Taken from [89].

The Prosonix Prosonitron P500 HD (Pfizer Global Manufacturing, Ireland) employs a 4.4 L cylindrical vessel design as shown in fig. 1.14 (c) & (d). A total of 21 transducers are uniformly distributed on the outer wall (maximum input power 600 W, operating frequency 20 kHz, total mass of the system is 49 kg) to achieve acoustic field focusing towards the reactor centre [89]. The spatial distribution of cavitation intensity for this apparatus is shown in fig. 1.14 (e). Its distribution characteristics are similar to those of the NPL reference vessel in §1.5.1.3, exhibiting a pronounced central focusing behaviour. Cavitation intensity is highest along the central axis, while the outer region shows relatively weaker, distributed in an annular pattern around the centre.

Flow-based reactors with transmitting walls have been experimentally investigated in wastewater treatment and lactose crystallisation. In the study on formic acid degradation, Gogate *et al* [121] reported that the 20-30-50 kHz tri-frequency hexagonal flow cell achieved a 4-8 fold higher energy utilisation efficiency, and a 1.5-20 fold increase in cavitation field than the sonotrode and ultrasonic bath, resulting in superior degradation performance. Zisu *et al* [124] investigated lactose crystallisation from concentrated whey using a Prosonix Prosonitron P500 at an energy density of 3.3 $J \cdot mL^{-1}$ and a flow rate of 11 $L \cdot min^{-1}$. The results showed that the crystallisation rate under sonication was higher than that achieved by stirring

within 3 h. Furthermore, the crystal size distribution obtained through sonication ranged from 38.39±10.02 µm, lower than the 57.9±17.71 µm achieved by stirring, demonstrating superior control over crystal size distribution.

1.5.2.2 Flow-based sonoreactors based on sonotrodes

Sonotrode-based continuous reactors represent another class of apparatus that combines high-intensity localised cavitation with flow-based systems.

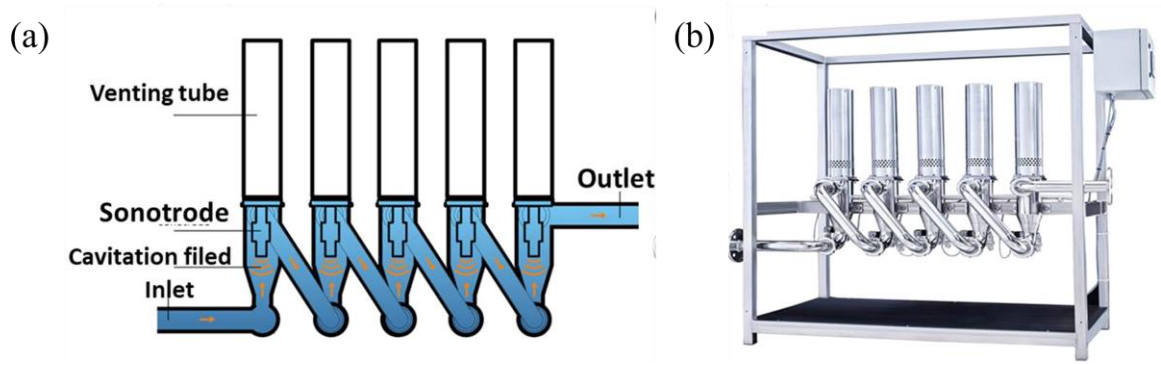

Fig. 1.15: (a) Scheme of ULTRAWAVES high-power ultrasonic system. (b) Photograph of ULTRAWAVES high-power ultrasonic system. Taken from [89].

The ULTRAWAVES high-power ultrasonic system (ULTRAWAVES Water and Environmental Technologies, Hamburg, Germany) as shown in fig. 1.15 (a) & (b) represents a typical series configuration [89]. This design sequentially arranges multiple sonotrodes within the reactor pipeline, subjecting the fluid to progressive sonication as it passes each tip. Such a system can utilise high-intensity cavitation to achieve cell or bacterial disruption and release of intracellular substances, or for sludge disintegration in wastewater treatment. The system can operate at an input power of up to 2 kW, with a processing capacity of approximately 2 $m^3 \cdot h^{-1}$.

1.5.2.3 Flow-based sonoreactors with high-intensity converging waves

The third flow-based design is geometrically similar to the cylindrical batch reactor described in §1.5.2.1. As shown in fig. 1.16 (a) & (b), Dion *et al* [125] developed and patented an acoustic reactor in which twelve prismatic piezoelectric transducers are arranged as an annular array around a 100 mm pipe fabricated from a compliant material (polytetrafluoroethylene, PTFE). High-intensity cavitation is concentrated in the central region within the pipe, fig. 1.16 (c), capable of perforating 1.5 mm thick hard Al alloy plates

within 5 min under full-power operating conditions. The system has been proposed for sludge floc sonication, with a maximum input power of 50 kW and a processing capacity of 9 $m^3 \cdot h^{-1}$. Notably, the design and fabrication of the system are relatively complex. The phase difference between adjacent transducers must be controlled to within 60° to achieve effective impedance matching between the transducers and the acoustic field. In addition, the vibration amplitude mismatch between transducers must be kept within an extremely narrow range to confine the cavitation region to the pipe centre.

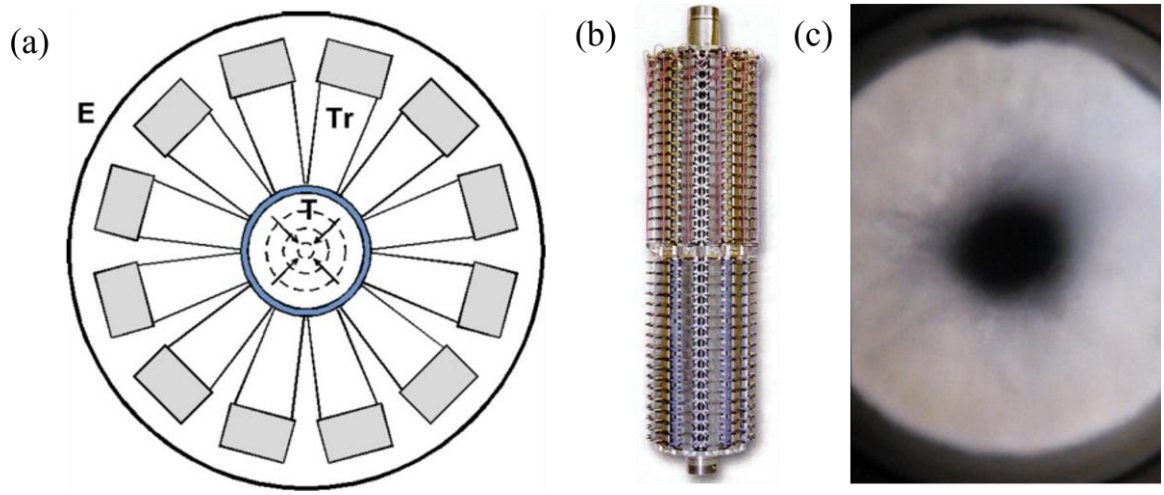

Fig. 1.16: (a) Schematic cross-section of the prismatic piezoelectric transducer-based cylindrical sonoreactor. (b) The core of the 50 kW cylindrical sonoreactor. (c) Cavitation region in the cylindrical sonoreactor. Taken from [125].

In summary, the continuous configurations outlined in §1.4.2 possess greater potential for high-throughput compared to the batch reactors described in §1.4.1. However, existing flow-based reactor designs generally operate at high input power levels, reaching up to 50 kW in some instances. Energy consumption and power supply configurations thus present critical constraints for large-scale industrial applications. The use of multiple transducers and synchronous control requirements significantly increase system complexity at the levels of driving electronics, control architecture, and integration. This leads to higher manufacturing costs while reducing system maintainability and scalability.

1.6 Thesis aims, objectives and contribution to knowledge

The preceding review of high-power ultrasonic devices and flow-based sonoreactors identifies a remaining design gap. Sonotrodes can generate intense cavitation, but their active

region is concentrated near the tip. Ultrasonic baths and cup-horn reactors provide wider treatment coverage, although the local cavitation field is generally less concentrated and strongly dependent on reactor geometry and acoustic coupling. Multi-transducer reactors can extend or focus the active region, but require multiple radiating elements and comparatively complex drive, impedance-matching and control arrangements. Consequently, there remains a need for a simple and modular reactor architecture in which a single radiating element can generate spatially distributed cavitation within an inline flow passage and can subsequently be combined with identical units for staged flow processing.

A related knowledge gap concerns the connection between transducer design and processing performance. Limited design-to-process evidence is available that links the electrical and mechanical behaviour of a tube-type ultrasonic source, the spatial distribution of cavitation within its bore, its material-processing capability, and its subsequent integration into a multiple-module flow system.

The overall aim of this thesis is therefore to develop and experimentally evaluate a modular tube-transducer architecture for spatially distributed cavitation and flow-based sonoprocessing, progressing from a single static module to a multiple-module recirculating prototype.

The specific objectives are to:

1. design, fabricate and electrically match a single radially poled tube-transducer module;

2. characterise the frequency response, backing-condition dependence and spatial cavitation field of the single tube transducer using acoustic and optical measurement methods;

3. compare the tube transducer with a conventional sonotrode as a controlled but geometrically non-equivalent reference, while acknowledging the limitations of this comparison;

4. evaluate whether the spatially distributed cavitation generated by the tube transducer can be translated into effective material-delamination performance, using graphite

removal from LiB anodes as the principal application case, and consider the engineering implications of damage to the copper current collector;

5. integrate three tube-transducer modules (fig. 1.17) in series within a recirculating system and evaluate the experimentally demonstrated operating range and principal engineering limitations of the resulting prototype.

Relative to the ultrasonic reactor configurations reviewed in this chapter, the principal contribution to knowledge is the integrated design and evaluation of a radially poled tube-transducer architecture from a single static module to a multiple-module recirculating system. The specific contributions comprise: (i) the detailed engineering implementation, electrical matching and acoustic and optical characterisation of a single tube-transducer module; (ii) experimental evidence connecting the spatially distributed cavitation field within the tube bore with material-delamination performance and current-collector damage; and (iii) the modular integration of three tube-transducer units into a recirculating prototype, together with identification of its experimentally demonstrated operating range and principal hydraulic limitation. The originality therefore lies in the design-to-process progression from single-module characterisation to multiple-module flow operation.

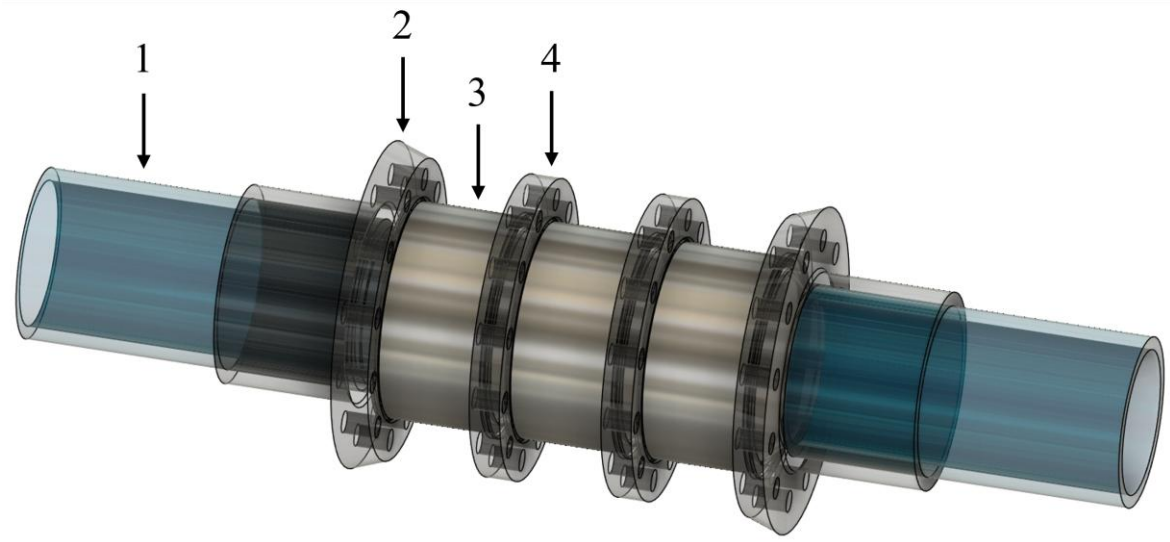

Fig. 1.17: Simple diagram of flow-based tube transducer system, 1. Pipe, 2. Pipe-to-tube connector, 3. Tube transducer, 4. Tube-to-tube connector.

Chapter 2

Technology critical metal retrieval from electronic waste and recycling methods

2.1 Overview of electronic waste

Electronic waste (E-waste) refers to electrical and electronic equipment (EEE) that has been discarded or retired by its owners [126], [127]. *THE GLOBAL E-WASTE MONITOR 2024* classifies E-waste into six categories: (1) temperature exchange equipment, (2) screens and monitors, (3) lamps, (4) large equipment, (5) small equipment and (6) small IT and telecommunication equipment, covering 54 product types in total [1]. In 2022, global E-waste production reached 62 Mt in total, amounting to approximately 7.8 kg per capita [126]. Based on an annual increase of 2.6 Mt, global E-waste production is projected to rise to 82 Mt by 2030 [126].

The rapid growth, low collection rates, and improper disposal of E-waste poses a series of risks to the environment and public health [126], [128]. E-waste contains hazardous compounds, including Mercury (Hg), Lead (Pb), Chromium (Cr), brominated flame retardants, and chlorofluorocarbons [129]. Based on 2022 data, 58 t Hg and 4,500 t plastics containing brominated flame retardants were released into the environment. The release of these pollutants causes persistent contamination of soil and water resources, and increases the risk of DNA damage, kidney damage, and cancer in humans [126]. In addition, 145 Mt of CO_2 were released into the environment due to the mismanagement of refrigerants, exacerbating global warming [126].

Alongside the environmental risks, E-waste possesses substantial resource and economic potential. Owing to its large quantities and the concentration of various technology critical metals (TCMs), E-waste is often described as an “urban mine” [130]. TCMs are particularly concentrated in end-of-life products such as mobile phones and computers; for instance, the Gold (Au) content is approximately 280 $g \cdot t^{-1}$, far exceeding that of conventional Au ores (typically 3-30 $g \cdot t^{-1}$) [131]. This marked disparity indicates that recovering TCMs from E-waste can be economically viable. In 2022, the raw materials contained in global E-waste were estimated to include 31 Mt of metals, with a total value of approximately $91 billion. The potential economic value of selected TCMs is summarised in table. 2.1 [126].

Table. 2.1: Potential value of selected TCMs from E-waste in 2022. Taken from [126].

Element	Production (kg)	Value ($)
Au	2.7×10^5	1.5×10^{10}
Ag	1.2×10^6	9×10^8
Ni	5.2×10^8	1.4×10^{10}
Pd	1.2×10^5	8×10^9
Rh	5.1×10^3	2.3×10^9
Co	3.4×10^7	2.3×10^9
Sb	2.8×10^7	3×10^8
Cu	2×10^9	19×10^9

2.2 Case study materials: printed circuit board and Lithium-ion battery

2.2.1 Printed circuit board

Waste printed circuit boards (PCBs) account for approximately 3-5% of the total mass of global E-waste [132]. A typical PCB consists of three main parts: a non-conductive substrate or laminate, conductive substrate printed on the surface or within the laminate, and component attached to substrate [133], fig. 2.1.

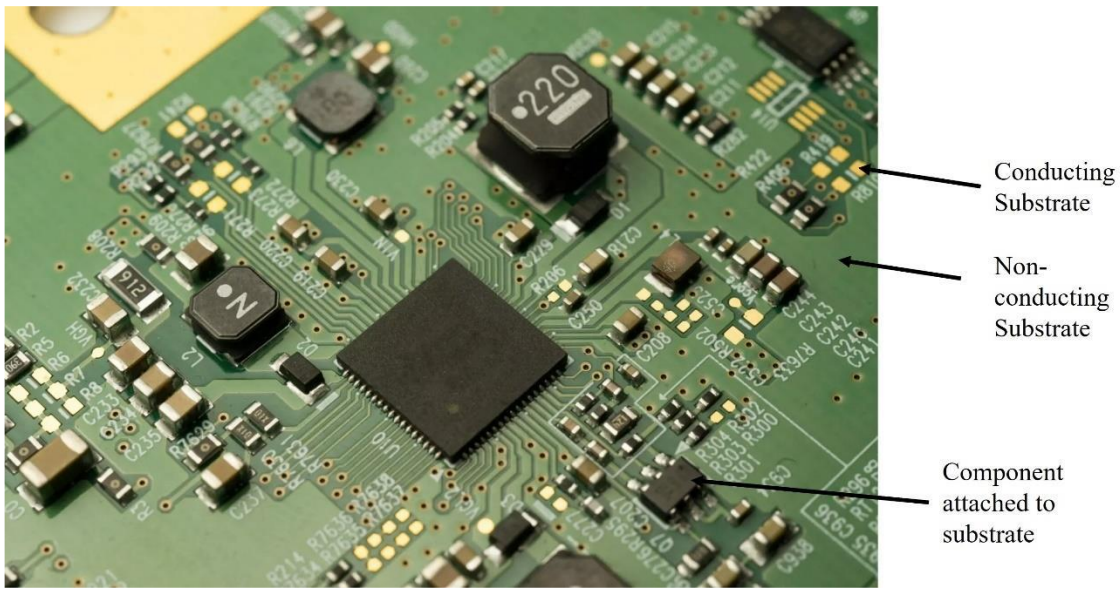

Fig. 2.1: Image of a PCB, in which components are connected via conductive pads on the non-conductive substrate. Taken from [33].

In terms of material composition, PCBs typically contain 30-35 wt% metals, 24-30 wt% resins, and 32-35 wt% refractory materials [134]. The average content of its metallic components can be summarised as follows: 11-28 wt% Copper (Cu), 8-36 wt% Iron (Fe), 3-20 wt% Aluminium (Al), 2-5 wt% Pb, 1-4 wt% Nickel (Ni), together with trace precious metals include 200-2800 ppm Silver (Ag), 150-2000 ppm Au, and 30-350 ppm Palladium (Pd) [134].

From a structural perspective, Cu commonly occupies 10-20% of the PCB area, forming the conductive layers that provide electrical connections between different components. Precious metals such as Au and Pd are used at contact points. Solder (primarily lead-tin) accounts for 4-6 wt% of a PCB and is used to join components to the conducting substrate [133]. In addition, certain Platinum (Pt) group metals are present in components such as relays, switches, and sensors [135].

The metal content of PCBs are typically 10-100 times higher than those of ores, underpinning their high recycling value [136]. However, improper disposal or informal recycling can release contaminants into the environment, posing severe risks to ecosystems and human health. This is largely attributable to the presence of heavy metals and brominated flame retardants, which are persistent and exhibit significant toxicity [137]. Moreover, the high degree of integration in PCBs leads to an intimate mixture of organics (epoxy resins, flame retardants), metal, and glass fibres, presenting substantial engineering challenges for material separation, recovery, and subsequent reuse [138].

2.2.2 Lithium-ion battery

Lithium-ion batteries (LiBs) are the core energy-storage devices for the new energy sector and are widely deployed in electric vehicles, portable electronics, renewable-energy integration, and grid-scale energy storage [139]. A typical LiB comprises components including the anode, cathode, electrolyte, separator, and casing [140], fig. 2.2.

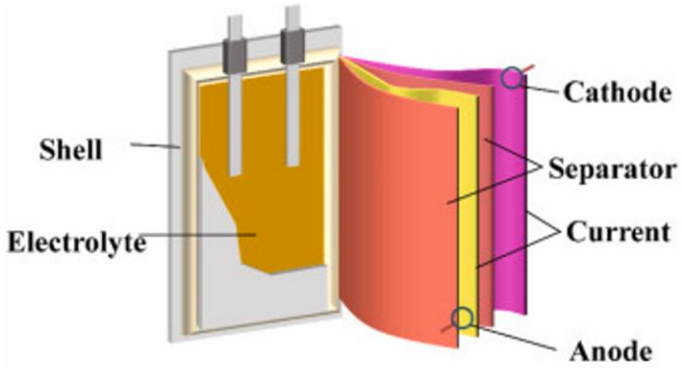

Fig. 2.2: Schematic diagram of the LiB components. Taken from [140].

The LiB anode primarily consists of a Cu foil current collector coated with graphite. Graphite powder is dispersed in an aqueous medium together with the binder styrene-butadiene (SBR), the thickener sodium carboxymethyl cellulose (CMC) and conductive agent acetylene black (SP) [141]. The slurry is then uniformly coated onto the Cu foil and subsequently vacuum-dried, rolled, and sheared to form the anode electrode [141]. The cathode consists of an Al foil current collector coated with active material, generally composed of lithium transition metal oxide, such as $LiCoO_2$ (LCO), $LiNi_xCo_yMn_{1-x-y}O_2$ (NMC), $LiFePO_4$ (LFP), $LiMn_2O_4$ (LMO) [142]. The cathode slurry is prepared by mixing the active material with the conductive agent SP, the binder Polyvinylidene difluoride (PVDF) and the solvent N-Methyl-2-pyrrolidone (NMP), followed by coating onto Al foil [141]. The subsequent preparation process for the cathode is similar to that for the anode.

The electrolyte comprises inorganic solutes such as $LiFP_6$, $LiBF_4$, $LiClO_4$, $LiCF_3SO_3$, and $Li(SO_2CF_3)_2$, and organic solvents such as dimethyl sulfoxide (DMSO), propylene carbonate (PC), and diethyl carbonate (DEC) [141], [142]. Polyethylene (PE), Polypropylene (PP) are commonly used as separator materials. The separator prevents direct contact between the cathode and anode, thereby avoiding internal short circuits, while allowing Li^+ transport through it [143]. The major components, material compositions, and their estimated cost proportions are summarised in table. 2.2 [142].

Table. 2.2: Composition, mass percentage and estimated material costs of commercial LiB. Taken from [142].

LiB components	**Material**	**Mass (wt%)**	**Estimated costs (%)**
Cell component	Steel or Al	20-25	2
Cathode	LCO, NMC, LFP, LMO	25-35	49
Anode	Graphite	10-19	16
Electrolyte	$LiPF_6$ dissolved in DMSO, PC, or DEC	9-15	6
Cathode current collector foil	Al	5-7	2
Anode current collector foil	Cu	4-9	5
Separator	PE, PP	1-12	16
Binder	PVDF	-	3
Others (additives)	Conducive carbon black, silicon, etc.	Balance	1

LiBs inevitably undergo ageing and failure processes, including capacity degradation, swelling, cracking and leakage during prolonged charge/discharge cycles, ultimately leading to retirement [143], [144]. Global demand for LiBs is projected to grow from 700 GWh in 2022 to 4,700 GWh by 2030 [145]. The service life of commercial LiBs averages approximately 10 years [146], with an energy density of approximately 300 $Wh \cdot kg^{-1}$ [147]. It is estimated that end-of-life LiBs will reach 15.7 Mt by 2040.

Aged LiB exposed to air is prone to a series of physicochemical reactions, including volatilisation, hydrolysis, oxidation and decomposition. Furthermore, residual charge in aged LiB can lead to short-circuiting during storage, increasing fire risk [148]. The cathode contains numerous TCMs, including Li, Cobalt (Co), Ni, and Al, and insufficient recovery can result in soil and water contamination [141]. The untreated anode graphite can easily lead to dust pollution [149]. The organic solvents in the electrolyte can volatilise and decompose, producing organic pollutants such as formaldehyde (CH_2O) and methanol (CH_3OH) [149]. Electrolyte salts (generally $LiPF_6$) are highly corrosive and react readily with water to form HF, causing fluorine pollution [150].

Additionally, aged LiBs are enriched in a range of TCMs. Reported mass fractions of TCMs in aged LiBs are substantially higher than those in natural ores, typically in the ranges of Co 5-20 wt%，Ni 5-10 wt%， Li 5-7 wt%，Cu 5-9 wt% [142], [151]. Graphite used for the

anode is a non-renewable resource; its market price generally ranges from $5,000-20,000 per tonne following mining and purification processes [152]. Consequently, the recycling of aged LiBs can mitigate resource scarcity and environmental burdens while offering substantial economic benefits. However, recycling technologies for aged LiBs remain immature, and systematic recycling infrastructures are not yet fully established, resulting in a global efficiency of only 5% [153].

In addition to the aged LiB, the LiB manufacturing process also generates production scrap, such as electrode scrap and substandard components [145]. With the expansion of LiB production, the quantity of production scrap is expected to increase markedly. Current assessments indicate a scrap rate of approximately 10% during LiB manufacturing [154], implying that production scrap could reach 1.57 Mt by 2030. Recycling must be considered at the point of scrap generation. Compared with aged LiBs, which have complex compositions and degraded performance, production scrap retains an intact structure and uniform chemical composition. It does not require complex steps such as discharging and dismantling. Direct recycling routes can be used to separate constituent materials more efficiently [145].

2.3 Traditional recycling methods for technology critical metals from PCBs and aged LiB

The resource recovery of PCBs and aged LiBs can be summarised into two main stages: pre-treatment and recycling. However, the specific processing routes are distinct due to significant differences in their structure and composition.

For PCBs, the pre-treatment process comprises three steps: manual dismantling, shredding, and physical separation [133]. Firstly, hazardous components (such as capacitors resistors, and relays) are selectively dismantled to prevent toxic elements from entering the main recycling process [133], [155]. Following the removal of hazardous fractions, PCBs are shredded to achieve size reduction. Subsequent physical separation steps split the metallic fraction from non-metallic constituents such as resin, glass fibre and plastic [133]. Common separation techniques include gravity separation, which exploits the density difference between metals (heavy) and non-metals (light), and electrostatic separation based on differences in electrical conductivity/resistivity [156]. The material enters the recovery stage after separation, where metals are refined and selectively recovered via pyrometallurgical

and/or hydrometallurgical routes [157]. Fig. 2.3 (a) outlines the general workflow for PCBs recycling.

Aged LiBs often retains residual charge, and direct dismantling may cause short circuits. Moreover, the electrolyte is flammable and volatile, posing fire and safety risks [158], [159]. Aged LiBs must be discharged prior to dismantling, and working under an inert atmosphere are commonly adopted during dismantling [153], [160]. The key components are sorted during the separation stage. The electrolyte can be fed into a pyrometallurgical unit, where the exothermic combustion helps reduce energy consumption [159]; the anode and cathode materials are crushed and then processed via pyrometallurgical and/or hydrometallurgical methods for metal recovery [153], [159]. A representative aged LiB recycling process is shown in fig. 2.3 (b).

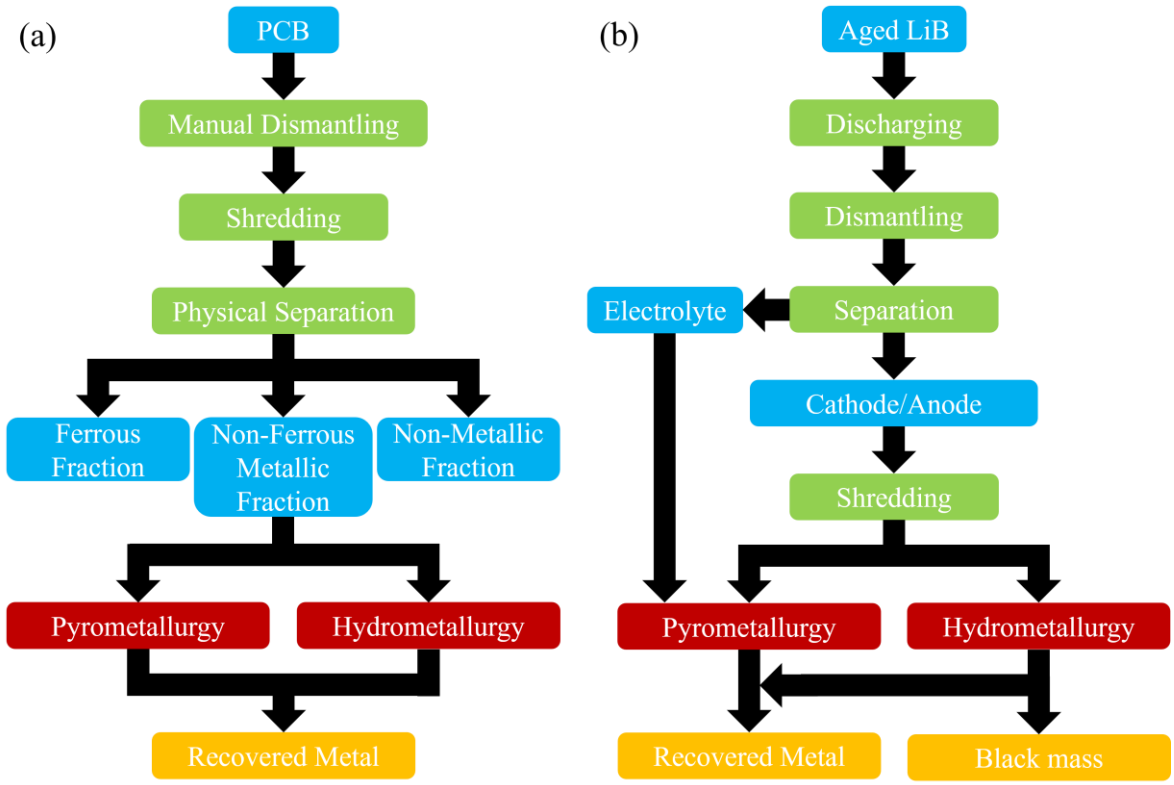

Fig. 2.3: Recycling process flowsheets for (a) PCB [133], [156], [161] and (b) LiB [158], [159], [162].

2.3.1 Pyrometallurgy

Pyrometallurgy is one of the most widely adopted metal-recovery routes in industrial practice. It can process a wide range of waste forms and is characterised by operational simplicity, as a relatively short process, enabling the recovery of multiple non-ferrous metals

[133]. Traditional pyrometallurgical processes involve feeding PCBs or LiBs directly into incinerators or smelting furnaces for high-temperature treatment, with furnace temperatures typically set above 1000°C [163], [164]. The organic components of both types of waste undergo pyrolysis and combustion at high temperatures, and the recoverable metals are ultimately obtained via downstream separation [159], [161].

Incineration/high-temperature oxidation is a relatively traditional recovery method, and the treatment process carries risks of both environmental pollution and resource losses. For PCBs, pollutants such as hydrogen bromide and organic bromine compounds may generate during processing, while metals often mix with glass fibres and other inorganic materials, typically requiring further processing [161]. For LiBs, decomposition of electrolytes and binders can produce corrosive gases containing hydrogen fluoride (HF) [159]. Although Cu, Ni, and Co can form molten alloys at high temperatures which facilitate recovery, other components are more readily lost. For instance, graphite is combusted, lithium oxide is difficult to reduce, and it tends to enter the slag along with Manganese (Mn) and Al, leading to loss [165]. Furthermore, the high energy consumption of pyrometallurgy processing contributes to the overall cost of recovery.

2.3.2 Hydrometallurgy

Hydrometallurgy refers to the process of chemically and/or electrochemically separating and extracting metals using leaching reagents. Hydrometallurgical processes offer advantages in the selective metal recovery compared to pyrometallurgy.

For PCBs, commonly used leaching reagents include mineral acids (such as H_2SO_4, HCl and HNO_3), cyanides, thioureas and halides [166], [167]. Mineral acids can be used for the selective recovery of metals. Base metals such as Zn, Sn, Fe and Al dissolve easily in dilute mineral acids, whilst Cu and precious metals (Au and Pd) dissolve under stronger oxidising conditions (e.g. concentrated HNO_3). However, Ag and Pb may form insoluble salts under acidic leaching conditions, limiting recovery efficiency [43]. Cyanides can effectively leach Au and Ag, but the high Cu content in PCBs increases cyanide consumption; the extreme toxicity of cyanides makes subsequent wastewater treatment an essential step [166], [168]. Thiourea leaches Au and Ag via complexation. It is less toxic and achieves Au leaching rates of up to 99%. However, its selectivity is poor, as it can simultaneously dissolve Fe, Cu, and Zn while leaching precious metals [166], [169]. Halide lixiviants (chlorine, bromine, iodine) exhibit fast leaching kinetics and good selectivity for precious metals, enabling Au recovery

through complexation. This technology however, is highly corrosive and oxidising, requiring safeguards such as corrosion-resistant stainless steels and rubber linings [166], [167].

For LiBs, commonly reported hydrometallurgical process include inorganic acid leaching (mineral acids), organic acid leaching and alkaline leaching [170]. Most metal compounds in LiBs readily react with mineral acids and dissolve into solution, whereas the "black mass" (comprising graphite, binder, and other impurities) is insoluble and can be filtered via solid-liquid separation. The toxic gases (e.g. Cl_2) may be generated when during the reaction of metals with mineral acids [170], [171]. Organic acids (e.g. formic acid, oxalic acid and citric acid) are weaker than mineral acids [170]. They offer the advantages of lower corrosion to equipment and lack of toxic gas generation [170], [171]. However, their slow leaching kinetics and high costs limit their further development [170]. Alkaline leaching can be divided into two categories: the sodium hydroxide (NaOH) system and the amine system [170], [172]. NaOH solutions can selectively dissolve the Al foil from cathodes but are unable to leach other valuable metals. Ammoniacal systems can achieve the separation and recovery of different valuable metals, but the ammonia nitrogen in the wastewater must undergo specialised treatment to meet discharge standards [170].

2.4 Deep eutectic solvents for TCMs recovery from PCBs

A study in 2001 found that co-heating from a group of quaternary ammonium salts and zinc chloride produced liquids with much lower freezing points, with the lowest melting point of 22-25 ℃ obtained from the co-heating of choline chloride with zinc chloride. Further studies led to a series of liquids formed by salts with hydrogen bonded donor subsequently. Abbott *et al* [173] named these liquids as deep eutectic solvents (DES).

DESs are eutectic liquid mixtures formed by hydrogen bonding of two or three inexpensive and safe components, one of which can be a hydrogen-bond acceptor (HBA) such as a quaternary ammonium salt and the other a metal salt or another hydrogen-bond donor (HBD), and the resulting DES possesses a lower melting point than that of any other single component [174].

2.4.1 The definition and classification of deep eutectic solvents

The general expression for DES is

$$Cat^{+}X^{-}{}_{z}Y \tag{2.1}$$

where Cat^{+} refers to any cation such as a ammonium, phosphonium, or sulphonium species, while *X* represents a Lewis base, typically a halide anion. *Y* denotes a Lewis or Brønsted acid that forms a complex anionic compound with *X*, and *z* is the number of *Y* molecules that interact with the anion [174].

For simplicity, Abbott *et al* [174] classified DESs into four types: *Type I* comprises quaternary ammonium salts and metal chlorides; *Type II* comprises quaternary ammonium salts and metal chloride hydrates; *Type III* consists of quaternary ammonium salts and HBDs; and *Type IV* consists of metal chlorides and HBDs.

Fig. 2.4 lists the structural chemical formulae of the common DESs-forming HBD and HBA. Due to the rich source and variety of components of trip DESs, the properties of DES, such as freezing point, viscosity, surface tension, electrical conductivity, density and thermal stability, can be regulated by modulating the component chemicals and ratios.

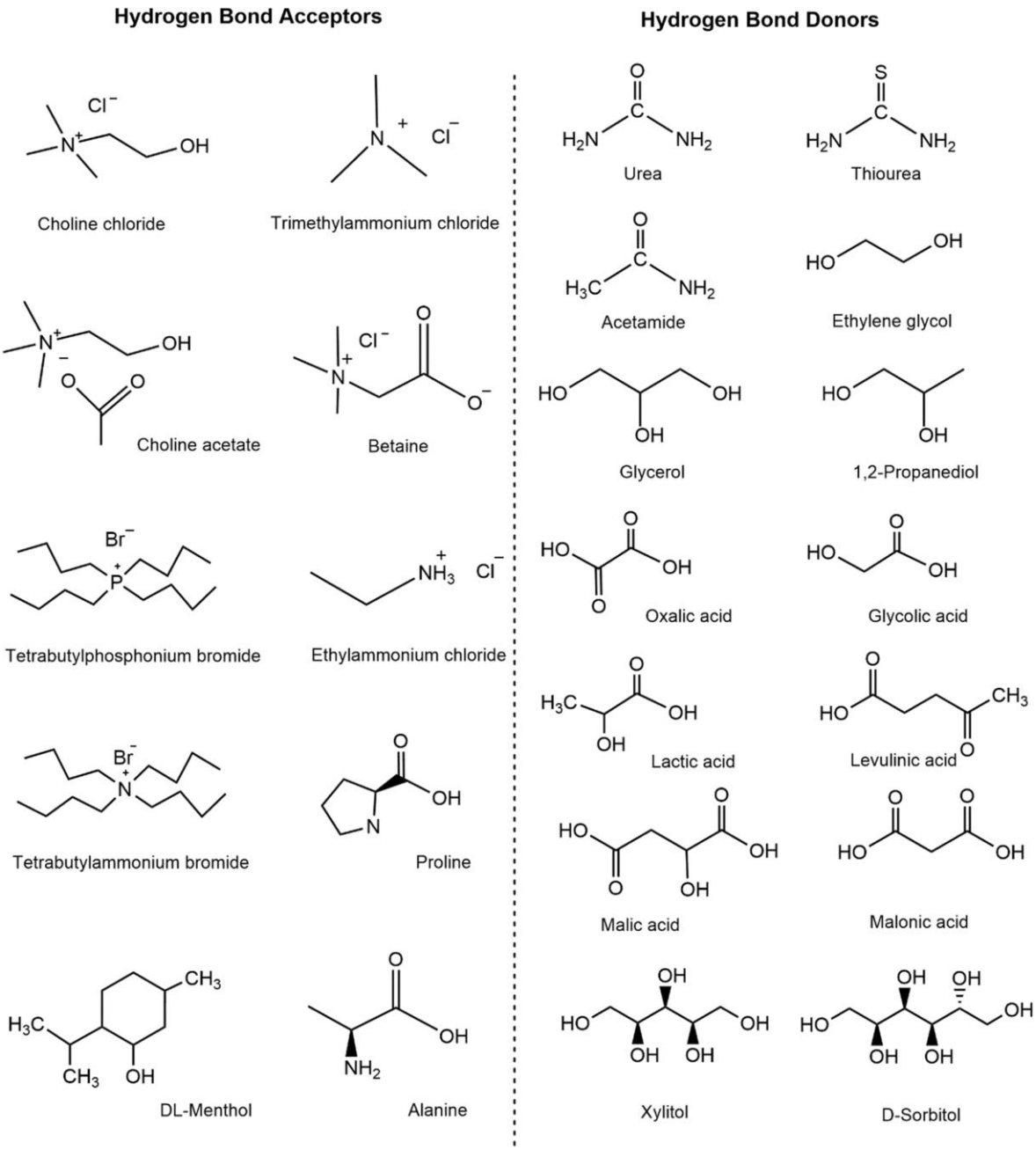

Fig. 2.4: Structure of HBD and HBA components of DESs. Taken from [175].

2.4.2 The preparation method

DESs are commonly prepared via a heating method that involves the homogeneous mixing of the salt and the hydrogen-bonded donor at room temperature or at a certain high temperature. Abbott *et al* [173] prepared a series of DESs from quaternary ammonium salts with carboxylic acids by first recrystallizing choline chloride as a quaternary ammonium salt in high-purity ethanol, filtering and vacuum drying, and the selected carboxylic acids were also vacuum dried prior to use. Then the two components are mixed, heated to 100 °C, and stirred. The heating is stopped when a colourless homogeneous liquid appears, and the liquid is subsequently cooled to room temperature at a rate of 1 °C·min^{-1}.

2.4.3 The properties of DES

2.4.3.1 The melting point

The melting point of DESs are lower than those of their individual components, typically below 100 ℃ [176]. For example, when choline chloride (ChCl) and ethylene glycol (EG) are mixed at a molar ration of 1:2, the resulting Ethaline-DES has a melting point of -66 °C, which is markedly lower than the 302 °C of ChCl and the -12.9 °C of EG [176]. The strength of hydrogen bond has a pronounced influence on the melting point of DESs: stronger hydrogen bond interactions disrupt the crystal lattice more effectively, leading a greater melting point depression. For DESs formed using the choline cation $[(CH_3)_3NCH_2CH_2OH]^+$ with counter anions $F^-, NO_3^-, Cl^-,$ and BF_4^-, combined with urea, the reported melting points are 1 ℃, 4 ℃, 12 ℃, and 67 ℃, respectively. Consequently, DESs with varying melting points can be obtained by selecting different HBD/HBA combinations [176], [177].

2.4.3.2 Viscosity

The viscosity of DESs is higher than that of conventional molecular solvents and is similar to that of ionic liquids, typically exceeding 100 centipoise (cP, 1cP = 1 mPa·s) at room temperature [178]. This relatively high viscosity is primarily attributed to the following factors: (1) The hydrogen-bond network formed between the components in DESs, which reduces the mobility of free molecules; (2) The larger ionic dimensions and smaller pore volumes within DESs; (3) Van der Waals forces and electrostatic interactions between the HBD and the cation-anion pair of the quaternary ammonium salt component [178], [179]. The viscosity of DESs is primarily influenced by the chemical properties of the components, temperature and water content, and generally decreases with increasing temperature [176]. Increasing water content can also reduce viscosity, although the amount must be carefully controlled. For example, in the case of ChCl-urea DES, a water content exceeding 15 wt% disrupts the structure of the DES molecular clusters [180].

2.4.3.3 Ionic conductivity

Electrical conduction in DESs is primarily governed by ionic migration [181]. The ionic conductivity of different DESs varies widely and is jointly influenced by viscosity, temperature, and composition [175], [178], [182]. Ionic conductivity is inversely proportional to viscosity: higher viscosity strongly hinders ion transport, resulting in lower ionic conductivity. Ionic conductivity generally increases with temperature, as an increase

in temperature reduces the viscosity of DESs. additionally, viscosity can be altered by adjusting the composition of the components, thereby further regulating ionic conductivity.

2.4.3.4 Surface tension

The surface tension of DESs exhibits a similar tendency to viscosity. It is primarily influenced by the strength of the interactions between HBD and HBA, and is also related to composition, molar ratio and temperature [182], [183], [184]. Reported surface tension for DESs generally fall within the range of 33-78 $mN \cdot m^{-1}$ [185], [186].

2.4.3.5 Density

The density of DESs depends on the choice of their components, molar ratios [183]. Most DESs have a higher density than water, with values between 1.0 and 1.35 $g \cdot cm^{-3}$ at 25 ℃ [187]. Conversely, hydrophobic DESs are generally lower than water [188]. The density of DESs generally decreases with increasing temperature [181].

2.4.4 Applications of DESs for the recovery of TCMs from PCBs

As described in §2.3, pyrometallurgy can be used to recover the TCMs from PCBs, but at the cost of high energy consumption, insufficient selectivity, and the emission of toxic gases. Hydrometallurgy offers advantages in terms of TCMs separation and purification. Its reliance on strong acids/ alkalis and toxic reagents however, leads to the generation of large volumes of wastewater and sludge. As a class of green solvents, DESs have attracted attention in the field of TCM recovery due to their widespread and readily available constituents, simple preparation process and low toxicity.

Sabzkoohi *et al* [189] immersed PCBs in Ethaline-DES for 72 hours and systematically evaluated the etching efficiency of TCMs. Upon the addition of 0.1 $mol \cdot L^{-1}$ iodine as an oxidising agent, the etching efficiency of Cu, Sn, and Ni all exceeded 75%. In contrast, the etching efficiency of all metals were below 15% without iodine addition, except for Sn, which achieved 100% recovery. These results not only demonstrate the feasibility of using DESs for TCMs recovery but also highlight the critical role of added oxidants in enhancing etching efficiency.

Building on this work, Saffaj *et al* [190] prepared five DESs using ChCl as the HBA and EG, malonic acid (MA), levulinic acid (LA), acetic acid (AA), and citric acid (CA) as the HBD, respectively, with 0.1 $mol \cdot L^{-1}$ iodine added as the oxidant in each case. Under

conditions of 65 ℃, a stirring speed of 300 rpm, a solid-liquid ration of 10 $g \cdot L^{-1}$, and passive soaking for 96 h, the ChCl:AA-DES exhibited the highest recovery efficiency and superior selectivity: recoveries of Cu, Ni, and Au all exceeded 90%, while limiting the recovery efficiencies if Al and Fe to 0% and 40%, respectively. Such selective etching behaviour is essential for enhancing TCM purity in subsequent processing.

Notably, the treatment time in the above studies remain relatively long. To shorten the leaching time, Rivera *et al* [191] prepared a DES using $CaCl_2 \cdot 6H_2O$ and EG in a 1:1 molar ration, and introduced 1 mol·L-1$FeCl_3$ as an oxidant to enable selective etching of metals from PCBs at 50 ℃ to achieve selective leaching of metal from PCBs. This DES selectively dissolved Cu, while Au an Ni were recovered directly by filtration, thereby reducing the etching time to 8 h. Furthermore, the etching time can be further reduced to 2 h by replacing $FeCl_3$ with $CuCl_2$.

2.4.4.1 Current limitations

Although selective leaching using DESs helps to simplify subsequent TCM separation and purification, their high viscosity markedly impedes mass transfer and the diffusion of metal ion during etching, reducing recovery efficiency.

To mitigate the limitations imposed by high viscosity, Rivera *et al* [192] introduced power ultrasound into $CaCl_2 \cdot 6H_2O$:Eg-DES with 0.1 mol·L-1 $CuCl_2$. Sonication was applied using a 20 kHz sonotrode (Branson Sonics, 1.25DCXa20-V) with a tip diameter of 20 mm in four 30 s bursts. The tip-to-sample distance was maintained at 1 cm, and the DES temperature was controlled between 50 and 60 ℃. The results showed that introducing power ultrasound suppressed the formation of a passivation layer on Cu surface, increasing the etching rate by more than 10,000 times under 80 $W \cdot cm^{-2}$. Further increasing the sonotrode input power can continue to reduce the duration required for etching.

Building on the above studies, chapter 4 of this thesis introduces power ultrasound into the Ethaline-DES system. By combining high-speed imaging (HSI) with the sonication at various input power levels, the ultrasound-enhanced process was monitored, and the mechanism of TCM separation on the PCB surface was investigated. Subsequently, the viscosity of the Ethaline-DES was reduced by introducing deionised water, thereby further improving the efficiency of TCM separation.

2.5 LiB recycling by sonication

The review in this section focuses on the direct ultrasonic delamination of graphite from the copper current collector; studies employing ultrasound primarily to enhance chemical leaching are not considered directly comparable because they involve a different recovery mechanism and material outcome.

Pyrometallurgical and hydrometallurgical processes are primarily used to recover TCMs (e.g. Co, Li, Ni, and Mn), whereas more challenging-to-recover materials such as graphite are often discarded [72]. Direct recycling has therefore attracted attention as a means of overcoming these limitations. It enables efficient recovery of active materials while retaining their original structure and electrochemical performance [193]. This approach can reduce recycling costs and broaden the range of recoverable materials. The separation of electrodes however, remains one of the challenges in direct recovery. Among existing separation methods, organic solvents such as N-Methyl-2-pyrrolidone (NMP) can dissolve polymeric binders and achieve separation of electrode materials, but issues such as solvent toxicity, high costs of recovery and purification, and environmental pollution remain [194]. Acoustic cavitation delamination techniques have attracted experimental research in the field of current collector-active material separation for their advantages of process efficiency, mild operating conditions, and environmental friendliness.

Ren *et al* [195] treated 1 cm × 1 cm size aged LiB anodes in water using a combination of 40 kHz ultrasonic bath (Skymen-JM-07D-40) and mechanical stirring. The results showed 98% graphite delamination efficiency after an 8-minute treatment at an input power of 182 W, 2000 r/min and room temperature. Based on this work, Yang *et al* [196] adjusted the water temperature to 30, 40, 60 and 80 °C and compared the effects of temperature variations on the recovery rate. The study found that as the temperature increased, the delamination efficiency of the graphite improved; at a water temperature of 80 °C, 5 minutes of sonication achieved 100% recovery of the copper foil. Although increasing the water temperature reduced the sonication duration required for complete delamination, the remaining duration of 5 min is still relatively long from the perspective of high-throughput processing and industrial scale-up.

More recently, Wiechers *et al.* [197] investigated the ultrasonic delamination of 30 mm-diameter anode production-scrap discs in water using a custom ultrasonic bath fitted with a 200 W, 29 kHz oscillator (Weber Ultrasonics AG, Karlsbad, Germany). The degree of

graphite delamination increased approximately linearly during the first 40 s, reaching about 97%, after which the delamination rate decreased markedly and the degree of delamination approached 100% by 120 s.

Sonotrodes have also been employed in experimental studies on LiB electrode recycling. *Jacobson* [33] used a 20 kHz sonotrode (Branson Sonics, 1.25DCXa20-V) with 20 mm tip diameter to sonicate 30 mm × 30 mm LiB cathode production scrap in water at 30% input power. With a 3 mm distance between the cathode and the sonotrode tip, 3 s of sonication produced a fully delaminated active material region with a diameter of approximately 20 mm. Sonication applied with a sonotrode can achieve delamination in a short time, but the cavitation coverage induced by the sonotrode tip is limited, making it difficult to cover the entire sample.

A flow-cell-type ultrasonic apparatus has also been evaluated for the aqueous delamination of LiB anodes. Trebeck *et al.* [198] treated 1 cm × 1 cm graphite-coated anode-foil pieces using a BioPush flow cell (Weber Entec GmbH, Ettlingen, Germany). Although the apparatus was described as a flow cell, the experiments were conducted as mechanically stirred batch tests, and no flow rate or recirculation conditions were reported. After 5 min at 20 °C, a reported ultrasonic power setting of 50% produced a delamination degree of 64.69%, compared with 29.04% at the 100% setting. At the 50% setting, increasing the water temperature to 60 °C raised the delamination degree to 92.65% after 5 min. The authors suggested that moderate power may produce more favourable cavitation dynamics and interfacial shear than full power, although cavitation activity was not measured directly. In separate deformation tests, 3 cm × 3 cm foil pieces were folded one to three times. Folding generally reduced delamination by limiting the accessible coated area and locally compacting the coating; when the smooth surface was folded inward and the specimen remained closed, a single fold was sufficient to prevent delamination.

Taken together, the available studies demonstrate that aqueous ultrasonic treatment can achieve effective delamination of LiB electrode coatings, but the reported performance depends not only on nominal ultrasonic power, but also on liquid temperature, mechanical agitation, sample geometry, prior deformation and the spatial distribution of cavitation. Ultrasonic baths provide relatively broad exposure but generally lower volumetric power density, whereas sonotrodes generate intense but highly localised cavitation beneath the tip. Direct quantitative comparison between studies remains difficult because ultrasonic power,

sample dimensions, treatment conditions and delamination metrics are reported inconsistently.

2.5.1 Current limitations

As described in §1.5, a sonotrode can generate highly intense cavitation, but the effective sonication region is confined to the vicinity beneath the tip. An ultrasonic bath can provide cavitation coverage over a larger volume. However, the local cavitation intensity is typically 100 times lower than that produced by a sonotrode.

Against the background above, the introduction of chapter 7 provides further review, experimental details and limitations of sonotrode- and ultrasonic bath-based approaches for LiB recycling, specifically. The experimental sections of chapter 7 also employs a novel static tube transducer configuration to sonicate LiB anode, and compares the results with those obtained using a conventional sonotrode, in a number of configurations. Chapter 8 further deploys the tube transducer within a flow-based system, to conduct experimental studies on the graphite delamination efficiency of LiB anodes, establishing a foundation for subsequent applications in industrial-scale continuous sonoprocessing.

Chapter 3

Principal experimental instruments and solvents

This chapter briefly outlines the key experimental apparatus and solutions used in chapters 4-8, along with the algorithms employed for analysing the data presented in this thesis. The advanced cavitation research apparatus of CavLab provided comprehensive experimental support for this work.

This chapter documents a combination of commercially supplied instruments, experimental methods previously established within CavLab, and apparatus designed, fabricated or adapted specifically for this doctoral project. The commercial sonotrodes, cameras, illumination systems, signal generator, power amplifier, impedance analyser and oscilloscope were commercially supplied instruments available for this research. The candidate was responsible for configuring and operating these instruments, selecting the experimental parameters, acquiring the experimental data and analysing the results, except where otherwise stated.

The general concept of the radially poled tube transducer and its initial static configuration were developed jointly within CavLab during this doctoral project. For the work presented in this thesis, the candidate was specifically responsible for the detailed design and fabrication of the experimental configuration; electrode connection; insulation and epoxy encapsulation; design and assembly of the supporting housing and experimental vessels; impedance characterisation and operating-frequency selection; design and fabrication of the impedance-matching transformers; integration of the electrical excitation system; and experimental characterisation and application of the tube transducer. Contributions from other researchers or technical staff are identified explicitly in the relevant sections.

The swPCD architecture was originally developed by Johansen et al. [29], while the 10 mm active-element configuration used in this thesis followed the subsequent CavLab modification reported by Jacobson [33]. The detector used in the present experiments was fabricated by the candidate according to this established design. The finite impulse response filtering method described in §3.7 was also based on an established CavLab signal-processing workflow. The candidate adapted this method for the present experiments and performed the acoustic-data processing and analysis reported in the results chapters.

This chapter is organised as follows: §3.1 introduces one source of ultrasound used for this work, the sonotrode. §3.2 describes the water tanks configured for the experiments. §3.3 details the cameras utilised for image acquisition. §3.4 introduces the illumination system for high-speed imaging (HSI). §3.5 presents the fabrication process of the static tube transducer configuration developed in CavLab and the selection of the operating frequencies. §3.6 introduces the apparatus for exciting the tube transducer. §3.7 describes the experimental devices for acquiring acoustic signals. §3.8 introduces the deep eutectic solvents (DESs) and their preparation procedures. §3.9 describes the sonochemiluminescence (SCL) solution and its preparation process.

3.1 Sonotrode

One of the ultrasonic devices employed in the §4 and §6 is the sonotrode (P100/7-20, Sonics), shown in fig. 3.1. It emits ultrasonic wave at a frequency of 20 kHz through a 113 mm length, 20 mm diameter Ti probe. The sonotrode is operated manually via a dedicated control console, featuring a maximum transducer displacement of 16 µm peak-to-peak and a maximum power output of 120 W. The desired displacement amplitude can be preset prior to operation. During use, the control console automatically regulates the output power to maintain the prescribed displacement amplitude, ensuring stable operating conditions irrespective of variations in the load.

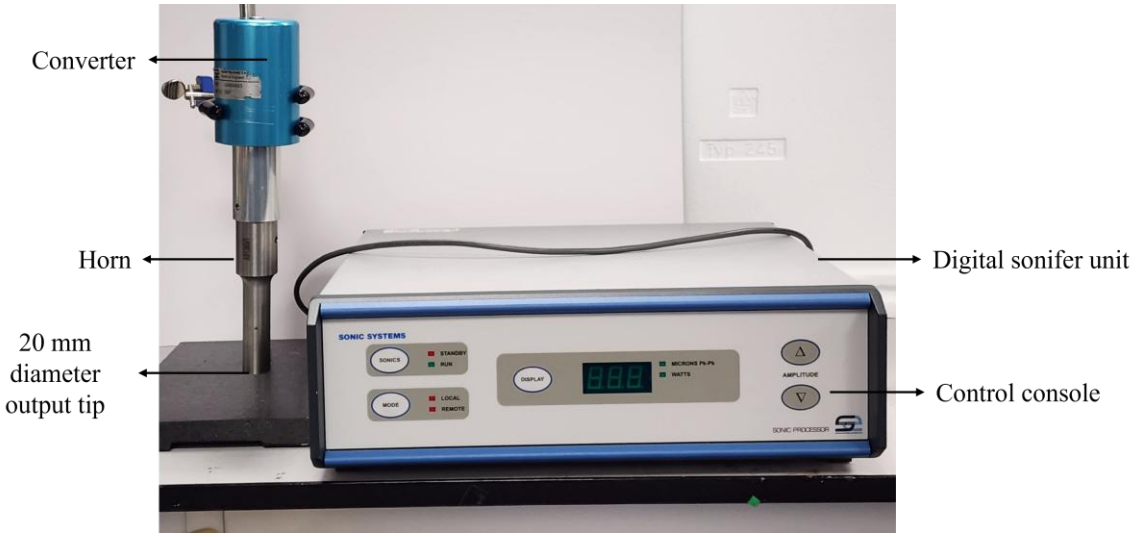

Fig. 3.1: Sonic Systems ultrasonic sonotrode, comprising the sonotrode, the output tip and the control console, to initiate and set input power for a sonication

3.2 Sonication tanks

To investigate the cavitation characteristics, three dedicated sonication tanks were designed, as shown in fig. 3.2 (a)-(c), enabling precise, stable and repeatable positioning of the swPCD, sonotrode and tube transducer. The tanks in fig. 3.2 (a) and (b) were modelled in Fusion 360 (Autodesk, California, USA) with dimensions of 200 × 200 × 150 mm³ and 100 × 100 × 100 mm³, respectively. The former was used to investigate the cavitation behaviour of the tube transducer under water-backed conditions, whereas the latter was employed to characterise the cavitation activity beneath the tip of the sonotrode. Both tanks were laser-cut from 3 mm thick transparent acrylic sheets and sealed with epoxy resin, ensuring watertight construction and providing full optical accessibility for HSI.

The third cylindrical vessel, depicted in fig. 3.2 (c), was also designed in Fusion 360 and fabricated by 3D printing. The inner diameter and width of the vessel match those of the tube transducer as described in §3.5.1, at 55.6 mm and 30.3 mm, respectively, with a wall thickness of 2 mm. Transparent observation windows were installed on both the front and back faces, with a 25 mm diameter port incorporated at the top to allow for the mounting of the sonotrode probe tip.

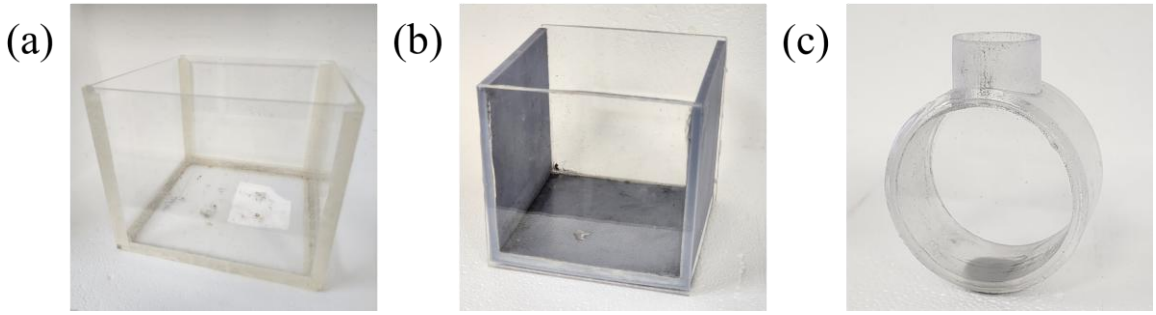

Fig. 3.2: Photographs of the three sonication tanks. (a) large tank. (b) small tank. (c) cylindrical vessel.

3.3 Optical imaging techniques

The choice of optical imaging techniques in each experiment was guided by its specific observational requirements. To image the transient processes such as nucleation, growth, and collapse of cavitation bubbles, a high-speed camera was employed to resolve the rapid temporal dynamics. In contrast, macroscopic processes, including the dispersion behaviour of particles or powders within the liquid, could be adequately recorded using a commercial camera operating at lower frame rates. For the sonochemiluminescence (SCL) experiments

of §5.3.3, with methodology described §3.9 below, the commercial camera was configured with a prolonged exposure time, allowing greater light accumulation and thereby enhancing the level of image detail.

3.3.1 High-speed imaging

The high-speed camera employed in this study for high-speed imaging was the Photron FASTCAM SA-Z 2100K (Photron, Tokyo, Japan), shown in fig. 3.3 [32]. This device is capable of a maximum frame rate of 2.1×10^6 frames per second (fps) and a maximum resolution of 1024 × 1024 pixels, with an inverse relationship between both parameters. Equipped with a 128 GB memory, the camera supports extended continuous recording durations, the length of which is determined by the selected frame rate and resolution. Additionally, the high-speed camera was fitted with a Zeiss Milvus 2/100M ZF.2 lens (Carl Zeiss, Oberkochen, Germany) to ensure high-resolution image quality and excellent optical focusing performance [33].

Fig. 3.3: Image of a Photron high-speed camera. Taken from [32].

3.3.2 Conventional imaging

The commercial camera employed in this thesis for conventional imaging was the Nikon Z8 (Nikon Corporation, Tokyo, Japan), capable of a maximum frame rate of 120 fps and a maximum resolution of 8256 × 5504 pixels, with both parameters exhibiting an inverse relationship [199]. In the SCL experiments, the camera captured the spatial distribution and

intensity variations of luminescence at a resolution of 5504 × 5504 pixels using a 15 s long exposure mode. For video recordings of graphite delamination from LiB anodes, the camera was configured at 3840 × 2160 pixels with 120 fps. Furthermore, the camera incorporates a Nikon Z 24-120 mm *f*/4 S lens (Nikon Corporation, Tokyo, Japan), ensuring high-quality optical resolution and image stability across varying fields of view and illumination conditions.

3.4 Illumination system for high-speed imaging

Owing to the extended dimensions of the tube transducer, uniform illumination across the entire internal region cannot be achieved with a single light source. To address this limitation, a dual illumination configuration as shown in §5.2 fig. 5.1 was adopted in this thesis. A pulse laser source (detailed in §3.4.1) was positioned at the centre, providing high-temporal-resolution illumination essential for capturing transient cavitation and shockwave events. At the same time, a continuously operating ring lighting (detailed in §3.4.2) array was arranged around the periphery to ensure sufficient and uniform illumination throughout the full bore of the tube.

3.4.1 Pulse laser illumination system

Fig. 3.4 depicts the synchronized 10 ns, 632 nm wavelength collimated pulsed laser system (CAVILUX Smart, Cavitar Ltd., Tampere, Finland). This system, based on shadowgraphic imaging principles, enables the visualisation of refractive index variations in the liquid arising from cavitation bubble collapse and the shockwaves [9], [29], [34].

This research combined the pulse laser illumination with Photron high-speed camera, enabling extended recording of acoustic cavitation shockwaves at higher pixel resolutions to provide reliable image data for subsequent analysis [33], [200]. To achieve precise temporal synchronisation between the laser pulses and the image acquisition, an external signal generator (Rigol DG4102, Rigol Technologies, Beijing) was employed to control the synchronous initiation of pulsed laser illumination and Photron camera imaging across different experimental modes.

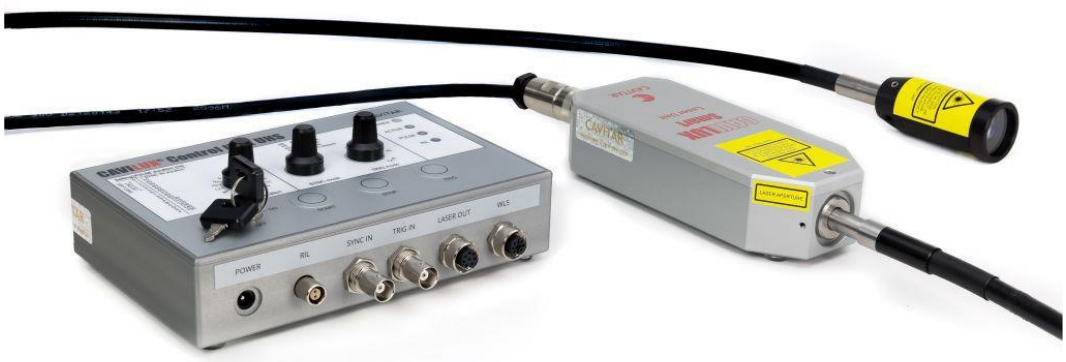

Fig. 3.4: Cavilux Smart Ultra-High-Speed illumination system, comprising the laser module, collimating lens, and control unit. Taken from[33].

3.4.2 Continuous light illumination system

The continuous light system, shown in fig. 3.5, compromised a 150 W halogen lamp (Thorlabs, Ely, UK) coupled to a fibre ring illuminator (FRI61F50, Thorlabs) mounted outside the vessel to illuminate the annular region. This configuration ensured that the surrounding region of the tube received adequate and uniformly distributed illumination.

Fig. 3.5: Image of continuous light source and ring illuminator.

3.5 Tube transducer

To generate a high-intensity cavitation within larger liquid volumes and promote the development of high throughput flow-based sonoprocessing system, a novel ultrasonic tube transducer was employed as the cavitation excitation source in this thesis.

3.5.1 Static tube transducer configuration fabrication

As shown in fig. 3.6 (a), the transducer comprises a single element radial piezoceramic tube (F3260232, CTS Ferroperm, Denmark), made from PZ26 material with dimensions: 63.4 mm outer diameter, 55.6 mm inner diameter and 30.3 mm height. Both inner and outer curved wall surfaces are coated with conductive silver electrodes. The tube transducer is excited to produce a pronounced radial vibration mode when an AC current of a specific frequency is applied to its two electrodes.

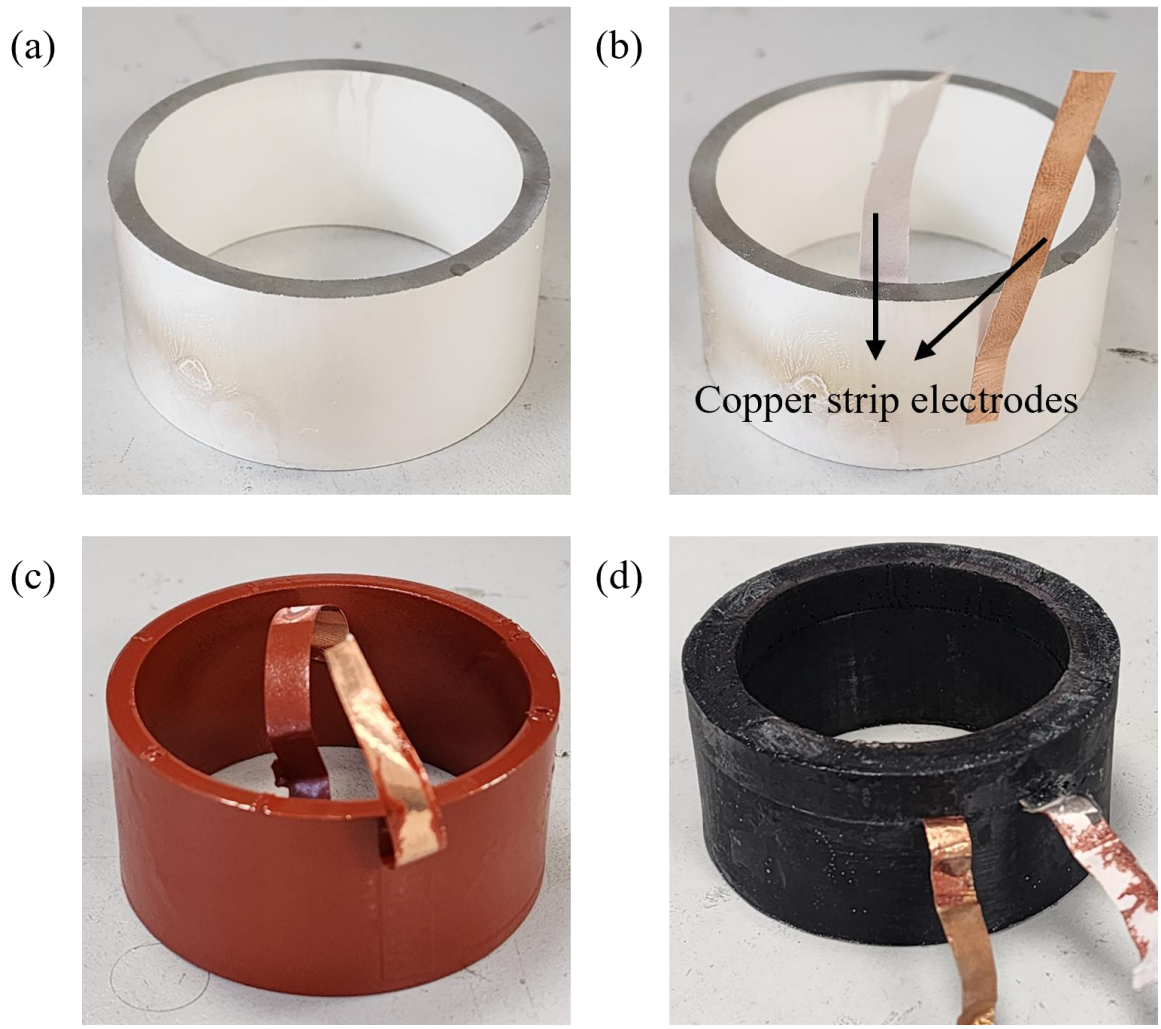

Fig. 3.6: Schematic of the fabrication steps for the tube transducer. (a) PZT tube. (b) Attachment of copper strip electrodes to the inner and outer surfaces to provide electrical connections. (c) Application of a polyurethane coating layer on the surface to provide

electrical insulation. (d) Application of an epoxy encapsulation layer to enhance mechanical strength and protect against cavitation erosion.

The following section will describe the manufacturing and assembly process for the static tube transducer configuration used in this thesis.

The overall structure of the static tube transducer configuration was composed of the following five components, fig 3.6:

1. Radially poled piezoceramic tube, fig 3.6 (a)
2. Power lead connections, etc
3. Polyurethane coating layer
4. Epoxy encapsulation layer
5. 3D-printed mechanical housing

3.5.1.1 Electrode connection treatment

First, the electrical connections for the tube transducer were prepared. As shown in fig. 3.6 (b), copper strips with a 6 mm width and 8 cm length were adhered to the inner and outer silver electrodes of the tube transducer, respectively, serving as the positive electrode and grounding electrode. Particular attention must be paid during adhesion to avoid contact between the two copper strips or between the strips and the opposite silver-coated electrodes to prevent short circuits. Then the non-adhered areas of the copper strips are covered with adhesive tape to ensure the electrical contact surfaces remain clean.

3.5.1.2 Polyurethane insulation coating treatment

Secondly, a polyurethane conformal insulating layer (Urethane Conformal Coating, CRC Industries, USA) was sprayed onto the tube transducer surface after electrode connection, as shown in fig. 3.6 (c). The coating was applied in multiple passes, each cured at room temperature under ventilated conditions to ensure uniformity. The tube transducer should be left at room temperature for 24 h after the final spraying to guarantee complete drying of the coating. According to the technical reference, the dried coating possesses a dielectric

strength of 40 kV/mm, providing effective electrical insulation and enhancing the adhesion of the epoxy resin coating applied in the third step.

3.5.1.3 Epoxy protective encapsulation layer

Polyurethane coating exhibits limited resistance to mechanical impact and cannot tolerate high-intensity cavitation erosion. Consequently, an epoxy resin (832HT epoxy resin, MG chemical, Canada) was employed as the final protective layer, encapsulating the entire tube transducer. The tube transducer was positioned within a custom mould to ensure uniform epoxy resin thickness, and then, placed in a constant-temperature heating chamber for curing at 60 ℃ for 3 h. The completed tube transducer is presented in fig. 3.6 (d). According to the technical reference, the cured epoxy layer exhibits a tensile strength of approximately 54 N/mm² and a compressive strength of 81.9 N/mm², which is sufficient to withstand the localised high-stress impacts caused by cavitation erosion. Its water absorption is below 0.1 %, preventing performance degradation in aqueous environments, and the excellent chemical stability enables subsequent sonication experiments involving DESs in the future.

3.5.1.4 Design and fabrication of the external support structure

The external supporting housing for the tube transducer was modelled in Fusion 360 (Autodesk, California, USA), and the configuration is shown in fig. 3.7, where (a) denotes the front housing and (b) the back housing. Both housing sections incorporate a 57.75 mm diameter circular aperture (red colour), ensuring the entire internal region of the transducer can be observed during experiments. At the interface between the front housing and the tube transducer, an annular recess (green colour) of 63 mm diameter and 3 mm in depth was designed to accommodate a front transparent viewing window, enabling direct imaging of the internal cavitation behaviour. The back housing was likewise fitted with a transparent window of the same dimensions to allow back-illumination.

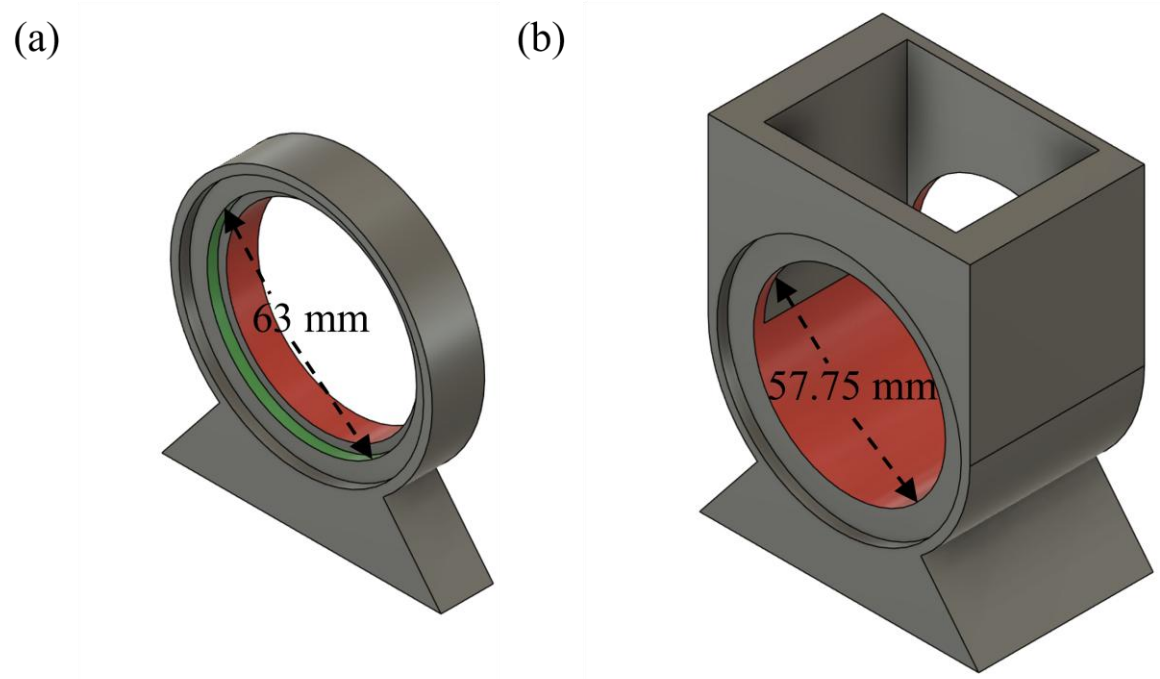

Fig. 3.7: Schematic of the external supporting structure for the tube transducer. (a) The front housing provides forward support, and the diameter of the green annular recess is 63 mm. (b) The back housing that allows for liquid filling or placement of the swPCD and offers back support, and the red circular aperture is 57.75 mm.

In addition, a rectangular opening was reserved at the top of the back housing to serve as a filling and access port, permitting both the injection of test liquids into the chamber and the placement of the swPCD for acoustic measurements. The entire housing assembly was fabricated by 3D printing.

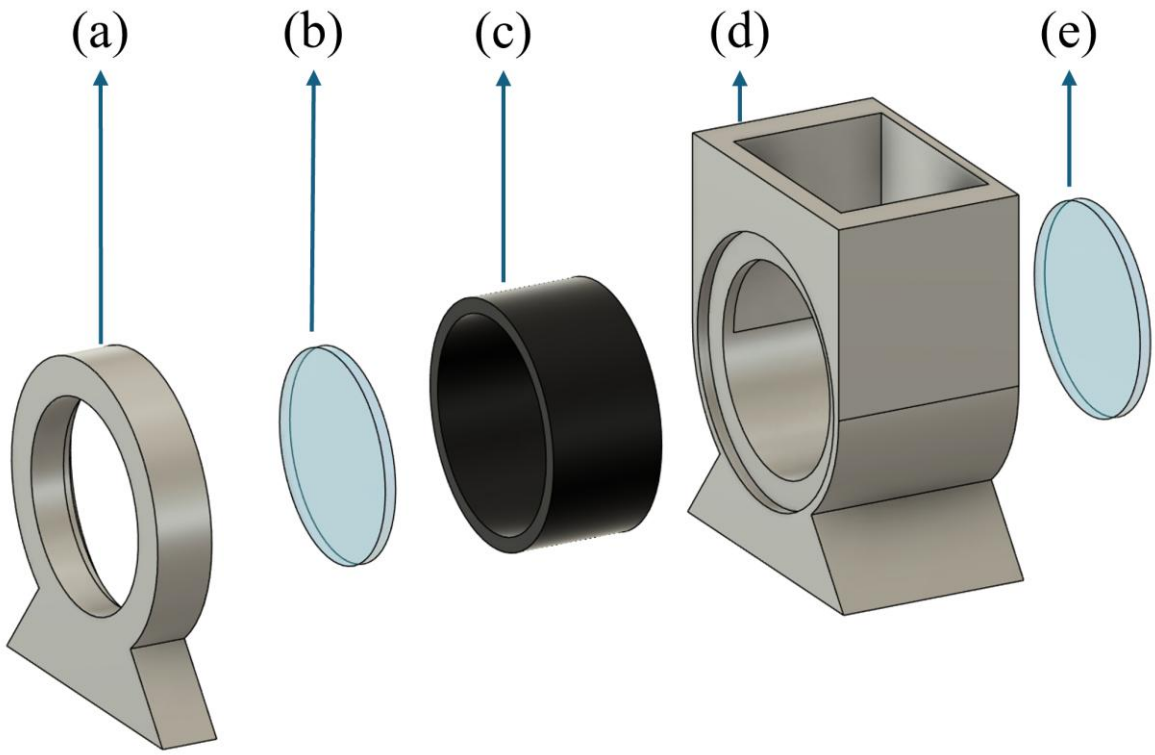

Fig. 3.8: Exploded view of the static tube transducer configuration.

Fig. 3.8 presents the exploded view of the static tube transducer configuration. Components (a) and (d) are the front and back supporting housings, respectively; (b) and (e) are the front and back transparent viewing windows; and (c) is the tube transducer body with the epoxy protective coating applied. The viewing windows were bonded to the supporting housings using Gorilla adhesive (Permanent Strong Liquid Adhesive, Gorilla Glue Europe Ltd., UK). The seal between the supporting housings and the tube transducer was made with silicone sealant (820, No Nonsense, Screwfix, UK) to ensure watertightness during operation.

The fully assembled static tube transducer configuration is shown in fig. 3.9. This configuration provided a stable and repeatable experimental platform for subsequent cavitation visualisation and acoustic signal acquisition.

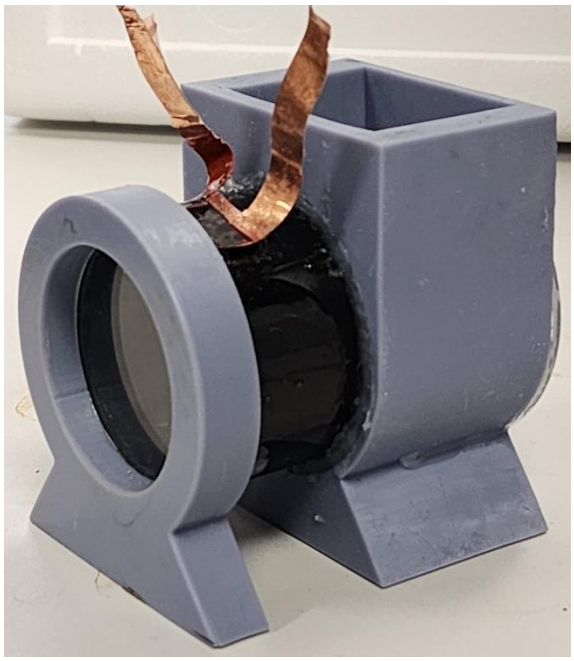

Fig. 3.9: Image of the assembled tube transducer with housing.

3.5.2 Impedance measurement and frequency selection

Two operating conditions of the tube transducer are examined in order to assess the cavitation performance under different boundary conditions in this thesis. In the first condition, referred to as the 'air-backed tube', the bore of the transducer is filled with water while its exterior surface is exposed to air. In the second condition, termed the 'water-backed tube' as shown in §5.2 fig. 5.1, both the interior and exterior of the transducer are in contact with water, such that the tube is fully water-loaded.

The impedance of the tube transducer was measured using an electrical impedance analyser (4294A, Keysight Technologies, CA, USA). The spectrum for air-backed tube is shown in fig. 3.10 (a) where the resonance of the fundamental radial mode is apparent at 16.79 kHz. This mode was targeted for generating an axially focused field for high intensity cavitation. The tube transducer was therefore excited by a sinusoidal voltage signal at this frequency for all air-backed water results presented. A second resonance frequency appearing at 54.15 kHz is the first axial mode, but the pressure field generated inside the tube bore at this frequency does not have the desired distribution and so was not applied in this study.

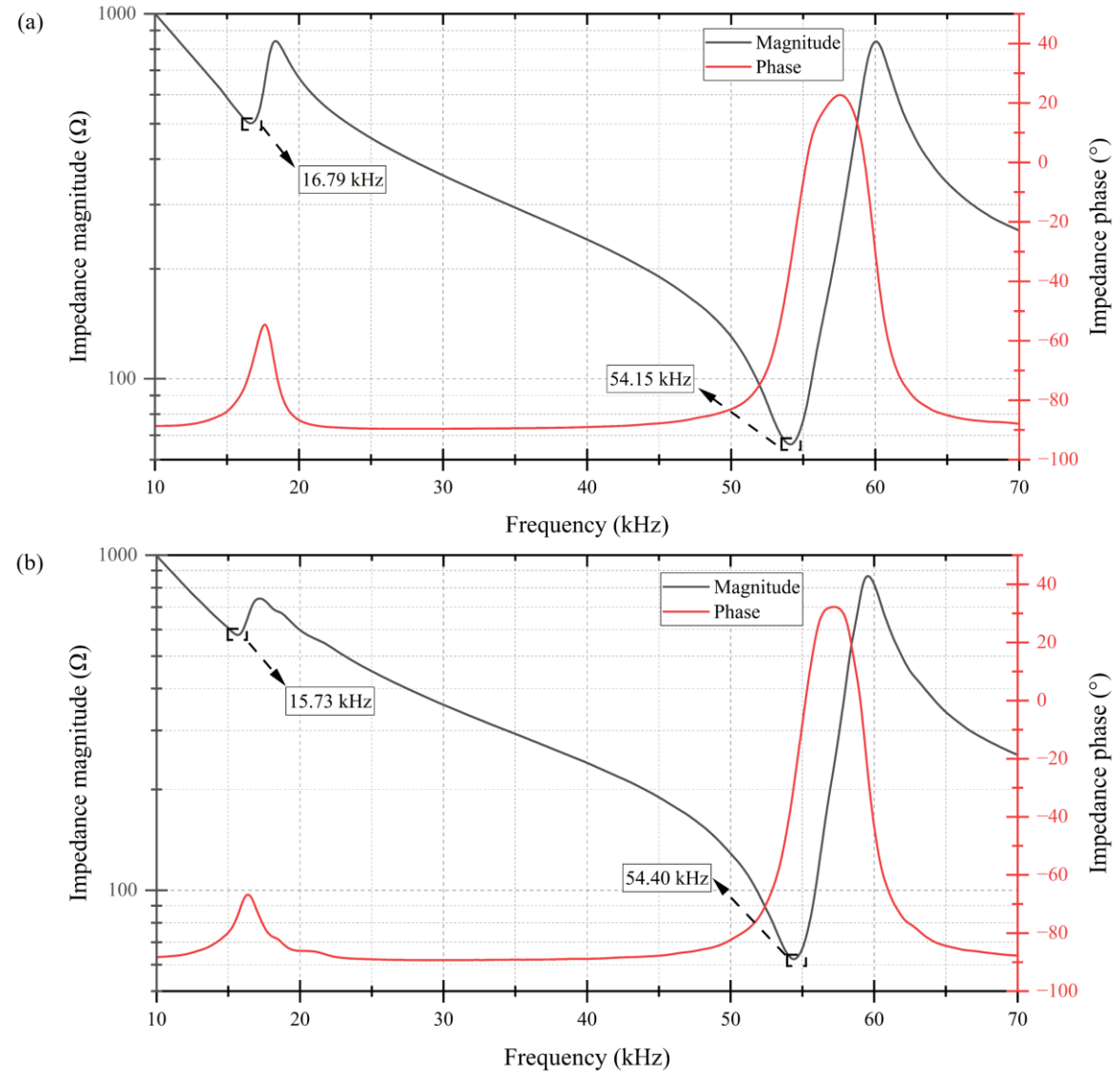

Fig. 3.10: (a) Measured electrical impedance and phase inside air-backed tube transducer. The first radial (16.79 kHz) and axial (54.15 kHz) resonance modes are indicated. (b) Measured electrical impedance and phase inside water-backed tube transducer. The first radial (15.73 kHz) and axial (54.40 kHz) resonance modes are indicated.

The measured impedance spectrum for the water-backed configuration is presented in fig. 3.10 (b). The resonance frequency associated with the fundamental radial mode occurs at 15.73 kHz, while the first axial mode resonates at 55.40 kHz. In line with the air-backed condition, only the first axial radial mode was used in this work to generate an axially focused, high-intensity cavitation field; accordingly, all water-backed experiments were carried out with the tube transducer driven at 15.73 kHz.

3.6 Electrical driving and impedance matching of the tube transducer

3.6.1 Signal generator-excitation source

A dual-channel signal generator (DG4102, RIGOL Technologies, Beijing, China) was used to provide both the excitation and timing signals for the experiments. The unit is capable of generating sinusoidal wave outputs up to 100 MHz with a sampling rate of 500 MSa/s.

This research utilized the signal generator to generate a 16.79 kHz (or 15.73 kHz) sinusoidal excitation signal, which was sequentially transmitted via the 'Output' BNC interface to a power amplifier. Then, it passed through an impedance matching transformer before being coupled to the tube transducer, which excited its radial vibration mode. Additionally, a synchronisation pulse signal output through the 'Sync' BNC interface triggered both the Photron high-speed camera and pulse laser illumination system, ensuring temporal synchronisation throughout the cavitation imaging process.

3.6.2 Power amplifier-voltage and power boosting stage

A crucial component in the tube transducer excitation system is the the power amplifier (1040L, Electronics & Innovation, USA). The amplifier operates over a frequency range of 10 kHz to 5 MHz and provides a voltage gain of approximately 55 dB. It is capable of delivering an maximum output power of 400 W and features purely resistive input and output impedance of 50 Ω. The unit was employed to amplify the low-amplitude sinusoidal signal supplied by the signal generator to a level sufficient for driving the tube transducer. This ensured that the tube transducer was excited at the desired resonance frequency with stable and effective ultrasonic output.

3.6.3 Impedance matching transformer

The signal generator and power amplifier both feature a standard output impedance of 50 Ω (purely resistive). The tube transducer, however, exhibits a relatively high complex impedance characteristic near its resonant frequency. Direct connection of the tube transducer to the amplifier would result in significant impedance mismatch, which would induce energy reflection and power dissipation at the interface. As a result, this impedance mismatch would diminish acoustic coupling efficiency and reduce cavitation excitation effectiveness.

An impedance matching transformer is a passive electromagnetic device that achieves impedance transformation through electromagnetic induction. The principle is illustrated in fig. 3.11 (a): a corresponding alternating magnetic flux is generated within the core when an alternating voltage is applied to the primary coil. The flux is coupled through the core to the secondary coil, inducing an alternating current on the secondary side. This provides the tube transducer with a boosted drive voltage.

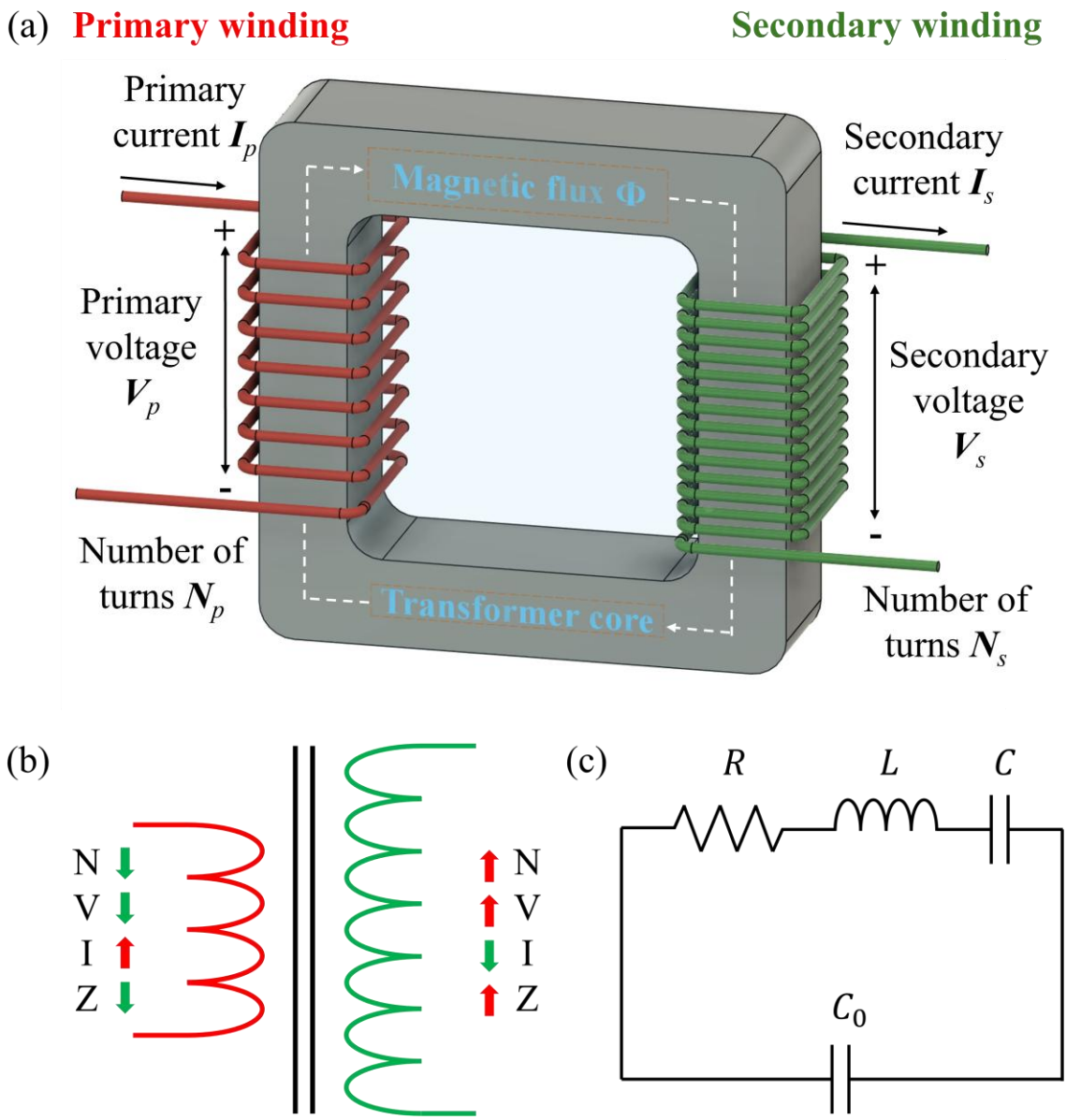

Fig. 3.11: (a) The impedance matching transformer schematic. Modified from [201]. (b) Circuit schematic diagram, illustrating the electric field transformation for each winding. (c) Butterworth-Van Dyke (BVD) equivalent circuit for the tube transducer.

In fig. 3.11 (b), the red wire denotes the primary coil connected to the power amplifier, while the green wire corresponds to the secondary coil linked to the tube transducer. Given that the power amplifier possesses a low-impedance, purely resistive output of approximately 50 **Ω**, while the tube transducer exhibits a higher equivalent impedance, the primary coil employs fewer turns and operates at a lower voltage. This relationship is described by eq. 3.1:

$$\frac{V_p}{V_s} = \frac{I_s}{I_p} = \frac{N_p}{N_s} = a \tag{3.1}$$

where V denotes voltage, I denotes current, N denotes the number of coil turns, and a denotes the turns ratio. The subscripts p and s correspond to the primary and secondary coils respectively.

The Butterworth Van Dyke (BVD) equivalent circuit model depicted in fig. 3.11 (c) characterises the equivalent impedance of a tube transducer at its resonant frequency. This model comprises an electrostatic branch and a mechanical vibration branch: the electrostatic branch consists of static capacitance C_0, describing the capacitive characteristics of the transducer in the absence of mechanical motion; while the mechanical vibration branch comprises dynamic resistance R, dynamic inductance L, and dynamic capacitance C. here, R characterises radiation losses and internal mechanical dissipation, whereas L and C jointly simulate the inherent resonant behaviour of the transducer. The expression for the resonant frequency f is given by eq. 3.2:

$$f = \frac{1}{2\pi\sqrt{LC}} \tag{3.2}$$

The phase at the resonant frequency can be corrected to near 0° using the equivalent inductance L_s generated by the secondary coil to counteract the effect of the static capacitance C_0. The corresponding relationship is given by eq. 3.3:

$$L_s = \frac{1}{(2\pi f)^2 C_0} = N_s \times A_L \tag{3.3}$$

where A_L denotes the inductance coefficient of the selected magnetic core. By utilising L_S and A_L, the required number of turns for the secondary coil can be calculated. The formula for determining the turns ratio a is shown in eq. 3.4:

$$a = \sqrt{\frac{Z_{in}}{R}} \tag{3.4}$$

where Z_{in} = 50 Ω represents the output impedance value of the power amplifier. Ultimately, the required number of turns for the primary coil can be calculated using eq. 3.1.

The selected transformer core (B66397G0000X187, TDK Electronic, Munich, Germany), transformer coil former (B66398W1024T001, TDK Electronics, Munich, Germany) and enamelled copper wire (0.78 mm diameter, 21 AWG, RS PRO, Corby, UK) are shown in fig. 3.12 (a)-(c) respectively. Fig. 3.12 (d)-(e) illustrate the specific manufacturing process for the transformer. The primary winding is wound onto the core first due to its lower number of turns; subsequently, an insulating tape layer is applied to its outer surface to isolate the primary and secondary windings. Then, the high-impedance winding is wound. Finally, the transformer core is assembled onto the completed coil assembly to obtain the complete impedance matching transformer.

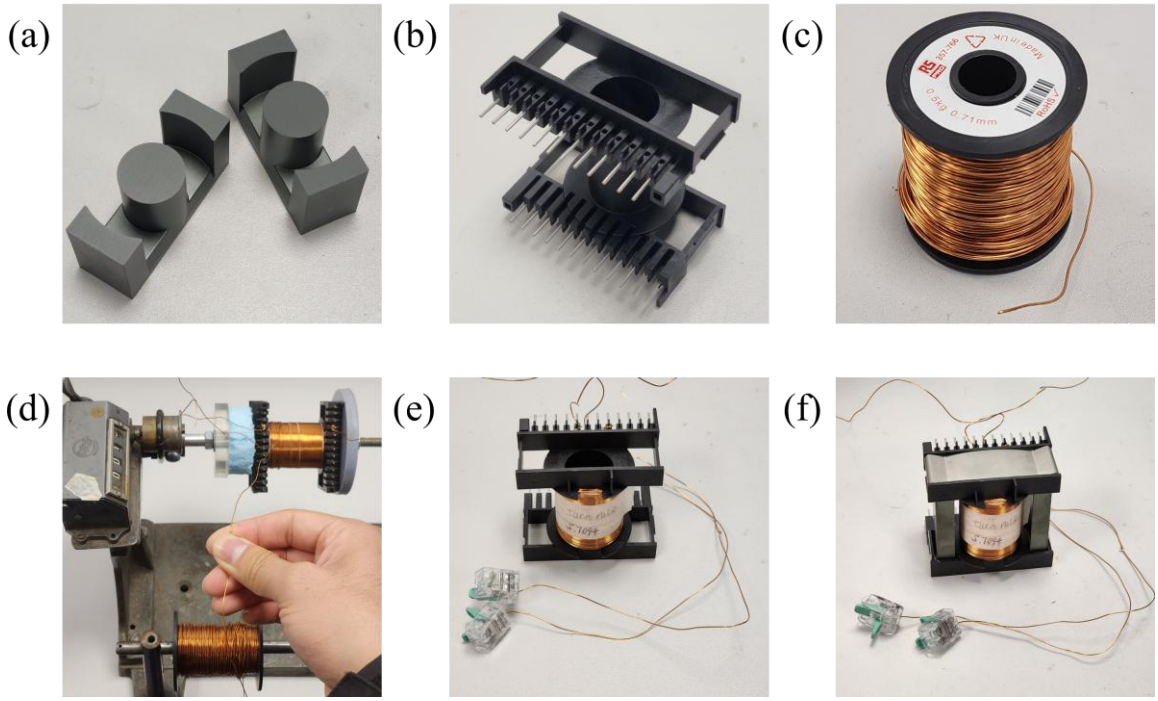

Fig. 3.12: Flowchart for the fabrication of impedance matching transformer. (a) Transformer cores. (b) Transformer coil former. (c) Enamelled copper wire. (d) Manually winding copper coils. (e) The completed impedance reducing coil. (f) The fully assembled impedance matching transformer.

This section produced corresponding impedance matching transformers for both air-backed water and water-backed water operating conditions, with coil turn ratios of 1:5.7 and 1:6.8 respectively.

3.7 Acoustic detection of cavitation emissions

3.7.1 Shockwave Passive cavitation detector (swPCD)

In most cavitation-mediated industrial applications, the collapse of high-intensity cavitation bubbles radiates intense shockwaves. Conventional hydrophones are not suitable for acquiring such acoustic emission data. A swPCD was developed in-house at CavLab to overcome this limitation and to record the acoustic signals induced by the tube transducer and the sonotrode. The operating principle of the swPCD and its sensitivity to cavitation signals below 5 MHz, compared with conventional hydrophones, have been discussed in §1.4.3.1. This section further details the specific fabrication process of swPCD.

The overall structure of the swPCD was composed of the following six components:

1. 50 Ω coaxial cable
2. BNC connector
3. The active element - 110 μm thick and 10 mm diameter PVDF
4. 3D printing case
5. Backing layer
6. Impedance matching layer

3.7.1.1 Case design and printing

The swPCD case, as shown in fig. 3.13, was modelled in 3D using Fusion 360. Its geometric dimensions comprise 12.5 mm outer diameter and 9.5 mm inner diameter. A stepped structure extending 1 mm inward with a diameter of 11 mm is incorporated at the front end of the case, serving as a support platform for the PVDF element. This structure ensures repeatable positioning of the PVDF and provides a geometric reference for the subsequent precise alignment of the matching layer and backing layer. A 3 mm diameter cable guide is

reserved along the case's axial direction to guide the coaxial cable through the inner boundary. The case was ultimately fabricated using SLA 3D printer (Form 3, Formlabs Inc., USA).

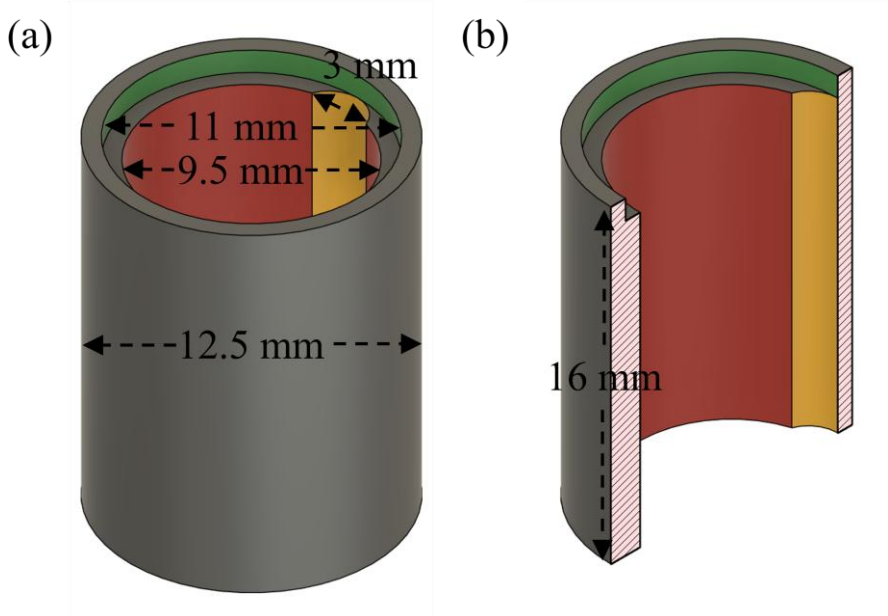

Fig. 3.13: (a) Schematic of the swPCD case, (b) Cross-section of swPCD case.

3.7.1.2 The fabrication process for swPCD

The complete fabrication process for the swPCD is presented in fig. 3.15 (a)-(h), comprising the following five steps.

1. BNC connector assembly

As shown in fig. 3.14 (a & b), one end of the coaxial cable is first securely soldered and fixed to the BNC connector, ensuring that the assembled swPCD achieves a reliable electrical connection with the oscilloscope.

2. Active element cutting and bonding

The 110 µm thick PVDF sheet was first cut into 10 mm diameter disc using a DSPIAE MT-C Stepless Adjustment Circular Cutter, fig. 3.14 (c). Subsequently, approximately 5 mm of the outer insulation was stripped from the opposite end of the coaxial cable as shown in fig. 3.14 (d). Both the internal grounding wire and the positive electrode wire were then braided into separate wire bundles to prevent short circuits during connection to the PVDF. The

positive lead was affixed to the upper surface of the PVDF disc using conductive silver epoxy adhesive, while the grounding lead was connected to the lower surface of the PVDF, fig. 3.14 (e). Following assembly, the component was left to cure at room temperature for no less than 24 h.

3. PVDF secured to the case

As shown in fig. 3.14 (f), the electrically connected PVDF disc was secured to the support platform at the front of the case using Gorilla glue. The coaxial cable within the case was simultaneously fixed along the pre-reserved groove position using adhesive dots to restrict its movement within the case.

4. Preparation of the backing layer

The backing layer was fabricated using a tungsten-epoxy composite material. The epoxy resin selected was the two-component Araldite® (CY 221) with hardener (HY 956 E), mixed in a 5:1 weight ratio. High-density tungsten powder (Fisher Scientific) was added to the epoxy resin according to the required volume, achieving a tungsten powder volume fraction of approximately 20% within the mixture. The two-component epoxy resin was thoroughly mixed first, followed by the gradual addition of tungsten powder under stirring until a viscous, uniform slurry was formed. This mixture was then poured into the swPCD case to form the backing layer and cured at room temperature for 24 hours, as shown in fig. 3.14 (g).

5. The preparation of the matching layer

The matching layer employs the same epoxy resin as the backing layer, but without the addition of tungsten powder. The pre-mixed epoxy resin is applied to the surface of the PVDF element at the front of the case and its surrounding area (fig. 3.14 (h)), then cured at room temperature for approximately 24 hours. Following curing, the front surface is ground to ensure the matching layer is flush with the front surface of the case, thereby achieving a smooth acoustic incident interface.

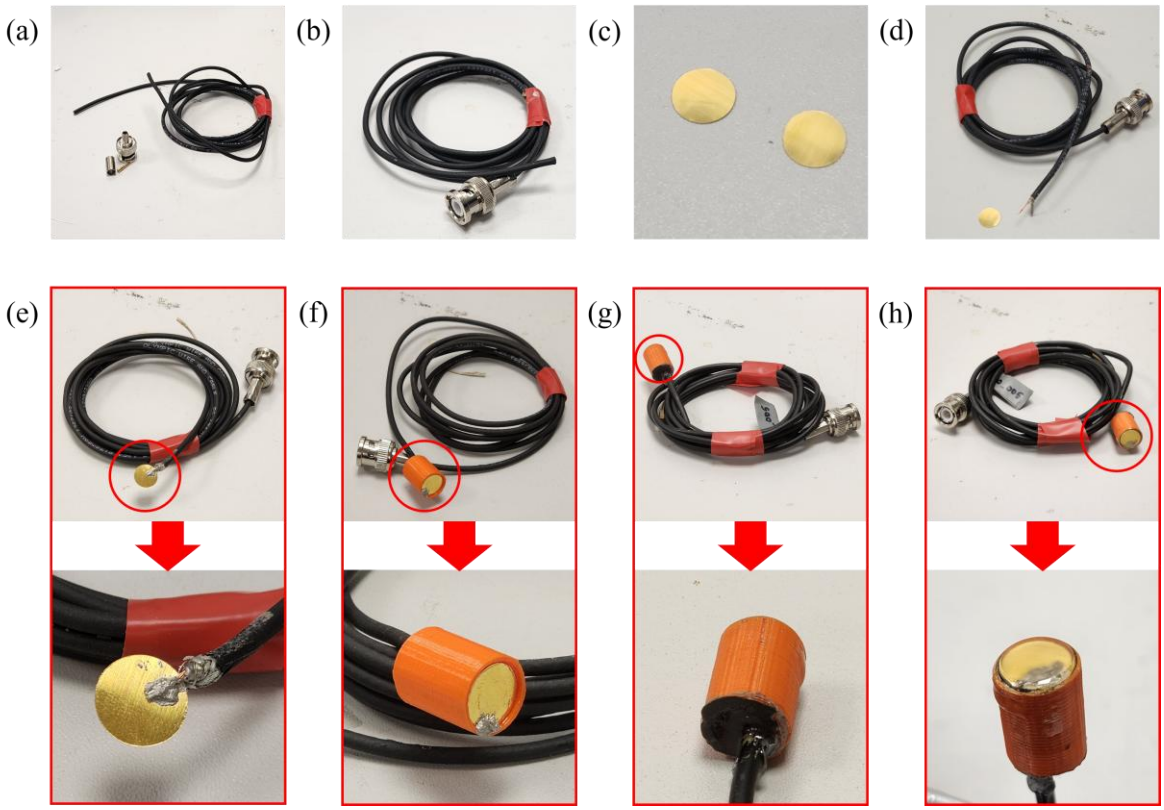

Fig. 3.14: Shockwave passive cavitation detector fabrication process. (a) Coaxial wire and BNC connector, (b) coaxial wire connect with BNC connector, (c) 10 mm diameter PVDF disks, (d) Stripped coaxial wire braided into positive and ground leads for PVDF disk bonding, (e) coaxial wire bonded to upper and lower PVDF surfaces with silver conductive epoxy, (f) PVDF with attached coaxial wire bonded to the case using epoxy, (g) adding the backing layer, (h) adding the matching layer to the front side. The lower images in (e)-(h) show magnified views of the components highlighted by the red circle.

3.7.2 Cavitation emission data collection

Acoustic signals detected by the swPCD were acquired and recorded by a Tektronix 5 Series oscilloscope (Tektronix, Berkshire, UK) with a maximum sampling rate of 6.25 GS/s, and displayed in real time in both time-domain and frequency-domain waveforms. The acoustic data were saved in .mat format, which facilitated subsequent filtering and feature extraction operations in MATLAB (MathWorks, MA, USA).

3.7.3 Filters used for processing acoustic signal data

Filters, which involves selectively passing or suppressing signal components within specific frequencies or frequency bands, is a common method in signal processing. Among digital filters, the four common types are high-pass, low-pass, band-pass, and band-stop filters, each

serving specific functions in signal processing. A high-pass filter (fig. 3.15 (a)) attenuates signals below the cut-off frequency f_c whilst allowing frequencies above f_c to pass. A low-pass filter (fig. 3.15 (b)) attenuates frequencies above f_c whilst permitting those below f_c to pass. A band-pass filter (fig. 3.15 (c)) permits signal components within the frequency band defined by f_{c1} and f_{c2} to pass through, while attenuating signals outside this band. A band-stop filter (fig. 3.15 (d)) attenuates signal within the frequency band between f_{c1} and f_{c2}, allowing signals outside this band to pass through.

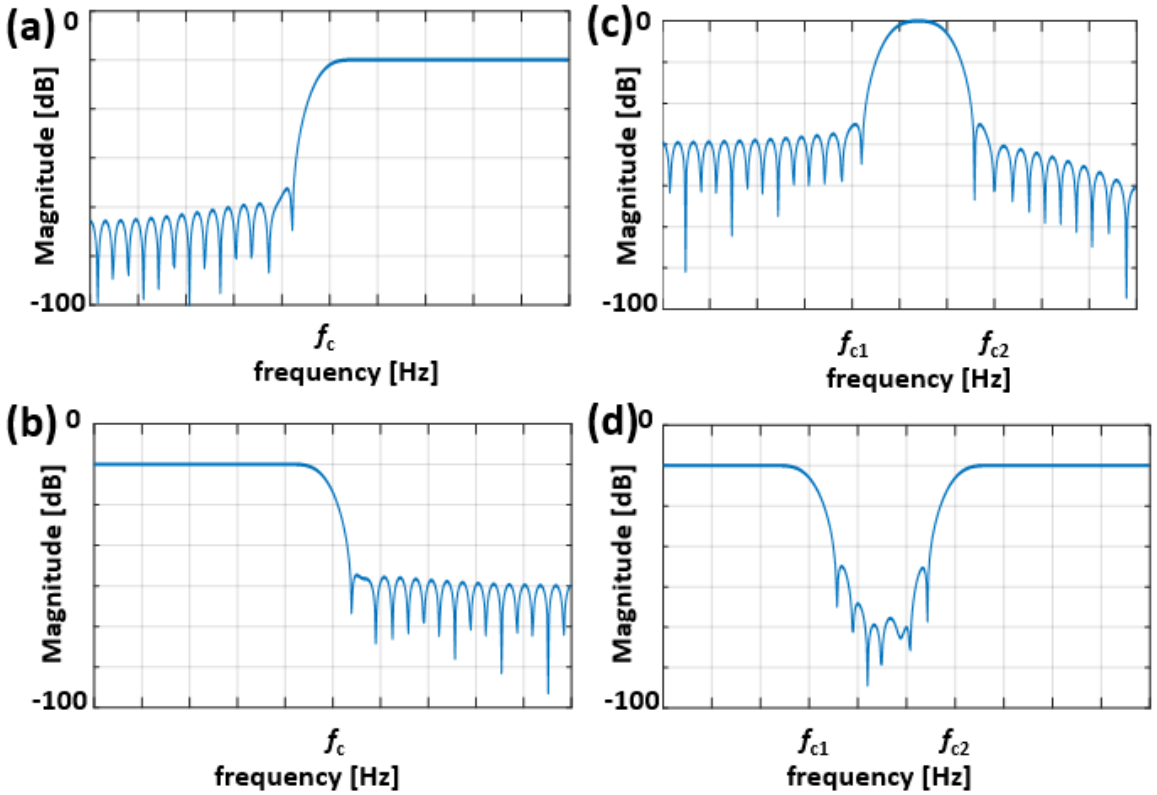

Fig. 3.15: (a) high-pass filter, (b) low-pass filter, (c) band-pass filter, (d) band-stop filter. Taken from [32].

The method employed in CavLab for processing acoustics signals using finite impulse response (FIR) digital filters is adopt in this thesis. The FIR filter is built into MATLAB 2025b (MathWorks), writing 'fir1'. The fundamental elements of the 'fir1' function contain the filter order (N) and the cutoff frequency f_c. Note that the N and f_c must satisfy N>0 and $0 < f_c < f_s/2$ (where f_s denotes the sampling frequency and $f_s/2$ represents the Nyquist frequency), respectively. The filter design proceeds in two stages:

- Generate the FIR filter coefficients using h = fir1(N, f_c, 'filter type'). Define the required filter type.

- Convolve the resulting filter with the raw swPCD data to obtain the filtered signal.

The complete MATLAB filtering code is provided in Appendix A.

3.8 Deep eutectic solvents selection and preparation

Deep eutectic solvents (DESs) are multicomponent liquids commonly formed by mixing a hydrogen-bond acceptor (HBA) with a hydrogen-bond donor (HBD). Interactions between the constituent species produce a substantial melting-point depression relative to the individual components, allowing the mixture to remain liquid at or near room temperature [176], [202]. Unlike conventional ionic liquids, DESs do not necessarily consist entirely of ionic species. The DES used in Chapter 4 was Ethaline, a Type III DES formed from choline chloride ($(CH_3)_3N(Cl)CH_2CH_2OH$, abbreviated as ChCl, Sigma Aldrich, purity ≥ 90%), acting primarily as the HBA, and ethylene glycol ($HOCH_2CH_2OH$, abbreviated as EG, Sigma Aldrich, purity ≥ 99%), acting as the HBD, at a ChCl:EG molar ratio of 1:2.

Ethaline-DES was selected as the reaction medium for the sonotrode-assisted delamination of technology critical metal (TCM)-containing layers from printed circuit boards (PCBs). It can be readily prepared from commercially available constituents and provides a chloride-rich liquid environment that supports the dissolution and transport of oxidised metal species. However, Ethaline itself was not treated as the oxidant in the present experiments. $FeCl_3$ or $CuCl_2$ was added at a final concentration of 0.1 mol L^{-1} as the oxidising agent responsible for promoting oxidative etching of the metallic layer, including the underlying copper layer. For the $FeCl_3$ - containing formulations, the overall oxidation of Cu can be represented by [191]:

$$Fe^{3+} + Cu^{0} \rightarrow Fe^{2+} + Cu^{1+} \quad (3.5)$$

For the $CuCl_2$ - containing formulations, the overall oxidation of Cu can be represented by [191]:

$$Cu^{2+} + Cu^{0} \rightarrow 2Cu^{1+} \quad (3.6)$$

The reaction and dissolution of the copper layer enabled delamination of the TCMs. Sonotrode-generated acoustic cavitation complemented this chemical process by enhancing interfacial mass transfer and producing mechanical effects, including shock waves, microjets and local fluid motion, which assisted the removal of the TCMs [192].

The viscosity of Ethaline DES is 37 mPa·s at 20°C [202], which is substantially more viscous than water. The high viscosity of Ethaline can restrict diffusion and interfacial mass transport and can also influence cavitation-bubble dynamics. De-ionised water was therefore added to Ethaline as a diluent to investigate whether changing the liquid composition improved cavitation activity and TCM delamination. Water addition changes not only viscosity but also other properties relevant to cavitation and metal dissolution, including density, surface tension, vapour pressure, ionic conductivity and acoustic attenuation [180]. The experiments should therefore be interpreted as an investigation of the coupled effects of solvent composition, cavitation and chemical action, rather than as a viscosity-only study.

Four Ethaline-de-ionised water volume ratios were investigated: 100:0, 80:20, 70:30 and 50:50. The four solvents used to investigate the effect of water dilution contained 0.1 mol L^{-1} $FeCl_3$. An additional 50:50 Ethaline-de-ionised water solvent containing 0.1 mol L^{-1} $CuCl_2$ was used to compare the effect of changing the oxidising agent. The experimental matrix therefore comprised four Ethaline-de-ionised water volume ratios and five liquid formulations, as summarised in Table 3.1.

Table. 3.1 Compositions of the Ethaline-de-ionised water solvents used in the Chapter 4 and 5 PCB delamination experiments.

No.	Ethaline (vol%)	De-ionised water (vol%)	Oxidising agent	Final concentration
1	100	0	$FeCl_3$	0.1 mol·L^{-1}
2	80	20	$FeCl_3$	0.1 mol·L^{-1}
3	70	30	$FeCl_3$	0.1 mol·L^{-1}
4	50	50	$FeCl_3$	0.1 mol·L^{-1}
5	50	50	$CuCl_2$	0.1 mol·L^{-1}

During preparation, the Ethaline DES was heated on a 60 °C hotplate and thoroughly mixed using a magnetic stirrer (fig. 3.16). $FeCl_3$ was then added gradually until a homogeneous, orange-yellow liquid was obtained. The mixed DESs was stored in a sealed container and left to stand for 24 h to ensure system stability, while avoiding direct sunlight.

The investigated solvents contained between 50 and 100 vol% Ethaline-DES. This experimental matrix was designed as an initial dilution study and was not intended to determine the minimum quantity of Ethaline-DES required for effective metal dissolution. Solvents containing less than 50 vol% Ethaline and an aqueous oxidant control were not investigated. Consequently, the 50:50 volume ratio represents the lowest Ethaline fraction examined and the best-performing composition within the investigated range, rather than an established minimum or globally optimal solvent composition.

Fig. 3.16: Preparation of a clear, homogenous Ethaline DES at 60 ℃ with stirring.

3.9 Sonochemiluminescence solvent preparation

SCL imaging was employed to visualize the active cavitation regions inside the tube transducer and below the sonotrode tip, in Chapter 5. In alkaline solution, luminol (5-amino-2,3-dihydro-1,4-phthalazinedione) reacts with hydroxyl radicals (•OH), which are generated during the sonochemistry process, to form 3-aminophthalate, which emits blue light [72], [203]. The brightness of SCL serves as an indicator of cavitation activity: higher brightness corresponds to more denser cavitation events [72].

The SCL solution was prepared as follows: First, add 20 mL of 5 M NaOH solution (98%, Fisher Scientific) to 980 mL de-ionised water and stir. Next, add 0.17 g of luminol powder

(>97%, Sigma-Aldrich) and stir until completely dissolved. All imaging experiments were performed within a light-shaded box in a darkroom to minimise interference from environment light.

3.10 Citric acid solvent preparation

After dismantling, aged LiBs are exposed to air, causing the graphite on the anode surface to react with residual electrolyte and atmospheric moisture to form inorganic products such as lithium carbonate (i.e., an ageing layer) [204] [205]. The ageing layer alters the interfacial state of the graphite coating, thereby inhibiting the efficiency of graphite exfoliation in water. The delamination efficiency of graphite tends to decrease as the duration of exposure to air increases [204]. Citric acid solutions can react with the ageing layer, restoring the graphite coating to a state that facilitates delamination.

In Appendix C, five citric acid solutions with concentrations of 0.1, 0.2, 0.3, 0.4, and 0.5 $mol \cdot L^{-1}$ were selected as the working media, with systematic comparisons of their effects on graphite delamination efficiency. Citric acid is a water-soluble organic acid and can be prepared at room temperature. Specifically, a prescribed amount of citric acid (Sigma Aldrich, purity ≥ 90%) was added to a beaker containing de-ionised water and mixed using a magnetic stirrer. A homogeneous solution is obtained within 3 minutes. After preparation, the solution is transferred to a sealed container for storage and kept in a light-protected environment.

Chapter 4

Technology critical metal delamination from printed circuit boards in Ethaline-DES

Chapter overview
Deep eutectic solvents (DESs) are showing strong potential for the environmental friendly recovery of technology critical metals (TCMs) from printed circuit boards (PCBs). However, the high viscosity of DES significantly limits mass transfer, such that passive TCM removal typically requires several hours of immersion. In this chapter, a power ultrasonic device - the sonotrode, is introduced for process intensification, providing a viable route to enhance TCM recovery efficiency in DES. This chapter focuses on pure Ethaline-DES, systematically characterising cavitation bubble collapse shockwave intensity across a broad input power range, using a passive cavitation detection method equivalent to Yusuf *et al* [34], described in §1.2.2. The results reveal a pronounced non-linear relationship between shockwave intensity and input power. Moderate input power generates more regular and stable cavitation shockwaves under the experimental configuration, yielding superior TCM delamination efficiency compared to high power. Dual perspective high-speed imaging (HSI) further indicates that stable bulbous cavitation structures formed at moderate power maintain sustained contact between bubble cluster and the PCB surface, thereby enhancing delamination efficiency. The time required for TCM delamination compared with passive immersion is reduced by 30-fold. Overall, parameter optimisation guided by the bubble collapse shockwave intensity, rather than simply increasing input power, is more effective for achieving efficient ultrasonic-assisted ionometallurgical processing.

Journal Paper
A mechanistic study identifying improved technology critical metal delamination from printed circuit boards at lower power sonications in a deep eutectic solvent. Ben Jacobson, **Shida Li**, Rodolfo Marin Rivera, Paul Daly, Christopher E. Elgar, Daniel M. Mulvihill, Andrew P. Abbott, Andrew Feeney and Paul Prentice.
Ultrasonic Sonochemistry, vol. 101, p. 106701, 2023.

Journal Paper
Observation of cavitation dynamics in viscous deep eutectic solvents during power ultrasound sonication. Ben Jacobson, **Shida Li**, Paul Daly, Christopher E. Elgar, Andrew P. Abbott, Andrew Feeney and Paul Prentice.
Faraday Discussions, vol. 253, p. 10.1039, 2024.

4.1 Motivation and context

Printed circuit boards (PCBs) represent around 3-5% of globally produced electronic waste (E-waste) [206]. However, PCBs contain up to 30-40 wt% of technology critical metals (TCMs) such as cadmium, chromium, copper, lead, manganese, nickel and tin. Additionally, the content of TCMs such as gold, silver, platinum and rare-earth elements can be at concentrations over 10 times that found in enriched mineral ores.

As described previously in Chapter 2, ionometallurgy is a new technique that is showing promise for recovering metals from E-waste using non-aqueous solvents such as deep eutectic solvents (DESs). Ionometallurgy offers distinct advantages over traditional hydrometallurgical and pyrometallurgical techniques, such as much lower temperature requirements, avoidance of toxic reagents and reduced water consumption [207]. DESs are cheap, easy to make from readily available chemicals like choline chloride and ethylene glycol as described in §2.4, and can be adapted for selectivity to specific metals. The primary drawback of DESs is the slow dissolution kinetics caused by high viscosity. The addition of redox catalysts has demonstrated improved etching rates of TCMs from PCBs and photovoltaics [191], [208]. However, this purely chemical-based enhancement remains mass transport limited. Rivera *et al* [191] employed a $CaCl_2 \cdot 6H_2O$: EG eutectic system containing 1 $mol \cdot dm^{-3}$ $FeCl_3$ to treat PCBs by immersion at 50 °C, and reported that approximately 8 h was required to remove the TCM disc. The high viscosity of DESs limits conductivity and

diffusion of metal ions, making them, alone, inefficient as replacements to traditional techniques.

Acoustic cavitation offers a viable route to addressing the limitations outlined above. By combing chemical and mechanical effects, this method facilitates intensification of ionometallurgy process. The application of power ultrasound within DES media enhances mass transfer efficiency [209] while simultaneously removing surface passivation layers [23]. Concurrently, the transient high temperature environment generated by cavitation bubble collapse promotes radical formation, thereby accelerating the reaction kinetics [210]. Previous studies have reported that power ultrasound can not only increase the leaching rate of metals from ores in strong acid systems [211] but also enhance the electrochemical leaching and redeposition of copper in Ethaline-DES [212], [213]. Nevertheless, the mechanism underpinning ultrasound enhanced ionometallurgy in the context of TCM delamination remain insufficiently understood, and further research is required to optimise ultrasonic parameters.

The aim of this experiment was to investigate the mechanism of TCM delamination by applying sonotrode sonications to PCB samples immersed in Ethaline-DES. Two representative input powers were selected based on cavitation activity characterisation results under different input powers in Ethaline. Sonication enhanced TCM delamination experiments were then performed under high-speed camera monitoring. The surface morphology of samples was conducted at fixed time intervals throughout the sonication to evaluate the delamination efficiency of the TCM layer.

4.2 Materials and methods

4.2.1 Preparation of Ethaline-DES

The DES used in this study was Ethaline. To investigate delamination efficiency, a redox catalyst of anhydrous iron (III) chloride ($FeCl_3$) was added at a ratio of 0.1 $mol \cdot L^{-1}$. The specific preparation process for the solvents is detailed in §3.8.

4.2.2 Experimental setup

This experiment was conducted using a 450 W sonotrode (Digital sonifier, Branson 450) operating at 20 kHz with a 230 mm long tapered Ti probe terminating in a 6.4 mm diameter tip. The input power for the sonotrode was set on the control console as a percentage, with a minimum setting of 10% and adjustable in 1% increments. The sonotrode tip was positioned 4 mm above the PCB, at a consistent immersion depth of 40 mm.

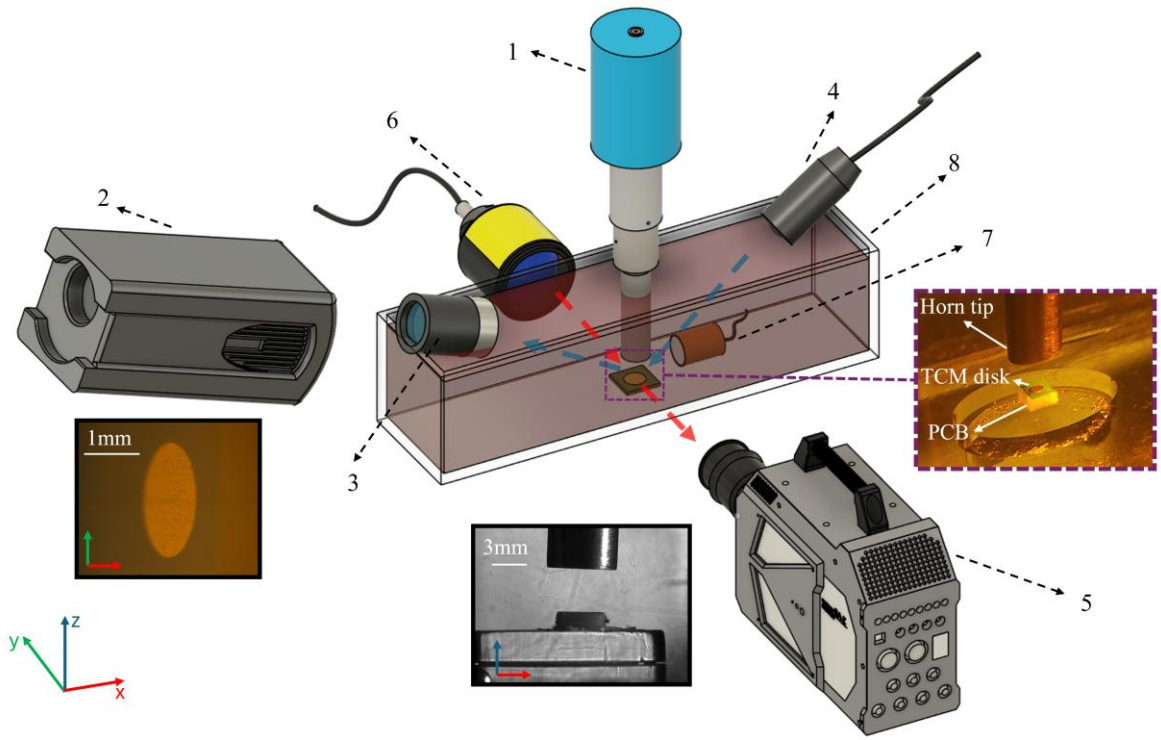

Fig. 4.1: Schematic diagram of the experimental setup for HSI and acoustic monitoring during sonication. Equipment items include (1) sonotrode, (2) Phantom high-speed camera, (3) objective lens, (4) white light illumination, (5) Photron high-speed camera, (6) pulse laser illumination, (7) swPCD, (8) 200 mm ×50 mm× 50 mm water tank. The purple dashed inset image indicates a magnified view of the sonication region, highlighting the sonotrode tip and the PCB substrate immersed in Ethaline. The left inset image shows the field of view (FOV) of Phantom high-speed camera, whereas the lower inset image shows the FOV of the Photron high-speed camera.

4.2.3 Printed circuit board samples

PCB samples used for the experiment were uniformly cut from larger boards (Atotech UK Ltd), fig. 4.2 (a). The material composition and layer thickness of the samples are shown in fig. 4.2 (b). Each sample contained a single TCM disc with a diameter of 2 mm. The diameter

of the sonotrode tip, relative to the PCB samples for the experiment, is denoted by the dashed circle around the PCB sample as shown in fig. 4.2 (c).

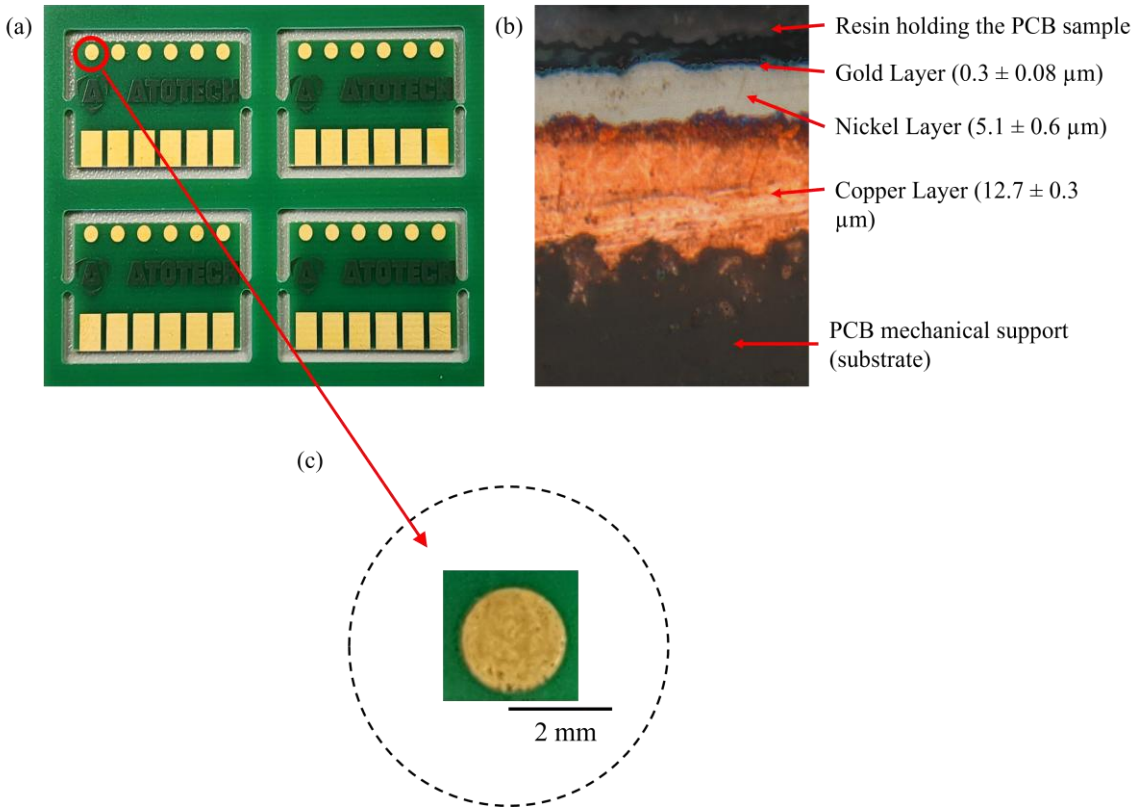

Fig. 4.2: (a) Gold-plated print circuit board. (b) Reflected light image of the metal layer contour. (c) 2 mm diameter disc PCB sample with dashed circle representing the scale relative to the 6 mm diameter Branson sonotrode tip.

4.2.4 Passive cavitation detection

Acoustic emissions from cavitation activity in Ethaline were recorded using an in-house fabricated shockwave passive cavitation detector (swPCD), whose structure and operating principle are detailed in §1.4.2 and §3.7.1. The swPCD was mounted on a three-axis translation stage to allow precise positioning within the tank, with its active element maintained approximately perpendicular to the axis of the horn (fig. 4.1). For all data presented, the distance between the swPCD and the horn tip was fixed at 10 mm, a positioning optimised for cavitation shockwave detection as described in §1.4.3.1.

The swPCD was connected to an oscilloscope (Tektronix 5 series, Berkshire UK), operated for data collection at 25 × 10^6 samples/s. The total recording duration of the acoustic emission was 200 ms, with the trigger set approximately 5 s after the onset of sonication to

ensure cavitation activity reached a steady state. Raw acoustic emission data was recorded in millivolts (mV) and, following detection by the swPCD, were processed in MATLAB (MathWorks, MA, USA) using the filtering procedure described in §3.7.2 to extract the frequency band associated with cavitation shockwaves, which was represented as voltage-time waveforms. The time-averaged shockwave content was quantified using the root mean square voltage (V_{rms}), based on five independent 200 ms records acquired for each parameter. The corresponding MATLAB code is detailed in Appendix A.

4.2.5 Dual perspective high-speed imaging

Front-view high-speed imaging of the cavitation activity during PCB delamination was performed using a Photron FASTCAM SAZ 2100 K high-speed camera (Photron, Bucks UK), fig. 4.1 component 5, with acquisition rates of 8,000 frames per second (fps). Illumination was provided by a synchronised 10 ns pulsed laser source (CAVILUX Smart, Cavitar, Tampere Finland) and coupled via a liquid light guide and collimating lens, fig. 4.1 component 6. This arrangement not only defined the effective temporal resolution (the duration of frame capture) but also enabled shadowgraphic HSI, as described in §3.4. Imaging was performed with a macro lens (Milvus 100 mm f/2M, Zeiss, Oberkochen, Germany), with the field of view (FOV) as shown in the lest inset of fig. 4.1. The image resolutions for the experiment were 1024 × 758, corresponding to spatial resolution of 39 $\mu m \cdot pixel^{-1}$.

Side-view HSI was performed using a Phantom high-speed camera (Vision Research, New Jersey USA; fig. 4.1, component 2) operating at 1000 fps to directly observe TCM delamination behaviour on the PCB during sonication. A long working distance 5× microscope objective lens (0.14NA Mitutoyo, Japan; fig. 4.1 component 3) was employed for this perspective, immersed at approximately 40° above the horizontal into Ethaline. Illumination was provided by a 150 W halogen lamp, coupled via a liquid light guide and collimating lens (Thorlabs, UK; fig.4.1 component 4). The left inset of fig. 4.1 shows the FOV for this imaging perspective. The gold layer of the TCM disc acts as a reflective surface, and the focal line extends along the y-direction, resulting in a slight defocus at both the proximal and distal edges of the disc.

4.2.6 Microscope image processing and delamination area calculation

At predefined time points during sonication, PCB samples were removed from the solvent, rinsed with de-ionised water and dried. The samples were then characterised using an

Alicona Infinite Focus G4 3D surface profilometer (Bruker-Alicona, Graz, Austria), with surface micrographs and topographical data acquired using a 5× objective lens (Bruker-Alicona).

The resulting 2D surface micrographs were imported into ImageJ (National Institutes of Health, Wisconsin, USA), and processing using a customised thresholding and segmentation macro to separate the TCMs from the underlying PCB substrate (fig. 4.3). Subsequently, the residual TCMs coverage area was calculated under each condition and compared with the initial TCMs area, thereby determining the percentage of TCMs remaining after sonication.

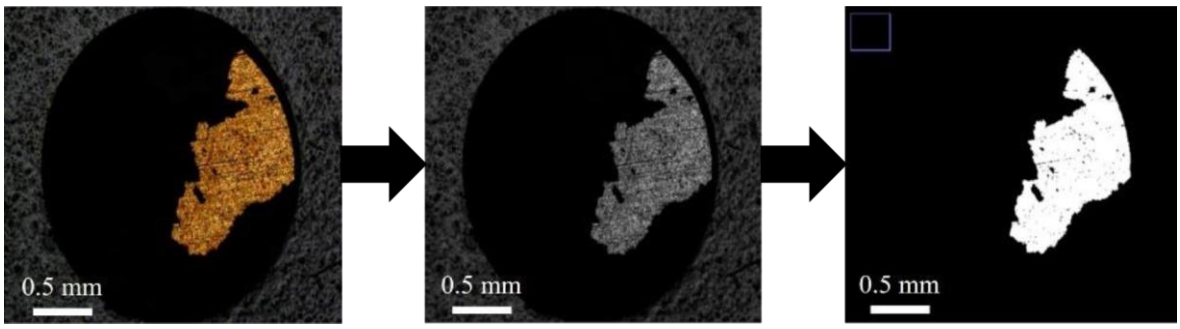

Fig. 4.3: Threshold-based segmentation in ImageJ used to separate TCM from the PCB substrate.

4.2.7 Data collection

Sonication was initiated manually via the sonotrode control console, while the remaining devices were synchronised through electronic triggering from a signal generator (DG4102, Rigol Technologies, Beijing, China). HSI was employed to capture representative TCM delamination behaviour and was triggered immediately prior to sonication to ensure the initial stage of the process was recorded.

The experiment adopted a staged, cumulative-processing approach. Samples were withdrawn for characterisation after every 10 s of cumulative sonication to obtain time-resolved data on the evolution of delamination. For each input power condition, five PCB samples were analysed, giving a total cumulative sonication time of 5 min. In addition, Phantom and Photron HSI were synchronised to record the full 10 s sonication interval in order to assess the influence of input power on delamination behaviour.

4.3 Results

4.3.1 High-speed imaging and swPCD data of cavitation at selected input powers in Ethaline

The following results present sample data from the characterisation of sonotrode generated cavitation in Ethaline at 60%, 70% and 90% input powers. The figures include representative HSI of cavitation development beneath the sonotrode tip, captured from the perspective of Photron high-speed camera, alongside 200 ms acoustic data recorded by swPCD during 10 s sonication. The three input power were selected based on the analysis of the cavitation shockwave content in the acoustic emission signals across all tested input powers, as detailed in §4.3.2. These input powers correspond to the key structural features in the V_{rms} versus input power plot, with 60% and 90% further utilised for TCM delamination observations in §4.3.3. PCB sample was not present for the data presented here, as the objective was to characterise cavitation behaviour in Ethaline rather than TCM delamination. The acrylic disc used to support PCB sample in delamination experiments remained in the setup, fixed at 10 mm from the horn tip to ensure consistent positioning and immersion depth. The presentation of the acoustic data follows that of Yusuf *et al* [34], who used swPCD to characterise the periodic shockwave emissions from bubble clusters in de-ionised water, using the same Branson sonotrode as the ultrasonic source used in the current study.

Fig. 4.4 (a) presents six representative frames from HSI sequence recorded at 8,000 fps, summarising the evolution of cavitation structure beneath the sonotrode tip at 60% input power. Within the first 1000 ms sonication, the cavitation cluster beneath the tip progressively evolved into a bulbous structure typically observed for sonotrode operation in viscous liquid [22], [94], [214]. Notably, the structure remained stable throughout the subsequent 9 s of sonication.

Fig. 4.4 (b) and (c) show swPCD data of the cavitation acoustic emissions, recorded approximately 5 s into sonication captured by fig. 4.4 (a). Fig. 4.4 (b) shows the filtered 200 ms voltage-time domain signal, whilst fig. 4.4 (c) presents a 2 ms signal segment extracted from the black-box region in (b) to reveal bubble collapse shockwave content. Fig. 4.4 (d) shows the corresponding cavitation noise spectrum obtained from the 200 ms record.

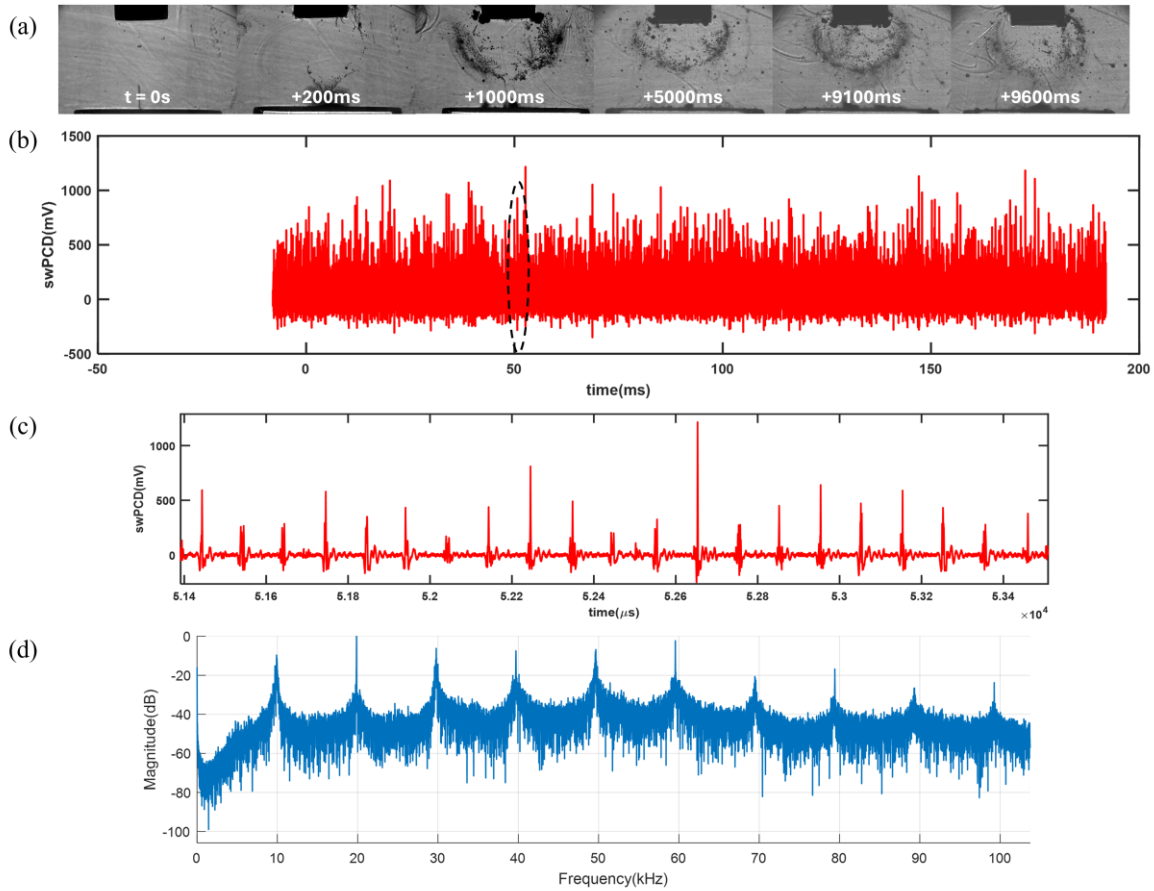

Fig. 4.4: (a) Representative HSI of cavitation structure evolution during 10 s sonication in Ethaline at 60% input power, with 6.4 mm diameter sonotrode tip serving as scale. (b) Time domain waveform of 200 ms acoustic signal acquired after 5 s sonication. (c) A 2 ms signal segment extracted from the black-boxed region in (b), illustrating the typical time domain features of bubble collapse shockwaves. (d) The cavitation emission noise spectrum obtained by applying a Blackman window and fast Fourier transform on the time domain signal in (b).

The important characteristics of the shockwave generated during the 60% input power sonication, are the shockwave timings at $2T_0$, where T_0 denotes the oscillation period of the sonotrode tip (T_0 = 50 µs at 20 kHz operating frequency). This result demonstrates that cavitation activity exhibits a period-doubling behaviour, wherein cavitation structure collapses once every two drive cycles. Research by Song *et al* [9] and Yusuf *et al* [34] as described in §1.2 of the previous research from CavLab indicate that such period-doubling behaviour manifests in the cavitation noise spectrum as peaks at $nf_0/2$ where n is any integer, fig. 4.4 (d). This corresponds to the $f_0/2$ harmonic and its higher harmonics. Fig. 4.4 (b) and (c) further indicated pronounced variability in shockwave amplitude, with peak varying between approximately 200 and 1000 mV.

Fig. 4.5 presents cavitation characterisation data at 70% input power. The bulbous structure forms earlier, becoming discernible at t=100 ms compared to fig. 4.4 (a). It also exhibits a smaller curvature radius beneath the tip, with bubble clusters appearing denser. However, the bulbous structure at 70% input power does not persist throughout sonication. It progressively retracts towards the sonotrode tip from t=800 ms and has fully disappeared by t=1500 ms. Subsequent cavitation behaviour more closely resembled that generated by the sonotrode in low viscosity liquid such as water [215], [216], but cavitation oscillations were markedly suppressed. This could indicate that the properties of liquid (including viscosity) can change on a timescale of several seconds under higher input power sonication.

Fig. 4.5 (b) and (c) present the acoustic data acquired at 70% input power. Although a few shockwave peaks exceed the recorded values at 60% input power, overall shockwave amplitudes do not increase with higher input power but instead exhibit a decreasing trend. Furthermore, the timings of shockwave emissions have changed: irregular emissions at T_0 and $3T_0$ are now observable, besides the $2T_0$. This indicates that the cavitation activity in Ethaline is transitioning from a period-doubling response towards a period-tripling behaviour at 70% input power, manifested as high-order harmonic response. Consistently, the spectrum peak at $nf_0/3$ (for all n) in fig. 4.5 (d) displays a lower magnitude and broadening. However, the spectrum peaks between nf_0 do not significantly exceed the spectral floor in the frequency range above 50 kHz.

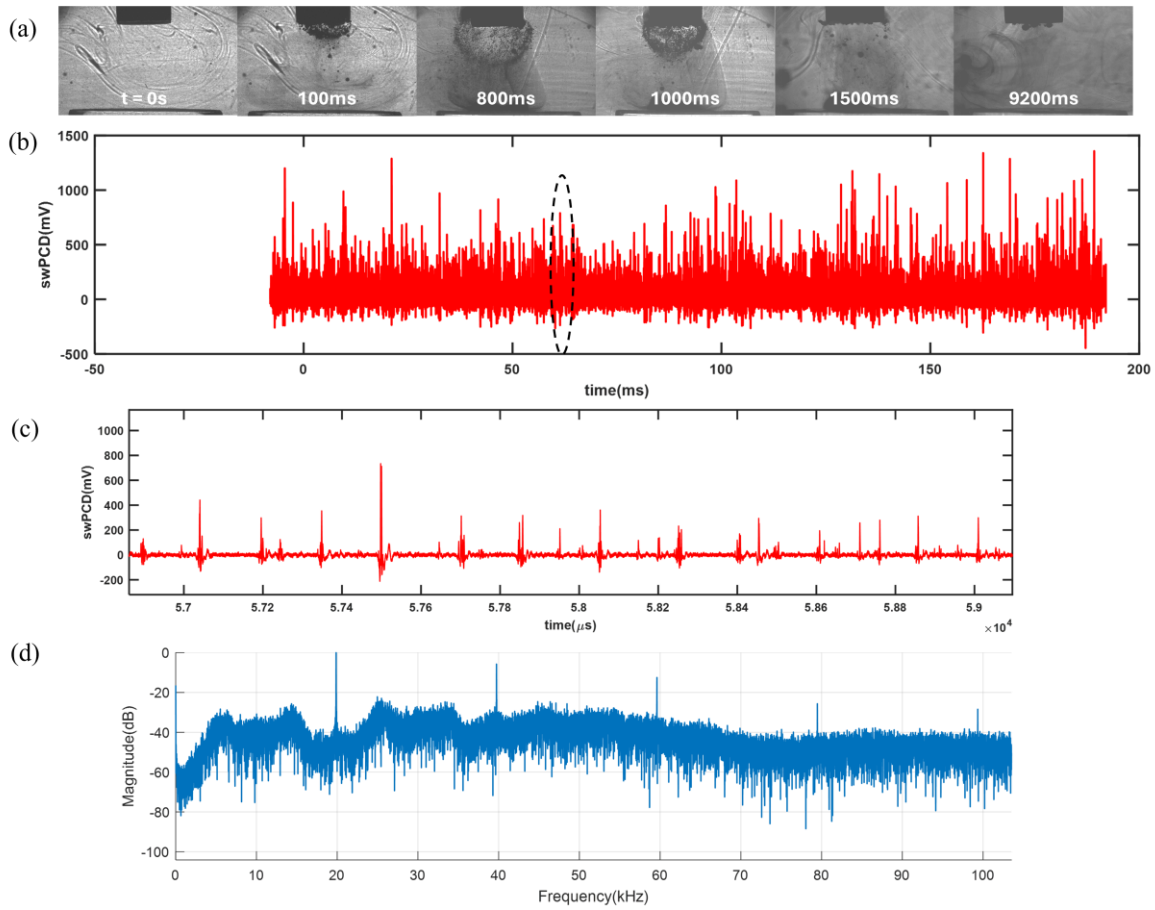

Fig. 4.5: (a) Representative HSI of cavitation structure evolution during 10 s sonication in Ethaline at 70% input power, with 6.4 mm diameter sonotrode tip serving as scale. (b) Time domain waveform of 200 ms acoustic signal acquired after 5 s sonication. (c) A 2 ms signal segment extracted from the black-boxed region in (b), illustrating the typical time domain features of bubble collapse shockwaves. (d) The cavitation emission noise spectrum obtained by applying a Blackman window and fast Fourier transform on the time domain signal in (b).

Fig. 4.6 (a) shows the HSI at 90% input power, where cavitation structure development accelerates further compared to 70% input power. The bulbous structure begins to form at t=50 ms, reaches maximum extent at t=700 ms, and then rapidly contracts, vanishing entirely by 1000 ms as the bubble cluster adheres closely to the tip surface.

Corresponding acoustic data indicate only a few high-amplitude shockwaves were generated within the 200 ms recording duration. In the 2 ms segment shown in fig. 4.6 (c), a feature with an amplitude below 100 mV appears at T_0, suggesting that sub-bubble clusters within the primary bubble cluster beneath the tip are collapsing with different phase relationships. Nevertheless, the majority of high amplitude shockwaves are detected at $4T_0$ timings,

corresponding to a period-quadrupling oscillatory response. Accordingly, the cavitation emissions spectrum in fig. 4.6 (d) exhibits bumps at *nf0/4* for all *n*, until beyond 70 kHz, where the sensitivity falls below the noise floor.

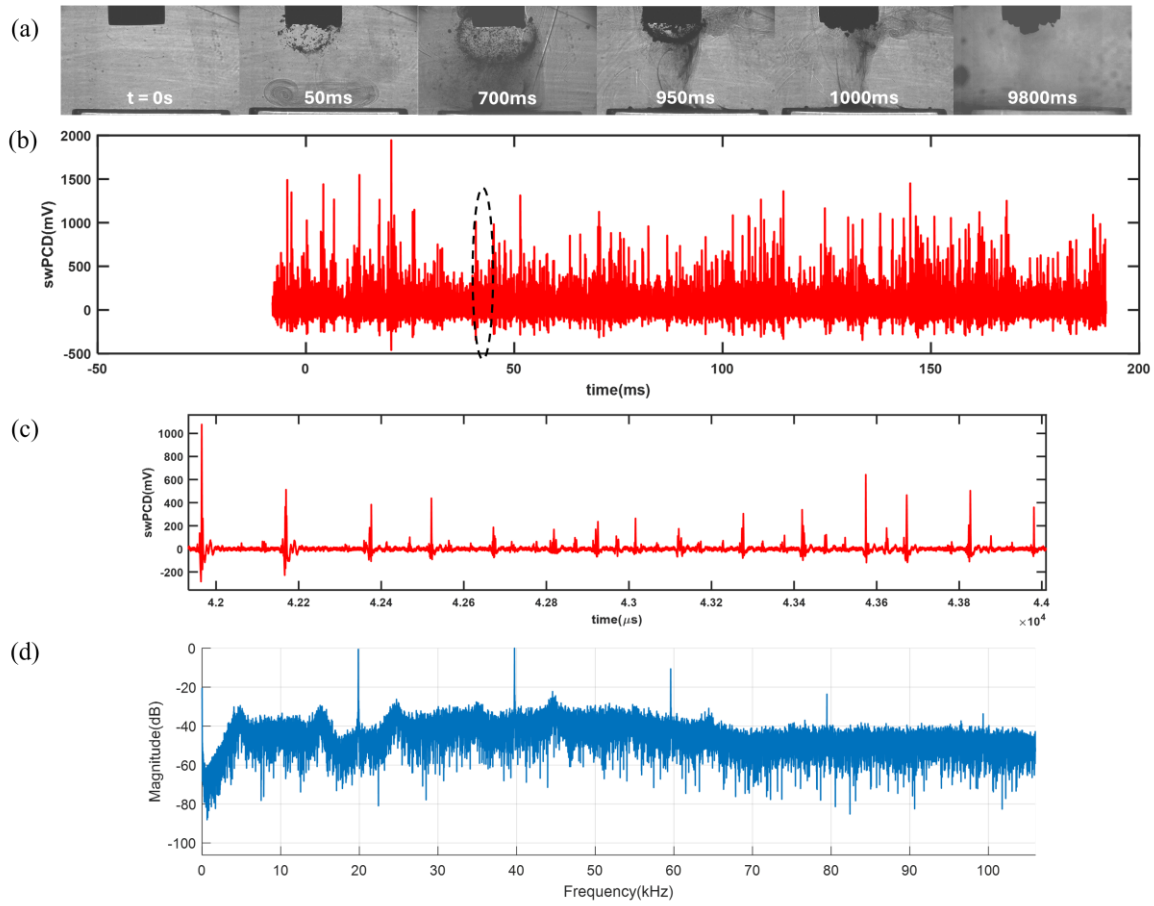

Fig. 4.6: (a) Representative HSI of cavitation structure evolution during 10 s sonication in Ethaline at 90% input power, with 6.4 mm diameter sonotrode tip serving as scale. (b) Time domain waveform of 200 ms acoustic signal acquired after 5 s sonication. (c) A 2 ms signal segment extracted from the black-boxed region in (b), illustrating the typical time domain features of bubble collapse shockwaves. (d) The cavitation emission noise spectrum obtained by applying a Blackman window and fast Fourier transform on the time domain signal in (b).

4.3.2 Characterisation of cavitation activity in Ethaline

Fig. 4.7 shows the relationship between the V_{rms} of cavitation intensity and input power in Ethaline without PCB. Following filter processing, each data point represents the mean of five independent 200 ms cavitation collapse shockwave signals acquired at the same input power. Previous research in CavLab as shown in §1.2.2 fig. 1.5 for sonication in de-ionised

water have demonstrated that V_{rms} exhibits a non-linear tendency on input power [34]. Consequently, the V_{rms} versus input power plot serves as a guide for selecting optimal input parameters in any cavitation mediated sonochemical or sonoprocessing applications.

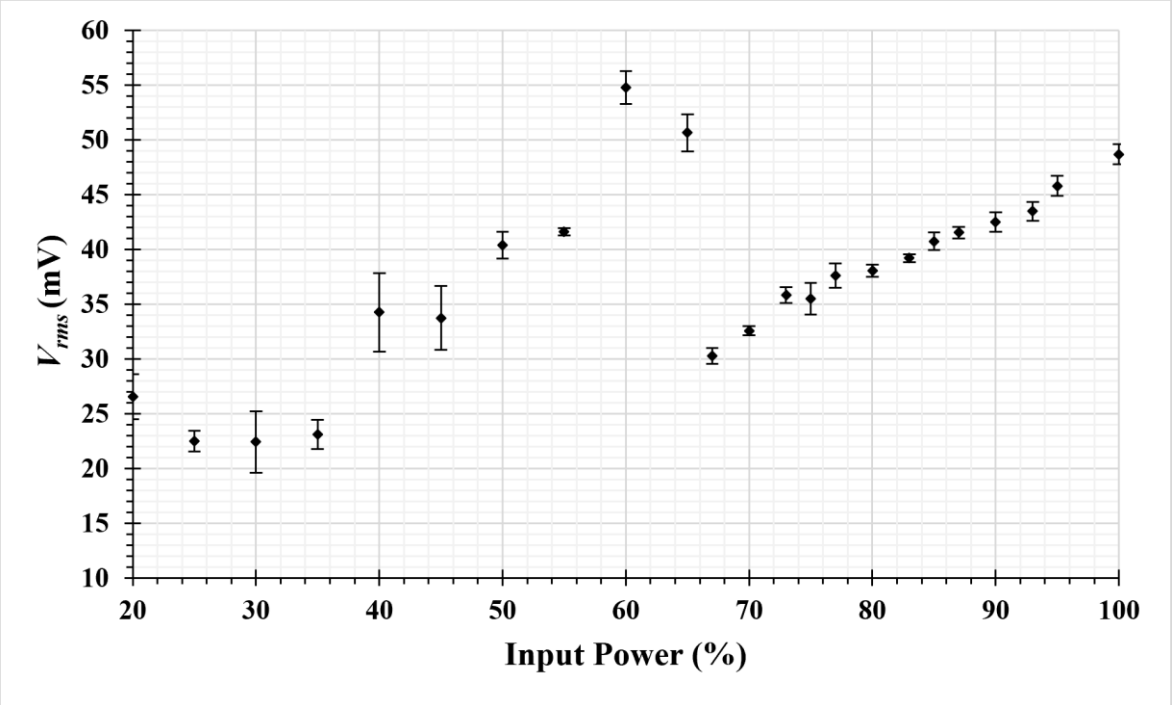

Fig. 4.7: The mean V_{rms} of the signal detected by swPCD during five 200 ms sonications at each input power.

Consistent with the results obtained in de-ionised water, fig. 4.7 also displays a pronounced non-linear behaviour. The shockwave generated in Ethaline at 60% input power reached the maximum intensity, nearly doubling compared to that at 70% input power. As described in §4.3.1, the cavitation at 70% input power were in a transitional state where the subharmonic response shifted from $2T_0$ to $3T_0$. Under the transitional condition, the collapse process of cavitation bubble clusters lacked the stable periodicity observed at 60% input power, resulting in irregular timing intervals for shockwave emission. It is evident that simply increasing input power does not necessarily yield higher cavitation intensity.

Therefore, 60% input power was selected as the primary operating condition for subsequent TCM delamination experiments in Ethaline. 90% input power was additionally chosen as the reference high power condition to establish sufficiently distinct comparative case. Similar cavitation characterisation investigations should be conducted for ultrasonic transducers with other geometric configurations and across different solvents to determine

their respective optimal operating parameters. As supporting evidence, the V_{rms} response in four liquids with different viscosities were additionally characterised, using a 500 W sonotrode (Ultrasonic Processor, Sonics VC-505) in a paper we published in *Faraday Discussions* [217]. The results indicate that a setup with 25% input power was able to generate more effective cavitation output in high viscosity liquids, further demonstrating the transferability of optimal input power across different media. Relevant experimental details are provided in the Appendix B.

4.3.3 Overview of TCM delamination performance at two selected input powers

This section records the surface morphology evolution of TCM discs during cumulative 5 min sonication at 60% and 90% input power, with measurements captured at 1 min intervals. Five PCB samples were tested at each input power. Each sample underwent six 10 s sonication before removal for surface morphology imaging, followed by return to Ethaline for next sonication.

Fig. 4.8 and fig. 4.9 represent Alicona surface microscopy images of the TCM discs at 60% and 90% input power, respectively. No discernible delamination features appeared on the sample surfaces at both input power following the first minute sonication. Although a pre-existing scratch on the surface of sample 1 in fig. 4.5 theoretically provided nucleation sites for cavitation bubbles and enhanced erosion, no TCM delamination was observed in this region. Initial delamination features emerged during the second minute sonication, manifesting as a small number of near-circular pits approximately 40-50 μm. Following the third minute sonication, the individual pits continued to expand and coalesce. Delamination area measurements based on surface microscopy indicated that the delamination ratio at 60% input power reached 68±13% significantly higher than the 40±10% at 90% input power after cumulative 5 min sonication. The trend corroborates the result in fig. 4.7 that the highest V_{rms} corresponds to 60% input power.

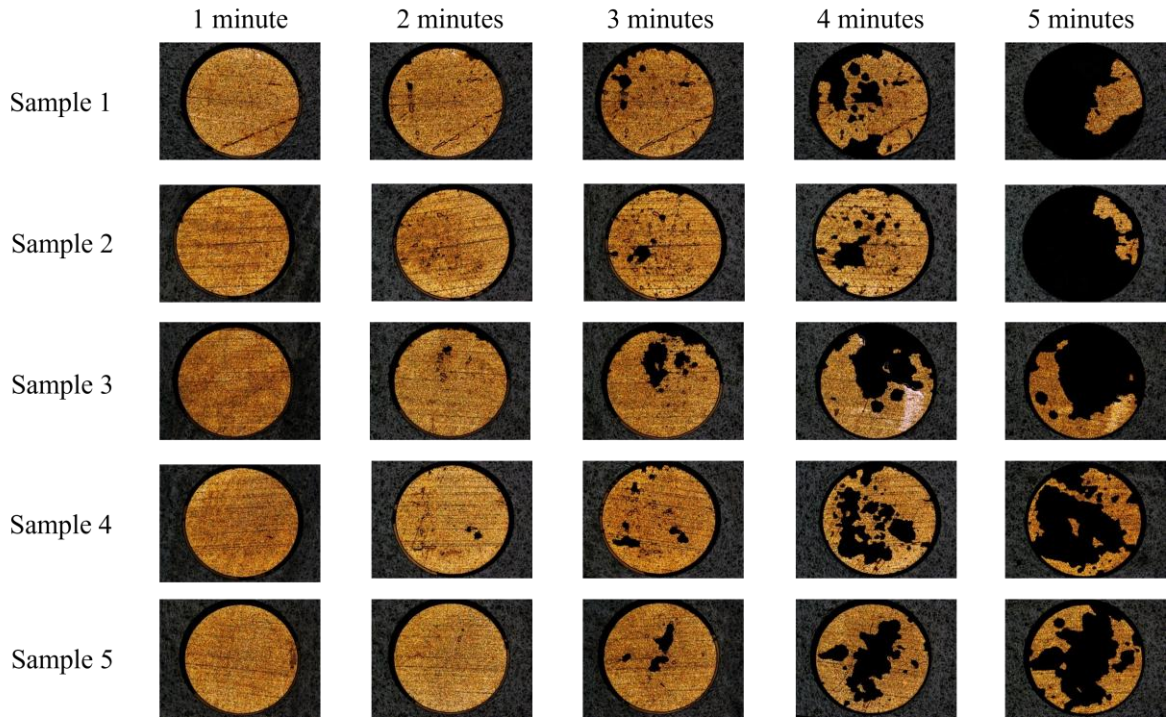

Fig. 4.8: Surface microscopy of the TCM discs on five PCB samples after sonication at 60% input power, acquired at 1 min intervals over a total sonication time of 5 min. Scale provided by the 2 mm diameter disc.

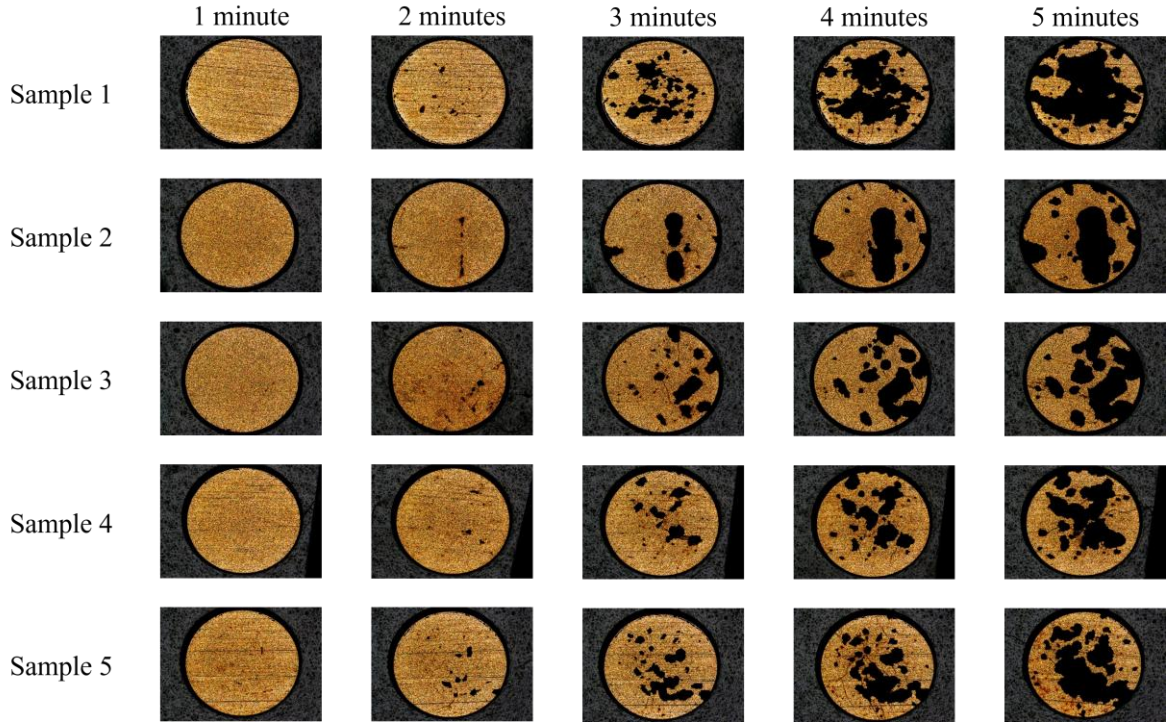

Fig. 4.9: Surface microscopy of the TCM discs on five PCB samples after sonication at 90% input power, acquired at 1 min intervals over a total sonication time of 5 min. Scale provided by the 2 mm diameter disc.

4.3.4 Dual-perspective high-speed imaging of TCM delamination

This section presents the imaging results of TCM delamination events on PCB surface, captured by Phantom and Photron high-speed camera at 60% and 90% input power. All observations were selected from the HSI dataset acquired in this study, and represent the evolution of cavitation structures and typical TCM delamination behaviour under each power condition.

Fig. 4.10 presents representative HSI of sample 2 acquired during the 31-40 s sonication interval of the fifth minute at 60% input power. The red dashed boxes highlight a typical delamination event, in which a TCM fragment is prised from the PCB surface and gradually transported outward under fluid flow. Notably, a bulbous cavitation structure persists beneath the sonotrode tip and remains in direct contact with the PCB surface. This cavitation structure formed at the edge of the sonotrode tip, extending downward along a curved trajectory before converging onto the PCB surface and thereby providing a stable cavitation interaction zone that promotes TCM delamination.

Fig. 4.10 presents representative dual-perspective HSI sequences acquired for sample 2 during the fifth minute of sonication at 60% input power, within the 31-40 s interval. Fig. 4.10 (a) shows the Phantom perspective imaging, revealing that the delamination of large TCM fragments was not instantaneous but progressed gradually through lifting, oscillation and eventual full separation. Specially, a fragment covering approximately 20% of the TCM disc area began lifting from the PCB substrate at 32 ms. The corresponding Photron imaging in fig. 4.10 (b) shows that the PCB surface is persistently covered by a cavitation bubble cluster around this time. The fragment remained partially attached to the substrate but oscillated continuously under the action of the surface bubble cluster before 1900 ms. The fragment fully delaminates and subsequently migrates outwards at approximately 1902 ms, and the event is clearly highlighted in the Photron imaging by the red dashed box and the magnified inset.

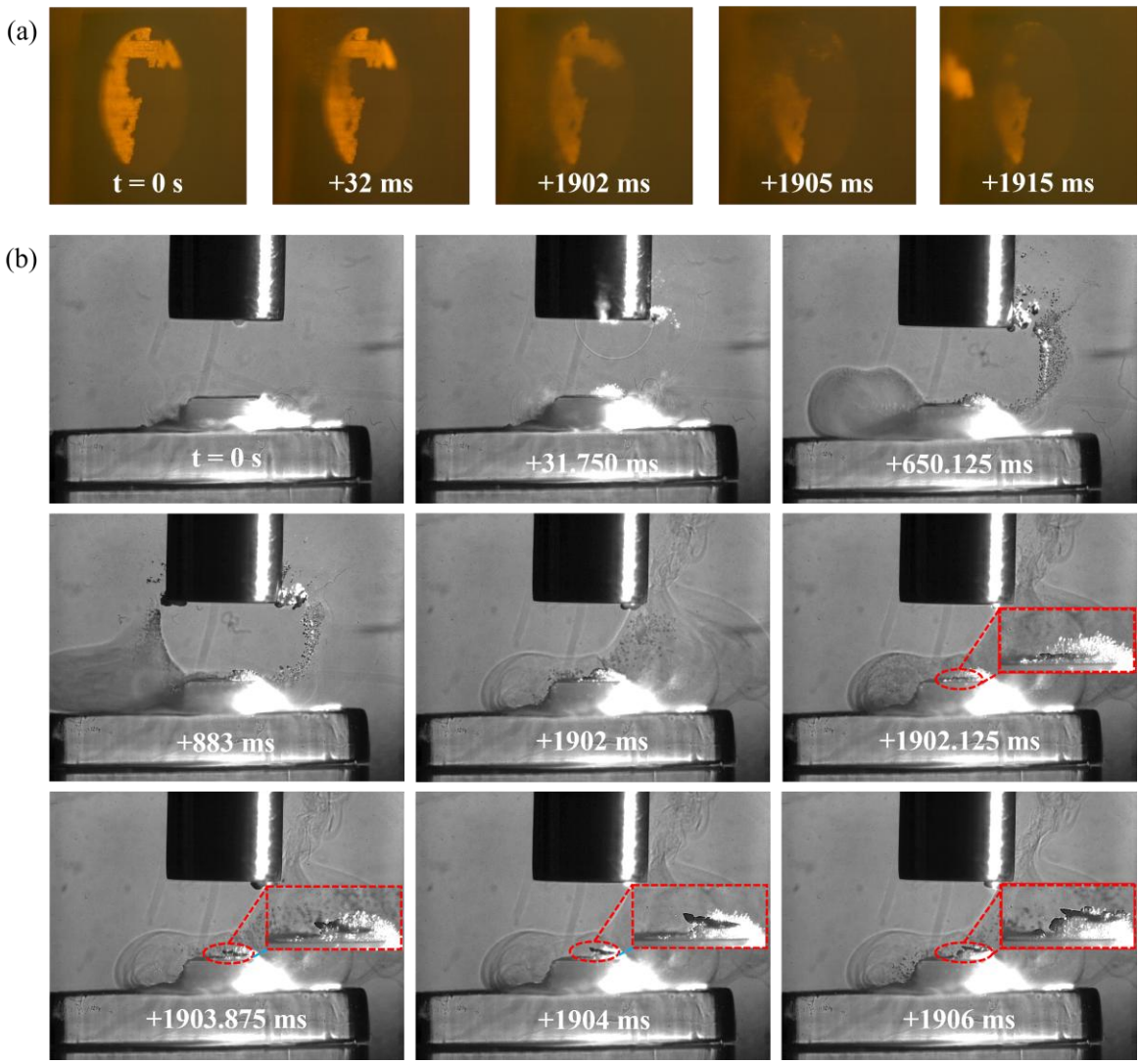

Fig. 4.10: Representative HSI acquired during the 31-40 s sonication interval of the fifth minute for sample 2 at 60% input power. (a) Phantom high-speed camera perspective, (b) Photron high-speed camera perspective. The region of TCM delamination is highlighted by the red dashed box and enlarged inset. Scale is provided by the 6.4 mm diameter sonotrode tip.

Fig. 4.11 displays representative HSI of sample 1 acquired during the 21-30 s sonication interval of the fifth minute at 90% input power. Compared to the delamination behaviour observed at 60% input power, no pronounced large-scale TCM fragment delamination events occurred at this power level, instead primarily exhibiting the delamination of tiny fragments. The cavitation structure during the initial 1100 ms of sonication resembled that observed at 60% input power, featuring a bulbous cavitation structure maintaining contact with the PCB surface. However, this structure exhibited larger size and more intense cavitation activity at 90% input power. As the sonication proceeded, the bubble cluster progressively contracted towards the sonotrode tip, as evidence by the image at t=1179 ms.

This bulbous structure had completely disappeared by t=1200 ms, with cavitation cluster concentrated near the tip. Correlating with the surface microscopy of the TCM discs in fig. 4.6, we hypothesise that the absence of direct cavitation bubble contact with the PCB surface negatively impacts the delamination process.

Fig. 4.11 displays representative HSI of sample 1 acquired during the 21-30 s sonication interval of the fifth minute at 90% input power. Compared to 60% input power, the overall extent of delamination during the fifth minute of sonication at 90% input power is lower, with delamination primarily manifesting as the removal of tiny TCM fragment. In the Phantom imaging as shown in fig. 4.11 (a), tiny fragment delamination is visible in the red dashed line boxed region at t=0 and 240 ms frames. The corresponding Photron imaging (fig. 4.11 (b)) likewise highlights this typical tiny TCM delamination event using a red dashed box. Regarding cavitation structure evolution, bubble clusters with greater coverage and higher local density were visible on the PCB surface during the first 1.1 s of sonication compared to observations at similar time scales under 60% input power. Cavitation activity progressively retracts towards the sonotrode tip as sonication continued. The bulbous cavitation structure and bubble cluster in direct contact with the PCB surface disappear entirely beyond 1200 ms, and cavitation activity manifested as a densely packed bubble cloud oscillating beneath the tip. This evolution is consistent with the degradation of bulbous cavitation structure observed at 90% input power in fig. 4.6 (a).

In the remaining delamination events at 60% input power (see appendix B for details), delamination was not confined to a specific moment, but could occur at any point during the 10 s sonication. This phenomenon, as indicated by fig. 4.5 (a), correlates with the stable formation of bulbous cavitation structure, which remains in continuous contact with the PCB surface. This provides a sustained and effective cavitation zone that intensifies the delamination process.

Conversely, no discernible TCM delamination events were observed at 90% input power beyond the first 1 s sonication. This indicates that delamination is weakened when the bubble cluster no longer maintains contact with the PCB surface.

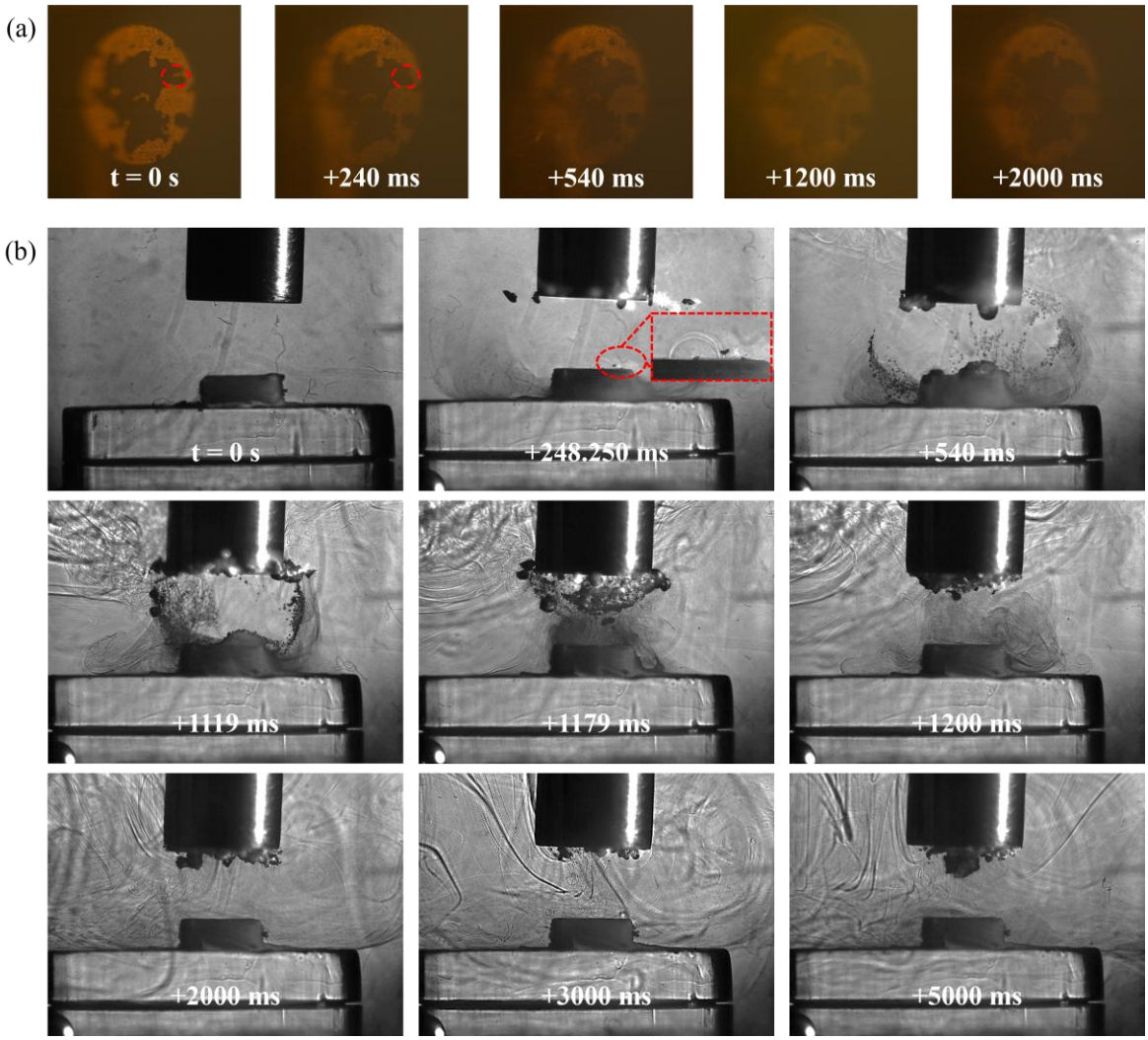

Fig. 4.11: Representative HSI acquired during the 21-30 s sonication interval of the fifth minute for sample 1 at 90% input power. (a) Phantom high-speed camera perspective, (b) Photron high-speed camera perspective. The region of TCM delamination is highlighted by the red dashed box and enlarged inset. Scale is provided by the 6.4 mm diameter sonotrode tip.

4.4 Discussion

Under the experimental conditions of this study, cavitation intensity was characterised by quantifying the bubble collapse shockwave within the acoustic signal. This approach provides an effective method for cavitation characterisation and input power optimisation. The results indicate that, sonication at medium input power indeed demonstrates superior TCM delamination performance compared to high power levels. The HSI indicates the mechanism primarily relates to the effective duration of cavitation structure interaction with the PCB surface. A stable bulbous cavitation structure forms beneath the sonotrode tip at 60% input power. This structure remains active throughout the whole sonication,

maintaining continuous contact with the PCB surface and thus providing a stable and effective cavitation zone for delamination. Although such cavitation structure initially forms at the 90% input power during sonoprocessing, they rapidly recede back towards the sonotrode tip. As a result, the active cavitation zone retreats from the PCB surface, leading to a significant reduction in both the cavitation intensity and sonication duration acting upon the TCM.

The two input powers used for TCM delamination experiments in this study were selected based on acoustic characterisation of cavitation emission signals in Ethaline. The relationship between V_{rms} and input power indicates that the highest cavitation bubble collapse shockwave content corresponds to 60% input power. This result arises from cavitation bubble cluster exhibiting a more regular and stable response to the sonotrode tip vibrations at this input power, whilst also being associated with the sustained existence of bulbous cavitation structure. However, the optimal input power can shift with liquid viscosity as reported in our published *Faraday discussions* work [217]. Furthermore, multiple parameters such as tip diameter, immersion depth of the tip, and temperature of the liquid can all influence the cavitation zone, and therefore shift the optimal operating power. Therefore, systematic characterisation of cavitation emission signals via acoustic detection remains a necessary step for identifying optimal driving parameters prior to initiating sonoprocessing.

The formation of bulbous cavitation structure beneath the sonotrode tip in viscous liquid has been reported in previous studies [22], [214]. Thiemann *et al* [22] showed that bubble jetting can occur at the periphery of the bulbous structure in concentrated sulphuric acid. The coupling of bubble collapse shockwave with jetting activity can induce pitting corrosion on the TCM disc, providing nucleation sites for cavitation and thereby enhancing delamination. Eddingsaas *et al* [214] similarly observed the bulbous structure at medium input power by using sonoluminescence detection in concentrated sulphuric acid, whereas the structure receded towards the tip and evolved into a conical structure at higher input power. This behaviour is highly consistent with the observations in this study at 60% and 90% input power. Overall, the sustained interaction between stable bulbous structure and pitting on the TCM surface is the key factors underlying the superior delamination performance at 60% input power compared with 90% in this study.

Compared with the passive immersion experiment of Rivera *et al* [191] on TCM delamination from PCB in $CaCl_2 \cdot 6H_2O$:EG eutectic solvent, the introduction of acoustic

cavitation in this study markedly enhances mass transport in the viscous liquid, thereby improving the TCM delamination efficiency by approximately 30-fold. Surface microscopy further indicates that, while sonication accelerates delamination efficiency, the process does not progress linearly with but instead exhibits a clear staged behaviour. Specially, only a small number of fine fragments are delaminated via pitting during the early stage of sonication, whereas larger sections are delaminated from regions surrounding these initial pits in the later stage.

4.5 Conclusion

This section demonstrates that quantifying the cavitation shockwave component within acoustic signals provides an effective method for evaluating cavitation intensity, thereby facilitating cavitation characterisation and energy consumption optimisation. The optimal input power selected based on this method maximises the delamination efficiency of TCM. The introduction of acoustic cavitation increases the delamination rate of TCM by approximately 30-fold compared to passive immersion, demonstrating the application potential of power ultrasound for accelerating TCM recovery in high-viscosity DES systems.

Chapter 5

TCMs delamination from PCBs in selected Ethaline-de-ionised water solvents

Chapter overview
Chapter 4 demonstrates that sonotrode-induced acoustic cavitation increased the delamination efficiency of technology-critical metals in Ethaline-DES by more than 30-fold. However, the high viscosity of Ethaline-DES continues to limit further improvements in delamination efficiency. The chapter conducts accelerated process validation by introducing de-ionised water into Ethaline to reduce viscosity, examining the effect of dilution on cavitation intensity and delamination efficiency. Acoustic measurements indicate that cavitation intensity is enhanced in the diluted solvents, and surface microscopy further confirms that the delamination rate has nearly doubled.

Conference Paper
Acoustic Cavitation Enhanced Delamination of Technology Critical Metals from Electronic Waste Using Green Solvents **Shida Li**, Ben Jacobson, Andrew Feeney; Christopher E Elgar; Andrew P Abbott and Paul Prentice
2024 IEEE Ultrasonics, Ferroelectrics, and Frequency Control Joint Symposium (UFFC-JS), Taipei, Taiwan, 22-26 September 2024, ISBN 9798350371901

5.1 Motivation and context

In Chapter 4, we enhanced the delamination efficiency of TCM by approximately 30-fold compared to passive immersion by introducing power ultrasound into the Ethaline-DES. Despite the significant advantages of ultrasound, the high viscosity of Ethaline remains a limitation, with a delamination efficiency of 68±13% after 5 min still insufficient for industrial application. Notably, Luo *et al* [218] demonstrated that reducing liquid viscosity can effectively enhance metal erosion efficiency within acoustic cavitation field, providing valuable guidance for further viscosity modification in this research. For context, this paper is briefly reviewed below.

Experimental study on the mesoscale causes of the influence of viscosity on material erosion in a cavitation field.

Jing Luo, Weilin Xu, Yanwei Zhai, Qi zhang.

Ultrasonics Sonochemistry, vol. 59, p.104699, 2019.

This study reported that adding a certain proportion of water to a high viscosity glycerol can improve the dynamic behaviour of cavitation bubbles. The acoustic cavitation experimental setup is shown in fig. 5.1 (a), with a sonotrode operating at a frequency of 20 kHz and an input power of 100 W. Beakers were filled with glycerol (Gl) solutions of varying viscosities, maintaining a liquid height of 100 mm. The cavitation erosion tests were performed on a mirror-polished 6063 aluminium alloy disc with a diameter of 15 mm. The sample was fixed at sonotrode tip and subjected to a cumulative 5 h sonication. The sample was removed every 30 min, rinsed with de-ionised water. The physical parameters of the solutions are listed in table 5.1.

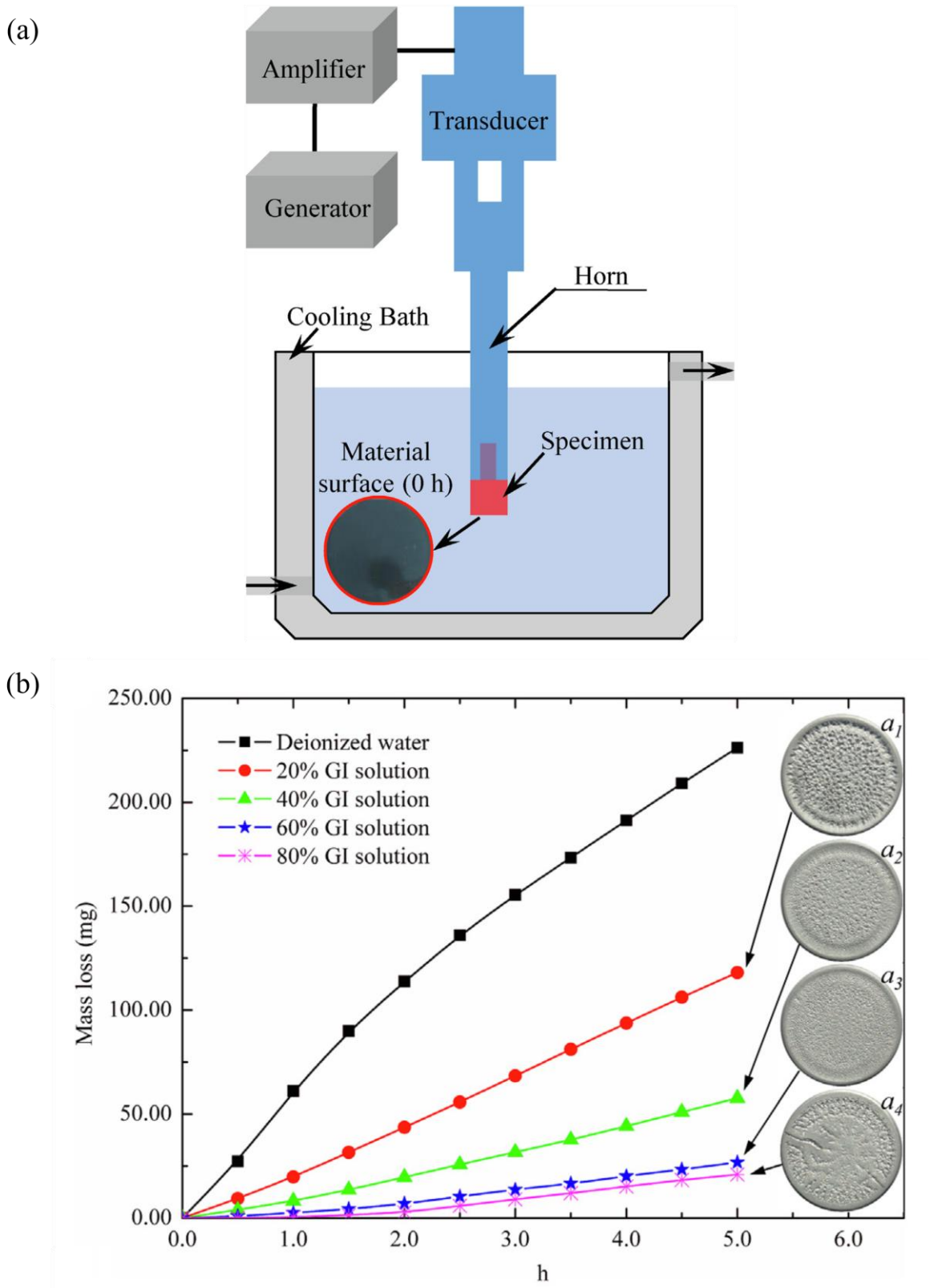

Fig. 5.1: (a) Acoustic cavitation system. (b) The change of cumulative material erosion in different viscous solutions. Taken from [218].

Fig. 5.1 (b) illustrates the variation in cumulative erosion of the aluminium alloy disc across five different viscosity solutions. The cumulative erosion of the sample increased with

extended sonication duration. Over the same sonication duration, the cumulative erosion progressively increased with decreasing viscosity. The surface morphology images of samples a_1 - a_4 further reveal the number and depth of pits on the sample surfaces in 60% and 80% Gl solutions were markedly lower than those in 20% and 40% Gl solutions after 5 h sonication at 100 W input power. It should be noted that, the erosion morphology on the sample surface in the 80% Gl solution exhibited distinct differences compared to the other three cases. The authors attribute this to the higher viscosity of the 80% Gl solution, which altered the cavitation structure. However, it did not alter the overall trend in cumulative erosion.

Table. 5.1: Physical properties of five solvents at 20 ℃. Taken from [218].

	De-ionised water	**20% Gl solution**	**40% Gl solution**	**60% Gl solution**	**80% Gl solution**
Solution preparation method	1000 ml de-ionised water	200 ml Glycerine + 800 ml de-ionised water	400 ml Glycerine + 600 ml de-ionised water	600 ml Glycerine + 400 ml de-ionised water	800 ml Glycerine + 100 ml de-ionised water
Density (g/cm3)	0.998	1.050	1.103	1.156	1.209
Viscosity (P)	0.0113	0.0314	0.0595	0.2052	0.690

Based on the findings reported by Luo *et al* [218], this section reduces the viscosity of Ethaline by adding de-ionised water at selected volume fractions, and evaluates the delamination efficiency of TCM from PCB surfaces.

5.2 Materials and methods

5.2.1 Preparation of Ethaline-de-ionised water solvents

To examine the effect of viscosity, de-ionised water was added to the Ethaline at varying volume fractions. To investigate delamination efficiency, two redox catalysts of anhydrous iron (III) chloride ($FeCl_3$) and anhydrous copper (II) chloride ($CuCl_2$) were added at a ratio of 0.1 $mol \cdot L^{-1}$, respectively. Each solvent mixture is displayed in Table. 5.2.

An initial screening range of 100-50 vol% Ethaline was selected to examine the transition from neat Ethaline to moderately diluted Ethaline-containing media while maintaining a constant total liquid volume and oxidant concentration.

Table. 5.2: Ethaline dilution volume fractions.

No.	Experiment solvents
1	Ethaline + 0.1 mol/L $FeCl_3$
2	80% (volume) Ethaline + 20% (volume) de-ionised water + 0.1 mol/L $FeCl_3$
3	70% (volume) Ethaline + 30% (volume) de-ionised water + 0.1 mol/L $FeCl_3$
4	50% (volume) Ethaline + 50% (volume) de-ionised water + 0.1 mol/L $FeCl_3$
5	50% (volume) Ethaline + 50% (volume) de-ionised water + 0.1 mol/L $CuCl_2$

5.2.2 Experimental setup

The experimental platform was constructed as shown in fig. 4.1, but two modifications were implemented in this study. Firstly, the ultrasonic source was replaced with a 120 W sonotrode (P100, Sonic Systems Ltd). Secondly, the previously employed dual-perspective HSI configuration was discontinued, with imaging conducted only from the Photron perspective. The detailed specifications and operating parameters of the sonotrode employed in this experiment are described in §3.1. Briefly, the sonotrode operated at 20 kHz with a 20 mm diameter tip, and the input is specified as the transducer peak-to-peak vibrational amplitude in the range of 0-16 μm, with the corresponding electrical input power was recorded at each setting. In this configuration, the sonotrode tip was positioned 6 mm above the PCB surface, at a fixed immersion depth of 15 mm.

5.2.3 Printed circuit board samples

This experiment conducted TCM delamination testing in a series of selected Ethaline-de-ionised water solvents, with three 3 mm in width and 4.5 mm in length TCM sections comprising each sample. The sample was cut from the PCB plate depicted in fig. 4.2. The tip diameter relative to the PCB samples is illustrated in fig. 5.2, indicated by a dashed circle.

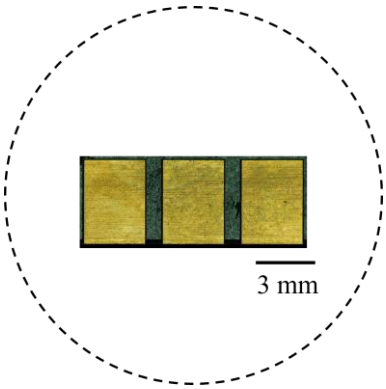

Fig. 5.2: Three rectangular PCB sample with dashed circle representing the scale relative to the 20 mm diameter Sonics sonotrode tip.

5.2.4 Experimental procedure

The configuration of the acoustic emission acquisition platform for cavitation activity is described in §4.2.4, and the layout of the Photron HSI system is presented in §4.2.5. In this study, the high-speed camera was operated at 5,000 fps with an image resolution of 1024 × 1024 pixels, corresponding to a spatial resolution of 54 μm·pixel^{-1}.

This experiment focused on the delamination efficiency comparisons between different solution systems. Samples were characterised at cumulative sonication durations of 150, 180, and 240 s based on each solution's delamination rate (corresponding to varying durations). HSI recorded a 15 s sonication process to capture representative TCM delamination behaviour. Three PCB samples were processed and analysed under each solution condition.

5.3 Results

5.3.1 Characterisation of cavitation activity in four selected Ethaline-de-ionised water solvents

Fig. 5.3 depicts the V_{rms} plots for four different Ethaline and de-ionised water volume fractions. Each plot is generated over a transducer peak-to-peak displacement amplitude range from 1 μm to 15 μm, at 15 incremental amplitudes. Each data point represents an average of five sonications at each sampled vibrational amplitude. Briefly, V_{rms} of the filtered cavitation emission signal is taken as representative of the average shockwave content within the signal generated during a sonication.

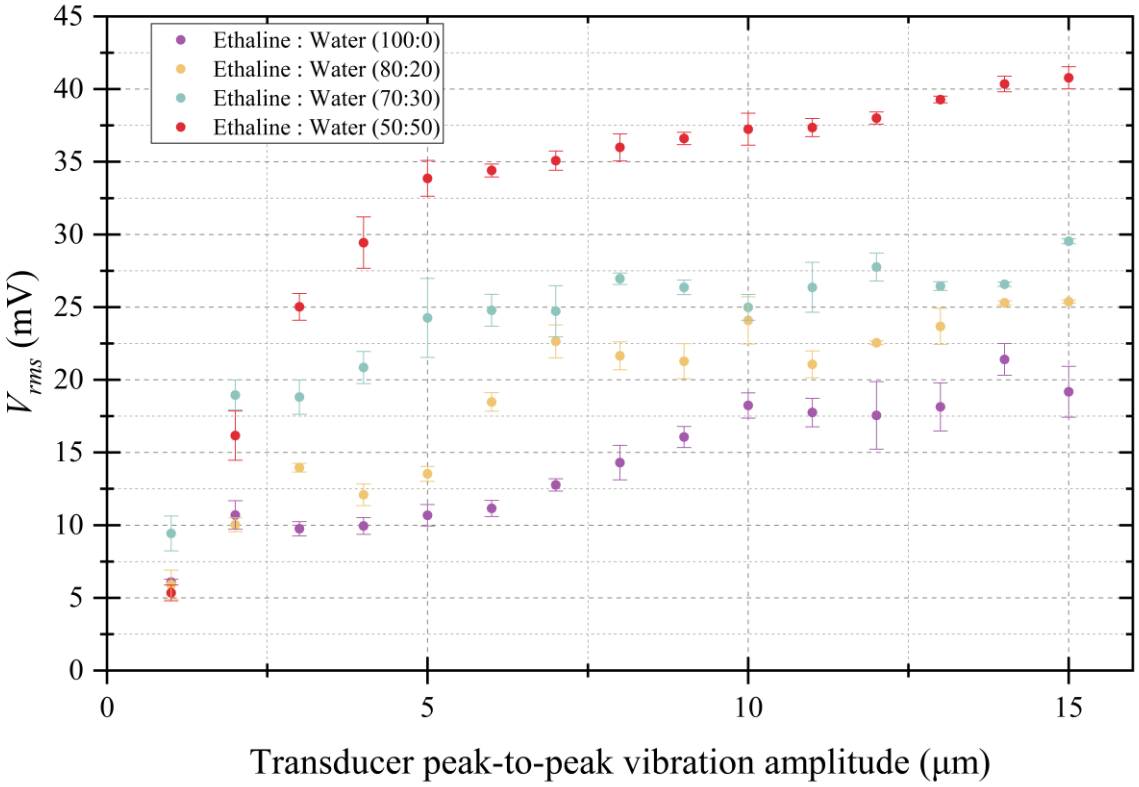

Fig. 5.3: The mean V_{rms} of the signal detected by swPCD during five 200 ms sonications at each transducer peak-to-peak vibration amplitude, conducted under four distinct Ethaline: de-ionised water volume ration conditions.

As shown in fig. 5.3, V_{rms} does not increase linearly but fluctuates with increasing horn tip amplitude. Overall, V_{rms} increased as the volume fraction of de-ionised water increased. This suggests that the higher viscosity solvents inhibit the generation of inertial cavitation bubbles. Thus, to maximise the cavitation efficiency through tailoring solvent viscosity, the solvent with a 50:50 volume fraction of Ethaline:de-ionised water would be optimal. Similar observations have been observed when tailoring solvent viscosity for processing of lithium-ion battery material [72]. In fig. 5.3 it is also evident that the trend in V_{rms} magnitude tends to flatten out as the transducer peak-to-peak vibrational amplitude increases. We observe a plateauing at around 5-8 µm in the diluted solvents and around 9 - 12 µm in pure Ethaline. From the perspective of energy consumption and cavitation efficiency, a fixed amplitude of 7 µm (equivalent to 21 W of electrical power) was selected for the driving amplitude for delamination experiments.

5.3.2 Overview of TCM-delamination performance at five selected Ethaline:de-ionised water solvents

In this section, surface microscopy of the PCB samples taken after sonication in each solvent are reported. Specifically, each PCB sample was exposed to a fixed duration of sonication with a total of three samples per solvent. Each solvent contained a redox catalyst of 0.1 $M \cdot L^{-1}$ $FeCl_3$ apart from the final dataset which contained 0.1 $M \cdot L^{-1}$ $CuCl_2$, discussed later.

Fig 5.4 is Alicona surface microscopy images of the TCM sections for each sample and solvent sonicated. It is evident that the increasing addition of volume fractions of de-ionised water results in a greater extent of delamination. Notably, this occurs over a shorter duration, with 100:0, 80:20 and 70:30 Ethaline:de-ionised water ratios sonicated for 240 seconds and subsequent 50:50 Ethaline:de-ionised water dilutions removing almost all the TCM from the PCB in 180 seconds. Replacing the redox catalyst with $CuCl_2$ further reduced delamination time to 150 seconds.

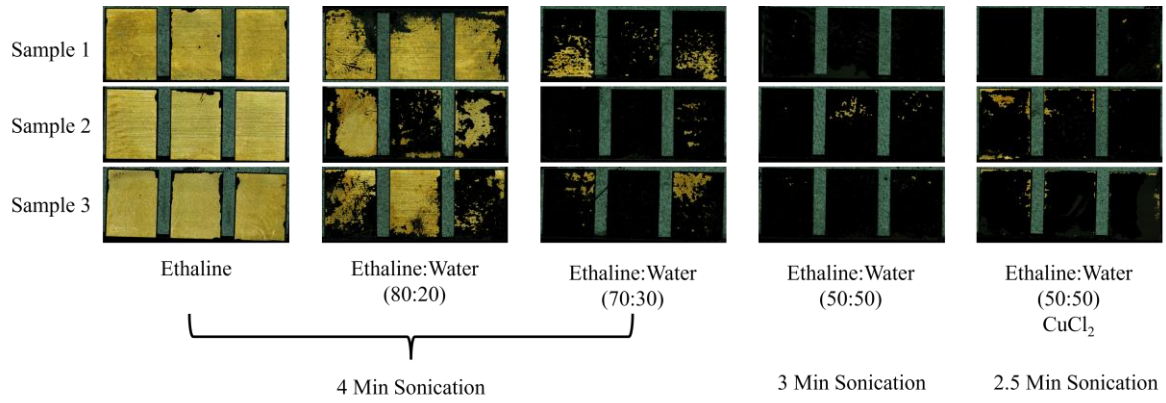

Fig. 5.4: Surface microscopy of the three PCD samples after sonication in each Ethaline:de-ionised water volume fraction ratio and redox catalyst. Scale provided by the single 3 mm wide TCM sections.

To quantify the delamination efficiency, the percentage of delamination for each solution was obtained by thresholding and segmenting the surface microscopy images. Fig 5.5 shows that delamination efficiency of over 90% is achieved in volume fractions containing 70:30 and 50:50 Ethaline:de-ionised water. Notably, delamination efficiency of > 97% is achieved in 50:50 Ethaline:de-ionised water solvent with both redox catalysts used.

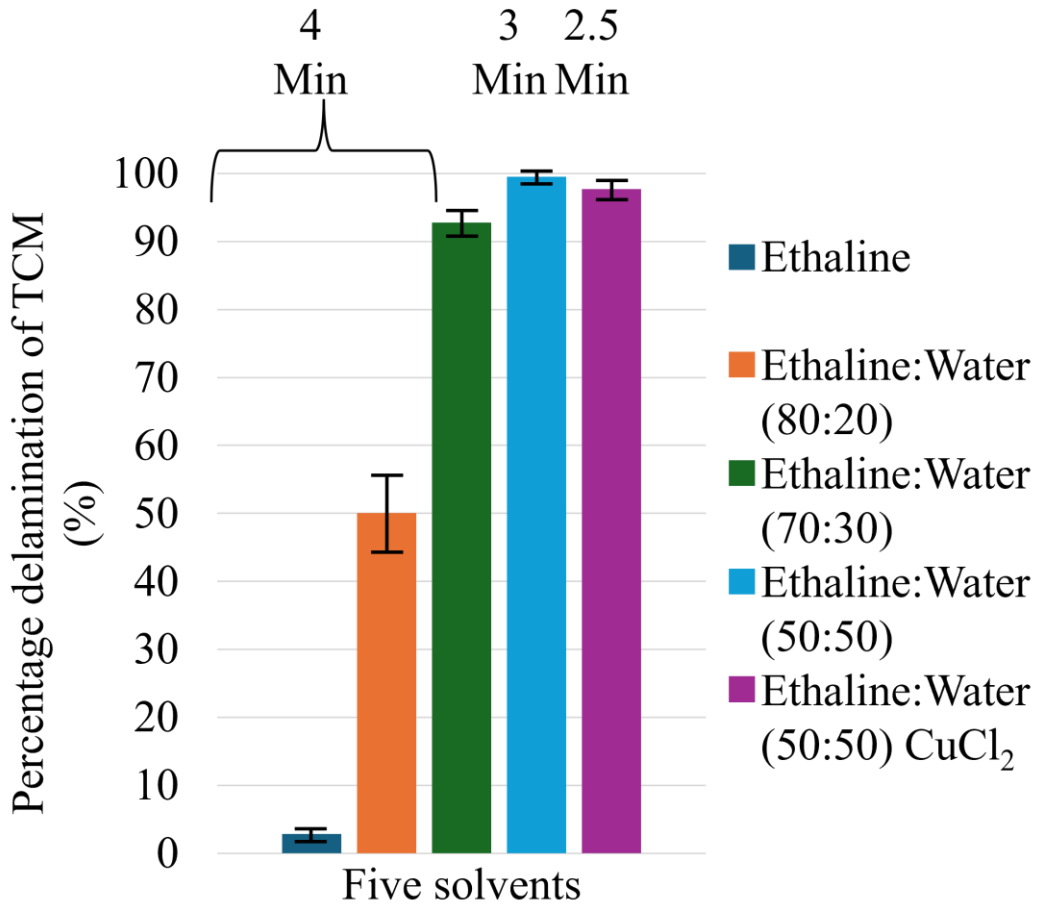

Fig. 5.5: Histogram of percentage delamination of TCM for each Ethaline:de-ionised water volume fraction after each prescribed sonication duration.

5.3.2.1 High-Speed Imaging (HSI) of TCM-delamination

Fig. 5.6 presents representative HSI of a small delamination event on the PCB surface captured in the 70:30 Ethaline:de-ionised water solvent. These observations were selected from the HSI dataset of a large number of delamination events recorded during the course of this study. During sonication, bulbous cavitation structure similar to that in fig. 4.10 can be observed at t = 20 and 28 ms. This structure enables cavitating bubbles aggregate on the sample surface. Oscillating bubbles near the PCB surface produce high velocity jets, whilst larger bubble clusters collapse violently, producing shockwaves that radiate spherically towards the PCB surface. These phenomena have a destructive effect on the PCB surface, pitting and fragmenting the TCM layer, eventually liberating it from the underlying PCB. At t = 20 and 46.4 ms within the area marked by the red circles in the images, we observe small fragments of TCM delaminated from the PCB, whereby microstreaming from the bubble cloud and acoustic streaming generated in the tank facilitate transport of these fragments outwards away from the surface.

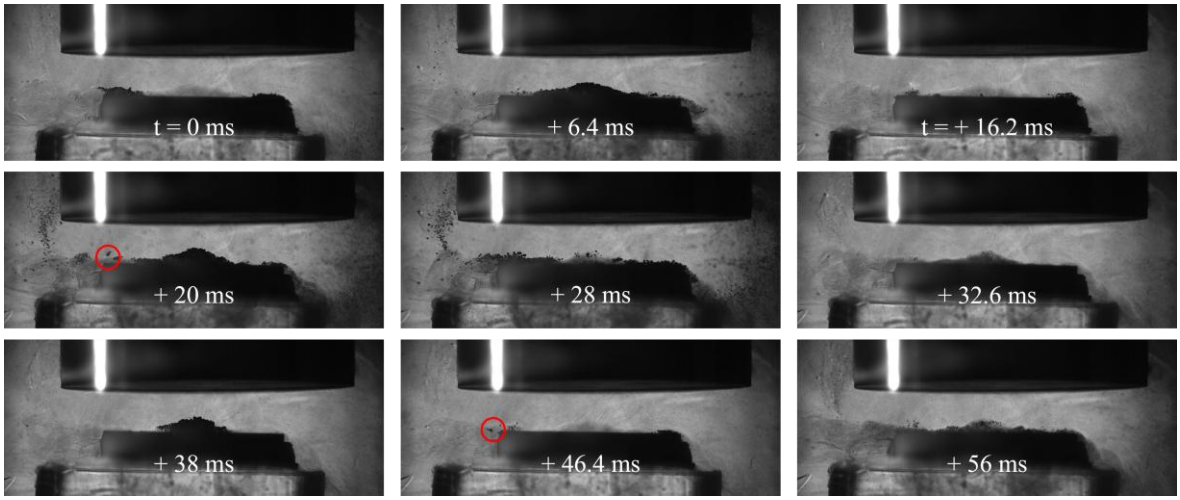

Fig. 5.6: Representative frames from a HSI sequence in 70:30 (Ethaline:de-ionised water) with $FeCl_3$ redox catalyst. Small delamination events with dislodged TCM fragments are observed within the red circle. Scale provided by the 20 mm tip diameter.

Fig. 5.7 presents a representative HSI sequence captured in the 50:50 Ethaline:de-ionised water solvent. Compared to fig. 4.17, the same bulbous cavitation structure remains observable in the present HSI dataset, its morphology however, exhibits a clear transition: the structure predominantly depicts a "filamentous" form in the higher viscosity 70:30 Ethaline:de-ionised solvent, whereas it transforms into broader "band-like" structure in the lower viscosity 50:50 Ethaline:de-ionised solvent. This morphological transition is clearly visible in the frames at t = 10, 25.8, 39.4, 46.2 and 51.2 ms, manifested as a band-like bubble cluster extending from the central region of the sonotrode tip towards the PCB surface. Concurrently, both the thickness and coverage of the cavitation bubble cluster near the PCB surface significantly increase in the 50:50 Ethaline:de-ionised solvent, forming a more complete envelope around the sample. Consequently, the PCB surface is subjected to a greater number of jet impacts and shockwave radiations over the same sonication duration, thereby promoting the fragmentation of the TCM layer and accelerating its delamination.

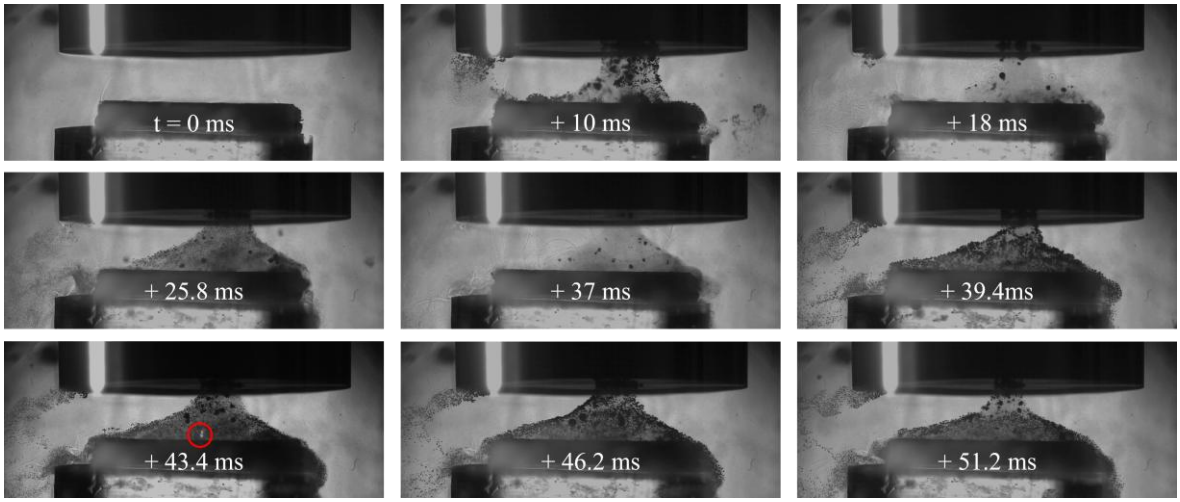

Fig. 5.7: Representative frames from a HSI sequence in 50:50 (Ethaline:de-ionised water) with $FeCl_3$ redox catalyst. Small delamination events with dislodged TCM fragments are observed within the red circle frame. Scale provided by the 20 mm tip diameter.

5.4 Discussion

Development of alternative green technologies for the recycling of electronic waste is a growing area of research. For translation from traditional techniques to ionometallurgy, the slow dissolution rates must be overcome. Through application of power ultrasound, etch rates can be improved, however, the high viscosity associated with DESs remains a limitation. In this section, we demonstrate the effect on cavitation strength and delamination efficiency of diluting the Ethaline with volume fractions of de-ionised water.

Under the current conditions, the cavitation strength, as measured by V_{rms}, was demonstrated to be directly related to the viscosity of the solvent. Through the addition of higher volume fractions of de-ionised water, the cavitation strength increased across the vibrational amplitude range measured. This is due to the reduction in viscosity contributing to a lower threshold for inertial cavitation and, hence, a reduction in the dampening of the bubble collapses as viscosity is reduced [94], [215]. Furthermore, the V_{rms} has a nonlinear dependence on vibrational amplitude, plateauing in each solution before the maximum vibrational amplitude is achieved. Importantly, this specific characteristic is dependent on a number of parameters such as tip diameter, immersion depth and vessel geometry.

The utility of DESs to separate TCMs from PCB substrates has been demonstrated in silent immersion conditions (no ultrasound) and under sonication, respectively. Rivera *et al* [191] noted limitations associated with the high viscosity of the DES and Chapter 4 demonstrated

improved reaction rates under sonication in pure Ethaline. Here, in response to the limitations of solvent previously discussed, this section reduces the delamination time by half compared to Chapter 4 by adjusting the de-ionised water content. The DES targets and solubilises the copper layer, via oxidation in the presence of the redox catalysts. Here, the mechanical action of the cavitating bubbles on the PCB surface enhance the delamination rate by penetrating the void space created by the copper solubilisation, liberating the surface gold layer. Rivera *et al* [191] demonstrated, in silent conditions, that $CuCl_2$ as a redox catalyst was capable of quicker etch rates on PCB substrates. This observation is also observed under sonication, with the 50:50 Ethaline:de-ionised water solvent removing over 97% of the TCM in less time when $CuCl_2$ was used as the redox catalyst.

The scope of this initial composition-screening study was limited to Ethaline:de-ionised water volume fractions ranging from 100:0 to 50:50. The purpose was to determine whether partial water addition could alleviate the high-viscosity limitation of neat Ethaline and improve cavitation-assisted delamination, rather than to identify the minimum Ethaline content required for the process or to minimise the total solvent inventory.

Formulations containing less than 50:50 Ethaline:de-ionised water solvent were not investigated. Consequently, the 50:50 formulation should be interpreted as the best-performing composition within the range examined, rather than as a global optimum or the minimum Ethaline fraction required for effective delamination. At higher water fractions, the effect of viscosity reduction would become increasingly coupled with changes in the hydrogen-bonding structure of the solvent, ionic conductivity, surface tension, metal and oxidant speciation, and chemical dissolution kinetics. A systematic investigation of this water-rich regime would therefore require additional physicochemical measurements and appropriate aqueous control experiments.

Future work should extend the investigated composition range to 40:60-0:100 Ethaline:de-ionised water solvent and include a water-oxidant control containing no Ethaline. Silent controls should also be conducted at each composition to distinguish chemical dissolution from ultrasound-induced mechanical delamination. Measurements of viscosity, density, surface tension, conductivity, temperature and copper dissolution rate would enable the respective physical and chemical contributions of water addition to be evaluated.

5.5 Conclusion

For any sonochemical or sonoprocessing application, parameter optimisation is a significant challenge, with large parameter spaces available. This includes parameters associated with the ultrasound as well as the chemistry of the solutions used. Here, the effectiveness of simple cavitation characterisation in any solution is demonstrated by measurement of the level of shockwave content within the emission signal. This allows optimisation in terms of power consumption from the ultrasound source. Additionally, we demonstrate that tailoring the viscosity of the etching solvent has a significant effect on delamination efficiency and rate. In this study, we associate the improved delamination efficiency with a reduction in viscosity resulting in improved mechanical action of the cavitating bubbles in the solvent. However, the chemical effect of adding large volume fractions of de-ionised water to DESs was not studied. Future work will therefore seek to further optimise etching solutions from both a mechanical and chemical perspective.

Chapter 6

Characterising the cavitation generated by the tube transducer versus the sonotrode

Chapter overview
Developing high throughput applications of sonochemistry and sonoprocessing is an outstanding ultrasonic engineering challenge that continues to limit widespread industrial adoption. Conventional mass-produced Langevin-based technologies, such as the sonotrode or cleaning bath transducers, are not particularly well suited to treating large liquid volumes or flow-based systems, with a compromise between cavitation intensity and distribution through liquid bulk typically required. The development of a tube transducer from a single element radially poled tubular piezoceramic, excited to generate an axially focused field is reported Firstly, to investigate the influence of external loading on cavitation intensity within the tube bore, a shockwave passive cavitation detector (swPCD) was employed to compare the cavitation intensity in de-ionised water under air-backed and water-backed conditions over a range of input powers. The results indicate that water-backed condition markedly attenuates cavitation intensity within the bore. Air-backed condition was more suitable at present for achieving high intensity cavitation and was therefore selected as the preferred configuration for subsequent experiments. High-speed imaging and sonochemi-luminescence are used to characterise the cavitation generated, which is also compared to the well-known activity at the tip of a sonotrode. The findings show that the tube transducer generates cavitation at sonotrode-like intensities or higher but distributed throughout the bore of the tube, with peak activity at the central axis. Subsequently, an optimisation of the sonication duration was achieved through the use of pulse modulation, resulting in a further increase in cavitation intensity at the same input power. Finally, a concept for applying the tube transducer to high throughput, flow-based processing was explored, providing insights for its potential utilisation in continuous sonoprocessing applications.

Journal paper
The tube transducer as a novel source for power ultrasound: A case study in delamination of graphite coating from lithium-ion battery anode **Shida Li**, Paul Daly, Ben Jacobson, Joshua Cooke, Chunhong Lei, Andrew P. Abbott, Andrew Feeney, Paul Prentice *Chemical Engineering and Processing - Processing Intensification,* vol. 225, p. 110813, 2026

6.1 Introduction

§1.5 systematically reviewed the structures of several commercially available power ultrasound devices based on Langevin transducer, together with the corresponding cavitation intensity and its spatial distribution. In brief, the sonotrode can generate an intense, localised cavitation zone in the liquid beneath the tip, although streaming effects often circulate smaller cavitating bubble clusters into the liquid bulk. Cavitation generated by the ultrasonic bath can extend to liquid volumes of several litres, but at a much reduced intensity compared to the sonotrode. As an attachment option for inverted sonotrode device, the ultrasonic cup enables a large diameter tip to be coupled directly to the liquid contained within the cup. This achieves superior cavitation distribution through a larger volume, than the localised cavitation generated with a narrower tip attachment dipped into a vessel of liquid, but inevitably at lower intensity due to the larger emitting surface. Another approach is to mount multiple bath-type transducers to cylindrical or polygonal shaped vessels, to achieve a focusing effect for intensification of the cavitation activity. Incorporating many bath-type transducers into a reactor design also allows for a larger volume of liquid to be addressed, and offers options such as multiple frequency sonications, but at the expense of cost and operational complexity.

This chapter presents the development of a transducer based on a radially poled tubular piezoceramic element, with the intention of addressing some of the limitations of conventional Langevin-based reactors. A static configuration of the tube transducer is developed to initially investigating the influence of the external loading conditions upon cavitation intensity within its bore. Specifically, two representative backing conditions - air-backed and water-backed, are considered as typical external load cases. A shockwave passive cavitation detector (swPCD) is used to capture and quantify cavitation shockwave signals in the liquid within the tube bore, enabling a comparative assessment of cavitation intensity under both backing conditions and identification of the optimal operating configuration.

Building on this foundation, high-speed imaging (HSI) and sonochemiluminescence (SCL) are further employed to conduct a comparative analysis of the activity, structure, and spatial coverage of cavitation bubble clusters within the tube bore and beneath a conventional sonotrode tip. The sonotrode experiments were performed in a cylindrical vessel with dimensions matched to the tube transducer to ensure a meaningful comparison. Several representative exposure configurations were then established by varying the vertical position of the sonotrode tip. The relative strengths of each exposure configuration are described and prospects for incorporating tube transducers into flow configurations for high throughput sonoprocessing and sonochemistry applications, discussed.

Details of the fabrication procedure for the static tube transducer configuration, the operating frequency, and the construction of the impedance matching transformer are provided in §3.5.

6.2 Materials & Methods

6.2.1 Excitation and triggering architecture of the experimental system

The yellow pathway in fig. 6.1 (a) illustrates the excitation process for the tube transducer. Equipment item 9 is a signal generator (DG4102, RIGOL Technologies, Beijing, China), used to generate sinusoidal voltage signals of 16.79 kHz and 15.73 kHz of 2 s duration, respectively, under air-backed, water-filled bore (air-backed condition) and water-backed water-filled bore (water-backed condition) set-up. The signal was input to a +55 dB power amplifier (1040L, Electronics and Innovation, USA) (fig. 6.1 (a) equipment item 10) to excite the tube transducer to generate a sonication. The 50 Ω output of the amplifier was matched to the tube transducer by electrical impedance matching transformer (B66397G0000X187, ETD59/31/22, N87, TDK EPCOS, Germany, equipment item 7) with turns ratio of 1:5.7 for air-backed condition and 1:6.8 for water-backed condition, respectively. A range of tube transducer input powers, determined by the voltage amplitude of the sinusoid set on the signal generator, were tested during preliminary experiments. Two powers were selected to provide an equitable comparison with the sonotrode (described below, §6.2.2) and to demonstrate the capabilities of the tube transducer. These are 55 W, to match the sonotrode input power used exclusively throughout this work and 106 W, the maximum tube transducer input power achievable by the equipment when the tube is filled with de-ionised water. The input power measurement method is detailed in §6.2.6.

The red pathway of fig 6.1 represents the triggering chain of the measurement system. The signal generator outputs an additional 1 V square wave signal, which is used to synchronise

the triggering of both the high-speed camera (fig. 6.1 (a) equipment item 8) and the digital delay generator (fig. 6.1 (a) equipment item 7). After imposing a delay of 0.7 s, the delay generator forwards the trigger signal to the oscilloscope (fig. 6.1 (a) equipment item 6), ensuring that data acquisition occurs precisely at the intended moment. Meanwhile, the swPCD (fig. 6.1 (a) equipment item 3) receives acoustic emissions generated by the tube transducer and delivers them to the oscilloscope along the green pathway, enabling the recording and analysis of the acoustic signal. Detailed information on the acoustic detection and filtering protocol is provided in §6.2.3.

6.2.2 Sonotrode

The cavitation generation of the tube transducer was compared to that of a commercial sonotrode (P100, Sonic Systems Ltd, UK), represented schematically in fig. 6.1 (b). This sonotrode has an operating frequency of 20 kHz, further details are provided in §3.1. A cylindrical vessel with dimensions matching those of the tube transducer (see §6.2.1) was used to provide a consistent experimental basis for this controlled proxy comparison. An aperture in the wall of the vessel receives the tip of the sonotrode, with three vertical tip positions tested as represented by coloured arrows: aligned to the top, centre and bottom of the vessel, approximately 5 mm above the lowest point. The sonotrode is used as a conventional high-intensity reference, not as a geometrically equivalent reactor. The comparison is a controlled but non-equivalent proxy benchmark at matched vessel volume and, for the 55 W comparison, matched electrical input power. Low-frequency plate and cup-horn reactors may be closer in field coverage; the relevant configurations are discussed in § 1.5.1.2 – § 1.5.1.3 and would be appropriate future direct comparators.

For this system, the tip displacement amplitude is user selected and maintained during the sonication, irrespective of the acoustic load, while electrical power from the driver is automatically varied to meet the displacement amplitude demands. Transducer peak-to-peak vibrational displacement from 0 µm to 16 µm can be selected, corresponding to transducer electrical input powers between 0 W to 120 W, according to the manufacturer's specifications. For this work, the maximum electrical input power that was attained for all sonotrode sonications in de-ionised water, was measured to be 55 W.

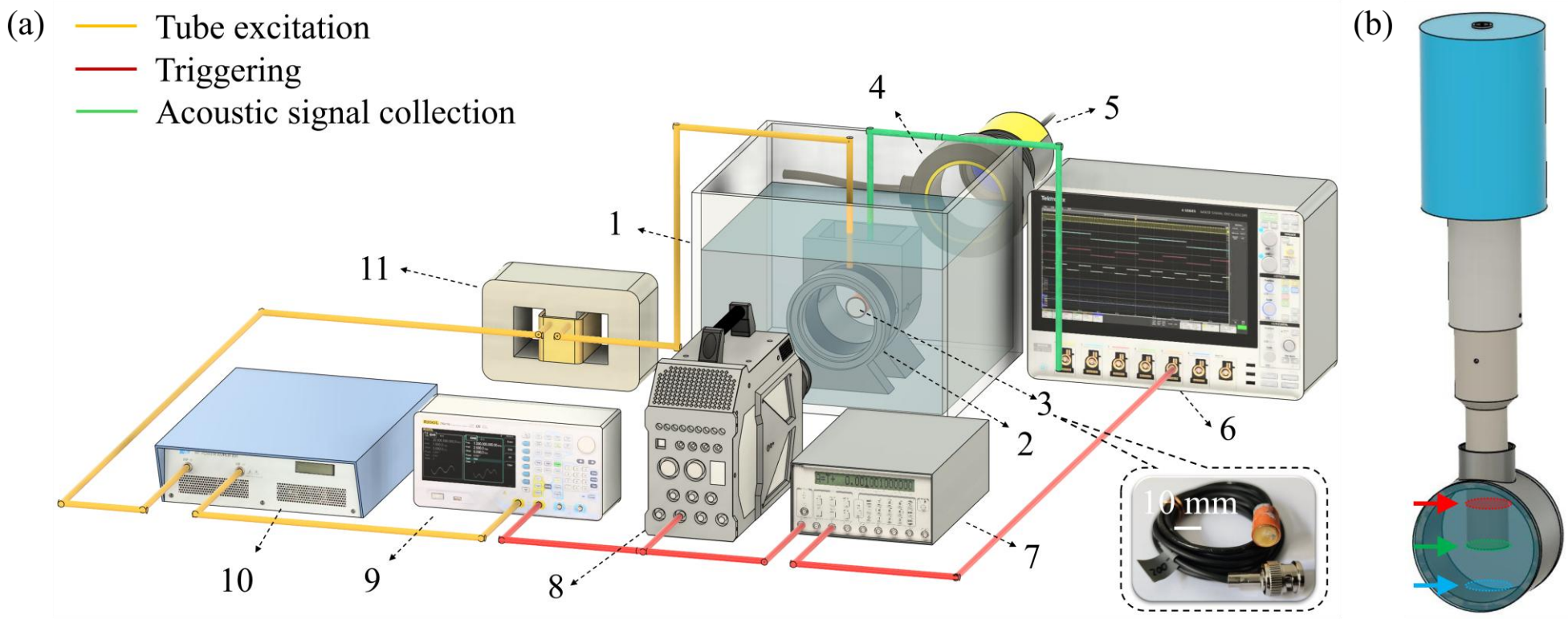

Fig. 6.1: (a) Schematic of the tube transducer experimental platform for high-speed imaging and acoustic data acquisition. Equipment items include (1) water tank, (2) tube transducer, (3) shockwave passive cavitation detector, (4) ring illumination, (5) laser illumination, (6) oscilloscope, (7) delay generator, (8) high-speed camera, (9) signal generator, (10) power amplifier, (11) impedance matching transformer. (b) A schematic of the sonotrode with the tip positioned centrally within a cylindrical vessel. Red, green and blue arrows denote the vertical position of the sonotrode tip in the top, centre and bottom positions.

6.2.3 Acoustic detection and filtering protocol

The swPCD (fig. 6.1 (a) equipment item 3) was mounted at a position of 5 mm outside the centre of the circular edge of the tube transducer via a 3-axis stage. All acoustic emission data were acquired over a duration of 200 ms, with the trigger point controlled by the delay generator (DG535, Stanford Research Systems, USA) as shown in fig. 6.1 (a) equipment item 7 at 0.7 s following the beginning of ultrasonic processing. An oscilloscope (Tektronix 5 series, Berkshire UK) as shown in fig. 6.1 (a) equipment item 6 was employed to display and store the time-domain data of the acoustic signals acquired by the swPCD in real-time at 25×10^6 samples·s^{-1}. The measured voltage signals were subsequently filtered according to the method described in §3.7 to extract characteristic components associated with cavitation activity. A total of 51 input powers were recorded, with five 200 ms acoustic signal acquisitions corresponding to each power.

6.2.4 High-speed imaging (HSI)

HSI of the cavitation inside the tube transducer and the cylindrical sonotrode vessel during a sonication was captured with a FASTCAM SA-Z 2100 K (Photron, Bucks, UK) high-speed camera, fig. 6.1 (a) equipment item 8. The high-speed camera recorded the cavitation activity for the entire 2 s duration of each sonication at 20,000 frames/s, through a macro-lens (Milvus 100 mm *f*/2M, Zeiss, Oberkocken, Germany). At this frame rate, imaging was achieved over 1024 × 1024 pixels, with a resolution of 54 µm·pixel^{-1}. Dual illumination fixtures, shown in fig. 6.1 (a) equipment items 4 and 5, ensured full illumination of the tube transducer and cylindrical vessel interiors. The peripheral regions were illuminated by a 150 W halogen lamp (Thorlabs, Ely, UK) coupled with a fibre ring illuminator (FRI61F50, Thorlabs). Central regions were irradiated by synchronous 10 ns laser pulses at 640 nm (CAVILUX Smart, Cavitar, Finland), coupled to a liquid light guide with a collimating lens attached to the output end. Further details of the high-speed camera and illumination setup can be found in §3.3 and §3.4.

6.2.5 Sonochemiluminescence (SCL) observation

SCL imaging was employed to qualitatively assess cavitation activity inside the tube transducer and the cylindrical sonotrode vessel. Sonications for each of the seven transducer configurations (see §6.2.1 and 6.2.2) were undertaken with the SCL working solution. For details on SCL solution preparation and the luminescence mechanism, see §3.9. It is noted that although SCL indicates activity associated with the generation of reactive species, this

also indirectly indicates the intensity of local cavitation activity [72]. To generate sufficient luminescence, sonications of 10 s durations were necessary. Images were captured using a Nikon Z8 digital camera equipped with a NIKKOR Z 24-120 mm *f*/4 s lens with a 10 s exposure time, *f*/4 aperture and 3200 ISO. No post-processing was applied to the captured SCL images.

Consequently, the original 24 bit true colour RGB images were converted to 8 bit greyscale images using the rgb2gray function in MATLAB. There were no instances of 0 value greyscale levels throughout these converted images and so a filter was created in Photoshop (Adobe Inc., San Jose, CA, USA) that assigned a 0 value to pixels corresponding to the transducers, vessels and exterior areas (the non-liquid areas that do not emit SCL) as shown in fig. 6.2 (a) & (b). Greyscale (fig. 6.2 (c)) level histograms of these altered images were calculated using the histogram function in MATLAB (R2025a, MathWorks, MA, USA) and the values corresponding to the 0 level were nullified. The histogram therefore represents the prevalence of 2^8 - 1 = 255 possible greyscale levels within the cylindrical sonotrode vessel and the tube transducer, in the processed versions of fig. 6.5 (a)-(e). The magnitude and prevalence of these greyscale levels correspond to the intensity and distribution of SCL, which in turn may be taken as an indicator of the intensity of the cavitation activity [219]. The MATLAB greyscale processing and histogram code refer to the Appendix A.

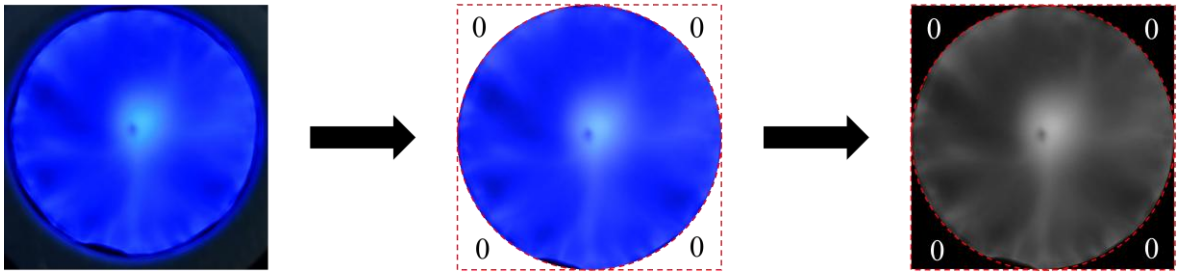

Fig. 6.2: The processing process of SCL image. (a) The original SCL image. (b) Apply zero-value filtering to the exterior of the tube bore. (c) Greyscale processing. The area enclosed by the red dotted line indicates regions with a greyscale value of 0.

6.2.6 Experimental procedure

Room temperature de-ionised water was employed as the liquid medium for all tests except the SCL experiment. Any observed differences in cavitation intensity can therefore be attributed to the transducer configuration or operating conditions.

Experiments were conducted under both air and water back loading conditions to investigate the internal cavitation behaviour of the tube transducer under different boundary constraints. To establish the water-backed condition, the tube transducer was immersed in a water tank (fig. 6.1 (a), item 1) measuring 20 × 20 × 15 cm, with its top position approximately 1 cm below the liquid surface.

Electrical power measurements were performed using a digital multimeter (117 TRUE RMS, Fluke, USA) connected between the impedance matching transformer and the tube transducer.

6.3 Results of characterising the cavitation generated by the tube transducer versus the sonotrode

The following results sections are organised to compare the cavitation generated by the tube transducer and the sonotrode.

- §6.3.1 employed passive cavitation detection to quantitatively characterise and compare the cavitation intensity within bore of the tube transducer under air-backed and water-backed conditions across a range of input power.

- §6.3.2 presents HSI results of cavitation activity generated by the sonotrode at 55 W, with the tip at three vertical positions within a cylindrical vessel, and by the air-backed tube transducer at two input powers (55 W and 106 W). This allows a comparison of the bubble distribution and structures that develop, during sonications with each configuration.

- §6.3.3 evaluates the spatial distribution and intensity of the cavitation activity via SCL imaging through qualitative observations and quantitatively, with greyscale histogram analysis.

6.3.1 Characterisation of cavitation activity inside the tube transducer under air and water backed conditions

The measured V_{rms} (time-averaged shockwave content, as described in §1.2.2) quantifies the intensity of bubble collapse shockwaves generated within the tube transducer, thereby reflecting the relative strength of cavitation activity. Fig. 6.3 shows the variation in the V_{rms} of acoustic emission from the tube transducer as a function of input power. Each data point represents the mean of five sonication measurements acquired at the same input power, with error bars indicating the corresponding standard deviation. Results obtained under both air-backed and water-backed conditions are presented for comparison. Yusuf *et al* [34]. noted that the V_{rms} obtained during sonication using sonotrodes in de-ionised water exhibit a non-linear relationship within input power. This characteristic plot can serve as a guide for selecting optimal input power, and the same approach can be extended to other sonochemistry and sonoprocessing applications mediated by cavitation bubble collapse.

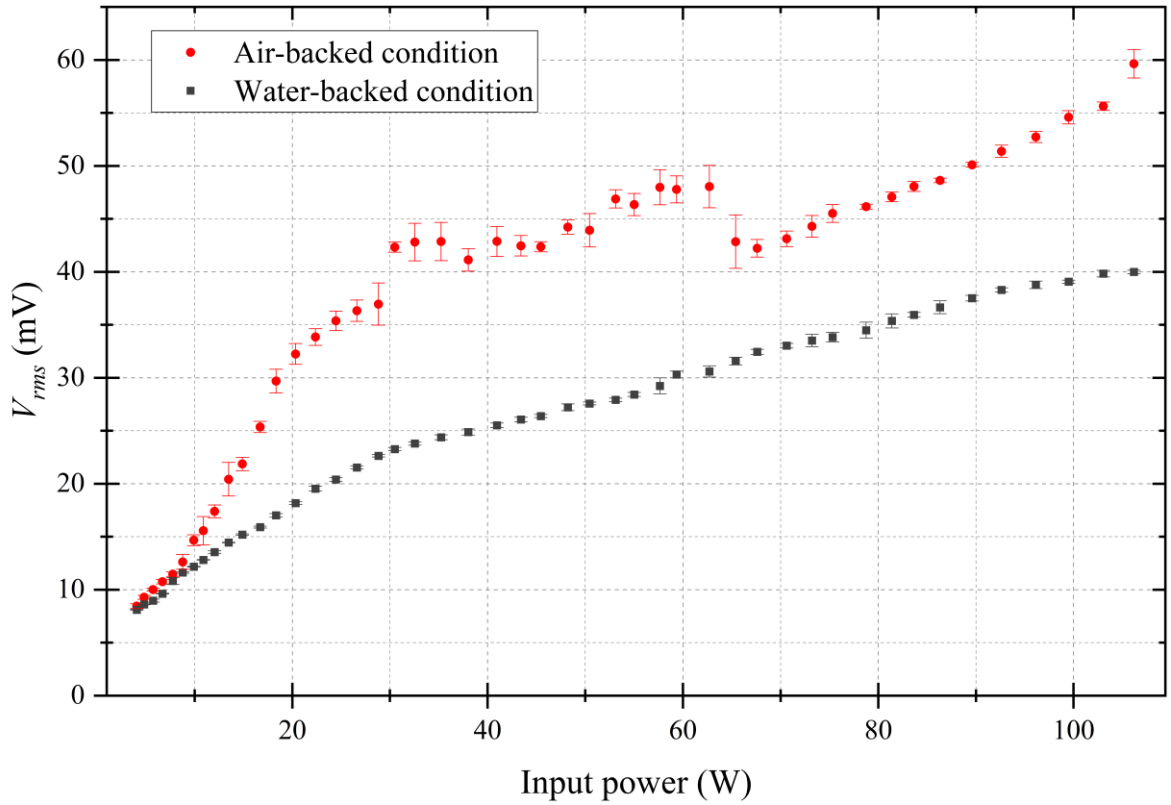

Fig. 6.3: The effect of 51 tube transducer input powers on the V_{rms} of captured acoustic emissions for air-backed condition (red, circular markers) and water-backed condition (black, square markers) condition.

The results in fig. 6.3 demonstrate that the V_{rms} exhibits non-linear growth with input power under both backing conditions. The increase in V_{rms} is more gradual with no pronounced decrease observed under the water-backed condition, and only a slight reduction in the rate of increase is evident at input powers of 30 W and 100 W. In contrast, V_{rms} under the air-backed condition exhibits a more pronounced fluctuating growth with increasing input power, typical for an ultrasonic transducer. A localised peak appeared around 63 W, followed by a mild decrease before V_{rms} rose again to a global maximum at approximately 106 W.

From the perspective of parameter selection, input power ranges corresponding to V_{rms} reductions should be avoided, as these may indicate non-resonant behaviour or enhanced non-linear damping, potentially leading to insufficient cavitation intensity. Notably, the V_{rms} for the air-backed condition is markedly higher than that for the water-backed condition when input power exceeds 10 W. To maximise cavitation shockwave intensity, subsequent experiments in this study therefore, employed the air-backed condition.

Finally, as the maximum available input power for the sonotrode used in comparative experiments under cylindrical vessel conditions is 55 W, this power level was selected to ensure a consistent reference for subsequent comparisons between the tube transducer and the sonotrode in terms of cavitation structure and spatial distribution. Additionally, 106 W was further selected as the high-power operating condition for subsequent experiments.

6.3.2 High-speed imaging (HSI) of the cavitation generated by sonotrode and tube transducer

Selected frames from HSI sequences captured at 20,000 fps (corresponding to the 20 kHz sonotrode frequency) of the cavitation generated by the sonotrode tip at the top, centre and bottom positions within the cylindrical vessel (as described in §6.2.2) are presented in fig. 6.4 (a) - (c), respectively. The central circular shadow feature throughout fig. 6.4 is an artefact of the combined illumination fixtures (fig. 6.1 (a), equipment items 4 and 5). Results from HSI of the tube transducer under air-backed condition are shown in fig. 6.4 (d) and (e) at 55 W and 106 W, respectively. These images are representative of the bubble structures that develop during the 2 s sonications in each of the respective configurations. The outlines of the sonotrode tip and the tube bore are indicated by a dashed orange line in (b) and (d).

Fig. 6.4 (a) and (b) indicates that in the top and middle tip positions the classic cone shaped bubble structure forms, remaining in contact with the tip for the duration of the sonication,

as has been extensively reported previously [93], [220], [221]. Small oscillating clouds of bubbles (indicated by red arrows) occasionally detach from the main conical structure and migrate downwards through the cylindrical vessel under the action of acoustic streaming. In fig. 6.4 (c), where the tip is closest to the bottom of the cylindrical vessel, cavitation activity is evident but the conical structure is not clearly formed in the constrained space. Cavitation bubbles are also observed along the shaft of the sonotrode probe (indicated by green arrows) as also previously reported for a tip sufficiently immersed within a liquid [95], [222], [223].

Fig. 6.4 (d) shows typical cavitation activity within the bore of the air-backed tube transducer at an input power of 55 W. An experimental and numerical investigation of similar bubble structures that form under a ramped excitation voltage in an equivalent tube transducer has recently been reported [224]. Initially, within approximately 50 ms of the sonication initiation, cavitation bubbles have rapidly formed many fine, radial filamentary structures throughout the bore of the tube, generating a densely packed cluster at the central, axial position. Bubbles and bubble clusters initially generated in the peripheral regions tend to migrate inwards, along these filamentary structures, “feeding” the central cluster. From approximately 100 ms of the sonication, the finer radial structures have combined to form more established filaments that, together with the central cluster, constitute the main activity for the remainder of the sonication.

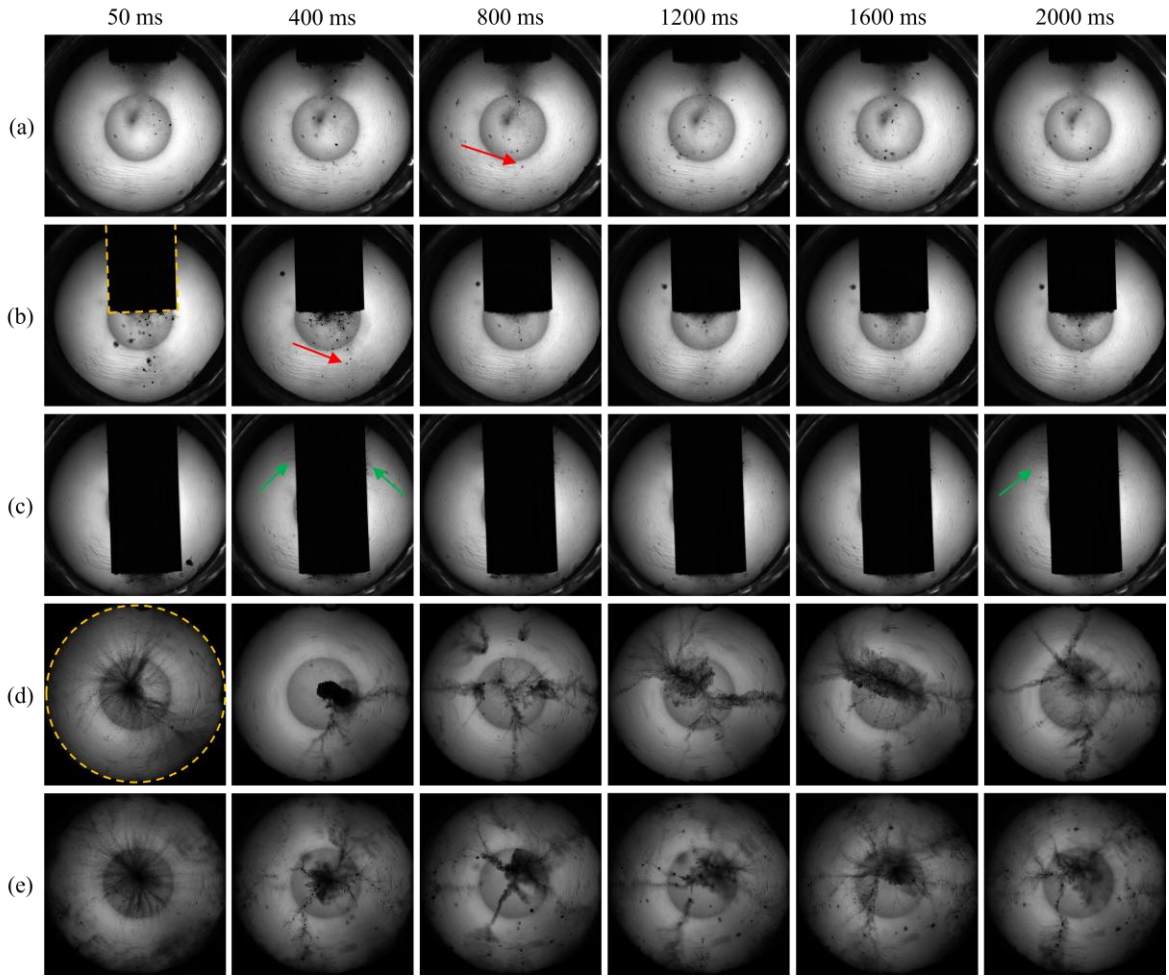

Fig. 6.4: Selected images from high-speed sequences captured at 20 000 frames/s, showing the acoustic cavitation generated by the sonotrode operating at 55 W, with the tip in the (a) top, (b) central and (c) bottom positions, and within the air-backed tube transducer at (d) 55 W input power and (e) 106 W. Scale is provided by the 20 mm diameter sonotrode tip. All sonications were 2 s in duration. The outlines of the sonotrode tip and the tube bore are shown by a dashed orange line in (b) and (d). Coloured arrows indicate small bubble clusters detached from the main conical structure (red) and cavitation along the shaft (green) for the sonotrode sonications.

In fig. 6.4 (e), at the higher input power of 106 W, cavitation bubbles fill the bore continuously throughout the sonication period. The bubbles exhibit a distinct spatial distribution and a larger central cluster form. More filamentary structures also form between the outer regions and the central cluster than at the lower power. These filament structures act as bubble migration channels and correspond to regions of intense cavitation activity, as confirmed by SCL images below, in §6.3.3.

These HSI observations demonstrate that the structure and distribution of cavitation bubbles generated by the sonotrode and tube transducers are notably different. For the sonotrode system, cavitation is localised to the tip according to the vertical position within the cylindrical vessel. In contrast, the filamentary structures generated by the tube transducer feed a cluster located on the central axis, channelling cavitation activity away from the inner surface of the transducer.

HSI in fig. 6.4 (d & e) indicates that during a single continuous 2 s sonication, the structure and coverage of the cavitation clusters within the tube bore exhibits time-varying characteristics. This implies that cavitation intensity and its effective action region are not constant over time, which in turn suggests an opportunity to optimise how the ultrasonic exposure time is distributed. This content will be investigated in further detail throughout Appendix C in terms of acoustic signals

6.3.3 Sonochemiluminescence imaging of the sonotrode and air-backed tube transducer

The SCL imaging of the sonotrode tip in its three positions and the tube transducer at each input power in fig. 6.5 (a-e), align broadly to the cavitation activity seen during the HSI, despite being captured over longer 10 s sonications.

Fig. 6.5 (a & b) are typical of previous SCL-based studies of cavitation at a sonotrode tip, confirming that the most intense and sonochemically active cavitation is contained within the conical bubble structure, in contact with the sonotrode tip. The luminescence beyond this region, extending down through the cylindrical vessel, is attributable to the smaller detached bubble clusters also seen during the HSI (indicted by red arrows in fig. 6.4 (a & b)). During the sonication with the tip in the centre position, fig. 6.5 (b), this extended luminescence region follows the lower inner surface of the cylindrical vessel. This is again consistent with the counter-rotating vortices known to be generated by the vibrating tip of a sonotrode, which will cause detached clusters to migrate along these trajectories, in this vessel geometry [225], [226]. The SCL imaging with the tip in its bottom position, fig. 6.5 (c), indicates intense cavitation activity within the constrained liquid region, as well as along the shaft of the submerged probe.

An SCL image of the tube transducer under air-backed condition with an input power of 55 W is shown in fig. 6.5 (d). Notably, luminescence is generated from all regions within the tube bore and is brightest at the central axis, corresponding to the large cluster that was

observed during HSI. The distribution is generally uniform away from this central region, although three radial lines of slightly higher intensity are present (indicated by red arrows), attributable to the filament structures observed by HSI, fig. 6.4 (d). An increase in air-backed tube transducer input power to 106 W enhanced the overall blue light intensity, as seen in fig. 6.5 (e), but the off-centre distribution is less homogenous. The central on-axis region is again brightest but high luminescence is also evident around the inner circumference of the tube and along radial regions, in accordance with the HSI of the cavitation activity, fig. 6.5 (e).

The SCL distributions in fig. 6.5 (a-e) are compared quantitatively in the image histogram of greyscale levels, shown in fig. 6.5 (f). The magnitude and prevalence of these greyscale levels correspond to the intensity and distribution of SCL, which in turn may be considered as an indicator of cavitation activity intensity. Terms for greyscale level ranges were defined to aid analysis as “invisible” for levels below 30, “low intensity” for levels between 30 and 40, and “high intensity” for levels greater than 40. An example of each is marked up in fig. 6.5 (a) as green, yellow and red boxes, respectively. The intensity and distribution of SCL is greatest for the sonotrode, when its tip is in the centre position where 21.06% and 52.79% of greyscale values are low intensity and high intensity, respectively.

The air-backed tube transducer generates brighter and more distributed luminescence at 55 W and 106 W input powers. For both input powers low and high intensity greyscale levels account for more than 99.60% of SCL image pixels and the majority of these - 97.07% for the 55 W configuration - are high intensity. While both input powers create unimodal distributions in the image histogram, at 106 W the distribution is narrower and its peak is positioned at a higher greyscale value. This indicates that at the higher input power, the sum of areas corresponding to intense cavitation activity increases and their distribution throughout the tube bore is more uniform. This quantitive comparison corroborates the visual comparison of fig. 6.5 (d & e) just described. The maximum greyscale level for the air-backed tube transducer, for both input powers, was 190. However, significantly more maximum level pixels were present at 106 W input power than at 55 W, again indicating that the spatial extent of the intensely cavitating region is more significant at the higher power. The maximum sonotrode greyscale level was 120.

In summary, these results indicate that for equivalent input powers the cavitation activity generated by the tube transducer is more intense than that produced by the sonotrode and that the activity is more distributed through the equivalent volume.

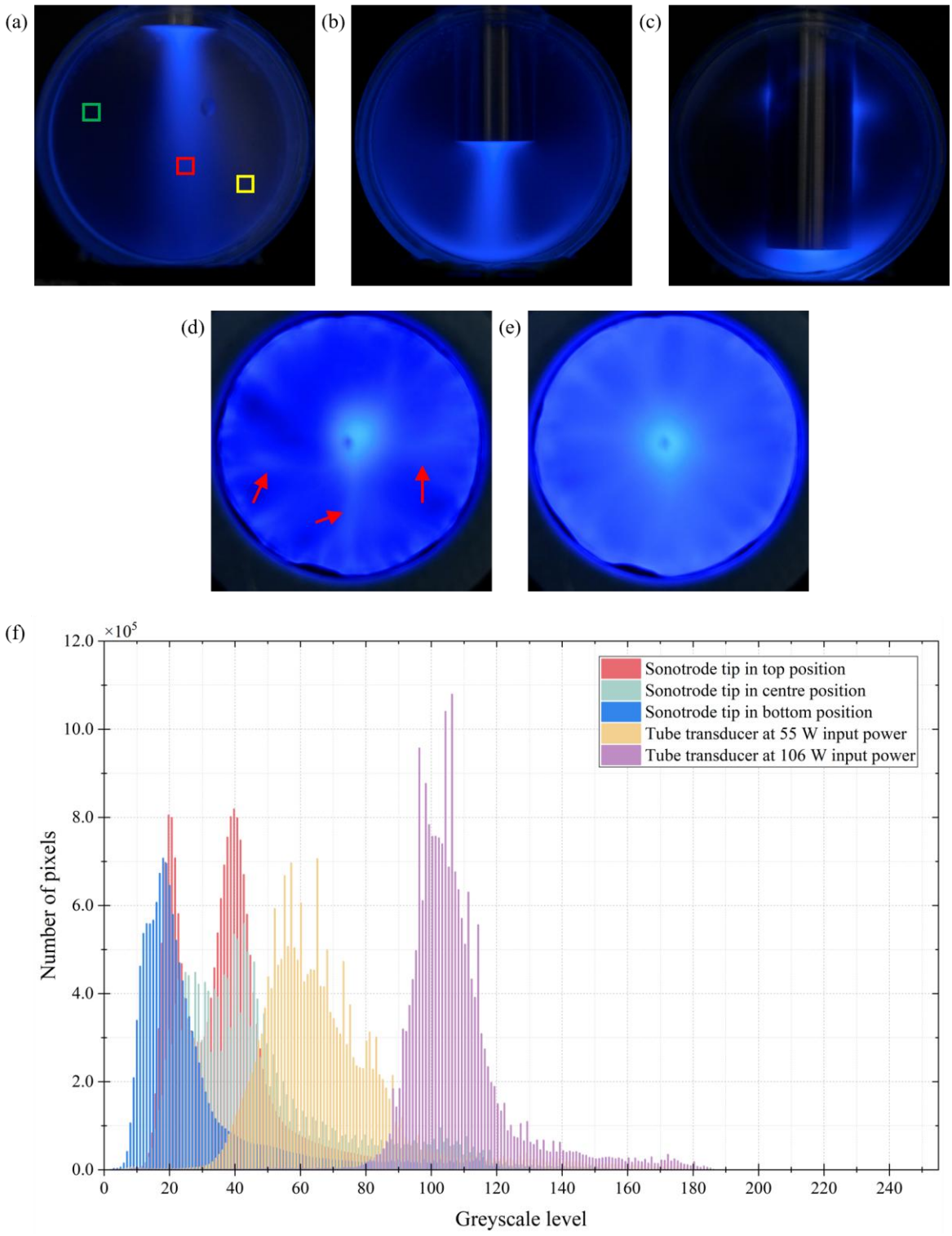

Fig. 6.5: SCL images obtained during 10 s sonications for the sonotrode at 55 W with the tip in the (a) top, (b) centre and (c) bottom positions within the cylindrical vessels, and the tube transducer at (d) 55 W and (e) 106 W input power. (f) Greyscale level histograms of (a)-(e) obtained by MATLAB greyscale processing. The boxes on (a) represent regions of greyscale values classified as invisible (< 30, green), low intensity (> 30, < 40, yellow) and high intensity (> 40, red). Red arrows in (d) indicate radial lines of luminescence, discussed in §6.3.3.

6.4 Discussion

This chapter quantitatively characterises the cavitation intensity within the bore of the radially poled piezoceramic tube transducer developed in §3.5, under both air-backed and water-backed conditions. The V_{rms} results indicate that, the cavitation intensity is significantly stronger in the air-backed condition over the same range of input powers. This difference can be attributed to the different levels of vibrational damping imposed by the backing medium. Compared with air, water has a higher viscosity and density, which reduces the vibration amplitude of the tube body and suppresses the generation of cavitation bubbles. This result highlights the importance of the backing conditions in determining the cavitation intensity produced by the tube transducer. Notably, conventional Langevin-type transducers mechanically pre-stress and constrain the piezoceramic stack using front and back masses. The acoustic impedance of the back mass is designed to exceed that of the front mass, so as reflect backward-propagating energy and promote forward wave transmission, thereby enabling more effective energy output at the intended radiating face [227]. Therefore, future work will investigate the implementation of a "solid backing", such as high-density metal backing layer, using rigid fixation and pre-loading to regulate the backing condition and evaluate its potential to further increase cavitation intensity within the tube bore.

After establishing the air-backed condition as the optimal configuration, this chapter compared the cavitation generated to that induced by a conventional sonotrode device, at similar input power. The HSI and SCL results indicate that the most active cavitation generated during a tube transducer sonication is found along the central axis, as anticipated for an inwardly focused, radial mode excitation. Cavitation is also generated throughout the bore of the tube, including along the emitting, inner curved wall, from which cavitating bubbles migrate inwards, particularly along radial filamentous bubble structures that form and feed the central cluster.

These optical observations suggest that the tube transducer cavitates liquids in a way that combines the advantages of the two common Langevin transducer deployments, described in the §5.1 Introduction. Cavitation at sonotrode-like intensity is distributed throughout the liquid bulk, similar to an ultrasonic cleaning bath. Moreover, the most active cavitation is removed from the emitting surface, in contrast to the cavitation at the tip of a sonotrode. This difference could be beneficial to applications such as food processing, where contamination

from tip erosion is a significant concern that has limited development and industrial adoption [125], [228].

Fig. C.2 should be interpreted as a temporal analysis of a single finite excitation rather than as a direct comparison of periodic pulse trains. The reduction in V_{rms} with increasing analysis-window duration indicates that the later stages of the excitation contained a lower mean-square shockwave signal than the initial transient. This behaviour is consistent with the HSI observations of the development and redistribution of the bubble cloud within the tube bore.

One possible explanation is that sustained excitation promotes bubble growth, coalescence and the accumulation of relatively inactive gas-rich bubbles, which may increase acoustic shielding and reduce the effective propagation of ultrasound through the liquid [229]. However, these mechanisms were not measured independently in the present experiment and should therefore be regarded as a mechanistic interpretation rather than as a directly demonstrated cause.

Under a repeated on/off protocol, the t_{off} may allow bubble clusters to collapse, disperse or partially dissolve before the next burst, potentially reducing shielding while retaining sufficient residual nuclei to initiate cavitation during the subsequent t_{on}. The resulting cavitation response would depend on both t_{on} and t_{off}, as well as the duty cycle and pulse-repetition frequency. Because no t_{off} was imposed or varied in the present experiment, the results do not establish an optimal periodic-pulsing protocol or an improvement in processing efficiency per unit energy. Instead, the comparatively high V_{rms} during the first 100 ms identifies a candidate t_{on} for subsequent pulse-train experiments in which t_{off} and total energy input are independently controlled.

6.5 Conclusion

This chapter experimentally characterises a novel high power ultrasonic source - a radially poled piezoceramic tube transducer. Results indicate that cavitation intensity within the tube bore exhibits high sensitivity to the external backing conditions, with air-backed configuration currently providing the optimal arrangement. Moreover, the tube transducer generates cavitation activity at sonotrode-like intensities but distributed through the bore of the tube, with peak activity at the central axial position. This bore wide, high intensity cavitation indicates that the tube transducer has potential advantages for continuous

sonoprocessing in flow-based configurations. The time-domain acoustic analysis showed that the mean shockwave content was highest during the initial 100 ms of the 2 s excitation and subsequently decreased as the cavitation field evolved. This characteristic start-up timescale provides a basis for selecting a candidate t_{on} for subsequent pulsed operation. However, optimisation of a complete pulse protocol requires independent investigation of the t_{off}, duty cycle and pulse-repetition frequency under energy-matched conditions.

Chapter 7

Assessment of ultrasonic delamination of graphite coating from lithium-ion battery anode: comparison of tube transducer and sonotrode

Chapter Overview

This chapter seeks to demonstrate that the potential advantages of the cavitation activity generated by the tube transducer, described in Chapter 6, translates to a 'real-world' application, specifically the delamination of graphite coating from LiB anode.

The delamination capability is first assessed for sections of intact anode production scrap sheet, in comparison to sonotrode sonications at two tip-to-sheet distances, in accordance with the most recent literature on this specific application (reviewed below). For the proposed use of tube transducers in flow processing, delamination of anode production scrap flakes is also assessed in static conditions, representative of the material that would be produced through an industrial shredding processes. Flake delamination results from sonotrode sonications in various configurations, for fair and meaningful comparison, are also presented.

Aged LiB anodes are treated using a combined "citric acid pre-soak + sonication" process, to assess for end-of-life recycling. The graphite delamination efficiency from aged LiB anodes was investigated under different citric acid concentrations and soaking times.

Finally, since the introduction of flakes may increase the availability of cavitation nuclei as compared to pure water, which could then modify the cavitation intensity generated for any given input power, the cavitation intensity of flake-loaded water is further characterised with shock wave passive cavitation measurements.

Journal paper
The tube transducer as a novel source for power ultrasound: A case study in delamination of graphite coating from lithium-ion battery anode **Shida Li**, Paul Daly, Ben Jacobson, Joshua Cooke, Chunhong Lei, Andrew P. Abbott, Andrew Feeney, Paul Prentice *Chemical Engineering and Processing - Process Intensification,* vol. 225, p. 110813, 2026*)*
This chapter was used for demonstration of the "inventive step" for United Kingdom (GB) patent application number 2416254.7, FLOW SONOPROCESSING APPARATUS, University of Glasgow.

Conference Paper
Pretreatment of aged lithium-ion battery anode to enable high-throughput sonoprocessing **Shida Li**, Paul Daly, Ben Jacobson, Andrew Feeney and Paul Prentice
1st International REACT Conference, Glasgow, November 2025

7.1 Motivation and context

As outlined in chapter 2, global demand for lithium-ion battery (LiB) is projected to increase from approximately 700 GWh in 2022 to 4700 GWh by 2030 [145]. Although most batteries enter the end-of-life recycling process after a 10-year lifespan [146], production scrap generated immediately and thus places a direct, near-term burden on recycling capacity. Current assessments indicate that the scrap rate in LiB manufacturing is on the order of 10% [154]. Assuming a typical energy density of 300 $Wh \cdot kg^{-1}$ [147], this corresponds to roughly 1.57 Mt of production scrap by 2030.

As described in §2.2.2, the LiB electrodes have a layered structure, in which the main component is a porous composite film composed of active material, polymer binder, and conductive additives, coated on both sides of current collector manufactured from TCMs. Conventional pyrometallurgical technologies recover only the TCMs fraction [230]. Hydrometallurgical technologies can, in principle, enable the recovery of both TCMs and active materials, but at the cost of using highly polluting reagents [231]. There is therefore a clear need for recycling processes that achieve the joint, high efficiency recovery of TCMs and active materials under greener, more sustainable conditions. Against this background, the present work adopts LiB anode production scrap and focuses on assessing the

performance of different sonoreactor configurations in promoting delamination of the graphite coating. Existing studies have predominantly employed commercial ultrasonic reactors - particularly sonotrodes and ultrasonic baths - to perform LiB anode delamination, and have reported a range of representative results. The relevant literature is therefore reviewed in the following subsections, organised according to the type of sonoreactor.

7.1.1 Sonotrode-based delamination of LiB anode

Lithium-ion battery recycling using high-intensity ultrasonication.

Chunhong Lei, Iain Aldous, Jennifer M. Hartley, Dana L. Thompson, Sean Scott, Rowan Hanson, Paul A. Anderson, Emma Kendrick, Rob Sommerville, Karl S. Ryder, Andrew P. Abbott. Green Chemistry, vol. 23, pp 4710-4715, 2021.

This work [72], [232] employed a commercial ultrasonic system (Branson Sonics, 1.25DCXa20V) with a maximum power output of 1250 W and an operating frequency of 20 kHz, equipped with a probe which tip is 20 mm diameter. This system was used to sonicate LiB anode immersed in de-ionised water in order to remove the graphite adhered to the copper foil current collector. Under conditions of a 5 mm tip-to-anode distance, a power intensity of 120 $W \cdot cm^{-2}$ from the sonotrode tip surface and a sonication time of 3 s, the authors reported almost complete removal of the graphite coating within an approximately circular treatment zone of about 10 mm diameter (fig. 7.1). The size and shape of this ‘treatment zone’ arise from the conical cavitation structure described in §1.3.1.1, which is formed beneath the probe tip. These results demonstrate the significant delamination capability of sonotrode-induced cavitation on graphite. However, they also reveal two critical limitations of such configurations: firstly, the probe must be positioned within only a few millimetres of the target surface; secondly, the effective cavitation zone is typically confined to a small, near-circular area. These factors constrain the potential for scalability of such processes towards larger treatment areas and higher throughput operation.

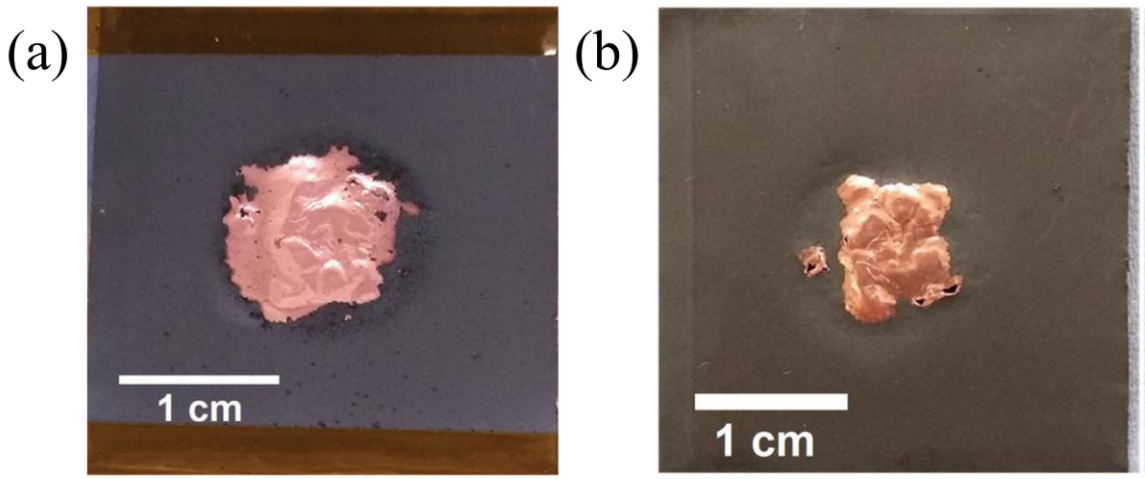

Fig. 7.1: Images showing the effect of sonication on graphite coating delamination from the LiB anode, (a) the front side, (b) the back side. Taken from [232].

To address these limitations, Lei *et al* [232] further developed a blade-type ultrasonic system. The device operates at 20 kHz with a maximum power of 2200 W, with edge of the blade (as indicated by the red dashed box in fig. 7.2 (a)), along which cavitation is induced, measuring 1.5 cm × 21 cm. This corresponded to a maximum power intensity of up to 70 $W \cdot cm^{-2}$. The overall structure of the system is shown in fig. 7.2 (a & b). Full size anode sheets with dimensions of 19.5 cm × 22.5 cm were manually fed at a speed of 2-3 $cm \cdot s^{-1}$, into an approximately 3 mm gap between the ultrasonic electrode and the sample tray in the delamination experiments.

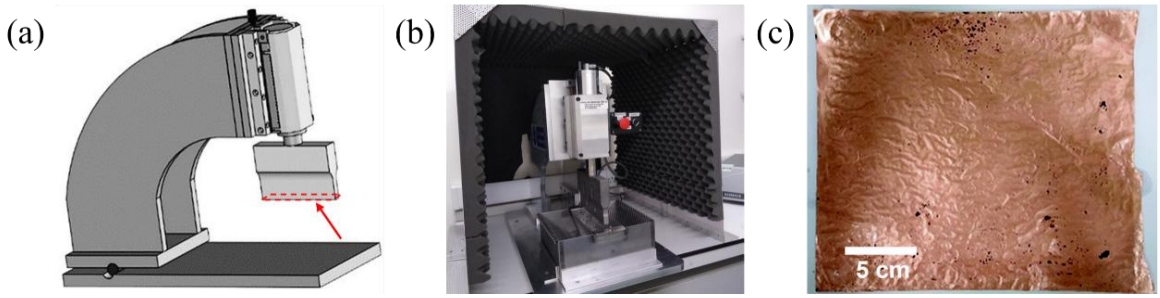

Fig. 7.2: (a) Ultrasonic system for graphite layer delamination from a full anode sheet (the red dotted box indicated by the red arrow denotes the edge of the blade), (b) photograph of apparatus, (c) image of copper foil after delamination. Taken from [232].

As shown in fig. 7.2 (c), this blade-type configuration was able to achieve almost complete removal of the graphite coating from the anode surface in a single pass, significantly

increasing the sonicated area per unit time. However, the sample must remain strictly confined within the narrow 3 mm gap relative to the ultrasonic electrode throughout the entire process, and this stringent geometric requirement continues to impose a substantial limitation on the practical applicability of the system.

7.1.2 Ultrasonic bath for batch delamination of LiB anode discs

Development of a Process for Direct Recycling of Negative Electrode Scrap from Lithium-Ion Battery Production on a Technical Scale and its Influence on the Material Quality.

Patrick Wiechers, Anna Hermann, Sofia Koob, Fabian Glaum, Marco Gleiß. Batteries, vol. 10, 218, 2024.

Ultrasonic baths, in addition to sontrodes, have also been employed for delamination of the graphite layer from LiB anode. Wiechers *et al* [197] used an ultrasonic bath (Weber Ultrasonics AG, Karlsbad, Germany) as depicted in fig. 7.3 (a), with internal dimensions of 28 cm × 20 cm × 10 cm, to sonicate 3 cm diameter LiB anode discs under aqueous conditions. The bath was operated at an output power of 200 W and a frequency of 29 kHz.

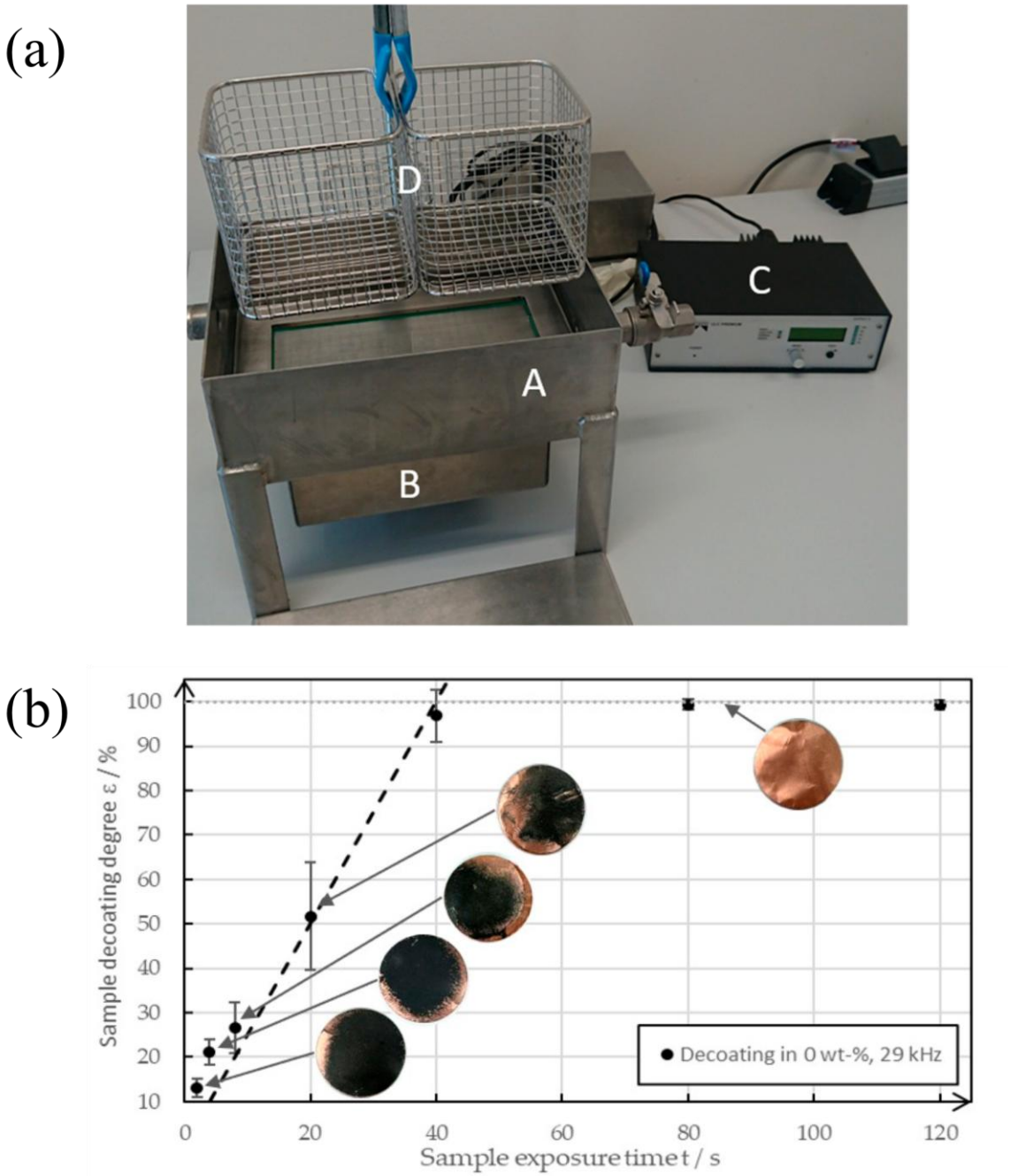

Fig. 7.3: (a) Ultrasonic system, include (A) ultrasonic bath, (B) ultrasonic oscillator, (C) frequency generator and (D) stainless-steel basket, (b) delamination behaviour under ultrasonic exposure ranging from 0 to 120 s at 29 kHz. Taken from [197].

As illustrated in fig. 7.3 (b), the degree of graphite delamination increased approximately linearly during the first 40 s of sonication. Thereafter, the delamination rate decreased markedly, approaching complete removal and reaching 100% after around 80 s. The slower delamination process relative to sonotrode limits the suitability of such bath configurations for high throughput applications.

7.2 Ultrasonic delamination of graphite coating from LiB anode production scrap

This section subjected intact anode sheet sections to sonications from a sonotrode with a 20 mm tip and the static tube transducer configuration. To further explore the capabilities of the tube transducer, this section also treats anode flakes and assesses graphite coating removal efficiency via "percentage remaining mass", post-sonication. The tube transducer performance is compared to various sonotrode configurations, where flakes were sonicated within a cylindrical vessel with dimensions that match those of the tube transducer, with the tip at various vertical positions. The relative strengths of each exposure configuration are described.

7.2.1 Materials and methods

7.2.1.1 Sonotrode & tube transducer

The designs and operating principles of the sonotrode and static tube transducer configuration used in this chapter have already been described in detail in §3.1 and §3.5, respectively. With regard to the experimental arrangements, the sonotrode experiments employed the same configuration as in chapter 6, whereas the tube transducer experiments used the air-backed, water-filled bore set-up, since the results in §6.3.1 demonstrated that this operating condition generates the most effective cavitation.

The electrical power measurement methods for both transducers are detailed in §6.2.6. The selection for input power for the experiments in this chapter remains consistent with that outlined in §6.3.2-6.3.3.

As the sonotrode used in this chapter does not support pulsed excitation, and to ensure comparability of experimental parameters, the optimal pulse duration conditions identified in Appendix C were not applied in this chapter. Instead, both the sonotrode and the tube transducer were operated under continuous excitation for the comparative experiments.

7.2.1.2 Lithium-ion battery (LiB) anode samples

Complete LiB anode sheets measuring approximately 23 cm × 20 cm, comprised of a 15 μm thick copper foil current collector coated on both sides with 70 μm layer of active material, fig. 7.4 (a), were sourced from Nissan Leaf batteries production scrap. The active material coat is composed of graphite (with an average particle diameter of 15 μm) and ca. 4.5 wt%

CMC/SBR binder [232]. The surface density of the LiB anode was measured as 0.030 $g \cdot cm^{-2}$ using high precision scales (PCE-BSK 310, PCE Instruments) with an accuracy of 0.001 g.

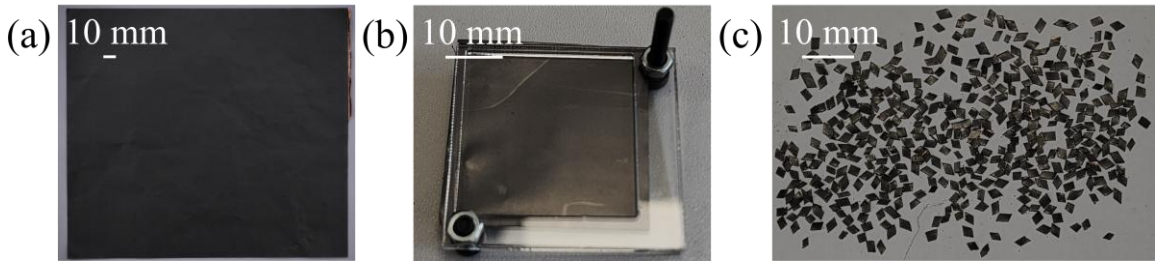

Fig. 7.4: (a) A complete LiB anode sheet. (b) A 3 cm × 3 cm intact LiB anode section mounted within a bracket. (c) LiB anode flakes with an effective area of 17 cm^2.

The experimental studies of Lei *et al* [72] show that a sonotrode with a 20 mm diameter tip at a distance of 5 mm from the surface of an intact LiB anode section, removes graphite coating from a circular area with a diameter of approximately 10 mm, from the side of the anode facing the tip. For the current work, an intact section of LiB anode was held within an acrylic mounting bracket, fig. 7.4 (b), and across the centre of the tube transducer, fig. 7.5 (a), or suspended horizontally beneath the sonotrode tip, fig. 7.5 (b). Within the bracket the anode section has an exposed area 3 cm × 3 cm (dimensions derived from the height of the tube transducer), with the section cut marginally larger for secure mounting. The sonotrode was operated at 55 W for 2 s, for tip-to-anode distances of 15 mm and 5 mm. The effects of tube transducer sonication on the intact section, when operating at 55 W and 106 W input powers for 2 s, were also tested. Five intact anode sections were sonicated for each of these two transducer configurations (two tube transducer input powers), as presented in §7.2.2.1.

In an attempt to reduce the dependence of sonoprocessing effects on the spatial distribution of the cavitation activity generated by the two transducer types used in this study, this chapter assessed the graphite coating delamination performance with LiB anode flakes, as seen in fig. 7.4 (c). A number of approaches to material recovery from end-of-life LiB anodes include mechanical crushing or shredding, suggesting the use of flakes is both valid and of practical interest [233], [234]. Batches of flakes of length and width less than 2 mm were cut from anode sheet, fig. 7.4 (c). Flake batches of effective areas up to 24 cm^2 were tested, as detailed in §7.2.2.5. Graphite coating removal was assessed by weighing dry anode flakes from each batch before and after each 2 s sonication. Five sample batches were tested for each of the five transducer configurations investigated (the sonotrode with three different tip

positions and the tube transducer at the two input powers), with data presented as the average ± standard deviation. Each batch of flakes was added to the water within either the bore of the tube transducer or the cylindrical vessel (prior to tip insertion), and allowed to settle to the bottom before the sonication was initiated, as indicated by the red arrows in fig. 7.7 and fig. 7.10.

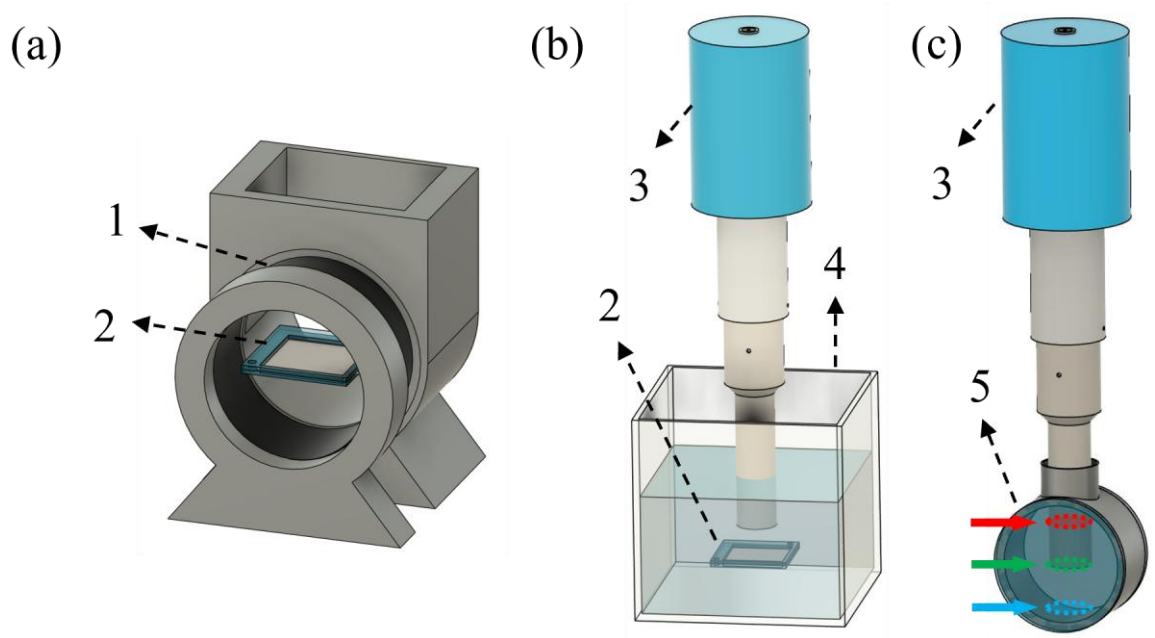

Fig. 7.5: Schematic of static tube transducer and sonotrode configuration for treat LiB anode section and flakes. (a) A static tube transducer configuration with an intact LiB anode section mounted horizontally in a custom-made bracket. (b) A schematic of the sonotrode configured to treat an intact LiB anode section. (c) A schematic of the sonotrode with the tip positioned centrally within a cylindrical vessel, used to treat flakes of LiB anode. Red, green and blue arrows denote the vertical position of the sonotrode tip in the top, centre and bottom positions. Equipment items include (1) tube transducer and housing, (2) 3 cm × 3 cm LiB anode section with bracket, (3) sonotrode, (4) 10 cm × 10 cm × 10 cm water tank, (5) cylindrical vessel.

7.2.1.3 Experimental procedure

De-ionised water at room temperature was the host liquid medium for all investigations. Any observed differences in cavitation intensity or graphite coating delamination performance can therefore be attributed to the transducer configuration or operating conditions.

Post-sonication imaging of intact anode sheet sections and batches of flake samples were taken with a surface microscope (SMZ-171, Motic, China; maximum magnification ×50).

7.2.1.4 Conventional imaging of graphite coating removal

Conventional video imaging at 120 frames/s captured the graphite coating delamination from LiB flakes within the tube transducer and the cylindrical sonotrode vessel, during sonications. A Nikon Z8 digital camera equipped with a NIKKOR Z 24-120 mm *f*/4 s lens as described in §3.3.2 was used. Imaging was undertaken over 3840 × 2160 pixels with 1/125 s exposure time, *f*/4 aperture and 3200 ISO.

7.2.2 Results

The following results sections are organised to compare the effectiveness of the various sonication configurations, using both the sonotrode and the tube transducer, in delaminating the graphite coating from LiB anode samples

- §7.2.2.1 presents the graphite coating delamination observations for the tube transducer on intact LiB anode sections. Results for three tip positions to the sonotrode and two input powers to the tube transducer are described.

- §7.2.2.2 presents the observations of graphite coating removal from LiB anode flakes, with an effective area of 4 cm^2, for each of the five transducer configurations investigated by the optical imaging techniques. The results represent the conventional imaging taken during sonications and a comparison of post-sonication "remaining mass percentage".

- §7.2.2.3 explores the effect of increasing anode flake effective area loading on the graphite coating delamination capability of the tube transducer, at 106W input power. A threshold is identified, beyond which delamination efficiency reduces due to overloading.

- §7.2.2.4 presents the conventional imaging of graphite coating delamination and percentage remaining mass data, for this threshold effective area.

- §7.2.2.5 presents the percentage remaining mass data for higher effective area under the five transducer configurations.

7.2.2.1 Graphite coating removal from 9 cm^2 intact lithium-ion battery (LiB) anode sections

The surfaces of intact LiB anode sections, with a nominal area of 3 cm × 3 cm, following a 2 s sonication are shown in fig. 7.6, for the four transducer configurations described in §7.2.1.2. Fig. 7.6 (a & b) show sections following treatment by the sonotrode for tip-to-anode distances of 15 mm and 5 mm, respectively. The effects of tube transducer sonication on sections, when operating at 55 W and 106 W input powers, are presented in fig. 7.6 (c & d). Each row in fig. 7.6 shows five replicates treated under the same transducer conditions and the labels “Front” and “Back” indicate upwards and downwards facing sides of the section as per fig. 7.6 (a & b), with respect to the sonotrode tip. In samples 1 to 4 of fig. 7.6 (a) the graphite coating has bulged away from the copper current collector on both the front and back sides, while on the front side of samples 2 and 3 these features have ruptured. These observations indicate that the adhesive bond between the active layer of graphite coating and the copper current collector has been broken. In all instances of fig. 7.6 (b), for a tip-to-anode distance of 5 mm, an approximately circular area of graphite coating has been removed from both sides of the section, to expose the copper foil. Image analysis in MATLAB determined that the diameter and area of the delaminated zone are approximately 2.2 cm and 3.8 cm^2.

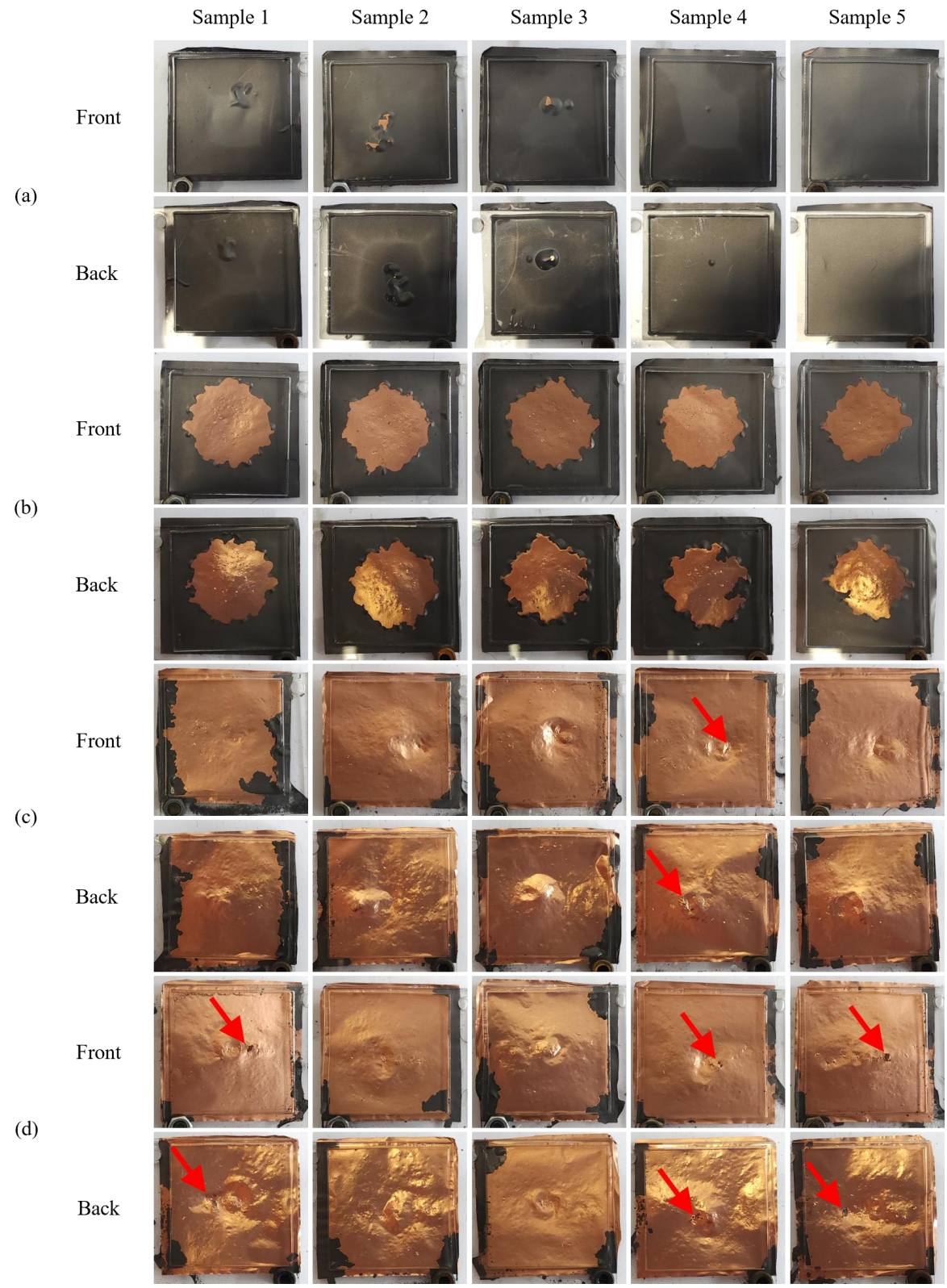

Fig. 7.6: The front and back surfaces of LiB anode sections mounted in brackets, with an exposed area of 3 cm × 3 cm, following a 2 s sonication for: Sonotrode at 55 W input power, with a separation distance of (a) 15 mm and (b) 5 mm between the tip and the anode section. Tube transducer at (c) 55 W and (d) 106 W input power. Each row shows five replicates treated with the same sonication conditions. Red arrows indicate puncture damage inflicted to the copper foil.

The intact section delamination capabilities of the tube transducer, at the two input powers, are shown in fig. 7.6 (c & d). Graphite coating has been removed from nearly all of the 3 cm × 3 cm areas and, in most cases, even the anode surface covered by the mounting bracket. Lei *et al* [232] suggests that intense bubble collapse shockwaves enable delamination by both peeling off of the graphite coating layer and flexing the electrode material to induce stress fracturing, while cavitation bubble jetting creates pits in the foil [72], [232]. The copper foil in fig. 7.6 (c & d) has also visibly buckled owing to the intensity of cavitation activity, and jet pitting has caused punctures, which are most prominent in samples 1 and 5 of fig. 7.6 (d), arrowed red.

These observations show graphite coating removal by the sonotrode is reduced when the distance between the sonotrode tip and anode section is increased. Even when the tip-to-anode separation distance is small however, the treatment zone is limited to 3.8 cm^2 (the tip area, approximately). In contrast, the tube transducer was not limited by the positioning of the sample and removed graphite coating from effectively all of the 3 cm × 3 cm surface of the section.

7.2.2.2 Graphite coating removal from anode flakes of 4 cm^2 effective area

To further test and (to some degree) mitigate the significant differences between the cavitation distributions generated by the sonotrode and tube transducer, LiB anode flakes were cut from 4 cm^2 of anode sheet. This allows for comparison with the sonotrode treatment described above, where 3.8 cm^2 of graphite coating was liberated from each side of a section (with the area rounded up for consistency with the 1 cm^2 increments of the flake loading investigation, §7.2.2.3, below). Graphite coating delamination from batches of LiB anode flakes with an effective area of 4 cm^2 is represented in fig. 7.7 for each of the five transducer configurations investigated, over 2 s sonications. Fig. 7.7 (a-c) depicts anode flake treatment by the sonotrode, at 55 W input power, with its tip in the top, centre and bottom positions, while fig. 7.7 (d & e) show the process in the tube transducer at 55 W and 106 W input powers.

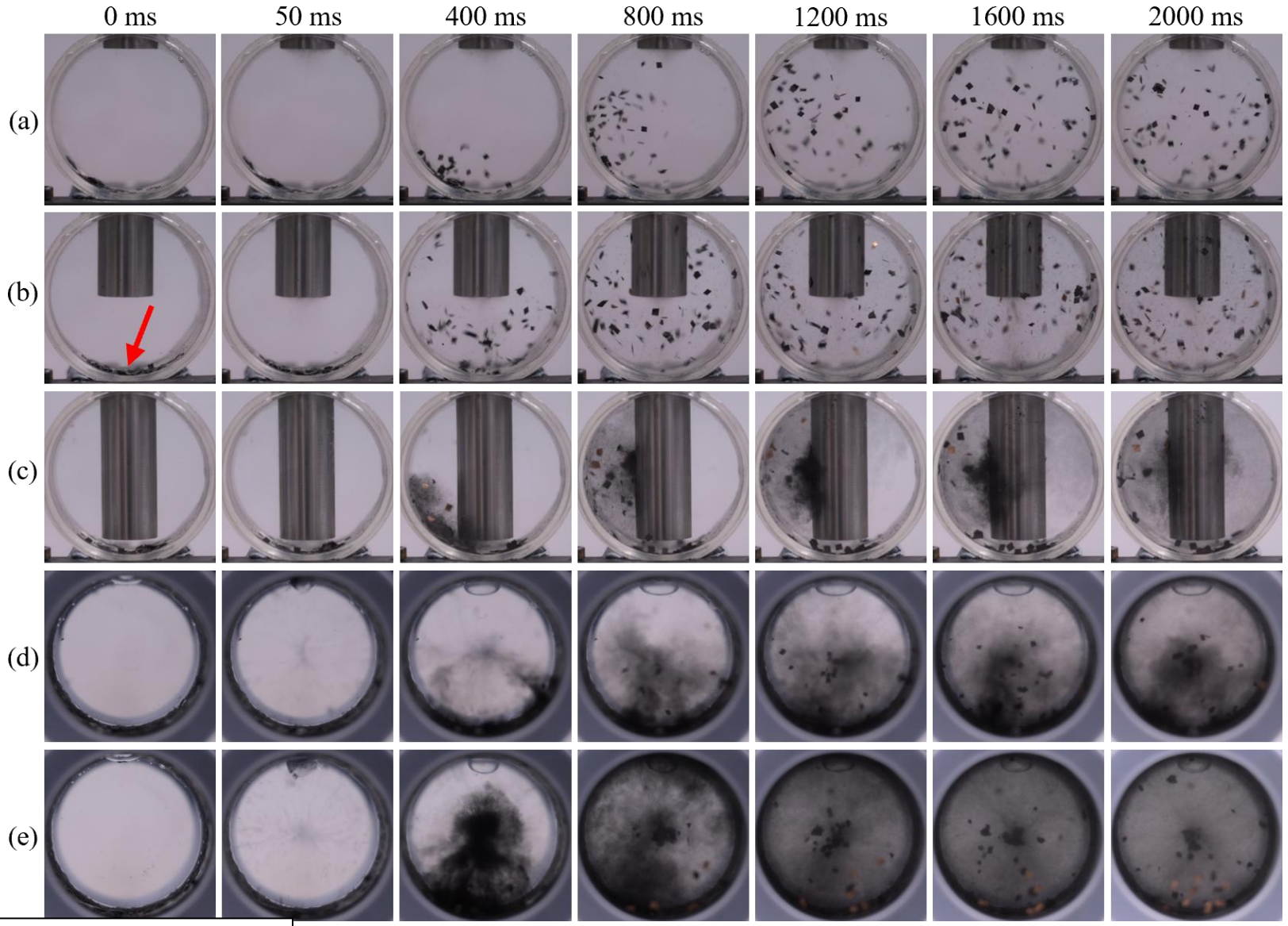

Fig.7.7. Caption on the following page.

Fig. 7.7: Images from a conventional recording of graphite coating delamination from 4 cm2 of LiB anode flakes, during a 2 s sonication with the sonotrode tip in the (a) top, (b) centre and (c) bottom position, and the tube transducer at (d) 55 W and (e) 106 W input power. Scale is provided by the 20 mm diameter sonotrode tip. The red arrow in (b) indicates the anode flakes settled at the bottom of the cylindrical vessel prior to sonication.

Prior to sonication by the sonotrode, the flakes have settled to the bottom of the cylindrical vessel, as indicated by a red arrow in fig. 7.7 (b). Fig. 7.7 (a & b) show that sonotrode sonications with the tip in the top and centre positions lift and disperse the flakes throughout the liquid volume. The degree of graphite coating delamination however, apparent by darkening of the water as graphite powder is liberated, is slight. Delamination is more evident in fig. 7.7 (c), with the sonotrode tip in the bottom position, close to the flakes. Graphite coating is liberated from the flakes mainly in the constrained volume below the sonotrode tip. A few flakes are displaced by the acoustic streaming and may be subject to delamination by the cavitation along the shaft, as identified by the HSI and SCL observations in chapter 6, later in the sonication. Acoustic streaming also propels a proportion of the liberated powder upwards through the vessel, where it also collects preferentially along one side of the sonotrode shaft. For all three tip positions, delamination only occurs for flakes close to the "active regions", as revealed by the optical imaging Result.

Although not visible in fig. 7.7 (d & e), owing to the housing components shown in fig. 3.9 and fig. 3.10 in chapter 3, the anode flakes have also settled to the bottom of the tube transducer, prior to sonication. During the first 400 ms of sonication, at both 55 W and 106 W input powers, the flakes remain on the bottom of the tube but graphite coating has clearly been delaminated. The liberated powder appears to gather along what may be the radial bubble filaments, identified by the HSI and SCL observations described in chapter 3, in the lower half of the transducer bore. From 800 ms, delaminated copper foil flakes are lifted from the bottom and transported through the tube bore, and liberated powder concentrates at the central on-axis position. Fig. 7.7 (e) indicates that the increase in tube transducer input power to 106 W increases the rate of flake delamination. Enhanced streaming also disperses liberated powder more evenly through the bore of the transducer, with a notable concentration at the central on-axis position, toward the end of the sonication.

The degree of graphite coating delamination from flakes with a 4 cm^2 effective area, in each of the transducer configurations, is quantified in fig. 7.8 and table 7.1. The "remaining mass

percentage" of fig. 7.8 is the mass of LiB anode flakes recovered from the liquid volume, following sonication, as a percentage of the pre-sonication mass. Each data point represents the average of five measurements, with error bars indicating the standard deviation. Complete removal of graphite coating from a batch of flakes results in a remaining mass value of 23%, indicated by the dashed line across the bar chart. A representative image of a batch collected from each transducer configuration is also presented in fig. 7.8.

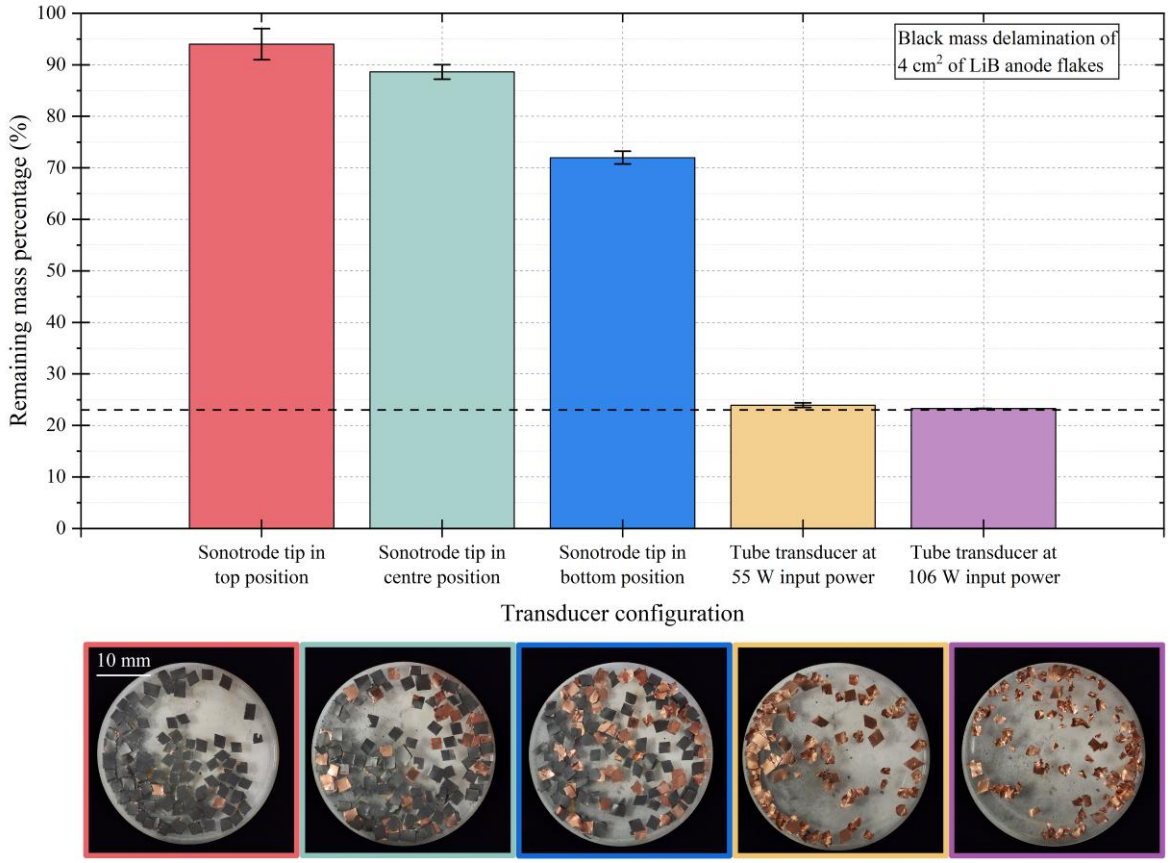

Fig. 7.8: Remaining mass percentage of LiB anode flakes with a 4 cm² effective area following 2 s sonications in each of the five configurations. Complete graphite coating removal is indicated by a dashed line at 23%. Also shown are pictures of the flake batches, post-sonication, for each configuration.

For top and centre sonotrode tip positions, remaining mass percentages of 94% and 89%, confirm the minimal delamination observed in fig. 7.7 (a & b). Percentage remaining mass decreased to 72% for the tip in the bottom position, in-line with the observation of fig. 7.7 (c). The tube transducer at both input powers effectively removes all graphite coating from all batches of flakes. Inspection of the recovered flakes of fig. 7.8 reveals further differences in the effects of sonications by the sonotrode and tube transducer configurations. The

morphology of flakes recovered following sonotrode treatment were largely unaffected and planar, while those recovered from the tube transducer were contorted and fragmented by the sonication. Based on the delamination results, the next section will further examine whether this performance can remain equally stable as the flake area is progressively increased.

Table 7.1: The mass removed from batches of LiB anode flakes with effective areas of 4 cm^2 and 17 cm^2, following 2 s sonications in each of the transducer configurations. Data is provided as the mean of five separate flake batches ± standard deviation, for each configuration.

Transducer configuration	**Mass removed** (mg) Effective area of LiB anode flakes	
	4 cm^2	17 cm^2
Sonotrode tip in top position	8 ± 4	5 ± 2
Sonotrode tip in centre position	17 ± 1	50 ± 15
Sonotrode tip in bottom position	34 ± 1	170 ± 26
Tube transducer at 55 W input power	89 ± 3	169 ± 13
Tube transducer at 106 W input power	89 ± 2	386 ± 2

7.2.2.3 Effect of increasing anode flake loading on the degree of graphite coating delamination

The effect of increasing the flake loading added to the tube transducer for 2 s sonications at 106 W input power, was investigated with effective area increments of 1 cm^2, fig. 7.9. Each data point represents the average measurements from five sonications, with error bars indicating the standard deviation.

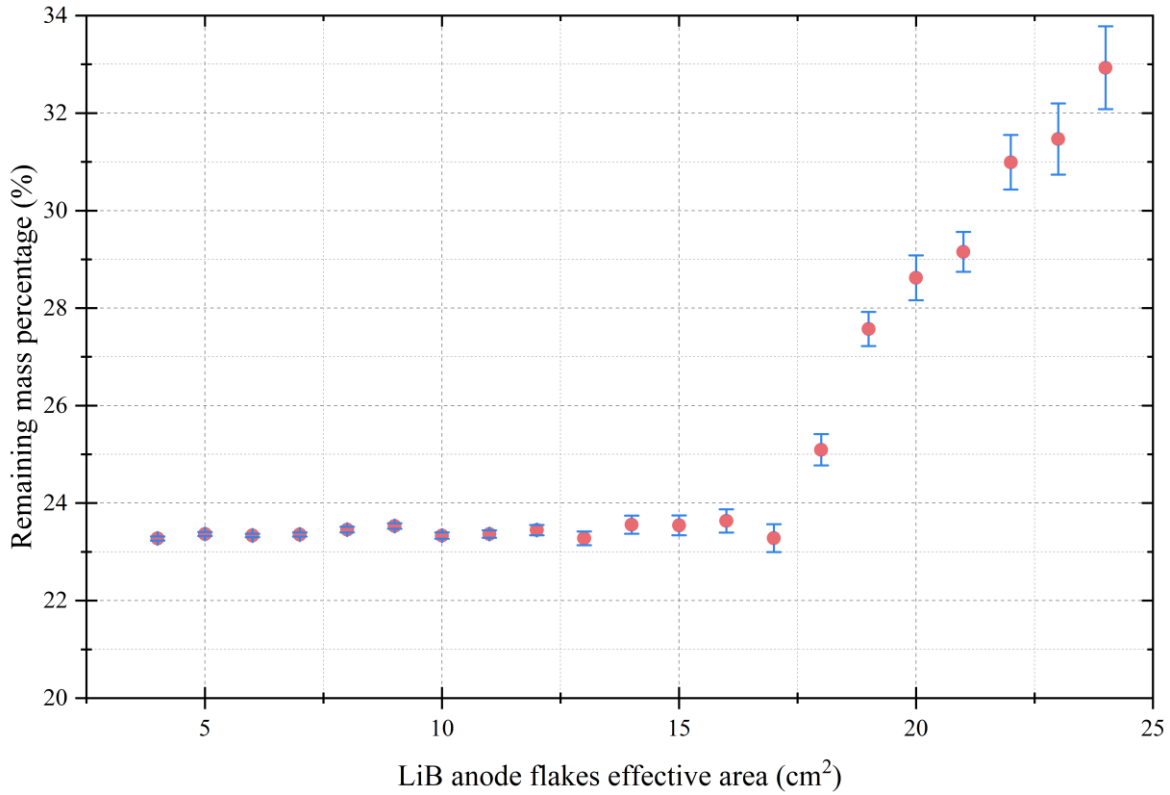

Fig. 7.9: The effect of LiB anode flake effective area on the remaining mass percentage recovered from the tube transducer, following 2 s of sonication at 106 W. A lower remaining mass percentage value indicates a higher degree of graphite coating delamination, with 23% representing complete removal.

For effective area loading up to and including 17 cm^2 remaining mass percentages were between 23% and 24%, corresponding to complete graphite coating removal. Remaining mass percentage thereafter increased with effective area load, to approximately 33% at 24 cm^2.

7.2.2.4 Graphite coating removal from anode flakes of 17 cm^2 effective area

Fig. 7.9 reveals a threshold effective area of 17 cm^2 for complete removal of graphite coating from a batch of anode flakes. Observations of the removal process for batches of flakes of this threshold effective area, in the five transducer configurations, are reported in this section.

Fig. 7.10 (a & b) show that during a 2 s sonication with the sonotrode at 55 W input power, with the tip in the top and centre positions, the flakes are agitated by the acoustic streaming induced by the sonication, similar to the lower effective area loading observations of fig. 7.7.

Once again, however, there is only slight darkening of the water indicating a low degree of delamination.

With the tip in the bottom position, fig. 7.10 (c), significant delamination occurs throughout the sonication. Clearly, the higher degree of darkening is due to more graphite coating powder being liberated from the higher number of flakes. The powder again tends to gather along the shaft of the sonotrode probe and delaminated copper flakes are apparent in the lower regions of the cylindrical vessel, later in the sonication.

Fig. 7.10 (d & e) depict the graphite coating removal process in the tube transducer at input powers of 55 W and 106 W, respectively. Powder liberated from the flakes, initially at the bottom of the tube, is once more transported upwards through the bore, initially collecting at the central on-axis region. At both powers, the water is almost completely blackened by the end of the 2 s sonication.

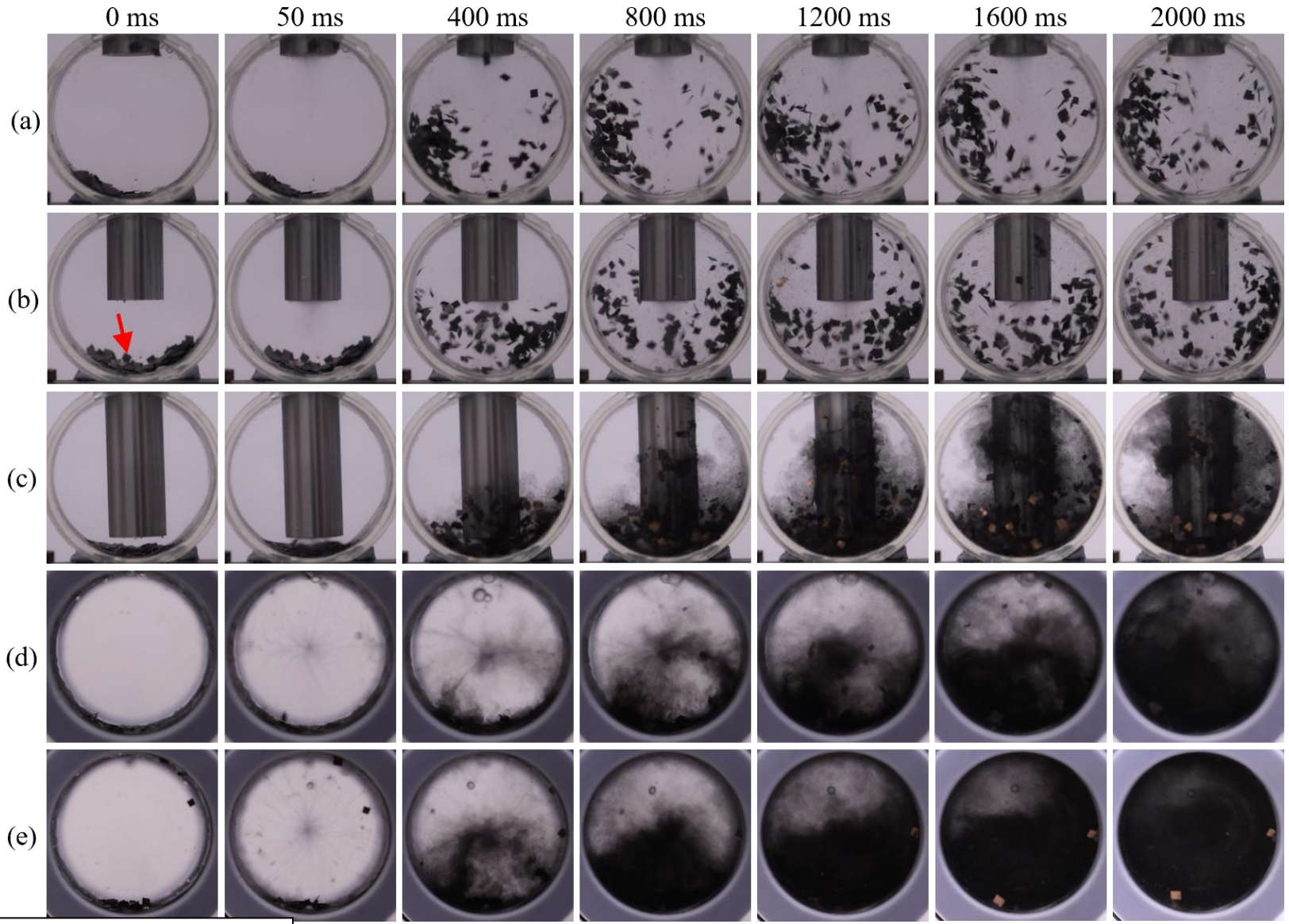

Fig.7.10. Caption on the following

Fig. 7.10: Images from a conventional recording of graphite coating delamination from 17 cm^2 of LiB anode flakes, during a 2 s sonication with the sonotrode tip in the (a) top, (b) centre and (c) bottom position, and the tube transducer at (d) 55 W and (e) 106 W input power. Scale is provided by the 20mm diameter sonotrode tip. The red arrow in (b) indicates the anode flakes settled at the bottom of the cylindrical vessel, prior to sonication.

The graphite coating removed from 17 cm^2 flake batches in each of the transducer configurations are quantified in fig. 7.11 and table 7.1. With the sonotrode tip in the top and centre positions 99% and 91% of the flake mass was retained. The sonotrode tip in the bottom position and the tube transducer with 55 W input power exhibited a similar degree of delamination, with both producing remaining mass percentages of 67%. The tube transducer at 106 W achieved complete removal, with a remaining mass percentage of 24%.

Images of the recovered flakes in fig. 7.11 gives further insights to the delamination caused by each configuration, across the population of flakes. With the sonotrode tip in the top and centre positions, it can be seen that the little delamination that did occur came from complete removal of graphite coating from a small number of flakes. This supports the assertion that delamination only occurs when streaming transports flakes to the active cavitation zone immediately below the tip. The recovered flake images for the bottom tip position and tube transducer at 55 W indicate that although the percentage remaining mass is similar, the tube achieved more uniform delamination across the population of flakes. As for the lower effective area batches, the recovered flakes from the tube transducer show signs of significant cavitation damage, especially at 106 W.

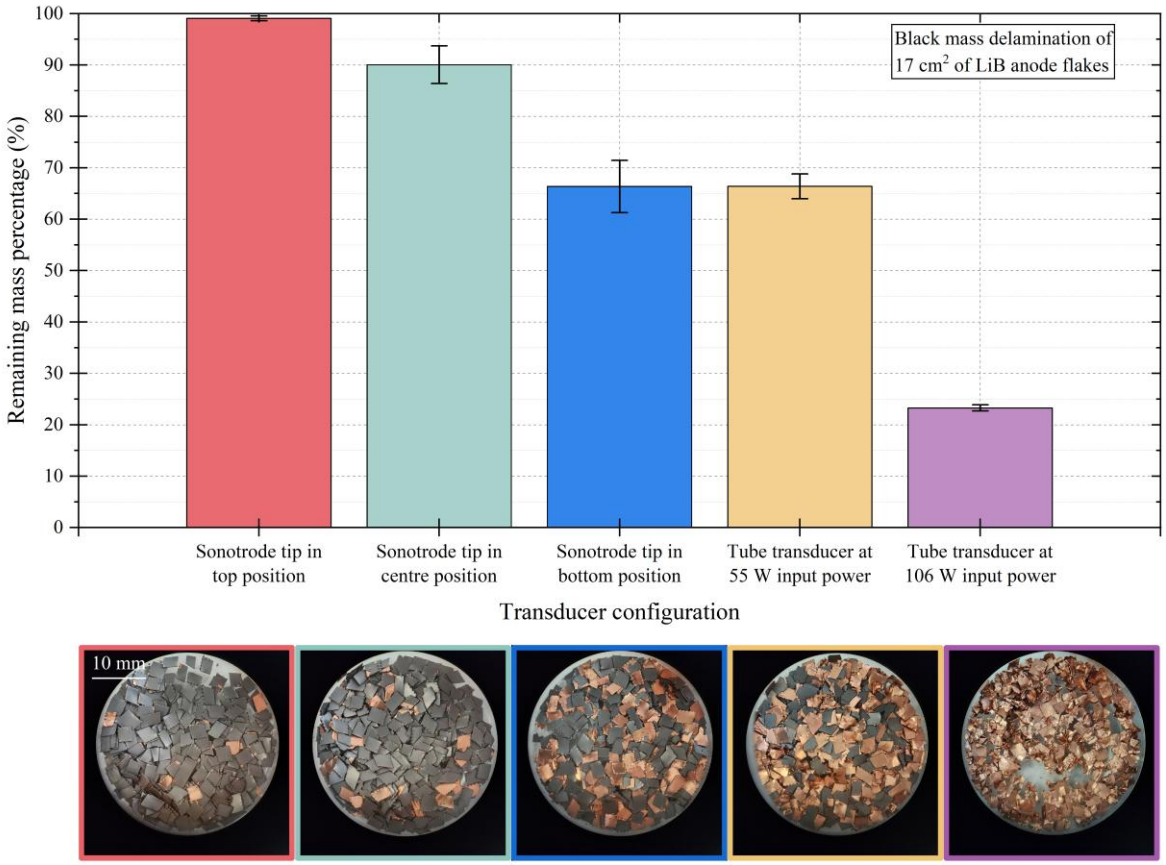

Fig. 7.11: Remaining mass percentage of LiB anode flakes with a 17 cm² effective area following 2 s sonications in each of the five configurations. Complete graphite coating removal is indicated by a dashed line at 23%. Also shown are pictures of the flake batches, post-sonication, for each configuration.

7.2.2.5 Graphite coating removal from anode flakes of 24 cm² effective area

As shown in fig. 7.9, once the total effective area of LiB anode flakes exceeds the threshold, the delamination efficiency of graphite coating gradually decreases with further increases in area. Accordingly, 24 cm² was selected as the high-loading condition to evaluate the graphite coating delamination efficiency under each of the five transducer configurations.

The delamination process for the graphite coating in this section is shown in fig. 7.12. compared with the 17 cm² anode flake sample in fig. 7.10, the delamination process of the 24 cm² flake sample exhibits an almost identical delamination behaviour. The only difference is that, owing to the larger effective area in fig. 7.12, the dispersed graphite concentration is noticeably higher at the same sonication time points.

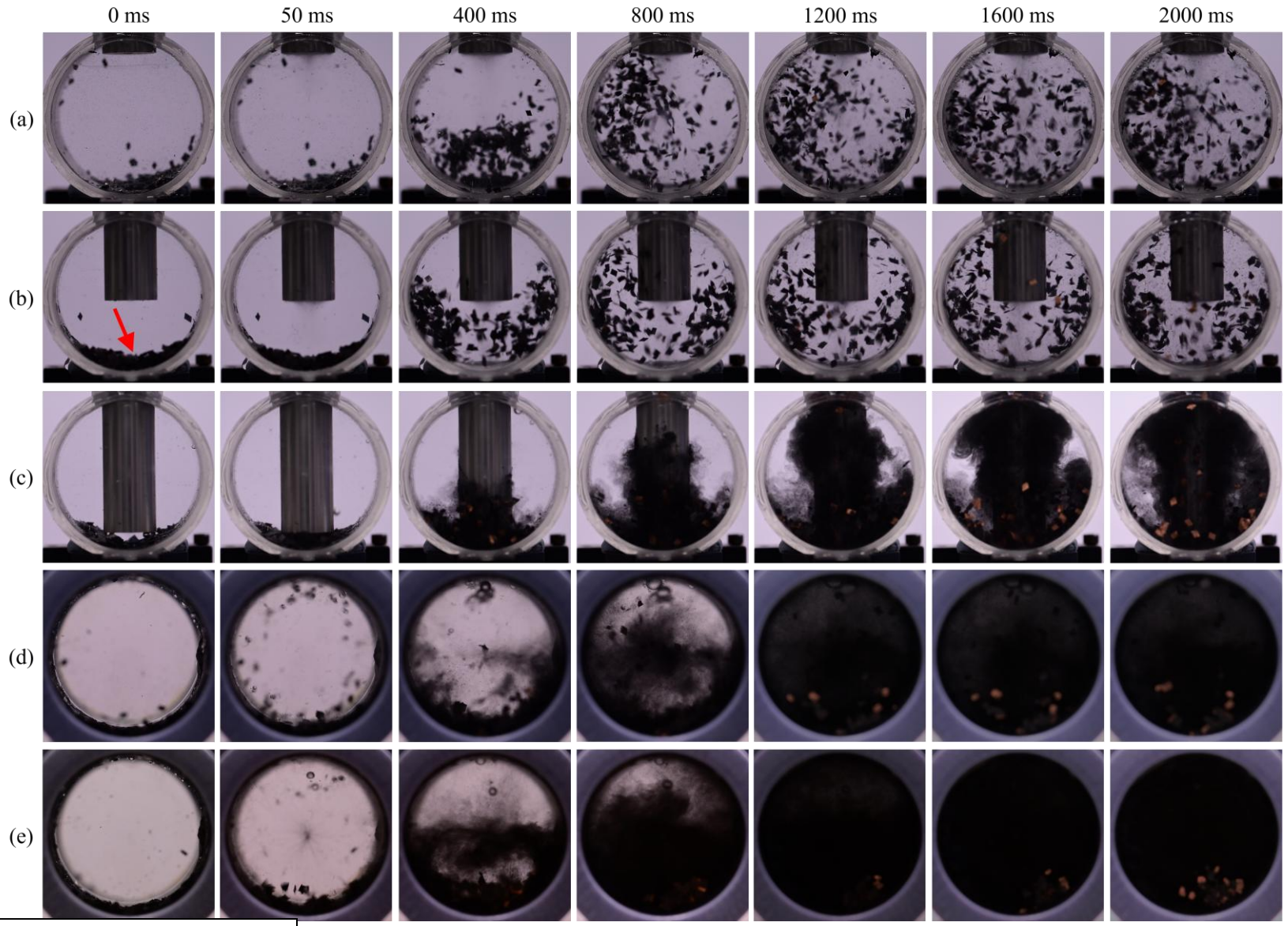

Fig.7.12. Caption on the following

Fig. 7.12: Images from a conventional recording of graphite coating delamination from 24 cm^2 of LiB anode flakes, during a 2 s sonication with the sonotrode tip in the (a) top, (b) centre and (c) bottom position, and the tube transducer at (d) 55 W and (e) 106 W input power. Scale is provided by the 20mm diameter sonotrode tip. The red arrow in (b) indicates the anode flakes settled at the bottom of the cylindrical vessel, prior to sonication.

Fig. 7.13 quantitatively compares the graphite coating delamination efficiency on LiB anode flakes with an effective area of 24 cm^2 under five transducer configurations. It also presents photographs of the recovered flake batches for each configuration. For the two arrangements with the sonotrode tip at the top and centre position, the recovered batch images are highly similar, with only minimal graphite delaminated from the flake surfaces. The corresponding remaining mass percentage were both 94%.

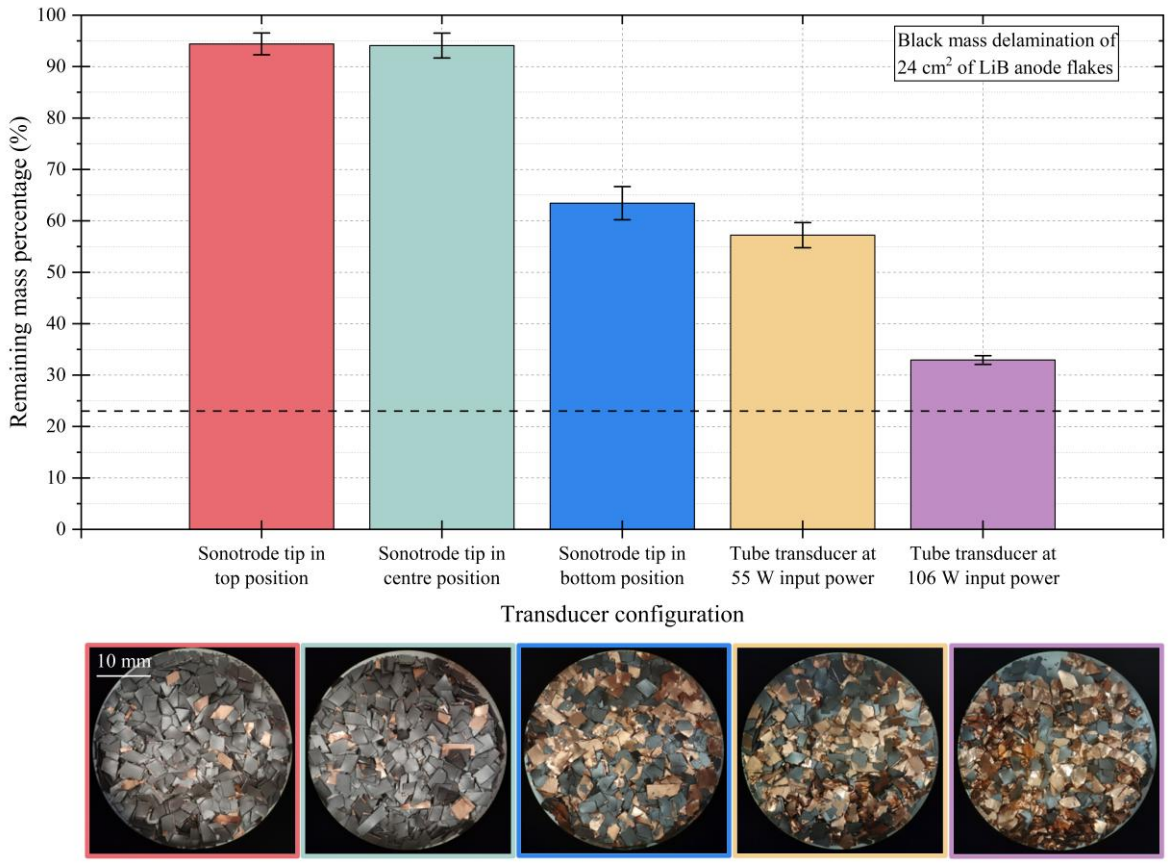

Fig. 7.13: Remaining mass percentage of LiB anode flakes with a 24 cm^2 effective area following 2 s sonications in each of the five configurations. Complete graphite coating removal is indicated by a dashed line at 23%. Also shown are pictures of the flake batches, post-sonication, for each configuration.

The remaining mass percentage further decreased to 63% compared to fig. 7.11 when the sonotrode tip was positioned at the bottom. In comparison, the tube transducer achieved an improved delamination efficiency, reducing the remaining mass percentage to 57% at 55 W input power. The graphite delamination results in the recovered anode flake images, however, showed little difference between the two transducer configurations. Increasing the input power to 106 W of the tube transducer does not achieve complete graphite delamination. Nevertheless, its 33% remaining mass percentage indicaes only a small amount of graphite is not effectively removed. This outcome is corroborated by the recovered flakes image: although the quantity of graphite flakes increased compared to fig. 7.11, the 106 W tube transducer conditions still demonstrated a significant advantage in graphite delamination over the other four transducer configurations.

7.3 Discussion

Based on the HSI and SCL results presented in chapter 6, this chapter systematically compares the performance of the tube transducer and the sonotrode in the graphite coating delamination process for LiB anode. It reveals the potential advantages of tube transducer in sonoprocessing applications by considering critical metrics including delamination efficiency, processable sample area, response to flake loaded, and citric acid pre treatment, for aged anode.

For the sonotrode delamination of an intact anode section, the constrained cavitating region at the sonotrode tip limits graphite coating liberation to an approximately 4 cm^2 circular area of the section. Similarly, the effectiveness of sonotrode delamination reduces rapidly as the vertical tip-to-anode distance is increased. We also note that two sided delamination can be achieved if the section is suspended within the liquid. For the same electrical input power of 55 W, the tube transducer removes effectively all graphite coating from both sides of the 3 cm × 3 cm section, when it is suspended within the bore. This result further confirms that active cavitation is generated throughout the tube transducer with an intensity that can be harnessed for sonoprocessing applications. Indeed, the cavitation intensity generated by the tube at both input powers and, to a lesser extent, the sonotrode tip in close proximity to the anode samples, is likely too high for this particular case study application. The pitting and puncturing of the copper foil for these configurations is not ideal for reuse and recycling purposes. Specific applications will benefit from sonication parameter optimisation, including input voltage and pulsing (pulse duration and duty cycle), to avoid overtreatment and minimise power consumption. As an engineering inference from these observations,

preservation of current-collector integrity should be treated as a co-objective of process optimisation. Puncturing or fragmentation may reduce the recovery of intact copper foil, introduce copper fines into the separated graphite, and bias the remaining-mass measurements if these fines are lost during filtration. Because copper loss was not quantified independently in the present study, the remaining-mass percentage should not be interpreted as a selective measure of graphite removal under conditions where collector fragmentation occurred. Ultrasonic exposure should therefore be optimised to achieve complete graphite removal while minimising subsequent damage to the exposed copper, rather than maximised solely to obtain the lowest remaining mass. Future work should report separate graphite-removal and copper-recovery yields, together with quantitative measurements of foil integrity and/or copper-particle-size distribution.

As described in §6.4, the primary motivation for developing the tube transducer is to enable a modular configuration in which multiple tube transducers can be integrated into a flow-through pipeline system. As the flowing liquid passes through each tube transducer, it is subjected to sonication. For such a system, an application such as LiB electrode delamination would require the use of anode flakes, rather than large intact sheets. Shredded or crushed material would be suspended in a liquid or solvent of choice for flowing through a pipe that incorporates as many tube transducers as required by the demands of the particular application.

In this work, however, all treated liquids were initially static, with all observed liquid motion due to acoustic streaming induced by the sonication. One consequence of this is that at the time of sonication initiation, flakes had settled to the bottom of the cylindrical vessel or tube transducer, under the action of gravity. For either effective area of flakes reported above, sonotrode sonications with the tip located in the top position produced negligible delamination, with only slightly more observed for when the tip was in the central position. Any delamination observed for these tip locations was due to streaming effects transporting flakes to, and through, the constrained cavitating region below the tip.

Sonotrode sonications with the tip in the bottom position meant that the constrained cavitating region at the tip was in close proximity to the flakes from the outset of the sonication. For the lower effective area of flakes, streaming effects acted to remove flakes from this region, resulting in less delamination than might be expected. For the higher effective area, however, the extra mass of flakes at the bottom appears to have suppressed the streaming induced motion, such that a greater proportion of flakes were subjected to the

cavitation within the constrained region. Indeed, this sonotrode configuration produced a similar degree of delamination as the tube transducer at the same electric input power. For the tube transducer, however, the initial location of the flakes at the bottom of the tube is not ideal for exploiting the on-axis region of highest intensity cavitation activity. Nonetheless, the tube transducer at the higher electrical input power of 106 W provided effectively complete delamination flake samples with effective areas up to 17 cm^2 - more than four times greater than the area treated by the sonotrode, on an intact section - over a 2 s sonication. Further V_{rms} measurements in Appendix D.1 showed that although the flake loaded increases the time averaged shockwave energy, it does not alter the variation tendency of V_{rms} with the input power. Consequently, it does not impose additional restrictions on power selection.

Subsequent experiments demonstrated in Appendix D.2 on aged LiB anodes highlights that pre-soaking in citric acid exerts a significant influence on the anode structure. In aged LiB samples, where water alone is insufficient in graphite delamination due to the aged nature of the LiB structure, the citric acid pre-soak allows enhanced delamination at levels comparable to production scrap LiB used throughout this chapter. The effect on recovered mass was apparent even at the lowest citric acid concentration of suggesting that even 0.1 $mol \cdot L^{-1}$ is sufficient to bring about partial softening or disruption of the binder layer. For higher concentrations and for longer immersion durations, the chemical swelling effect on binders (such as PVDF), and the complexing dissolution effect on the copper foil surface oxide layer, become more pronounced, thereby effectively weakening the interfacial bonding between the active materials and current collectors. With the original interfacial bonding substantially weakened, subsequent sonication in de-ionized water demonstrated that the anode was more readily delaminated by cavitation microjets and shock waves. This fully demonstrates that the removal of graphite coating from anode via sonication is a viable processing route even when the anode is aged, a condition that is to be expected in industrial applications.

In a flow-pipe configuration, flakes (or other particles of shredded material) may be expected to pass through the embedded tube transducers, suspended within the flowing liquid. The characterisation of the cavitation field generated would suggest that this will further enhance the performance of the tube transducer, over the static liquid results presented here, for which we relied on streaming effects to transport flakes off the bottom. In flow, flakes will enter the tube transducer distributed across the cross-sectional area of the bore, and will thereby be subjected to the distributed cavitation field, including the most intense on-axis region. Such a system will clearly require substantial optimisation, in terms of system parameters

including (but not limited to) flow rate, shred size and concentration, number and spacing of tube transducers along the pipe, as well as sonication parameters including frequency, input power, and pulsing protocols for the transducers.

7.4 Conclusion

The research of this chapter demonstrates that in the case study of graphite coating delamination on LiB anode, tube transducer sonication exhibits multiple significant advantages over conventional sonotrode. These include higher delamination efficiency, a larger effective treatment area, and enhanced stability when subjected to increased flake loaded and on aged electrodes pretreated with citric acid. Ongoing and future work will develop this technology for high throughput flow-based sonoprocessing and sonochemistry applications.

Chapter 8

Initial assessment of multiple tube transducers for flow-based sonoprocessing of lithium-ion battery anode

Chapter Overview

The tube transducer has demonstrated a broader cavitation distribution and superior sonoprocessing potential compared to a sonotrode. However, these initial experiments were conducted under static conditions, whereas the intended deployment is within a flow-pipe configuration for up-scaling and continuous processing. This chapter reports on the development of a flow-based re-circulation system using three tube transducers in series, for sonoprocessing of aged LiB anode flakes.

This chapter first evaluates the influence of flow rates in a 0.5 $mol \cdot L^{-1}$ citric acid solution on cavitation intensity within the re-circulation system at a fixed input power of 106 W per transducer. Then, the effects of three operation variables - operation duration, processing load (measured as effective area concentration) and flow rate - are examined to determine their respective effects on graphite delamination efficiency from aged LiB anode flakes. Collectively, these studies point to optimal operating parameters of the re-circulation system for the current prototype, providing an engineering basis for achieving continuous sonoprocessing.

8.1 Motivation and context

The following work in this chapter demonstrates the first testing of a flow-based apparatus. By embedding three tube transducers in series within a pipeline and using pumping to enable continuous transport of the working liquid and LiB fragments, the fragments can be exposed to sonication as they pass through the transducer bore.

In the re-circulation system, achieving stable and efficient sonoprocessing requires coordinated optimisation of multiple engineering and acoustic parameters. These include (but are not limited to) the spacing of tube transducers deployed along the pipeline, ultrasonic operating parameters (frequency, input power, and the pulse protocol), as well as operation duration of the system, concentration (processing load), and flow rate. These variables collectively determine the residence characteristic of the sample within the cavitation zone, the transport and coalescence behaviour of cavitation bubble clusters, and the maintenance of inertial cavitation.

In particular, the flow rate not only affects the residence time of the sample in the cavitation zone, but also prevents bubble coalescence and clustering by counteracting the primary and secondary Bjerknes forces, thereby ultimately influencing the cavitation intensity [235], [236]. Three papers have directly investigated the influence of flow on the cavitation generated by given sonoreactor system that has relevance to the work presented in this chapter. Some details are provided below.

Characterization of stable and transient cavitation bubbles in a milliflow reactor using a multibubble sonoluminescence quenching technique.

B. Gielen, J. Jordens, J. Janssen, H. Pfeiffer, M. Wevers, L.C.J. Thomassen, L. Braeken, T. Van Gerven. Ultrasonics Sonochemistry, vol. 25, pp 31-39, 2015.

Gielen *et al* [237] investigated the response of sonoluminescence (SL) intensity to flow rate in a 10 × 10 × 155 mm glass flow cell driven by a disc-type transducer (MP Interconsulting, type MPI-DISK-SPZT8-500X35), fig. 8.1 (a). The signal generator and power amplifier provided 46 kHz sinusoidal excitation, and the photon-counting head (PCH) was used to quantify the SL yield. The flow rate was expressed using the dimensionless Reynold (*Re*)

number. At a calorimetric power of 5 W, SL intensity increased with *Re* and reached a plateau as the *Re* approached 2000 (before the flow became turbulent, *Re* = 2300) as shown in fig. 8.1 (b). The authors attributed this trend to reduced bubble coalescence and clustering, as flow rate increased before the onset of turbulence. Once *Re* reached 2000, further suppression of coalescence did not occur, and the amount and size of the bubbles remain constant.

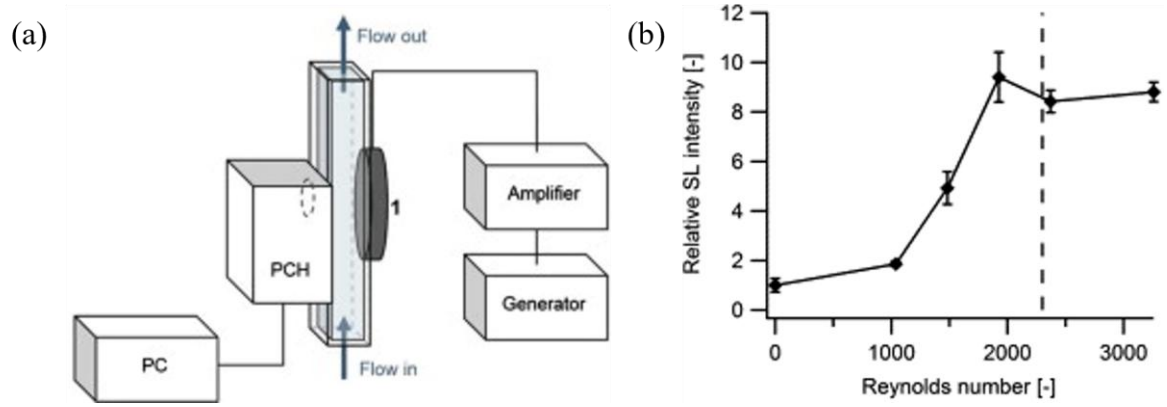

Fig. 8.1: (a) Schematic of a millireactor with a disc-type transducer bonded to the outer wall. (b) SL intensity of ultrapure water as a function of flow rate at 46 kHz. Taken from [237].

Multibubble sonoluminescence enhancement by fluid flow.

S.-I. Hatanaka, H. Mitome, K. Yasui and S. Hayashi. Ultrasonics, vol. 44, Supplement 1, pp. e435–e438, 2006.

Hatanaka *et al.* [235] investigated the influence of imposed liquid motion on multibubble sonoluminescence (SL) and sonochemiluminescence (SCL). The experimental system comprised a rectangular stainless-steel vessel with internal dimensions of 100 × 100 × 140 mm, driven by six parallel-connected Langevin-type transducers. Four transducers were mounted on the base and two on opposing side walls, as shown in fig. 8.2 (a). Directional liquid circulation at 4 $L \cdot min^{-1}$ was compared with the condition without circulation, while complementary experiments used aqueous luminol solution to examine the SCL response. At 23 kHz, liquid circulation markedly changed the dependence of SL intensity on electrical input power, fig. 7.8 (b). In the intermediate-to-high power range, where SL quenching occurred without circulation, the circulating condition produced a substantially higher SL

signal, reaching approximately three times the non-circulating value at around 100 W. The authors attributed this enhancement to fluid motion dispersing cavitation bubbles and limiting bubble coalescence and cluster formation, thereby reducing the acoustic shielding and SL quenching associated with large bubble clusters. However, the enhancement was condition-dependent: at relatively low ultrasonic powers, increasing liquid motion could reduce both SL and SCL, whereas at higher powers the SCL response increased more strongly than the SL response.

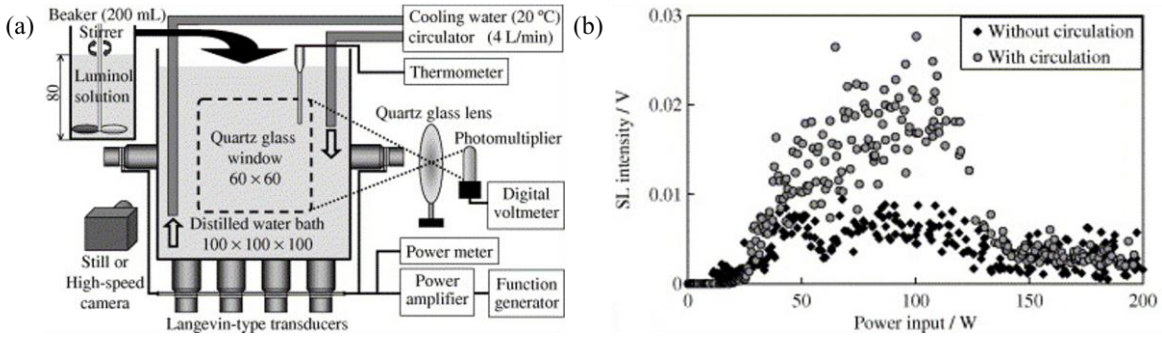

Fig. 8.2: (a) Circulationg flow system experimental setup. (b) Comparison of the flow effects on sonoluminescence (SL) at 23 kHz. Taken from [235].

Impact of high flow rates and increased viscosity of digested sewage sludge on the cavitation intensity in ultrasonic tube reactors.

J. Bandelin, T. Lippert, J. E. Drewes, K. Koch. Chemical Engineering and Processing – Process Intensification, vol. 152, Article 107925, 2020.

Bandelin *et al.* [238] investigated the combined effects of flow velocity and liquid rheology on cavitation in an ultrasonic tube reactor, fig. 8.3 (a). The 25 kHz reactor had a nominal power of 1,000 W and comprised a 2-inch stainless-steel tube with an internal diameter of 53 mm. It was incorporated into a 47 L closed recirculation system. A hydrophone positioned at the centre of the reactor was used to quantify the cavitation noise level. Water and digested sewage sludge (DS) obtained from the Freising and Traunstein wastewater-treatment plants were examined, corresponding to average flow velocities between 0 and 2.08 m s^{-1}. As shown in fig. 8.3 (b), the effect of flow was non-monotonic and dependent on the rheology of the liquid. At approximately 0.4 $m \cdot s^{-1}$, the cavitation intensity in DS was reduced by 11% relative to stationary sonication. However, flow velocities between 0.8 and 1.3 $m \cdot s^{-1}$

increased the cavitation intensity by up to 9%. The authors suggested that this local enhancement could be explained by the shear-thinning behaviour of DS, whereby increasing shear reduces the apparent viscosity and partly alleviates its cavitation-inhibiting effect. At higher flow velocities, the cavitation noise level decreased markedly in both water and DS, with reductions of up to 49%, while the signal from the more viscous Traunstein sludge approached zero at the highest flow rates. These results demonstrate that liquid motion can enhance cavitation within a limited operating range, whereas excessive flow and the associated high-Reynolds-number conditions can suppress cavitation. The authors therefore recommended maintaining sludge motion during sonication without exceeding the laminar-flow range under the conditions investigated.

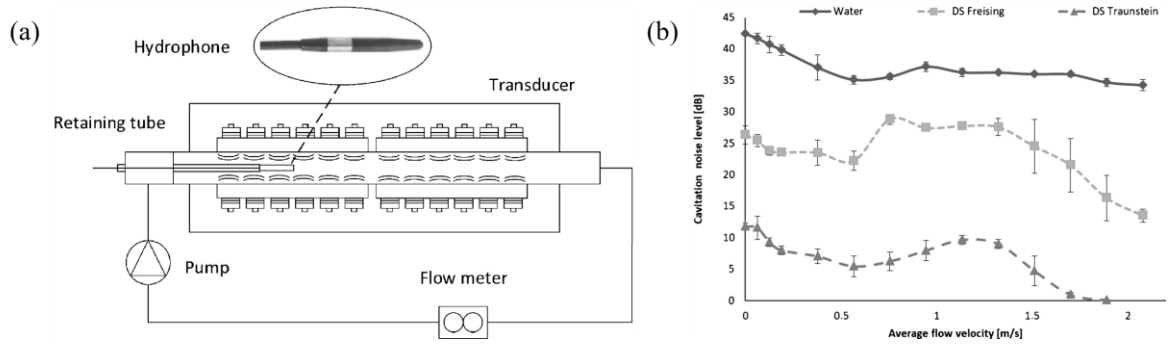

Fig. 8.3: (a) Experimental setup with a 2-inch tube reactor, hydrophone, pump, and flow meter. (b) Cavitation noise level in water and digested sludge from Freising and from Traunstein in relation to the average flow velocity. Error bars denote standard deviation. Taken from [238].

Taken together, these studies demonstrate that the effect of flow on acoustic cavitation is neither universally beneficial nor necessarily monotonic. Hatanaka et al. [235] showed that imposed liquid motion can disperse cavitation-bubble clusters and reduce acoustic shielding, but that the resulting change in SL and SCL depends on ultrasonic input power. Gielen et al. [237] observed an increase followed by a plateau in SL intensity within a milliflow reactor under nominally laminar conditions, whereas Bandelin et al. [238] reported a rheology-dependent response in a tube reactor, with limited enhancement at intermediate flow velocities followed by substantial suppression at higher velocities. Gielen et al. [237] is therefore considered here as one controlled example of a flow-induced enhancement and plateau response, rather than as a universal model for flow-assisted cavitation.

Direct quantitative comparison between these studies and the present system is not possible because they differ in ultrasonic frequency, reactor geometry, liquid properties, flow range and cavitation metric. Hatanaka et al. and Gielen et al. measured light emission through SL or SCL, Bandelin et al. [238] measured hydrophone cavitation-noise level, whereas the present study uses the filtered shockwave V_{rms}. Collectively, these studies provide a qualitative framework in which moderate flow may improve bubble dispersion and reduce clustering or acoustic shielding, while excessive flow may disrupt bubble growth and collapse or reduce residence within the active acoustic region. The net response must therefore be established experimentally for each reactor and liquid system.

This chapter describes the design and testing of a three-tube transducer re-circulation system and focuses on four key variables that may be expected to influence system performance: pulse duration, total operating time (operation duration), effective area concentration, and flow rate. The solution used in the re-circulation system for all experiments in this chapter is 0.5 mol·L^{-1} citric acid solution. In chapter 6, V_{rms} is first measured in this working solution under static conditions, within the re-circulation system before testing under three laminar flow rates. The V_{rms}-pulse duration relationship is systematically measured and compared to quantify the coupled effects of pulse duration and flow rate, on the time averaged shockwave content. Subsequently, under conditions of a fixed input power of 106 W, the effects of operation duration, effective area concentration and flow rate on the graphite delamination efficiency of aged LiB anode flakes, are investigated.

8.2 Materials & methods

8.2.1 Design and fabrication of a three-tube transducer re-circulation system

8.2.1.1 The three-tube transducer module

The re-circulation system described in this chapter consists of three tube transducers connected in series, with closed-loop circulation of the liquid achieved using a peristaltic pump (Verderflex Economy EV8000, VERDER Ltd., UK). For such a system, custom-made connections were designed as shown in fig. 8.4, with 3D geometries and cross sections, modelled in Fusion 360 (Autodesk, California, USA) and fabricated using an SLA 3D printer (Form 3, Formlabs Inc., USA). Fig. 8.4 (a) shows the pipe-to-tube connector, which connects a clear PVC pipe (OD 32 mm, ID 28.4 mm; Part No. 6051-P2, RS Components Ltd., UK) to the three-tube transducer module. An annular groove (red arrow) is machined into the

upper part to fit an O-ring (OD 65 mm, ID 55 mm; RS PRO O-ring, RS Stock No. 196-5161, RS Components Ltd., UK), providing both sealing and vibration-damping functions. Twelve M6 bolt holes are uniformly distributed around the flange for fastening, and the bottom opening is designed to insert and connect the pipe.

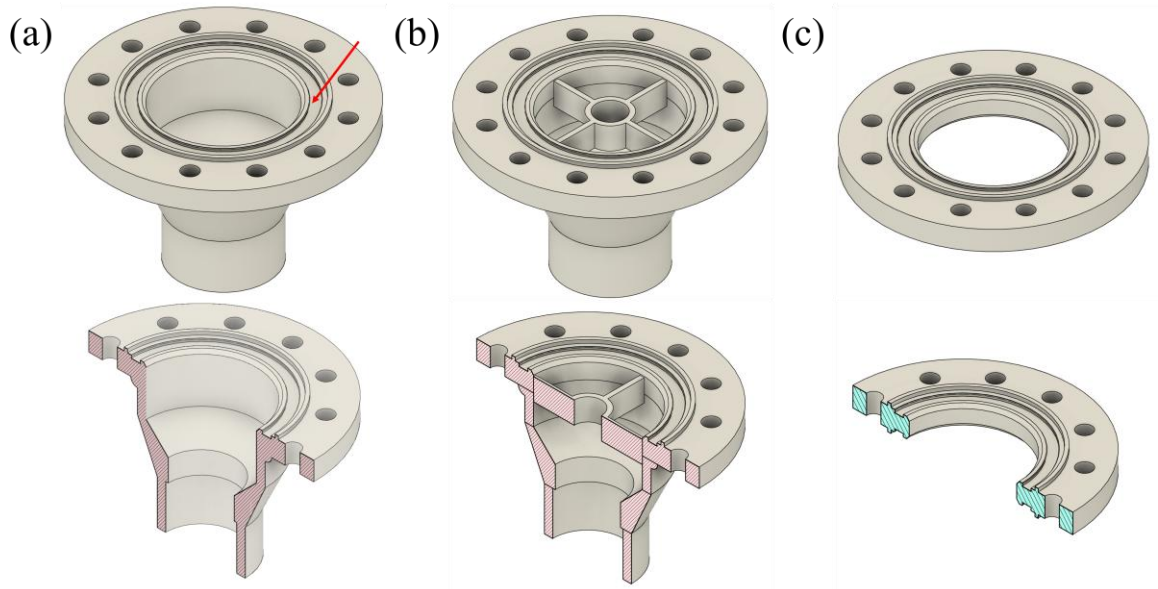

Fig. 8.4: Diagram of 3D printed tube transducer connectors, (a) Pipe-to-tube connector (the red arrow indicates the location of the annular groove), (b) Pipe-to-tube connector for fixing the swPCD, (c) Tube-to-tube connector.

Fig. 8.4 (b) presents a pipe-to-tube connector designed for swPCD installation. Based on the design in fig. 8.4 (a), a central mounting feature was added to hold the swPCD, enabling real-time collection of cavitation emission signals during operation. The remaining geometry is identical to that of fig. 8.4 (a). Fig. 8.4 (c) shows the tube-to-tube connector, which provides an end-to-end interface between adjacent tube transducers, thereby forming a modular three-tube transducer system.

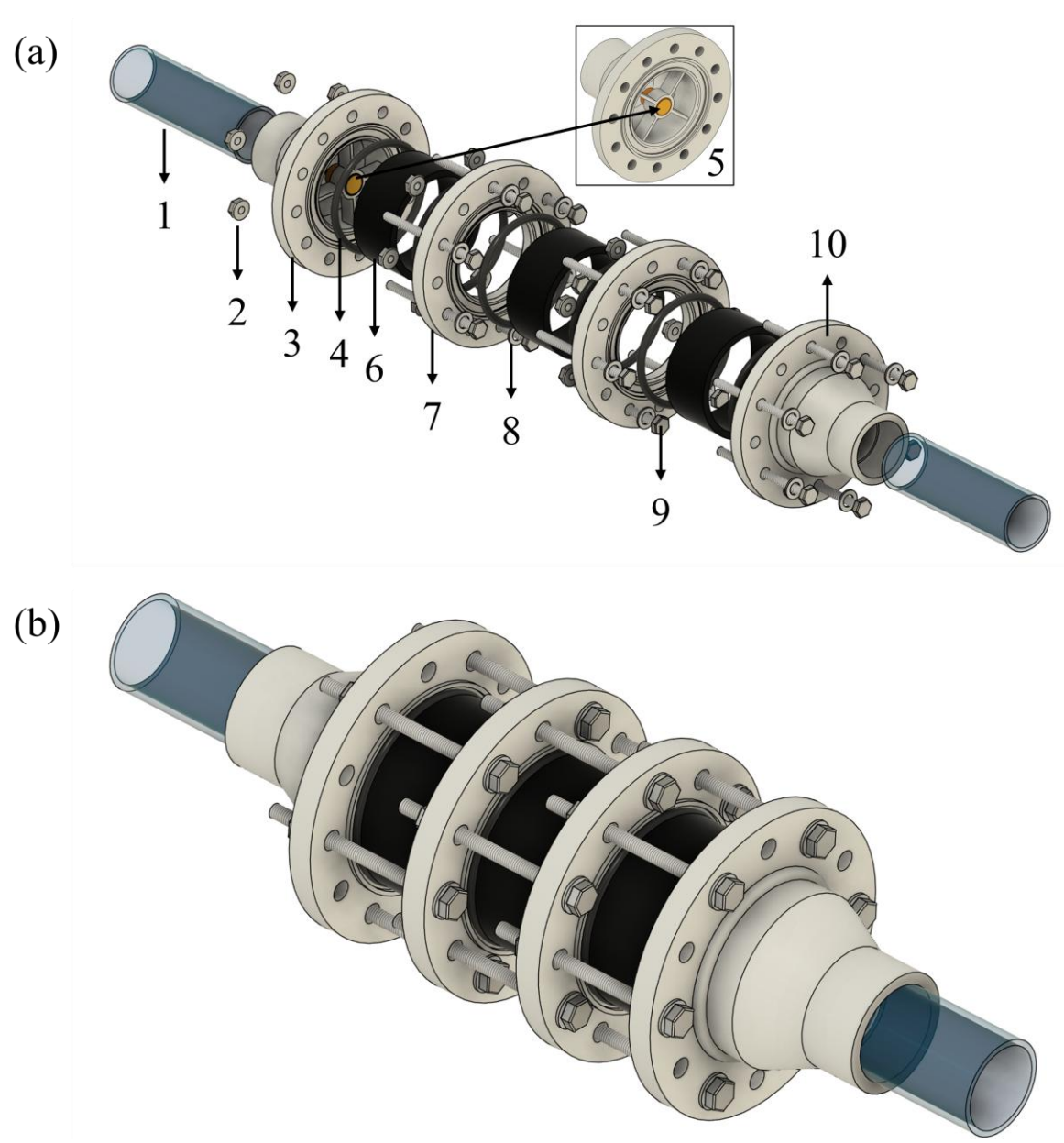

Fig. 8.5: (a) Exploded view of a three-tube transducer in series module. Components include (1) PVC pipe, (2) nut, (3) pipe-to-tube connector for fixing the swPCD, (4) rubber O-ring, (5) swPCD, (6) tube transducer, (7) tube-to-tube connector, (8) bolt washer, (9) bolt, (10) pipe-to-tube connector. (b) Mounting diagram for the three-tube transducer series module.

Fig. 8.5 illustrates the assembly approach and overall configuration of the three-tube transducer module. The geometric parameters of the tube transducer and the detailed fabrication procedure are provided in §3.5.1. Fig. 8.5 (a) shows an exploded view of the series module, in which three tube transducers are arranged sequentially along the pipe axis and connected stage-by-stage via flanged joints, forming a continuous flow pathway. This flange-based assembly provides good scalability, as the length of the sonication section can be adjusted by adding or removing transducer modules. The enlarged view highlights the

integrated swPCD mounting feature at one end of the module, enabling real-time acquisition of cavitation emission signals. Fig. 8.5 (b) presents a schematic of the fully assembled module.

8.2.1.2 The re-circulation system

Fig. 8.6 presents the 3D geometries and cross-sectional schematics of the pipe connectors used for the re-circulating the citric acid-anode flake suspension through the three-tube transducer module. Fig. 8.6 (a) shows the pipe-to-feed port connector. The two side ports are connected to the pipeline, while the upper port serves as an inlet for introducing LiB flakes into the re-circulation system. Fig. 8.6 (b) shows a 90° pipe elbow connector used to connect the three-tube transducer module to the remaining circulatory pipeline. The inner diameters of the connectors in fig. 8.6 (a)-(b) are 32 mm. Fig. 8.6 (c) shows the pipe-to-pump connector, which interfaces the pipeline with the 14 mm inner diameter rubber tubing of the peristaltic pump, thereby completing the re-circulating flow loop. The port connected to the peristaltic pump was designed with an inner diameter of 10 mm.

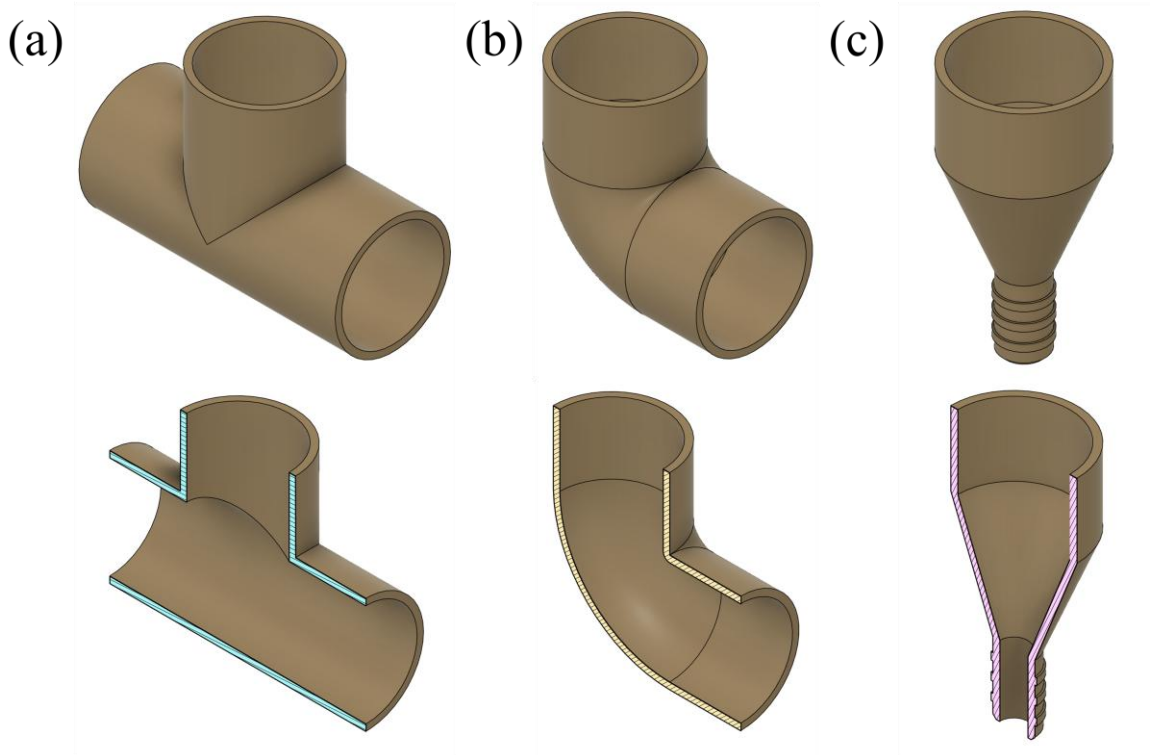

Fig. 8.6: Diagram of 3D printed pipe connectors, (a) Pipe-to-feed port connector, (b) Pipe elbow connector, (c) Pipe-to-pump connector.

The assembled re-circulation system, including drive electronics is shown in fig. 8.7. This system drives the re-circulation loop via a peristaltic pump (component 1). Given the limited maximum flow rate that the pump can provide, a horizontal or inclined configuration would cause flakes sample to deposit and accumulate within the tube bore, thereby affecting re-circulation stability. Consequently, the re-circulation system employs a vertical configuration to minimise deposition and maintain stable transport. The direction of flow is indicated with red arrows. A signal generator (component 2; DG4102, RIGOL Technologies, Beijing, China), supplied sinusoidal excitation signals at 16.79 kHz via cables depicted yellow to three +55 dB power amplifiers (component 3; 1040L, Electronics and Innovation, USA). The 50 Ω output of each amplifier was impedance-matched to the corresponding tube transducer via an impedance transformer (component 4; turns ration 1:5.7). Driving procedures and equipment specifications are as detailed in §3.6. The methodology for cavitation signal detection is described in §8.2.3.

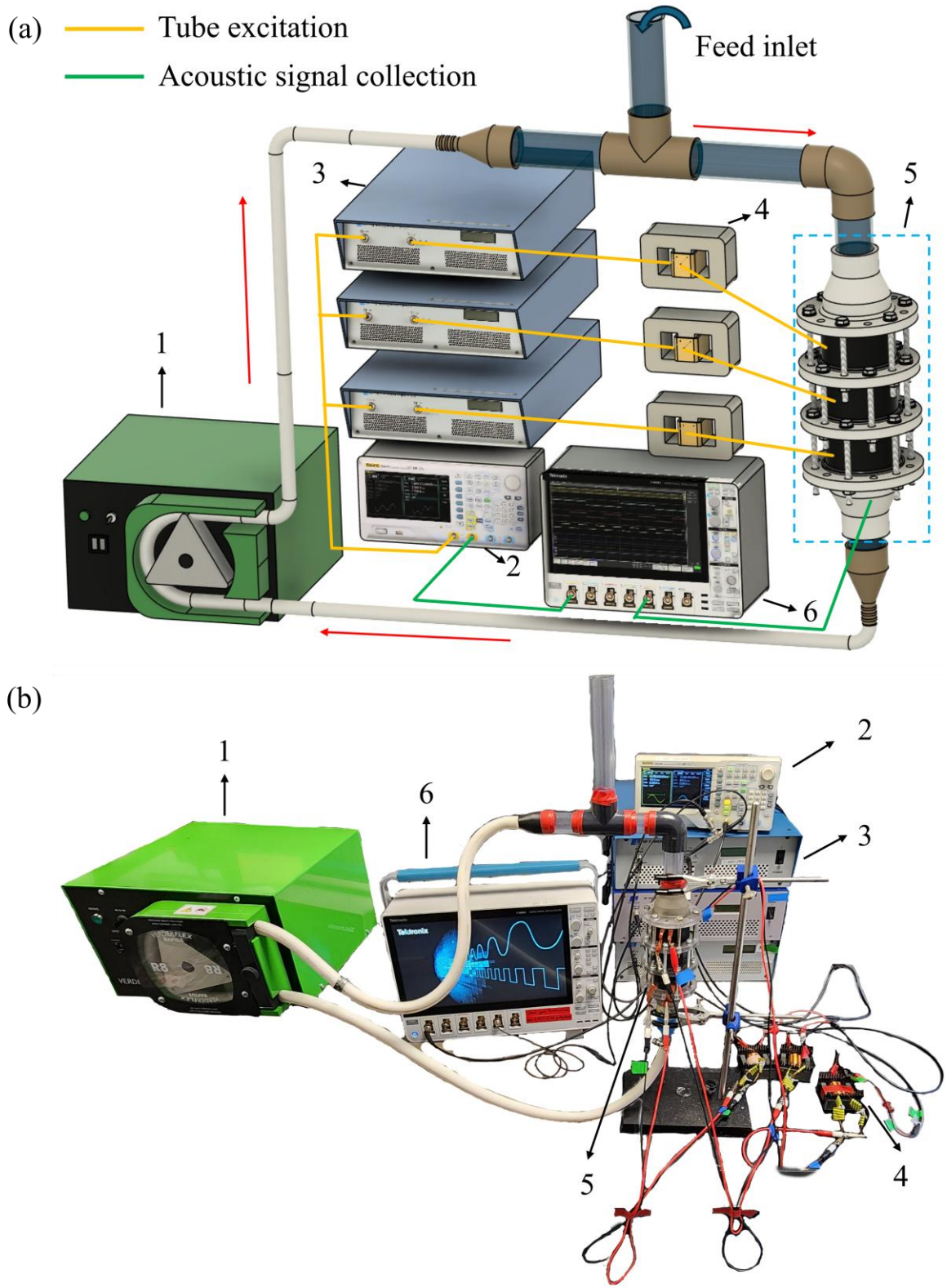

Fig. 8.7: (a) Schematic of the re-circulation system. (b)Image of the re-circulation system. Equipment items include (1) peristaltic pump, (2) signal generator, (3) power amplifiers, (4) impedance matching transformers, (5) the three-tube transducer module (blue dotted box), (6) oscilloscope. The red arrow in (a) indicates the direction of fluid flow.

As described in §6.3.1, the maximum input power for one tube transducer is 106 W, where the highest V_{rms} is achieved. Accordingly, all experiments in this chapter employed 106 W as the input power per tube transducer, giving a total power of 318 W for the three-tube transducer module. The overall volume of the re-circulation system was measured to be 900 mL.

8.2.2 Citric acid solution

As described in §3.10, citric acid solutions can react with inorganic products (e.g. lithium carbonate) formed on the surface of aged LiB anodes, thereby weaking or removing the aging layer and restoring the graphite coating to a state that is more readily delaminated. In accordance with the results of Appendix D.2 a citric acid working solution of 0.5 $mol \cdot L^{-1}$ was selected for the re-circulation system in all the experiments in this chapter. The preparation procedure and material information for the citric acid solutions are provided in §3.10.

8.2.3 Acoustic detection and filtering protocol

The green signal pathway in fig. 8.7 indicates that the signal generator provides a synchronous trigger signal whilst the tube transducer is being driven. This signal is used to trigger the oscilloscope (Tektronix 5 series, Berkshire UK) to display and store the time-domain data of the acoustic signals acquired by the swPCD, at a sampling rate of 25×10^6 $samples \cdot s^{-1}$. The recorded signals were subsequently filtered following the procedure described in §3.7, to extract components associated with cavitation activity.

The swPCD was installed using the pipe-to-tube connector shown in fig. 8.4 (b). Its placement is illustrated in the enlarged view in fig. 8.5 (a), such that the swPCD is positioned on the pipe centreline. The axial distance between the front-face of the swPCD and the plane of the tube transducer rim was 5 mm, within the assembled module. To compare V_{rms} under different pulse duration conditions, swPCD measurements were taken over 100, 200, 300, 400, 500, 1000, and 2000 ms, respectively, at an input power of 106 W, and flow rate of 0, 60, 80, and 100 $mL \cdot s^{-1}$ (see §8.2.6 for the flow rate calculation). The corresponding V_{rms} values were then calculated and compared for each pulse length.

8.2.4 Aged LiB anode flakes sample

The aged LiB anode flakes used in this chapter are identical to those employed in Appendix C. The volume of the static tube transducer configuration was measured to be 100 mL. The results in §7.2.2.3 show that the maximum effective area that could be completely delaminated within the static tube transducer configuration is 17 cm^2. To facilitate comparison between the processing capacity of the static tube transducer configuration and that of the re-circulation system, an "effective area concentration" is defined in this chapter as the area that can be effectively sonicated per unit reactor volume, given by:

$$Effective\ area\ concentration = \frac{Effective\ area}{Volume\ of\ the\ whole\ re-circulation\ system} \quad (8.1)$$

From Eq. (8.1), the maximum effective area concentration under the static tube transducer configuration (as described in §3.5) is 170 $cm^2 \cdot L^{-1}$. Accordingly, 170 $cm^2 \cdot L^{-1}$ is used as a baseline with integer multiples used to assess processing capacity under flow, specifically 170, 340, 510, 680, and 850 $cm^2 \cdot L^{-1}$.

Procedures for acquiring images of the anode flakes are detailed in §7.2.1.3.

8.2.5 Flow rate of the pump

To establish the flow rates (Q) generated by the pump, the PVC pipe was disconnected from the pipe-to-pump connector, allowing the pump to deliver citric acid solution continuously into a beaker for 5 s at a prescribed rotational speed.

The maximum flow rate achievable with the present system was 100 $mL \cdot s^{-1}$. Experimental observations indicated that aged LiB anode flakes could not be maintained in stable circulation within the pipe, tending to settle or become trapped, when the flow rate was below 60 $mL \cdot s^{-1}$. Accordingly, three flow rates of 60, 80, and 100 $mL \cdot s^{-1}$ were selected to compare graphite delamination efficiency at a fixed operation duration.

The formula for calculating the flow velocity (u) within the three-tube transducer module at different flow rates is

$$u = \frac{Q}{\pi(D/2)^2} \quad (8.2)$$

Where D (0.0556 m) is the inner diameter of the tube transducer. At flow rates of 60, 80, and 100 mL·s^{-1}, the u within the three-tube transducer module are 0.0247, 0.033, and 0.0412 m·s^{-1}, respectively.

The formula for calculating the Re number for flow inside a circular pipe [239] is

$$Re = \frac{\rho u D}{\mu} \tag{8.3}$$

where ρ (1.02×10^{3} kg·m^{-3}) is the density of the 0.5 mol·L^{-1} citric acid, and μ (1.23×10^{-3} Pa·s) is the dynamic viscosity [240]. Based on the Eq. (8.3), the Re number are 1139, 1522, and 1899, respectively, under the flow rate of 60, 80, and 100 mL·s^{-1}. All values are below the laminar-turbulent transition threshold (Re = 2300). Therefore, the flow conditions examined in this chapter can be regarded as laminar.

8.2.6 Operation duration & sonication duration

Appendix D.2 employed a "passive soaking followed by sonication" procedure to investigate graphite delamination from aged LiB anode flakes. In contrast, this chapter adopts synchronous soaking in flow and sonication: flakes are sonicated as they enter the tube bore during re-circulation, whereas in the pipe sections outside the transducer they undergo soaking. The operation duration refers to the total system operation time from start to finish. Five operation durations - 0.5, 1.0, 1.5, 2.0, and 2.5 min - were investigated to compare the graphite delamination efficiency of the system as a function of processing time.

In this chapter, the sonication duration is defined as the cumulative time for which a given sample resides within the active region of the three-tube transducer module over a specified operation duration. Let t_r denote the residence time of a sample during a single pass through the three tube transducers. In practice, t_r was obtained by starting the timer when one LiB flake entered the three-tube transducer module and stopping it when the same flake left the module. This measurement was repeated ten times to obtain a representative value at one flow rate. At flow rates of 60, 80, and 100 mL·s^{-1}, t_r was measured to be 1.8, 1.2, and 0.8 s, respectively. Let t_c denote the time required for one complete circulation through the re-circulation system; the corresponding measured values of t_c were 22.5, 15, and 10 s, respectively. Accordingly, the number of circulation cycles, N, completed within a given operation duration can be calculated using Eq. (8.4)

$$N = \frac{Operation\ duration}{t_c} \tag{8.4}$$

The cumulative sonication duration of the sample over the full operation duration is denoted by T_{SD}, and is calculated according to Eq. (8.5)

$$T_{SD} = 0.5 \cdot N \cdot t_r \tag{8.5}$$

As this study employs a pulse protocol with t_{on} = t_{off} (i.e., a 50% duty cycle), the corresponding term in the Eq. (8.5) should be multiplied by 0.5. To evaluate the differences in graphite delamination efficiency of aged LiB anode flakes at different flow rates within a specified operation duration, and to examine the underlying causes, the comparative analysis is presented in §8.3.4.

8.3 Results

The following results are presented to evaluate the influence of key operating parameters on the graphite delamination efficiency of aged LiB anode flakes with the re-circulation system, and are organised as follows:

- §8.3.1 quantitatively characterises and compares the cavitation intensity at different pulse durations using passive cavitation detection at 106 W input power, under static conditions and three flow rates.

- §8.3.2 compares graphite delamination outcomes across five operation durations using aged LiB anode flakes at 170 $cm^2 \cdot L^{-1}$ effective area concentration, 200 ms per pulse cycle, 106 W input power and 100 $mL \cdot s^{-1}$ flow rate.

- §8.3.3 performs graphite delamination experiments at five effective area densities to evaluate the maximum processing-load that can be processed under 200 ms per pulse cycle, 106 W input power, 100 $mL \cdot s^{-1}$ flow rate, and 2 min operation duration.

- §8.3.4 compares graphite delamination efficiencies at three flow rates under 106 W input power, 510 $cm^2 \cdot L^{-1}$, and 1.5 and 2 min operation durations.

8.3.1 Characterisation of cavitation activity inside the re-circulation system under pulsed sonication

Fig. 8.8 shows the dependence of V_{rms} on pulse duration for the re-circulation system operated at 106 W input power, 0.5 mol·L^{-1} citric acid concentration, and 0, 60, 80, and 100 mL·s^{-1} flow rates. The control condition is defined as the V_{rms} of static tube transducer configuration shown in fig. C.2 of Appendix C, in which the tube bore is filled with de-ionised water. Each data point represents the mean of five independent measurements acquired at the same pulse duration, with error bars indicating the corresponding standard deviation. The calculated V_{rms} quantifies the time-averaged shockwave content associated with bubble collapse within the acoustic emission signal for a given pulse duration and can be used as an indicator of inertial cavitation intensity.

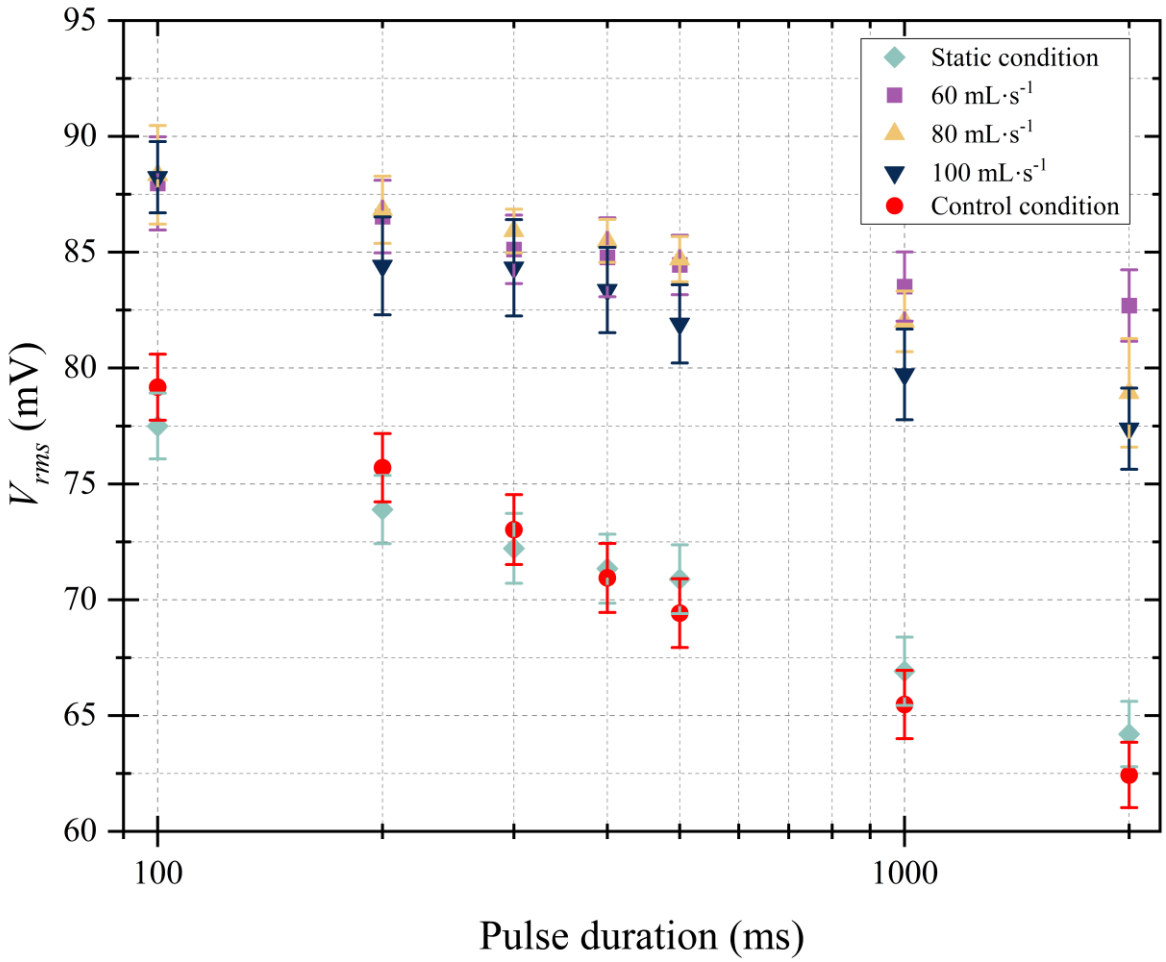

Fig. 8.8: V_{rms} measured by swPCD inside the three-tube transducer module as a function of pulse duration, under 0.5 mol·L^{-1} citric acid solution, 106 W input power, static condition, and 60, 80, and 100 mL·s^{-1} flow rates. The control condition refers to the static tube transduce model shown in fig. C.2 of Appendix C, with the tube bore filled with de-ionised water. Error bars represent the standard deviation.

As shown in fig. 8.8, V_{rms} in the re-circulation system exhibits an overall decreasing trend with increasing pulse duration. Under the static condition, the shape of the V_{rms}-pulse duration curve, the V_{rms} magnitude range and the extent of decay are comparable with control condition. This indicates that, changing the de-ionised water to citric acid solution does not significantly alter the shockwave intensity under the present conditions. This may be due to the fact that a 0.5 $mol \cdot L^{-1}$ citric acid solution is relatively similar to water in terms of key physical properties such as density and viscosity. Consequently, the cavitation dynamics are not significantly affected.

When the flow rate was increased to 60, 80, and 100 $mL \cdot s^{-1}$ (laminar flow conditions), the V_{rms} for all pulse durations shifted upwards, indicating that the introduction of flow can significantly increase the shockwave intensity. Nevertheless, the overall decreasing trend of V_{rms} with increasing pulse duration remained unchanged. The rate of V_{rms} decay varies with flow rate: at longer pulse durations (1000 and 2000 ms), V_{rms} is relatively lower at higher flow rates. Notably, at a pulse duration of 100 ms, the V_{rms} values at the three flow rates almost coincide and represent the maximum within the tested parameter range. Based on this V_{rms}-pulse duration relationship, subsequent experiments selected t_{on} = 100 ms and set t_{off} = 100 ms to form a complete pulse cycle. It can be observed, however, that there is little effect of pulse duration on V_{rms} in flow at all flow rates tested. Additionally, in the current setup, the peristaltic pump has a limited range of flow rates available and, as indicated in fig. 8.8, therefore there is limited variation in observed V_{rms} for each flow rate tested. Future work could investigate a greater variation in flow rate to assess any impact beyond what was observed in this chapter.

8.3.2 Delamination efficiency of aged LiB in flow as a function of operation duration

To evaluate the graphite delamination efficiency of the re-circulation system at different operation durations, experiments were performed at 200 ms per pulse cycle, 106 W input power, 0.5 $mol \cdot L^{-1}$ citric acid concentration, and 100 $mL \cdot s^{-1}$ flow rate. Aged LiB anode flakes at an effective area concentration of 170 $cm^2 \cdot L^{-1}$ were sonicated under 0.5, 1.0, 1.5, 2.0, and 2.5 min operation duration, and delamination performances was compared over each duration. The remaining mass percentage in fig. 8.9 is defined as the mass of anode flakes recovered from the liquid after sonication, expressed as a percentage of the initial total mass prior to sonication. The dashed line indicates a reference remaining mass value of 23%,

corresponding to complete removal of the graphite coating with full recovery of the copper foil flakes. Each bar represents the mean of five independent experiments conducted at the same operation duration, with error bars denoting the standard deviation. Because citric acid solution was used, the copper foil after sonication was prone to surface oxidation upon exposure to air, causing its colout to resemble that of graphite and affecting the observation. Therefore, no pictures are included in this section.

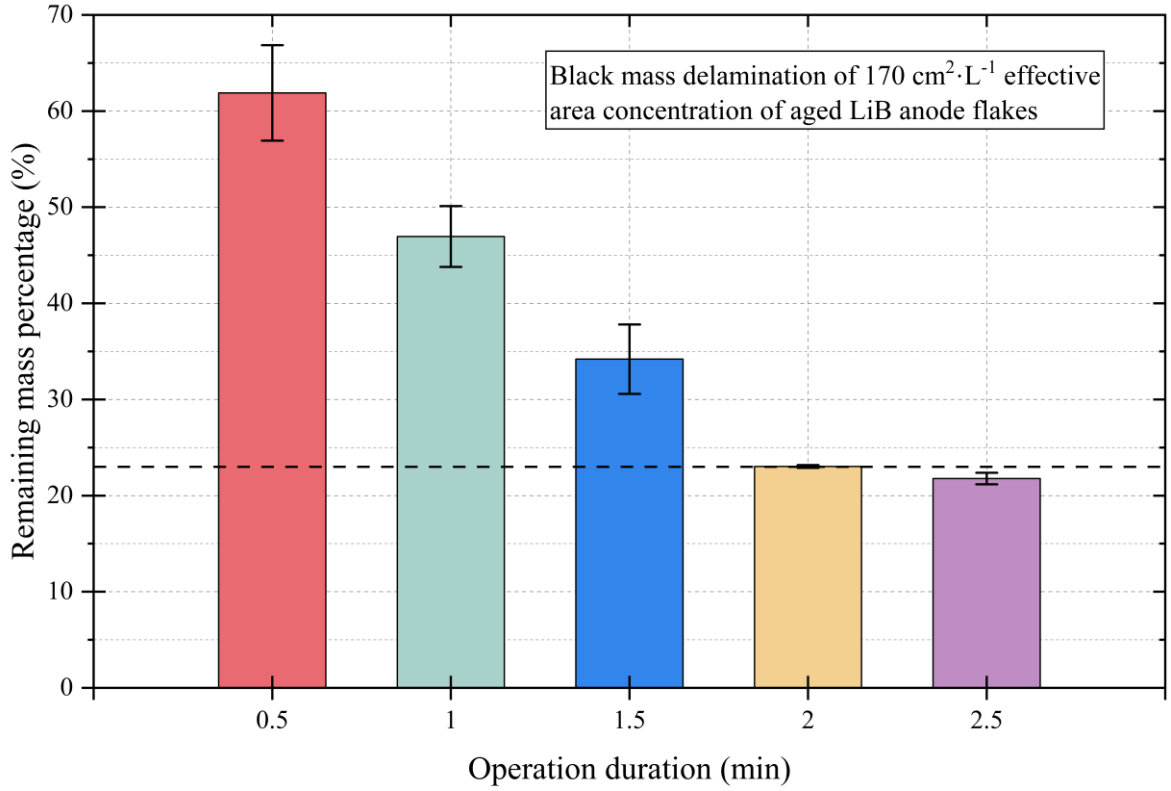

Fig. 8.9: Remaining mass percentage of aged LiB anode flakes with 170 $cm^2 \cdot L^{-1}$ effective area concentration following 0.5, 1, 1.5, 2, and 2.5 min operation durations at 200 ms per pulse cycle, 106 W input power, and 100 $mL \cdot s^{-1}$. Complete graphite coating removal is indicated by a dashed line at 23%.

As shown in fig. 8.9, the remaining mass percentage decreases overall with increasing operation duration, as would be expected. A 2 min operation duration achieves a remaining mass percentage of 23%, indicating that the graphite coating has been fully removed. When the duration is further extended to 2.5 min, the remaining mass percentage decreases to 21%, i.e., below the complete delamination baseline. This reduction is attributed to prolonged sonication causing partial fragmentation of the copper foil and the generation of fine debris. Such debris is readily lost during subsequent separation, often being removed together with graphite, thereby leading to a loss in recovered copper foil mass.

Overall, 2 min can be taken as a representative operation duration under the present operating conditions, achieving complete graphite delamination while maintaining effective recovery of intact copper foil. Both insufficient and excessive operation duration are therefore detrimental to achieving optimal overall performance.

8.3.3 Delamination efficiency of aged LiB as a function of mass loading quantity

The maximum processing load capacity for the re-circulation system was assessed by varying the effective area concentration of aged LiB anode flakes (170, 340, 510, 680, and 850 $cm^2 \cdot L^{-1}$). Other system variables were kept consistent, namely a 200 ms per pulse cycle, 2 minute operating duration, 0.5 $mol \cdot L^{-1}$ citric acid concentration, 106 W input power, and flow rate of 100 m $L \cdot s^{-1}$. The graphite delamination performance at each loading conditions was then compared.

As shown in fig. 8.10, the remaining mass percentage was consistently 23% when the effective area concentration was $\leq$ 510 $cm^2 \cdot L^{-1}$, indicating stable and complete graphite delamination at these load levels. Accordingly, the maximum stable processing load of the system can be identified as ~510 $cm^2 \cdot L^{-1}$ under the present operating parameters, which is approximately three times the maximum load of the static tube transducer configuration in chapter 7 (170 $cm^2 \cdot L^{-1}$). When the load was increased to 680 $cm^2 \cdot L^{-1}$, the remaining mass percentage rose to 26%, suggesting that a small fraction of graphite remained. At 850 $cm^2 \cdot L^{-1}$, the remaining mass percentage further increased to 34%, indicating a larger proportion of graphite that was not fully delaminated.

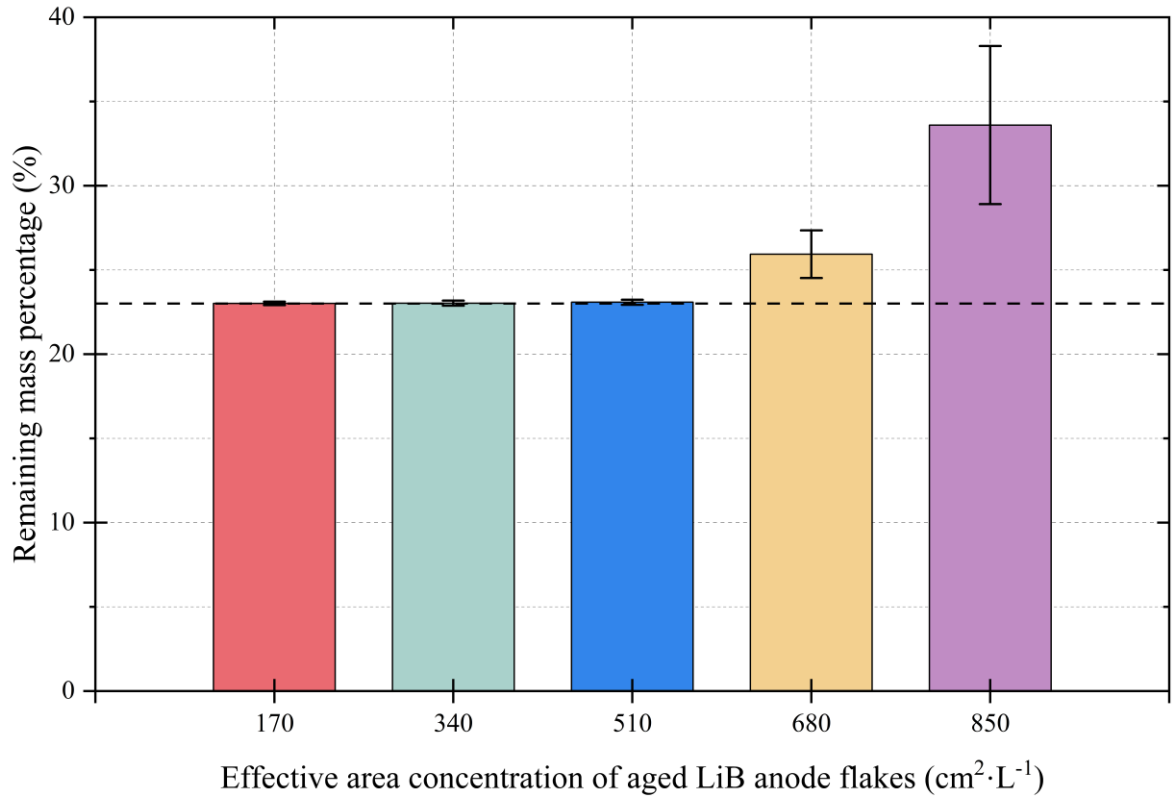

Fig. 8.10: Remaining mass percentage of aged LiB anode flakes with 170, 340, 510, 680, 850 $cm^2 \cdot L^{-1}$ following 2 min operation duration at 200 ms per pulse cycle, 106 W input power, and 100 m $L \cdot s^{-1}$ flow rate. Complete graphite coating removal is indicated by a dashed line at 23%. Also shown are pictures of the flake batches, post-sonication, for each effective area concentration of aged LiB anode flakes.

The reduction in delamination efficiency at high load is primarily attributable to a geometric bottleneck in the pipework. As shown in fig. 8.6 (c), the port of the pipe-to-pump connector that interface with the pump tubing has an inner diameter of 10 mm, which is substantially smaller than that of the main re-circulation line (clear PVC pipe; ID 28.4 mm). This abrupt reduction in cross-sectional area promotes flake accumulation at high load, leading to localised blockage. Such a blockage reduces the re-circulation throughput and consequently decreases the effective frequency with which the samples enter the transducer bore, as well as altering their residence characteristics. This limitation is a function of the peristaltic pump available for processing and not of the three-tube transducer module itself. Greater processing capabilities could be realised with the addition of a larger diameter pump system to limit cross-sectional area reductions within the system.

Observation during the experiments indicated that blockages typically occurred towards the end of the run at 680 $cm^2 \cdot L^{-1}$ effective area concentration, resulting in a reduced

delamination efficiency. When the effective area concentration was increased to 850 $cm^2 \cdot L^{-1}$, port blockage occurred after approximately 1.5 min in all five repeat experiments. Therefore, 510 $cm^2 \cdot L^{-1}$ can be regarded as the maximum stable sonication load of the re-circulation system under the current system geometry and operating parameters.

8.3.4 Delamination efficiency of aged LiB as a function of flow rate

To evaluate the impact of flow rate on graphite delamination efficiency in the re-circulation system, comparative experiments were performed at 200 ms per pulse cycle, 106 W input power and 510 $cm^2 \cdot L^{-1}$ effective area concentration with three different flow rates of 60, 80, and 100 $mL \cdot s^{-1}$.

As shown in fig. 8.11, the remaining mass percentage was 23% at all three flow rates for an operation duration of 2 min, indicating that the stable and complete graphite delamination was achieved under these parameters. Conversely, for the operation duration of 1.5 min, the remaining mass percentages in all three cases are higher than 23%, indicating incomplete delamination of the graphite. Moreover, the values vary within the range of 34-38%, with the maximum difference less than 4%, confirming that the delamination efficiency is relatively insensitive to the narrow range of flow rates that are testable with this re-circulation system.

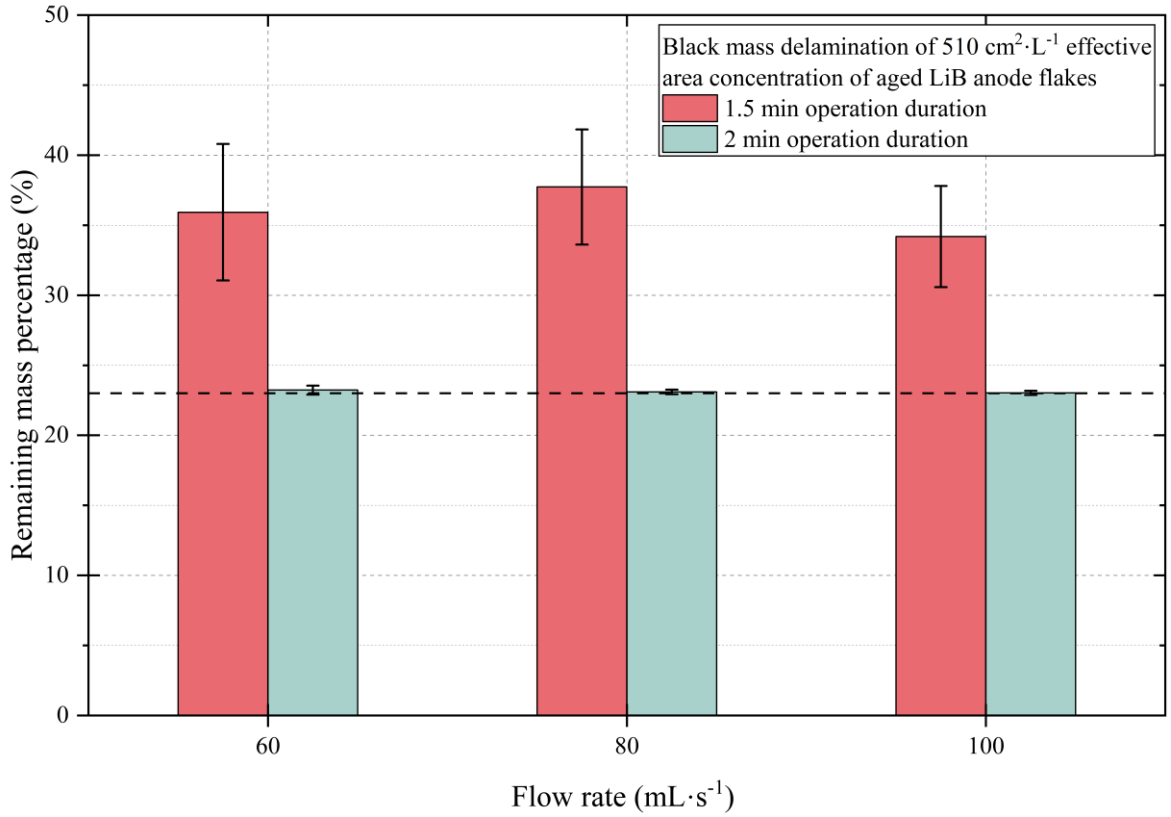

Fig. 8.11: Remaining mass percentage of aged LiB anode flakes with 510 $cm^2 \cdot L^{-1}$ following 2 min operation duration at 200 ms per pulse cycle, 106 W input power under 60, 80, and 100 $mL \cdot s^{-1}$. Complete graphite coating removal is indicated by a dashed line at 23%.

The simplified calculations in table 8.1 provide further insight into this behaviour. Although changing the flow rate alters the circulation period and the total number of circulation cycles, the cumulative sonication duration of the flakes within the three-transducer module over a total operation duration of 1.5 min is approximately 3.6 s for all three flow conditions. Consequently, the effective cavitation exposure time experienced by the samples remains the same, leading to only minor differences in delamination performance across the tested flow rates.

Table 8.1: Re-circulation characteristics and cumulative residence time within the tube transducer module at three flow rates under 1.5 and 2 min operation duration.

	Flow rate, Q (mL·s^{-1})	**Operation duration (min)**	**Residence time per pass through the three-tube transducer, t_r (s)**	**Cycle time for a sample to complete one full cycle, t_c (s)**	**Total number of circulation cycles, N**	**Cumulative sonication duration within the three-tube transducer, T_{SD} (s)**
	-		-	-	$90/t_s$	$N \cdot t_m \cdot 0.5$
1	60	1.5	1.8	22.5	4	3.6
		2			5.3	4.8
2	80	1.5	1.2	15	6	3.6
		2			8	4.8
3	100	1.5	0.8	10	9	3.6
		5			12	4.8

8.4 Discussion

Building on the cavitation characterisation and graphite delamination experiments using the static tube transducer configuration described in chapter 6 and 7, this chapter presents a proof-of-concept investigation of multiple tube transducers in a flow configuration. Using graphite delamination results of aged LiB anode flakes, the study systematically investigated the effects of pulse duration, operation duration, effective area concentration, and flow rate on delamination efficiency. The results indicate that under 200 ms per pulse cycle (t_{on} = 100 ms, t_{off} = 100 ms) and 2 min operation duration, the re-circulation system can achieve complete graphite delamination and increase the maximum stable processing load per unit volume to three times compared with the static tube transducer configuration. In addition, the performance degradation at high load conditions revealed an engineering limitation of the current prototype during transportation, providing clear direction for optimisation.

The comparative results for V_{rms} under different pulse durations and flow rates indicate that, within the conditions investigated, recirculating flow produced an overall higher V_{rms} than the static-liquid condition. However, the V_{rms} values associated with the selected pulse duration were similar at the three flow rates examined. The increase relative to the static condition is qualitatively consistent with the flow-induced dispersion of bubble clusters and reduction in acoustic shielding proposed by Hatanaka et al. [235] and Gielen et al. [237].

However, the similarity between the three flow-rate conditions does not demonstrate that the present system entered the plateau regime reported by Gielen et al., because the two studies differ in reactor geometry, ultrasonic frequency, liquid properties, flow range and cavitation metric. Moreover, Bandelin et al. [238] demonstrated that sufficiently high flow velocities can suppress cavitation in a tube reactor. The present results therefore show only that the detected V_{rms} was relatively insensitive to flow rate over the limited range of 60-100 mL·s^{-1}, rather than establishing a universal plateau response. High-speed imaging was employed to examine cavitation within the static tube-transducer configuration, but the present recirculating system does not provide sufficient optical access for equivalent observations under flow. Future reactor designs incorporating optical windows could therefore be used to examine the underlying bubble dynamics and test the proposed interpretations directly.

An overall decrease in V_{rms} was observed as the excitation duration increased, with the 100 ms condition producing the highest mean V_{rms} within the investigated range, although the differences between excitation durations under flow were relatively modest. The selection of t_{on} = 100 ms and t_{off} = 100 ms should therefore be regarded as the preferred condition within the tested range rather than as a generally applicable optimum. Furthermore, because all processing experiments employed $t_{on} = t_{off}$, the separate effects of on-time, off-time and duty cycle were not isolated. Yusuf *et al.* [241] demonstrated in a static ultrasonic nitrogen-fixation system that varying t_{off} at fixed t_{on} can substantially affect process performance. Although that result does not provide a direct quantitative prediction for the present flow-based delamination process, it identifies off-time as an additional optimisation variable. Future experiments should therefore vary t_{on} and t_{off} independently while controlling the total ultrasonic on-time or delivered energy.

Increasing the operation duration from 0.5 to 2 min progressively reduced the remaining-mass percentage, which reached the nominal complete-delamination baseline of 23% after 2 min. Further treatment to 2.5 min reduced the remaining mass to 21%. Together with the wrinkling and pitting observed after prolonged exposure in Chapter 7, this supports fragmentation of the exposed copper collector and loss of fine copper-containing debris during separation as a plausible engineering interpretation. Copper loss was not quantified independently, however, and the remaining-mass percentage is no longer a selective measure of graphite removal once collector fragmentation occurs. The 2.5 min result should therefore be interpreted as evidence that exposure beyond that required for delamination may compromise collector integrity, rather than as a direct measurement of copper loss. Accordingly, exposure should be optimised to stop when graphite removal is complete rather

than maximised. Future work should report separate graphite-removal and copper-recovery yields, together with measurements of foil integrity or particle-size distributions.

A remaining-mass percentage of 23% was maintained at effective area concentrations up to 510 $cm^2 \cdot L^{-1}$, whereas the values increased to 26% and 34% at 680 and 850 $cm^2 \cdot L^{-1}$, respectively. Thus, 510 $cm^2 \cdot L^{-1}$ represents the maximum stable loading only for the current system geometry and operating conditions. Re-circulation repeatedly transported the flakes through the three active regions and avoided the persistent bottom settling observed in the static tube configuration. A more uniform presentation of the flakes to the cavitation field is therefore a plausible explanation for the increased stable loading, but spatial dispersion and individual flake trajectories were not measured.

Moreover, the static and re-circulating experiments were not fully matched: they differed in the number of active transducers and total electrical input power, liquid medium, material condition, exposure protocol and operation duration. Consequently, the approximately threefold increase relative to the static configuration should be attributed to the complete three-tube re-circulating system rather than to flow-induced dispersion alone. It demonstrates increased stable loading under the selected system-level conditions, but does not establish a threefold improvement in intrinsic acoustic efficiency or volumetric throughput.

No clear systematic difference in delamination was resolved between flow rates of 60 and 100 $mL \cdot s^{-1}$. After 1.5 min, the remaining-mass percentages were within the relatively narrow range of 34–38%, whereas all three flow rates produced a value of 23% after 2 min. The simplified residence-time calculation gives cumulative nominal sonication durations of approximately 3.6 s after 1.5 min and 4.8 s after 2 min at each flow rate, which may partly explain the similar delamination outcomes. This calculation nevertheless assumes that the measured transit time is representative of all flakes, that pass-to-pass trajectories and cavitation exposure are comparable, and that the 50% duty-cycle correction adequately represents the interaction between each flake and the pulsed field. It does not account for velocity profiles, flake slip and rotation, local recirculation, blockage or temporal variations in cavitation activity. Furthermore, the Reynolds numbers of 1139-1899 describe nominal bulk flow within the uniform tube bore; peristaltic pulsation and abrupt contractions elsewhere in the loop may generate local disturbances. The results therefore demonstrate limited sensitivity to flow rate only within the operating window and measurement

resolution of the present prototype, rather than general independence of delamination from flow rate.

The downward vertical arrangement was selected primarily to maintain transport stability with the available peristaltic pump. A horizontal or inclined arrangement increased the tendency of flakes to accumulate near the lower pipe-to-tube connections, whereas downward flow combined pumping with gravitational transport and maintained more reliable re-circulation. This choice may also shorten the residence of individual flakes within the active regions. Upward flow could, in principle, oppose gravitational settling and alter the residence-time distribution, but the present pump could not transport the flakes reliably in this orientation. A higher-capacity pump would enable a controlled comparison between upward and downward operation. Whether upward flow improves delamination remains a design hypothesis rather than a demonstrated method of reducing operation duration.

The transmitting-wall and converging-wave flow reactors reviewed in §1.5.2.1 and §1.5.2.3 employ externally mounted transducer arrays to generate distributed or centrally concentrated cavitation. Some of these designs provide high processing capacities but require substantial installed electrical power and coordination of multiple transducers. By contrast, each tube-transducer module uses a single inward-radiating piezoceramic tube, and the present experiments demonstrate that three independently driven units can be connected in series without phase synchronisation between a large external array. This supports the modularity of the design and the feasibility of distributed electrical driving. However, the present results do not establish lower specific energy consumption, linear scaling of processing capacity, industrial throughput or continuous single-pass performance. Direct energy-efficiency comparison with the larger reactors reviewed in Chapter 1 would therefore be premature.

Finally, the reduction in performance at high loading was associated with a geometric transport bottleneck rather than an observed limitation of cavitation generation by the three tube transducers. Flake accumulation occurred at the pipe-to-pump connector, where the internal diameter decreased from 28.4 to 10 mm. Blockage generally developed towards the end of experiments at 680 $cm^2 \cdot L^{-1}$ and after approximately 1.5 min in all five repeat experiments at 850 $cm^2 \cdot L^{-1}$, reducing re-circulation throughput and the frequency with which flakes entered the active regions. This repeated observation identifies a direct engineering priority for the next prototype: larger pump tubing and connectors, together with smoother transition geometries, should be tested to minimise abrupt contractions. Subsequent

experiments would then be required to determine whether removal of this bottleneck increases the stable processing load or reveals a new limitation associated with cavitation exposure, pumping or solids handling.

8.5 Conclusion

This chapter develops a re-circulating system comprising three tube transducers and evaluates its continuous-processing capability using graphite delamination from aged LIB anode flakes as the performance metric. At 106 W input power, the system reproducibly achieved complete graphite delamination under a 200 ms per pulse cycle (t_{on}:t_{off} = 50:50) and an operation duration of 2 min, while increasing the maximum stable processing load to 510 $cm^2 \cdot L^{-1}$ (approximately three times that of the static tube transducer configuration). Future work will focus on further optimisation of the re-circulation system to increase the maximum achievable load and to extend its application to other ultrasonic processing tasks, such as the recovery of metallic silver from fragmented photovoltaic panels.

Conclusions

The following points summarise the main findings of this thesis. This is followed by a brief discussion that links the experimental results from chapter 4 - 8 to the literature, industrial applications and future research.

- The sonotrode is amongst the most extensively used high-power ultrasound devices in industry. However, studies characterising its cavitation intensity and cavitation dynamics in different solvents are limited. In §4.3.1, sonotrode-induced cavitation in Ethaline-DES was characterised using a combination of high-speed imaging (HSI) and acoustic detection. The primary bubble cluster generated under the horn tip undergoes periodic collapse at subharmonic frequencies of f_0/m (where m is an integer), with m increasing with input power. Based on the acoustic signals acquired via swPCD, a transitional power range with an indeterminate value of m (corresponding to higher input powers) can be identified. The time-averaged shockwave content, V_{rms}, exhibits a local minimum within this power range (§4.3.2). Consistently, HSI shows that the bulbous cavitation structure retracts towards the tip at higher input powers. Based on the acoustic and optical evidence, input power conditions suitable for E-waste recycling applications were identified.

- Dual-perspective HSI from §4.3.4 reveals a direct link between technology critical metal (TCM) delamination from PCBs and the cavitation jets and shockwaves. These effects induce initial pitting on the TCM surface, exposing the underlying copper layer. Subsequent leaching of the copper layer by Ethaline creates conditions for direct interaction between cavitation bubble and surface, causing the TCM to delaminate from the PCB substrate. The introduction of acoustic cavitation can increase the delamination rate by more than 30 times compared to passive etching. To address the high viscosity limitation of Ethaline, a strategy of adding de-ionised water was employed in §5.3.1. This yielded cavitation intensity at the same transducer peak-to-peak amplitude, further doubling the delamination efficiency, demonstrating a strong synergistic effect between solvent properties and the ultrasonic parameter optimisation.

- To address the imbalance between cavitation intensity and coverage in existing ultrasonic transducers, a radially poled, inwardly focused tube transducer was developed as a novel power ultrasound source. Characterisation of the cavitation

acoustic signals from the static configuration in §6.3.1 demonstrated that the backing conditions significantly influence the cavitation intensity within the tube bore, thereby identifying an optimal configuration based on air-backed condition. Combined results from §6.3.2 about HSI and §6.3.3 about sonochemiluminescence (SCL) demonstrate that the tube transducer achieves cavitation coverage across the entire bore, with cavitation intensity reaching levels comparable to the near-field beneath the sonotrode tip. In contrast to sonotrode cavitation however, which is largely confined to the vicinity of the tip, the tube transducer offers greater engineering advantages in expanding the effective treatment volume and enabling flow-based configuration.

- The capability of the tube transducer for LiB anode graphite delamination and suitability for continuous processing were demonstrated in §7.2, thereby establishing the performance limits of the prototype system. In comparative tests with a static configuration of equivalent geometric dimensions, the tube transducer achieved overall higher graphite delamination efficiencies than sonotrode. Acoustic detection in Appendix D.1 was used to quantify the effect of graphite powder released during delamination on cavitation intensity. The results indicate that it does not alter the selection of the optimal input power whilst variations in nucleation conditions can enhance cavitation intensity. Targeting continuous industrial applications, a three-tube transducer series re-circulation system was constructed and operated under pulsed excitation. An optimal single excitation duration was identified from the V_{rms}-pulse duration relationship in §8.3.1. Complete graphite delamination was achieved within a total operating duration of 2 min, and the maximum load processing capacity was increased to three times that of the static configuration.

Chapter 1 outlines the fundamental concepts and key physico-chemical effects of acoustic cavitation, establishing the conceptual framework used in subsequent chapters. It presents a critical review of cavitation monitoring methods and, in combination with the acoustic measurement research by Yusuf *et al* [34] on the relationship between cavitation intensity and input power, lays the methodological foundation for representing inertial cavitation intensity using V_{rms}. Finally, this chapter summarises the structural trade-off between cavitation intensity and distribution in commercial power ultrasonic devices from the perspective of reactor configuration, promoting the subsequent motivation to address this conflict using a novel tube transducer.

Chapter 2 focuses on the environmental risks posed by E-waste (particularly PCBs and LiBs) and the value of the TCMs they contain. It provides a systematic overview of mainstream recycling routes and highlights the limitations of traditional recycling methods in terms of energy consumption, selectively recovery and pollution control. This chapter further emphasises that DESs offer advantages in terms of low pollution and potential selective recovery however, their high viscosity limits mass transfer and dissolution kinetics, making it difficult to achieve high-efficiency recovery. This motivates the engineering research question addressed in this thesis - using power ultrasound as a processing intensification tool to assist green solvent based recycling.

Chapter 4 and chapter 5 focuses on Ethaline-DES and first determines the optimal input power for maximum cavitation intensity using passive cavitation detection. Dual-perspective HSI was then used to elucidate the delamination mechanism of TCM from the PCB surface. The impact of the cavitation jet can induce initial pitting on the metal surface, thereby causing the TCM layer to delaminate from the substrate in the from of fragments. The introduction of power ultrasound significantly improved the delamination efficiency compared with passive immersion. Further, the cavitation intensity was enhanced and the delamination efficiency was more than doubled by diluting Ethaline with de-ionised water to reduce the solvent viscosity. Demonstrates the application potential of acoustic cavitation combined with DES for green and efficient recovery of TCMs.

Chapter 6 establishes the first systematic characterisation of a radial polarisation tube transducer using a static configuration. The influence of external backing conditions on cavitation intensity within the tube bore is clarified, and an optimal configuration is determined accordingly. Subsequently, the tube transducer and sonotrode were compared under comparable geometries using HSI and SCL methods, revealing the full-range distribution of cavitation within the tube bore and the more active characteristics in the central axial region, thereby demonstrating its feasibility as an ultrasonic source in a flow system.

Chapter 7 taking the delamination of graphite from LiB anodes as a case study to translate the cavitation distribution advantages into material-processing performance. Under comparable geometric and power conditions, the delamination behaviour of the static tube transducer configuration and a commercial sonotrode is systematically compared for both sheet and flake LiB production waste samples, with their respective advantages and limitations discussed in terms of processing efficiency, effective sonication area, and

sensitivity to processing load. Concurrently, a combined citric acid pre-soaking and sonication protocol is introduced for aged anodes to evaluate the contribution of aged layer weakening to delamination efficiency. Supplementary acoustic tests are conducted to discuss the influence of released graphite particles on cavitation intensity and parameter selection strategy, thereby laying the groundwork for the flow approaches in chapter 7.

Chapter 8 addresses the demands of continuous and high throughput processing by developing a prototype three-tube transducer series re-circulation system and introduced pulsed excitation under flow conditions as a means of optimising the effective cavitation duration. First, the V_{rms}-pulse duration relationship was compared under static and laminar flow conditions to identify representative pulse parameters. The effects of operation duration, effective area concentration, and flow rate on graphite delamination efficiency were then systematically evaluated, establishing the stable operating window and performance limits of the current prototype. Finally, localised blockage caused by sudden constrictions in the piping geometry was identified as the dominant failure mode under high effective area concentration, thereby providing a clear direction for future scale-up and engineering optimisation.

This study demonstrates that a series connected, re-circulation system based on the novel tube transducer has strong potential as a tool for the environmentally friendly and efficient recycling of E-waste. To further optimise this system, the first step is to address blockage failures caused by sudden reductions in pipe diameter within the series system. This can be achieved by increasing the bore sizes of the pump ports and connectors, and by optimising the geometry of the transition sections to raise the upper limit of the effective area concentration that can be processed. Secondly, parameters such as the duty cycle of the pulse signal, solvent temperature and oxidant concentration can be incorporated into the experimental design, and the effects of these optimisation parameters on cavitation intensity can be evaluated using acoustic detection methods. Building upon the validated concept of modular integration of the tube transducer, future work should involve conducting feasibility assessments for a wider range of E-waste fragments and solvent systems, whilst verifying and iteratively optimising the flow system structure against engineering criteria such as continuous operation, maintainability and scalability.

Appendix A

Matlab Scripts

This section describes the MATLAB scripts used in this thesis. The MATLAB scripts used to filter the acoustic data acquired by the swPCD, to extract the acoustic spectra from the swPCD data, and to perform greyscale processing and calculate greyscale values for the SCL images are all presented in the relevant sections.

A. 1 Matlab filtering and frequency codes

The filtering Matlab codes used are described in § 3.7.3 Filters used for acoustically detected data. Comments are added to the codes for easy understanding.

```
%% load data

close all
clear all

load('filename.mat');

t = time;
y = data;
L = length(data);
dt = t(2,1)-t(1,1);

fs = 1/dt;
f0 = 16.79e3;
y = y * 1000; % converting to mV

Fcut1 = fl; %lower frequency threshold
Fcut2 = 4e6; %upper frequency threshold

%% low-pass filter at 10 MHz to remove high frequency noise

h_lpf = fir1(2^9, 10e6/(fs/2));
slpf1 = convn(y, h_lpf', 'same');

FS = fs;

%% high-pass filter at 50 Hz to remove line noise

h_hpf = fir1(2^9, 50/(fs/2), 'high');
slpf1y = convn(slpf1, h_hpf', 'same');
```

```
%% high-pass filter at f0 Hz to remove line noise

h_hpf = fir1(2^9, f0/(fs/2), 'high');
slpf1y = convn(slpf1, h_hpf', 'same');

%% bandpass filter across range of swPCD sensitivity

h_bpf = fir1(2^9, [Fcut1 Fcut2]/(FS/2), 'bandpass');
sig1 = convn(slpf1y, h_bpf', 'same');

%% Plot filtered signal

figure ()
plot(t*1e6,sig1,'r','LineWidth',1.5);
grid on;
set (gca, 'FontName', 'Times New Roman');
set (gca, 'FontSize', 10);
set(gca,'FontWeight','bold');
xlabel('time (\mus)');
ylabel('Voltage (mV)');
title('Filtered time domain data');

%% Frequency Spectrum of signal

[SLPF1 w1] = freqz(sig.*blackman(length(rms(sig))),1,2^21,fs);
figure('unit','normalized','position',[0.1 0.1 0.8 0.8]);
subplot(2,1,1);
hold on;
plot(w1/1e6,db(abs(SLPF1)/max(abs(SLPF1))),'LineWidth',1);
grid on;
xlabel('Frequency(MHz)');
ylabel('Magnitude(dB)');
title('Frequency response of acoustic emission');
```

A. 2 Calculation of SCL image greyscale

```
clear all
close all

%% read file

filename_1='*.png';

%% show information of the figure

imfinfo(filename_1);

%% read colorful image

img_1=imread(filename_1);
```

```
%% show colorful image

imshow(img_1);

%% transfer to greyscale image

imgray_1=rgb2gray(img_1);


figure(1)
imshow(imgray_1);
impixelinfo
hist_im_1=imhist(imgray_1);

figure(2)
b=bar(hist_im_1,'blue') % calculate histogram
b.FaceColor = "#0072BD";
b.EdgeColor = "#0072BD";

alpha(0.5);
legend('Input power = * W');
xlim([0,255]);
xlabel('Luminous Intensity')
ylabel('Number of Pixels')
grid on
hold off
```

Appendix B

B.1 Shock wave content with the emission signal overall measured input powers in four different liquids

The appendix contains material adapted from the co-authored publication: *Observation of cavitation dynamics in viscous deep eutectic solvents during power ultrasound sonication*. The candidate was the second author of this work and contributed to the experimental work and data processing. The material is included here as supplementary context for the thesis and is clearly distinguished from the main thesis chapters.

Journal Paper
Observation of cavitation dynamics in viscous deep eutectic solvents during power ultrasound sonication. Ben Jacobson, **Shida Li**, Paul Daly, Christopher E. Elgar, Andrew P. Abbott, Andrew Feeney and Paul Prentice.
Faraday Discussions, vol. 253, p. 10.1039, 2024.

In §B.1, filtered acoustic data are presented for four liquids as the power is increased from 20% to 70%. The root mean square voltage (V_{rms}) of the signals acquired during each sonication is used to quantitatively characterise the time-averaged shock wave content in the acoustic signal. Fig. B.1 shows the mean V_{rms} from five sonications, with error bars indicating the standard deviation. Previously, Yusuf *et al* [34] reported this method in detail in water under a 450 W Branson sonotrode, as well as in Ethaline-DES, with the aim of optimising cavitation output for TCM layer delamination from PCB [242].

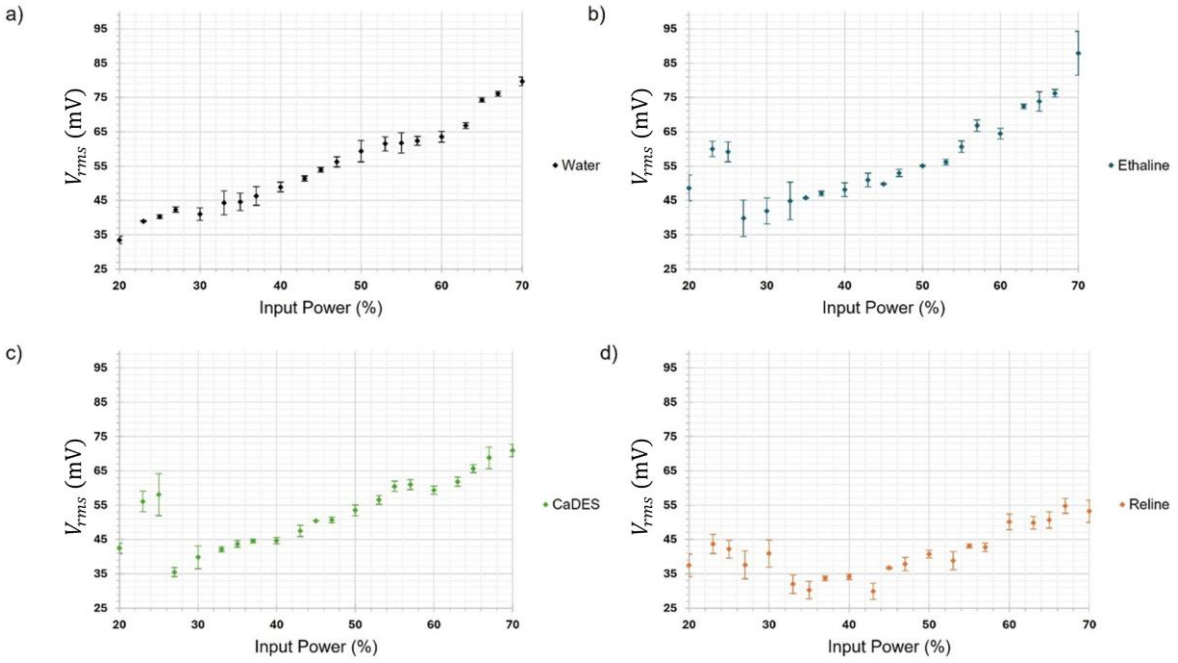

Fig. B.1: Mean V_{rms} from five 200 ms sonications at each input power of the Branson ultrasonic horn, detected by the swPCD during sonications in (a) Water, (b) Ethaline, (c) CaDES and (d) Reline. Taken from [217].

Fig. B.1 (a) shows a plot of the V_{rms}-input power in water. Yusuf *et al* [34] provide a detailed description of the trend in V_{rms} shown in this figure. In general, V_{rms} tends to increase as the sonotrode input power increases. This is because the increase in input power leads to an increase in the amplitude of the sonotrode tip, which in turn causes an increase in the size of the bubble clusters and results in a larger amplitude of the bubble collapse shock wave. However, in Fig. B.1(a), there are certain dips or plateau regions in the V_{rms} at input power levels of 30% and 50%-60%. In these regions, an increase in sonotrode input power does not increase V_{rms}. Yusuf *et al* [34] found that at these input power levels, the cavitation response is transitioning from one subharmonic order to the next, which implies that the bubble collapse period has increased by one acoustic cycle. For example, at 30% input power, the bubble collapse period transitions from $4T_0$ to $5T_0$, resulting in a decrease in V_{rms}. This phenomenon is related to the attenuation of cavitation radiation intensity caused by the inefficient periodicity of bubble cluster. A detailed discussion can be found in [34].

The equivalent V_{rms}-input power plots for Ethaline and CaDES are shown in fig. B.1(b) and (c), respectively. As illustrated, the trends in cavitation collapse shock wave intensity for these two liquids are very similar across the 20%-70% input power range. V_{rms} decreases for both DESs at an input power of approximately 60%, whilst it tends to stabilise at an input power of approximately 40%. However, the most striking feature is the sharp drop in V_{rms} as

the input power increases from 25% to 30%. This drop is associated with a change in the cavitation cluster structure, which transitions from a large spherical cloud (T_0) undergoing intense cavitation in every cycle to a smaller cavitation region beneath the tip of the horn, which oscillates and gradually expands over several successive cycles.

The V_{rms}-input power plot for Reline, however, exhibits distinctly different characteristics (see fig. B.1 (d)), with a broader region of decline in the 30%-50% input power range, primarily attributable to stronger shockwave attenuation in the higher-viscosity DES. These plots inherently provide a valuable assessment of the potential positive and negative effects of input power on sonochemical applications, as they quantify the cavitation collapse shockwave intensity during sonication by monitoring the shock wave content detected in each liquid.

B.2 Dual-perspective HSI of TCM-delamination at 60% input power

The appendix contains material adapted from the co-authored publication: *A mechanistic study identifying improved technology critical metal delamination from printed circuit boards at lower power sonications in a deep eutectic solvent*. The candidate was the second author of this work and contributed to the experimental work and data processing. The material is included here as supplementary context for the thesis and is clearly distinguished from the main thesis chapters.

Journal Paper
A mechanistic study identifying improved technology critical metal delamination from printed circuit boards at lower power sonications in a deep eutectic solvent. Ben Jacobson, **Shida Li**, Rodolfo Marin Rivera, Paul Daly, Christopher E. Elgar, Daniel M. Mulvihill, Andrew P. Abbott, Andrew Feeney and Paul Prentice.
Ultrasonic Sonochemistry, vol. 101, p. 106701, 2023.

Fig. B.2 shows a representative dual-perspective HSI captured for sample 2 at the fifth minute of sonication under the input power of 60%. This image contains a wealth of data and fully reflects the major events occurring over an extended period within a complex cavitation environment. In the text below, only the key features are outlined.

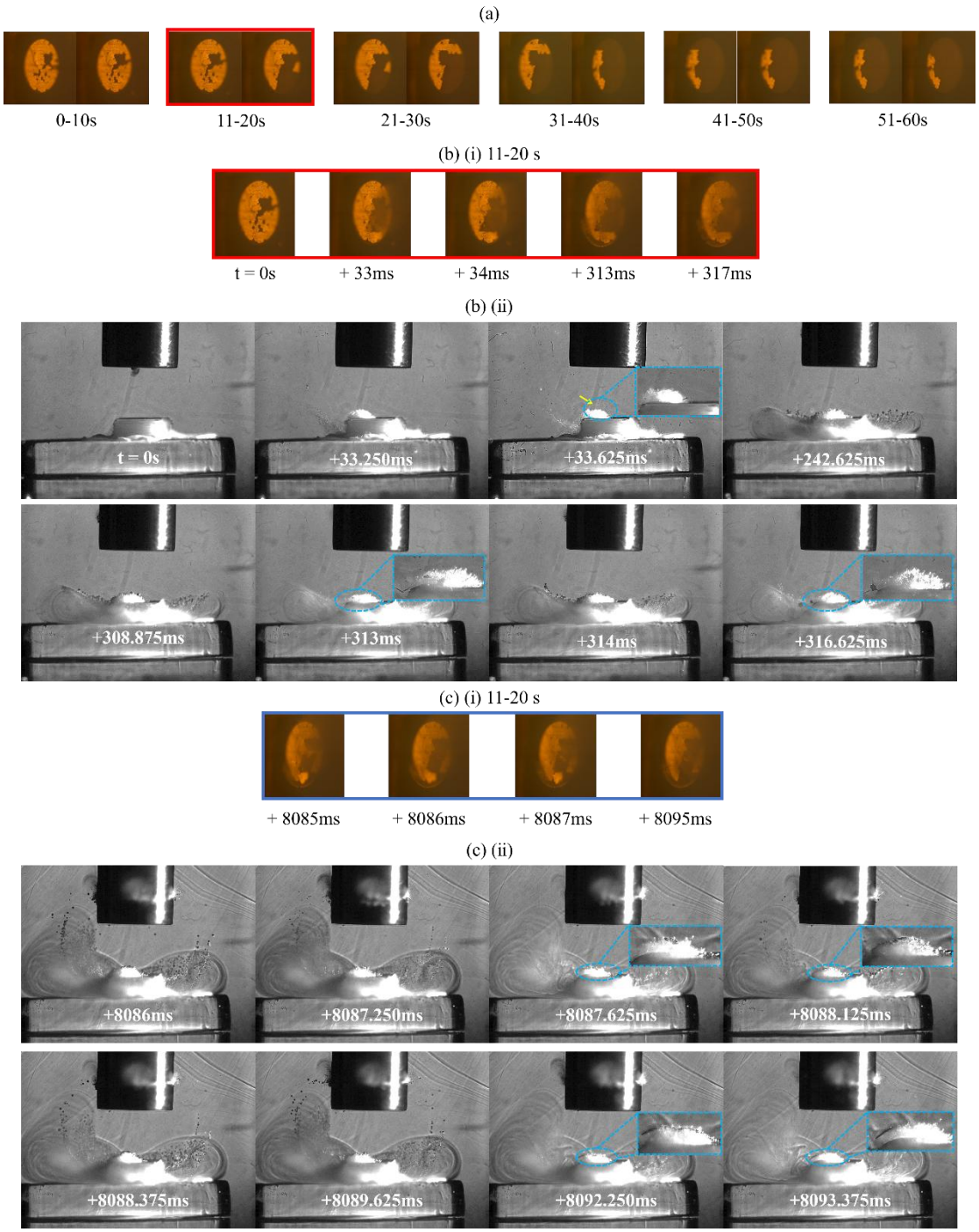

Fig. B.2: (a) Single images of the TCM disk from the Phantom camera perspective, before and after each of the 10 s sonications, from the fifth minute at 60 % input power for sample 2. (b)-(c) Combination (i) Phantom and (ii) Photron frames from HSI sequences, of specific delamination events at different points during the sonication. Bubble collapse shockwaves are arrowed yellow, TCM fragments within zoomed insets arrowed blue, throughout the Photron imaging. Image sequences available in movie format as supplementary material. Scale provided by (i) the 2 mm Ø TCM disk, (ii) the 6.4 mm Ø tip. Taken from [217].

As shown in fig. 4.8, extensive delamination occurred in all samples following 5 minutes of sonication at 60% input power. Fig. B.2 (a) shows that during the 11-20-second sonication period in the fifth minute, the TCM on sample 2 underwent delamination covering a total area of approximately 0.79 mm^2 (accounting for approximately 25% of the total area of the TCM disc), whilst after the 31-40-second sonication, less than 20% of the TCM disc remained.

Phantom high-speed sequences (fig. B.2 (b) (i) and (c) (i)) record three pronounced delamination events observed during the one-minute cumulative sonication. However, the Photron images associated with fig. B.2 (b) (ii) and (c) (ii) capture critical characteristics of cavitation cluster structure at 60% input power, distinguishing it from cavitation at 90% input power (fig. 4.11). Particularly, a cluster of cavitation bubbles exhibiting continuous, dense and intense cavitation is observed, maintaining contact with the PCB surface throughout the 10-second sonication at 60% power. A second intriguing feature is the bulbous-like bubble filaments, which curve away from the edges and sides of the horn tip whilst extending downwards towards the PCB surface. Previous reports have noted the occurrence of such bulbous-like structures during sonication of high-viscosity liquids [22], [94], [214], and this feature also appears in the cavitation characterisation of the DES experiments in chapter 4. With regard to the TCM delamination phenomena observed in fig. B.2, the curved bubble filaments apparently sustained the energy supply to the persistent cavitation clusters on the PCB surface during the sonication at 60% input power.

Fig. B.2 (b) (i) shows the initial 317 ms during the 11–20-second sonication (highlighted by the red box in fig. B.2 (a)), during which a small segment of a single TCM fragment undergoes delamination., A TCM fragment is lifted away from the PCB surface at 33 ms, although it has not yet been completely delaminated. Corresponding Photron HSI sequences in fig. B.2 (b) (ii) show that at 313 ms, this TCM fragment was lifted from a continuous cavitation cluster on the PCB surface. Shock waves generated by bubble collapse (indicated by yellow arrows in the figure), observed for example at 33.625 ms, confirm that cluster on the PCB surface was undergoing intense cavitation.

Fig. B.2 (c) shows HSI images taken from dual perspectives following the same 10-second sonication, during which another TCM delamination event occurs soon after 8 seconds from the start of the sonication (i). Fig. B.2 (c) (ii) indicates that the clusters on the PCB surface remained stable during the full duration of the sonication. The imaging results from these two perspectives again strongly suggest that, compared to the early stage of sonication

shown in fig. B.2 (b), a larger volume of TCM debris gradually detached from the PCB surface over a few milliseconds, followed by signs of complete delamination and dislodgement, a process visible in the Phantom images between 8087 and 8089 ms and confirmed by the Photron image at 8092.250 ms.

Appendix C

Temporal evolution of cavitation and implications for pulsed operation

C.1 Introduction

HSI in fig. 6.4 (d & e) indicates that during a single continuous 2 s sonication, the structure and coverage of the cavitation clusters within the tube bore exhibits time-varying characteristics. This implies that cavitation intensity and its effective action region are not constant over time, which in turn suggests an opportunity to optimise how the ultrasonic exposure time is distributed. In other words, for a given energy input, an appropriate choice of excitation duration may increase the effective cavitation intensity achieved per unit energy.

Continuous excitation can be implemented by directly specifying the signal parameters such as frequency, amplitude, and excitation duration, using a signal generator. In addition to continuous excitation, pulse-width modulation (PWM) is one of the most commonly adopted temporal modulation schemes in power ultrasonics [243]. Periodic on/off switching can be introduced on the basis of continuous sinusoidal excitation, as shown in fig. C.1.

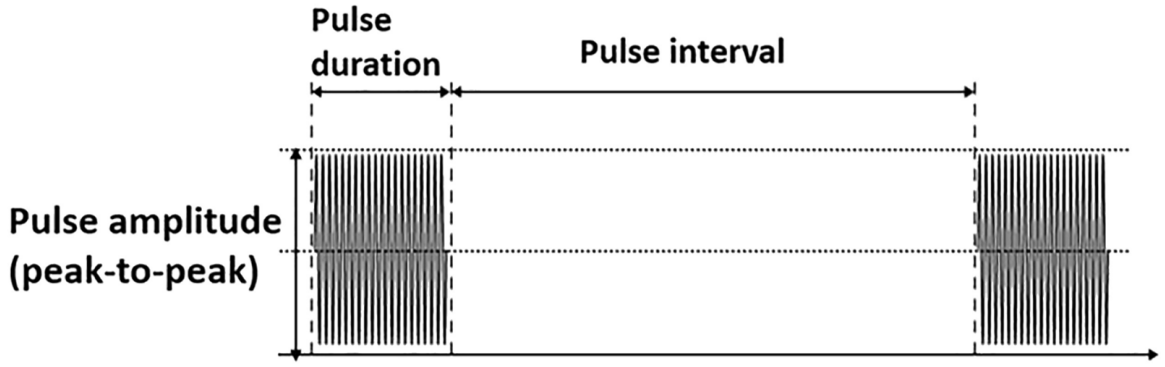

Fig. C.1: Illustration showing pulse amplitude, pulse duration (when ultrasound is applied), and pulse interval (the quiet time between bursts of ultrasonic irradiation). Taken from [241].

Typically, t_{on} denotes the excitation "on" time of the transducer (pulse duration), and t_{off} denotes the "off" time (pulse interval). The duty cycle is defined as the ratio of the two:

$$K = \frac{t_{on}}{t_{off}} \qquad (C.1)$$

The effect of pulsed excitation on acoustic cavitation is governed jointly by the t_{on}, t_{off}, K and pulse-repetition frequency [2], [32], [229]. During the t_{on}, cavitation nuclei are activated and the bubble population develops, producing collapse shock waves. Continued excitation may, however, promote bubble growth, coalescence and the accumulation of gas-rich bubbles, increasing acoustic scattering, absorption and shielding. During the t_{off}, larger bubble structures may collapse, disperse or partially dissolve, thereby reducing shielding before the subsequent burst. At the same time, residual nuclei may provide a cavitation-memory effect and facilitate nucleation when excitation resumes.

Consequently, an t_{off} that is too short may not allow sufficient recovery of the acoustic field, whereas an excessively long t_{off} may allow the active nuclei to dissolve and reduce the total number of cavitation events delivered over a fixed processing period. The optimum pulse protocol is therefore system-dependent and cannot be defined by the t_{on} alone. Comparisons between continuous and pulsed excitation must also distinguish instantaneous input power from average power and total energy input [229], [241], [244].

Compared to continuous excitation, pulsed excitation has been reported to enhance process efficiency in various sonochemical and sonoprocessing systems. Casadonte *et al* [244] compared continuous excitation with 1 Hz pulsed operation in a 400 kHz ultrasonic cup horn for the degradation of the industrial dye Acid Orange. At an acoustic power input of 6.6 W, pulsed sonication increased the degradation rate of Acid Orange by more than threefold. For ultrasonic nitrogen fixation, Yusuf *et al* [241] sonicated 6 mL de-ionised water using a 200 kHz spherically focused ultrasonic transducer (H-149, Sonic Concepts, Bothwell, WA, USA) at 148.5 $W \cdot L^{-1}$ power density, while continuously sparging air at 19 $L \cdot min^{-1}$. For a total sonication duration of 60 s, a pulse protocol with t_{on} = 4 ms and t_{off} = 80 ms increased the nitrogen-fixation efficiency by at least eightfold compared with continuous excitation.

Accordingly, this section will utilise the experimental platform shown in fig. 6.1 to investigate pulsing parameters for delivering optimal cavitation activity.

C.2 Methodology

C.2.1 Platform

This experiment was used only for acoustic acquisition, the high-speed camera, ring illuminator, laser illuminator and delay generator were not installed. The excitation of the tube transducer and the oscilloscope acquisition were synchronously triggered by the signal generator.

C.2.2 Acoustic detection and filtering protocol

To compare V_{rms} under different pulse duration conditions in de-ionised water, two-second sonication signals were truncated at 100, 200, 300, 400, 500, 1000, and 2000 ms, respectively, at an input power of 106 W. The corresponding V_{rms} values were then calculated and compared for each pulse length. The recorded signals were subsequently filtered following the procedure described in §3.7 to extract components associated with cavitation activity.

C.3 Results of characterisation of cavitation activity inside the tube transducer under pulsed sonication

Fig. C.2 shows the relationship between V_{rms} within the tube transducer and pulse duration at 106 W input power. Each data point represents the mean of five independent measurements acquired at the same pulse duration, with error bars indicating the corresponding standard deviation.

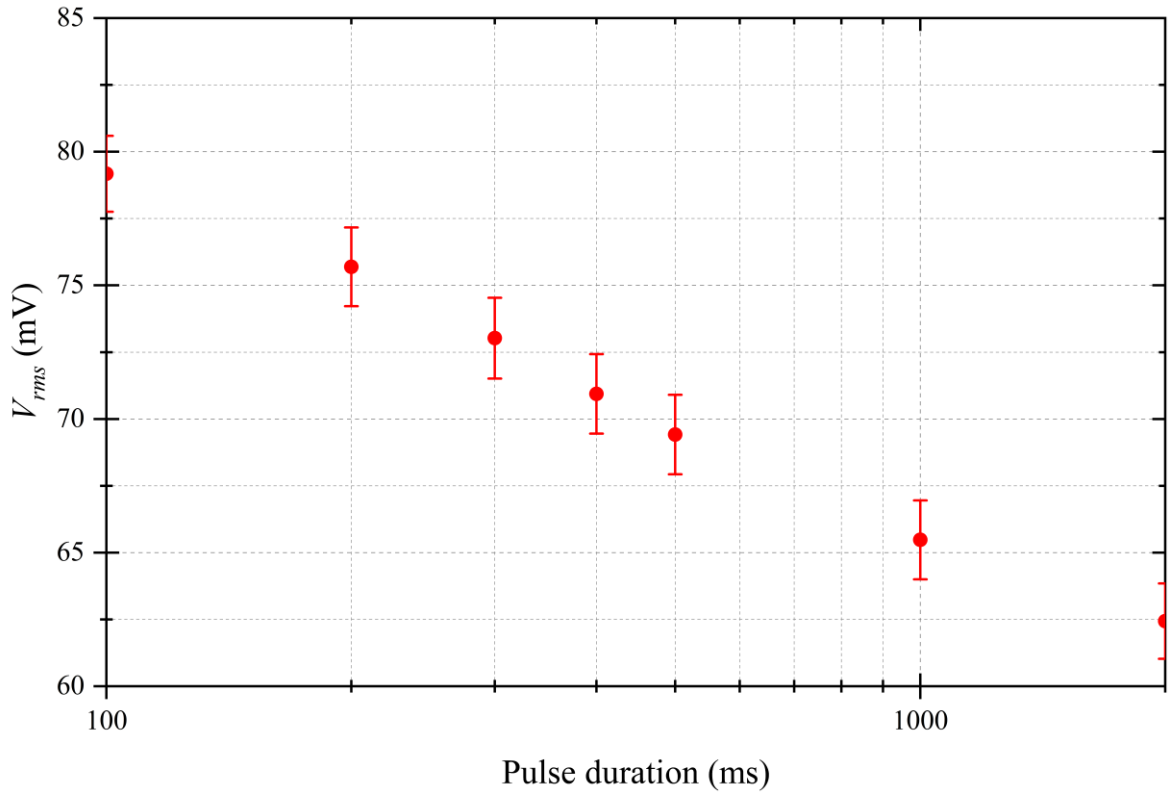

Fig. C.2: V_{rms} measured by swPCD inside the tube transducer as a function of pulse duration under 106 W input power. Error bars represent the standard deviation.

Within the range of pulse durations tested, V_{rms} exhibits a monotonically decreasing behaviour with increasing pulse duration, indicating that the shockwave content is closely related to the pulse duration and suggesting the existence of a characteristic time scale that is more conducive to achieving higher collapse shockwave intensities. This trend is consistent with the HSI observation in fig 6.4 (e). During continuous excitation, the structure and spatial coverage of the cavitation bubble cluster within the tube bore evolve dynamically over time. Consequently, the cavitation intensity is not constant but varies over the exposure period. Comparing the two conditions of 100 ms and 2000 ms, the former has a V_{rms} approximately 27% higher, further indicating that under the same input power conditions, using a shorter pulse duration can increase the time-averaged shockwave content and thereby enhance inertial cavitation output.

Appendix D

D.1 Effect of flake loading on the cavitation activity within the tube transducer

As discussed in §1.1, suspended solid particles in a liquid can act as cavitation nucleation substrates, thereby reducing the cavitation threshold. During sonication with the tube transducer, delaminated graphite from the surface of LiB anode flakes can disperse into the liquid, increasing the number of potential nucleation sites and consequently altering the cavitation threshold. Such changes may shift the V_{rms}-input power relationship shown in fig. 6.3 from §6.3.1, subsequently affecting the delamination of the optimal input power. This section therefore examines the following hypothesis: at any given input power, the introduction of anode flakes modifies the cavitation conditions generated within the tube transducer bore.

D.1.1 Method of passive cavitation detection

The summary of characteristic result regarding the time-averaged shockwave content (V_{rms}) in de-ionised water within the static tube transducer configuration as a function of input powers is detailed in §6.3.1. The results of §7.3.2 employs the acoustic signal detection platform from §6.2.3 compares the variation in V_{rms} when 17 cm^2 of LiB anode production scrap flakes sample is added. Input power increment sampling aligns with that employed for de-ionised water in §6.2.6.

D.1.2 Result

The effect of tube transducer input power on the V_{rms} of an acoustic emission (captured and processed using the method detailed in §6.2.6) is presented in fig. D.1 for two tube transducer loading conditions. In the first, referred to as the “control” condition, the reservoir contained only de-ionised water, this data originates from V_{rms} obtained under the air-backed water condition in §6.3.1. In the second, termed the “flake loading” condition, a 17 cm^2 sample of LiB anode flakes was added to the de-ionised water. Each data point represents the average of five independent measurements recorded at the same input power, with error bars depicting the standard deviation. Under the flake loaded condition, anode flakes were removed and replaced after each batch of five sonications. Again, these V_{rms} measurements are an indicator of the degree and extent of cavitation bubbles collapse shockwaves within

the tube transducer, and this study also determines the impact of LiB anode flakes on cavitation activity.

Under the control condition, V_{rms} increased nonlinearly with increasing input power, typical for an ultrasonic transducer. A localised peak appeared around 63 W, followed by a mild decrease before V_{rms} increased again to a global maximum at approximately 106 W. This maximum indicates that cavitation shockwave intensity is strongest at 106 W. Input powers corresponding to the local V_{rms} minimum should be avoided in practical operation, as these may reflect off-resonance behaviour or increased nonlinear damping [34], [242].

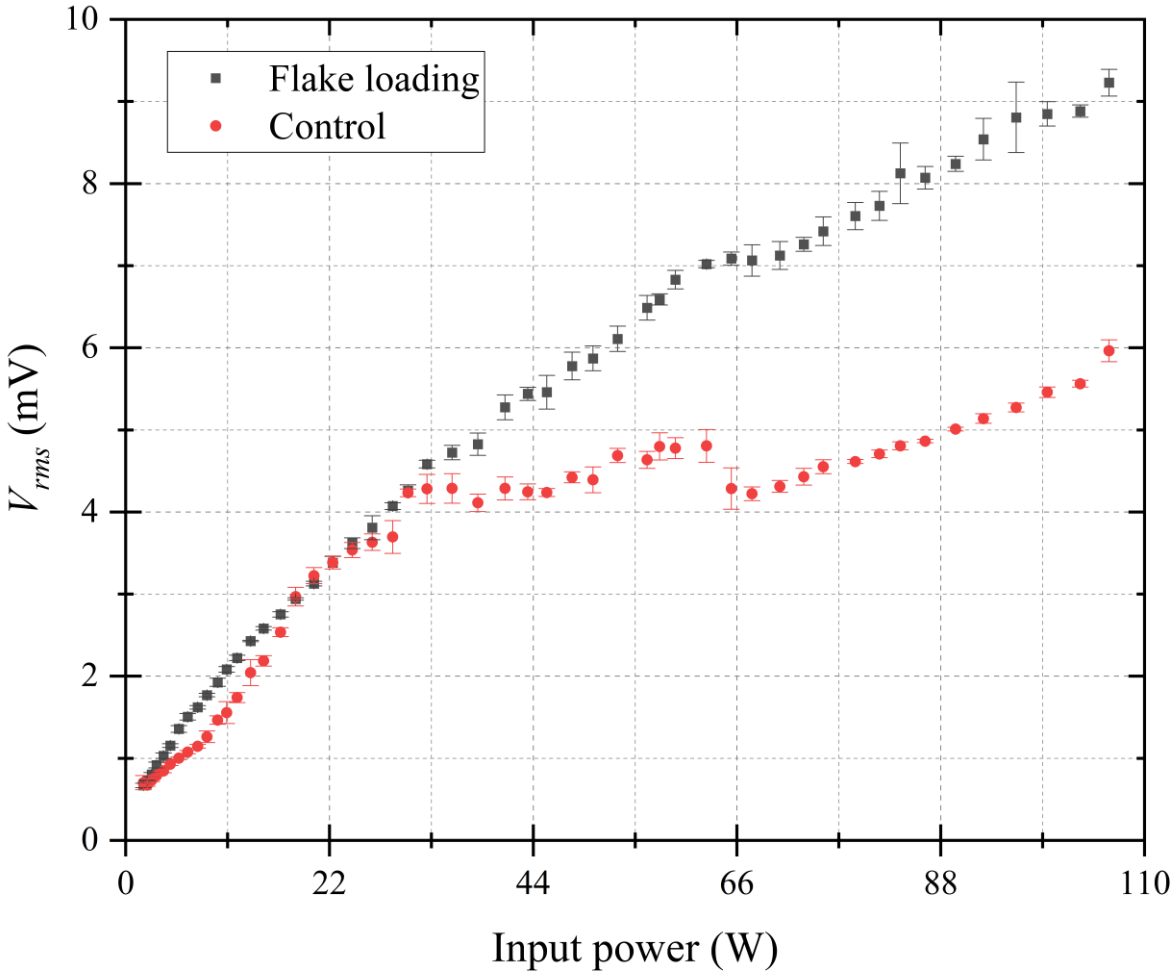

Fig. D.1: The effect of 51 input powers on the V_{rms} of captured acoustic emissions for control (red, circular markers) and flake loaded (black, square markers) conditions. In the flake loaded condition, 17 cm^2 sample of LiB anode flakes were added to the deionised water. The control condition is just de-ionised water. See §7.2.1.3 for details of the capturing and processing method.

A broadly similar nonlinear trend was observed under the flake loading condition. At input powers below 33 W, V_{rms} was slightly higher than in the control condition. As the input power was increased, V_{rms} continued to rise, and the local drop between 63 W and 68 W disappeared, indicating that the presence of solid particles promotes enhanced cavitation emissions. Above 68 W, V_{rms} increased steadily until reaching its global maximum at 106 W, where values were substantially higher than those recorded in the control condition.

The repeated occurrence of V_{rms} maximum at 106 W - but at a significantly elevated level compared with the control condition - demonstrates that flake loaded did not inhibit the transducer's performance. Indeed, the presence of solid particles may serve as cavitation nuclei that lower the threshold for bubble formation, and thereby increase the cavitation energy within the transducer. It is concluded then that the tube transducer continues to generate efficient and stable cavitation even when subjected to flake loaded conditions.

D.2 Citric acid assisted ultrasonic delamination of graphite coating from aged LiB anode

Conference Paper
Pretreatment of aged lithium-ion battery anode to enable high-throughput sonoprocessing **Shida Li**, Paul Daly, Ben Jacobson, Andrew Feeney and Paul Prentice
1st International REACT Conference, Glasgow, November 2025

D.2.1 Motivation and context

In addition to transducer configuration, the state of the LiB anode itself also has a significant impact on delamination efficiency. In contrast to the LiB anode production scrap, aged LiB anodes that have been exposed to ambient moisture for extended periods develop surface lithium carbonate layers, which inhibit the detachment and dispersion of graphite in aqueous media [204]. This, in turn, renders sonication in water alone ineffective at delamination of the aged LiBs. Weak acid pre-treatment has been shown to mitigate these aging effects by dissolving the surface carbonate layer [245], thereby restoring the anode surface to a state more susceptible to cavitation-assisted delamination. For instance, Marshall *et al* [246]

sonicated aged LiB anode sheets in a 40 kHz, 50 W ultrasonic bath which contains 0.02 $M \cdot L^{-1}$ oxalic acid solution for 30 min, achieving complete removal of the graphite coating. Although this process route demonstrates the feasibility of sonication in acid for delaminating aged LiB anodes, the prolonged processing time renders the overall treatment rate insufficient to meet the demands of high throughput TCM recycling.

Given that the surface condition of the aged LiB anode can significantly influence the sonication delamination behaviour, a batch of aged anodes was further selected for comparative investigation, simulating industrial operating conditions. Compared with an ultrasonic bath, the tube transducer caused significantly greater damage to the copper foil during the graphite delamination process. If the "simultaneous sonication in a weakly acid medium" (i.e., concurrent exposure to acid and cavitation) were adopted, the copper foil would be more susceptible to fragmentation under prolonged high-intensity cavitation, producing fine copper particulates. During the post-sonication filtration step, these fine copper particles would be removed together with the graphite particles, leading to unintended copper losses and errors in the calculation of the remaining mass percentage, thereby compromising the accuracy of recovery-efficiency assessment. On the basis, a two-step strategy of "citric acid pre-treatment followed by ultrasonic delamination" was employed in this section. Specially, these aged anodes were pretreated by immersion in citric acid solutions prior to sonication, to evaluate the effects of varying solution concentrations and immersion times on subsequent cavitation delamination in the tube transducer.

D.2.2 Materials and methods

Aged anode samples stored for over one year were selected for sonication in the final experiment to simulate commercial operating conditions. Aged anode flakes with an effective area of approximately 17 cm^2 were immersed in citric acid solutions (detailed in §3.10) of varying concentration (0.1, 0.2, 0.3, 0.4, and 0.5 $mol \cdot L^{-1}$) for controlled durations (1, 3, 5, 7, and 9 min), in order to systematically evaluate the combined effect of solution concentration and pre-treatment time on restoring the delamination efficiency.

Procedures for acquiring images of the anode flakes are detailed in §7.2.1.3.

D.2.3 Effect of citric acid pre-sonication treatment on graphite coating removal from aged anode flakes with an effective area of 17 cm^2

The evolution of anode flake delamination over a 2 s sonication in the tube transducer following 5 min immersion in 0.0, 0.1 and 0.5 $mol \cdot L^{-1}$ solutions are presented in fig. D.2 (a)-(c).

Fig. D.2 (a) shows a conventional recording in which the aged LiB anode flakes was immersed for 5 min in water, followed by 2 s sonication at 106 W in the tube transducer. Throughout the process, only slight darkening of the liquid was observed, indicating a very low degree of delamination. Fig. D.2 (b & c) showed that, when the citric acid concentration was increased to 0.1 $mol \cdot L^{-1}$ and 0.5 $mol \cdot L^{-1}$, respectively, the concentration of suspended graphite in the water rose markedly, indicating graphite had been effectively delaminated from the flakes. A higher citric acid concentration corresponded to a greater release of graphite. In both images, the delaminated copper foil was clearly observed adhered to the front observation window. However, the dispersed graphite did not form a high concentration suspension state that completely obscured the field of view compared with fig. 7.10 (e).

The "remaining mass percentage" of aged anode flake batches with 17 cm^2 effective area, following treatment in varying citric acid conditions, followed by a 2 s sonication in tube transducer, is presented in fig. D.2. Each treatment condition was applied separately to five anode batches and so the data in fig. D.2 are presented as an average ± the standard deviation.

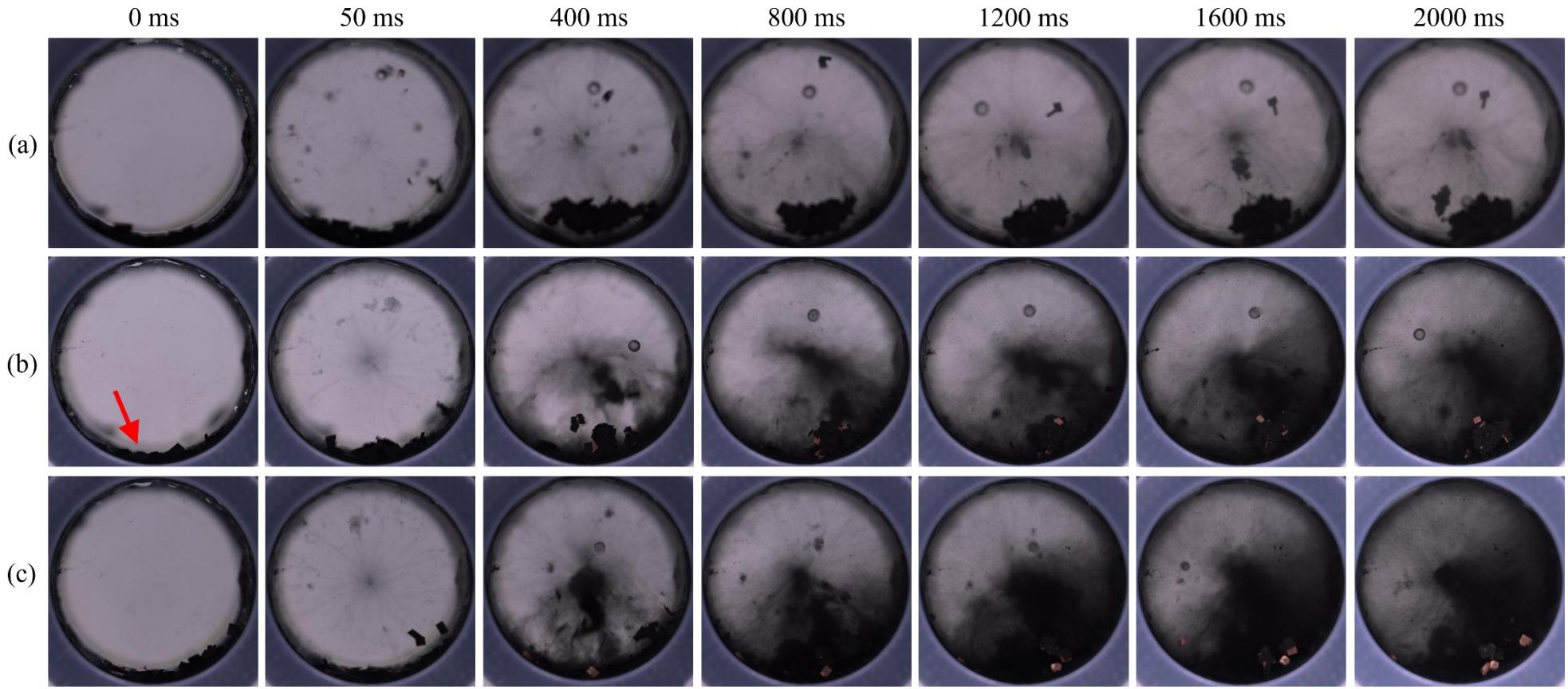

Fig D.2: Images from a conventional recording of the delamination evolution process following 2 s sonication following 5 min immersion in (a) 0.0, (b) 0.1 and (c) 0.5 mol·L^{-1} citric acid solutions. Scale is provided by 55.6 mm inner diameter tube transducer. The red arrow in (b) indicates the anode flakes settled at the bottom of the bore, prior to sonication.

Negligible coating was removed following pre-sonication treatment in water for any of the durations. Replacing water with a 0.1 mol·L^{-1} citric acid solution caused a decrease in the remaining mass percentage for each duration while the changes were more significant for longer durations. Incremental increases in concentration caused further reductions in remaining mass percentage, which, again, were greater for longer immersions. However, the relation was not linear, and duration extension became decreasingly impactful. Complete delamination was obtained following 7 min immersion in 0.4 mol·L^{-1} citric acid, and 5 min in 0.5 mol·L^{-1} citric acid. In totality, increases in citric acid concentration and of immersion duration, together or separately, cause an increase in the graphite delamination from aged LiB anode. Regarding the phenomenon observed in fig. D.2 (c) where the graphite concentration in the de-ionised water is lower than that in fig. 7.10 (e), it is hypothesised that the graphite does not disperse into the water in a finely powdered form after delamination, but instead remains as relatively large particles, thereby resulting in a lower apparent suspension concentration.

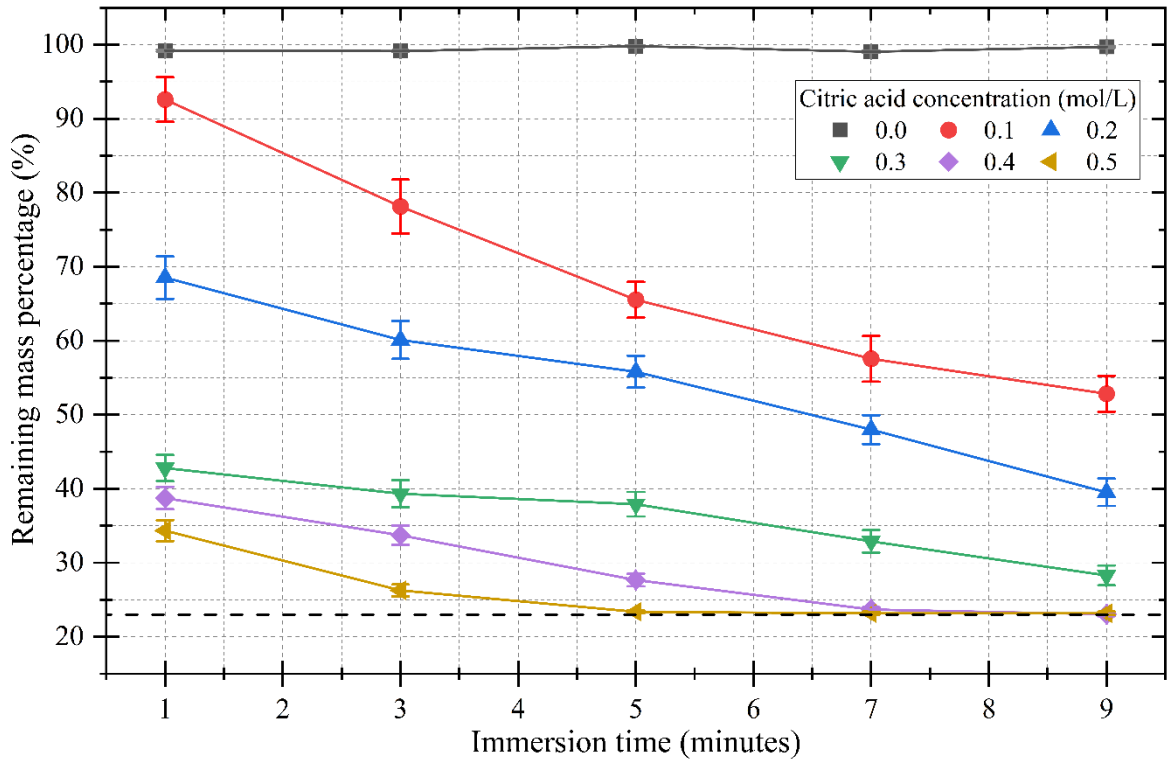

Fig. D.3: The remaining mass percentage of aged anode flakes (17 cm^2 effective area) recovered following 2 s of sonication in tube transducer at 106 W. The flakes were pre-treated by timed immersion in citric acid solutions with various concentrations Complete graphite coating removal is indicated by a dashed line at 23%.

Fig. D.3 demonstrates that the pre-sonication immersion of the anode flake batch in 0.5 mol·L^{-1} citric acid for 5 min is the most time efficient pre-sonication treatment that leads to complete graphite coating delamination. Fig. D.4 compares the remaining mass percentage of aged anode flake batches, with 17 cm^2 effective area, recovered from each of the five transducer configurations following this efficient treatment and exposure to 2 s of sonication. Because citric acid solution was used during pre-treatment, the copper foil after sonication was prone to surface oxidation upon exposure to air, causing its colout to resemble that of graphite and affecting the observation. Therefore, no pictures are included in this section.

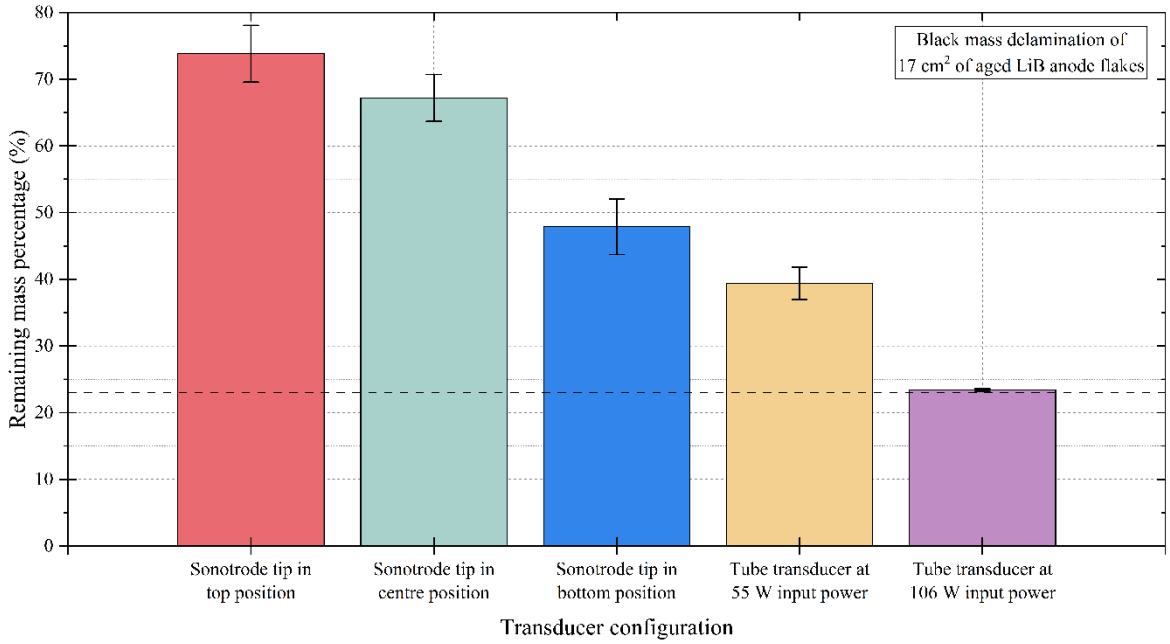

Fig. D.4: Remaining mass percentage of aged LiB anode flakes (17 cm²) after 2 s sonication in each of the five transducer configurations, following a 5 minute immersion in 0.5 mol·L^{-1} citric acid. Complete graphite removal is indicated by the dashed, black line at 23%.

Similar to §7.2.2.4 on the delamination of anode production scrap, the results show that decreasing the separation between the sonotrode tip and flakes, initially settled in the cylindrical vessel, leads to greater graphite coating removal. However, in this section the remaining mass percentages for this aged anode are less than for the anode production scrap, suggesting that the binding union is weaker following treatment than in its fresh state. Further, in §7.2.2.4 the sonotrode tip in its bottom position and the tube transducer at a matched 55 W input power led to the same remaining mass percentage, here while in this section the tube transducer caused markedly more delamination. The tube transducer at 106 W input power delaminates all graphite coating in 2 s as anticipated from the fig. D.4 result.

In totality, the tube transducer is more effective than a conventional sonotrode in removing the graphite coating from a batch of anode flakes with a 17 cm^2 effective area.

Bibliography

[1] M. Ashokkumar, ‘The characterization of acoustic cavitation bubbles – An overview’, *Ultrasonics Sonochemistry*, vol. 18, no. 4, pp. 864–872, Jul. 2011, doi: 10.1016/j.ultsonch.2010.11.016.

[2] T. G. Leighton and R. E. Apfel, ‘The Acoustic Bubble’, *The Journal of the Acoustical Society of America*, vol. 96, no. 4, pp. 2616–2616, Oct. 1994, doi: 10.1121/1.410082.

[3] J. Gao *et al.*, ‘Novel drying pretreatment technologies and their applications in the food industry’, *FMR*, vol. 3, no. 1, pp. 0–0, 2023, doi: 10.48130/FMR-2023-0014.

[4] W. Lauterborn and R. Mettin, ‘Acoustic cavitation: Bubble dynamics in high-power ultrasonic fields’, in *Power Ultrasonics*, Elsevier, 2023, pp. 23–52. doi: 10.1016/B978-0-12-820254-8.00005-1.

[5] T. Thanh Nguyen, Y. Asakura, S. Koda, and K. Yasuda, ‘Dependence of cavitation, chemical effect, and mechanical effect thresholds on ultrasonic frequency’, *Ultrasonics Sonochemistry*, vol. 39, pp. 301–306, Nov. 2017, doi: 10.1016/j.ultsonch.2017.04.037.

[6] I. V. Smirnov, N. V. Mikhailova, B. A. Yakupov, and G. A. Volkov, ‘Analysis of Dependences of Threshold Parameters for Acoustic Cavitation Onset in a Liquid on an Ultrasonic Frequency, Hydrostatic Pressure, and Temperature’, *Tech. Phys.*, vol. 67, no. 2, pp. 161–170, Feb. 2022, doi: 10.1134/S1063784222030057.

[7] B. Li, Y. Gu, and M. Chen, ‘An experimental study on the cavitation of water with dissolved gases’, *Exp Fluids*, vol. 58, no. 12, p. 164, Dec. 2017, doi: 10.1007/s00348-017-2449-0.

[8] R. A. Roy, S. I. Madanshetty, and R. E. Apfel, ‘An acoustic backscattering technique for the detection of transient cavitation produced by microsecond pulses of ultrasound’, *The Journal of the Acoustical Society of America*, vol. 87, no. 6, pp. 2451–2458, Jun. 1990, doi: 10.1121/1.399091.

[9] J. H. Song, K. Johansen, and P. Prentice, ‘An analysis of the acoustic cavitation noise spectrum: The role of periodic shock waves’, *The Journal of the Acoustical Society of America*, vol. 140, no. 4, Art. no. 4, Oct. 2016, doi: 10.1121/1.4964633.

[10] F. Reuter and R. Mettin, ‘Mechanisms of single bubble cleaning’, *Ultrasonics Sonochemistry*, vol. 29, pp. 550–562, Mar. 2016, doi: 10.1016/j.ultsonch.2015.06.017.

[11] A. Vogel, S. Busch, and U. Parlitz, ‘Shock wave emission and cavitation bubble generation by picosecond and nanosecond optical breakdown in water’, *The Journal of the Acoustical Society of America*, vol. 100, no. 1, pp. 148–165, Jul. 1996, doi: 10.1121/1.415878.

[12] K. S. Suslick, ‘Sonochemistry’, *Science*, vol. 247, no. 4949, pp. 1439–1445, Mar. 1990, doi: 10.1126/science.247.4949.1439.

[13] Y. G. Adewuyi, ‘Sonochemistry: Environmental Science and Engineering Applications’, *Ind. Eng. Chem. Res.*, vol. 40, no. 22, pp. 4681–4715, Oct. 2001, doi: 10.1021/ie010096l.

[14] N. Pokhrel, P. K. Vabbina, and N. Pala, ‘Sonochemistry: Science and Engineering’, *Ultrasonics Sonochemistry*, vol. 29, pp. 104–128, Mar. 2016, doi: 10.1016/j.ultsonch.2015.07.023.

[15] A. Taha *et al.*, ‘Sonoprocessing: mechanisms and recent applications of power ultrasound in food’, *Critical Reviews in Food Science and Nutrition*, vol. 64, no. 17, pp. 6016–6054, Jul. 2024, doi: 10.1080/10408398.2022.2161464.

[16] A. Philipp and W. Lauterborn, ‘Cavitation erosion by single laser-produced bubbles’, *J. Fluid Mech.*, vol. 361, pp. 75–116, Apr. 1998, doi: 10.1017/S0022112098008738.

[17] O. Lindau and W. Lauterborn, ‘Cinematographic observation of the collapse and rebound of a laser-produced cavitation bubble near a wall’, *J. Fluid Mech.*, vol. 479, pp. 327–348, Mar. 2003, doi: 10.1017/S0022112002003695.

[18] Y. S. Kannan, B. Karri, and K. C. Sahu, ‘Letter: Entrapment and interaction of an air bubble with an oscillating cavitation bubble’, *Physics of Fluids*, vol. 30, no. 4, p. 041701, Apr. 2018, doi: 10.1063/1.5025122.

[19] P. Cui, Q. X. Wang, S. P. Wang, and A. M. Zhang, ‘Experimental study on interaction and coalescence of synchronized multiple bubbles’, *Physics of Fluids*, vol. 28, no. 1, p. 012103, Jan. 2016, doi: 10.1063/1.4939007.

[20] C. D. Ohl and R. Ikink, ‘Shock-Wave-Induced Jetting of Micron-Size Bubbles’, *Phys. Rev. Lett.*, vol. 90, no. 21, p. 214502, May 2003, doi: 10.1103/PhysRevLett.90.214502.

[21] J. M. Rosselló, W. Lauterborn, M. Koch, T. Wilken, T. Kurz, and R. Mettin, ‘Acoustically induced bubble jets’, *Physics of Fluids*, vol. 30, no. 12, p. 122004, Dec. 2018, doi: 10.1063/1.5063011.

[22] A. Thiemann, F. Holsteyns, C. Cairós, and R. Mettin, ‘Sonoluminescence and dynamics of cavitation bubble populations in sulfuric acid’, *Ultrasonics Sonochemistry*, vol. 34, pp. 663–676, Jan. 2017, doi: 10.1016/j.ultsonch.2016.06.013.

[23] M. Lamminen, ‘Mechanisms and factors influencing the ultrasonic cleaning of particle-fouled ceramic membranes’, *Journal of Membrane Science*, vol. 237, no. 1–2, pp. 213–223, Jul. 2004, doi: 10.1016/j.memsci.2004.02.031.

[24] N. S. M. Yusof, B. Babgi, Y. Alghamdi, M. Aksu, J. Madhavan, and M. Ashokkumar, ‘Physical and chemical effects of acoustic cavitation in selected ultrasonic cleaning

applications', *Ultrasonics Sonochemistry*, vol. 29, pp. 568–576, Mar. 2016, doi: 10.1016/j.ultsonch.2015.06.013.

[25] S. Aghapour Aktij, A. Taghipour, A. Rahimpour, A. Mollahosseini, and A. Tiraferri, 'A critical review on ultrasonic-assisted fouling control and cleaning of fouled membranes', *Ultrasonics*, vol. 108, p. 106228, Dec. 2020, doi: 10.1016/j.ultras.2020.106228.

[26] B. Gerold *et al.*, 'Directed jetting from collapsing cavities exposed to focused ultrasound', *Applied Physics Letters*, vol. 100, no. 2, p. 024104, Jan. 2012, doi: 10.1063/1.3676414.

[27] L. Van Wijngaarden, 'Mechanics of collapsing cavitation bubbles', *Ultrasonics Sonochemistry*, vol. 29, pp. 524–527, Mar. 2016, doi: 10.1016/j.ultsonch.2015.04.006.

[28] F. Reuter, C. Deiter, and C.-D. Ohl, 'Cavitation erosion by shockwave self-focusing of a single bubble', *Ultrasonics Sonochemistry*, vol. 90, p. 106131, Nov. 2022, doi: 10.1016/j.ultsonch.2022.106131.

[29] K. Johansen, J. H. Song, and P. Prentice, 'Performance characterisation of a passive cavitation detector optimised for subharmonic periodic shock waves from acoustic cavitation in MHz and sub-MHz ultrasound', *Ultrasonics Sonochemistry*, vol. 43, pp. 146–155, May 2018, doi: 10.1016/j.ultsonch.2018.01.007.

[30] T. Y. Wu, N. Guo, C. Y. Teh, and J. X. W. Hay, *Advances in Ultrasound Technology for Environmental Remediation*. in SpringerBriefs in Molecular Science. Dordrecht: Springer Netherlands, 2013. doi: 10.1007/978-94-007-5533-8.

[31] J. H. Song, A. Moldovan, and P. Prentice, 'Non-linear Acoustic Emissions from Therapeutically Driven Contrast Agent Microbubbles', *Ultrasound in Medicine & Biology*, vol. 45, no. 8, pp. 2188–2204, Aug. 2019, doi: 10.1016/j.ultrasmedbio.2019.04.005.

[32] L. A. Yusuf, 'Optimising Acoustic Cavitation for Industrial Application', p. 266.

[33] B. Jacobson, 'Acoustic Cavitation Characterisation in Viscous Deep Eutectic Solvents for Optimisation of Sonoprocessing of Technology Critical Materials', p. 328.

[34] L. Yusuf, M. D. Symes, and P. Prentice, 'Characterising the cavitation activity generated by an ultrasonic horn at varying tip-vibration amplitudes', *Ultrasonics Sonochemistry*, vol. 70, p. 105273, Jan. 2021, doi: 10.1016/j.ultsonch.2020.105273.

[35] B. Savun-Hekimoğlu, 'A Review on Sonochemistry and Its Environmental Applications', *Acoustics*, vol. 2, no. 4, pp. 766–775, Oct. 2020, doi: 10.3390/acoustics2040042.

[36] P. Riesz and D. BerdahI, ‘Free Radical Generation by Ultrasound in Aqueous and Nonaqueous Solutions’.

[37] P. Riesz, T. Kondo, and C. M. Krishna, ‘Sonochemistry of volatile and non-volatile solutes in aqueous solutions: e.p.r. and spin trapping studies’, *Ultrasonics*, vol. 28, no. 5, pp. 295–303, Sep. 1990, doi: 10.1016/0041-624X(90)90035-M.

[38] S. Merouani, A. Dehane, and O. Hamdaoui, ‘Ultrasonic destruction of surfactants’, *Ultrasonics Sonochemistry*, vol. 109, p. 107009, Oct. 2024, doi: 10.1016/j.ultsonch.2024.107009.

[39] J. Dewulf, H. Van Langenhove, A. De Visscher, and S. Sabbe, ‘Ultrasonic degradation of trichloroethylene and chlorobenzene at micromolar concentrations: kinetics and modelling’, *Ultrasonics Sonochemistry*, vol. 8, no. 2, pp. 143–150, Apr. 2001, doi: 10.1016/S1350-4177(00)00031-6.

[40] T. Sidnell, R. J. Wood, J. Hurst, J. Lee, and M. J. Bussemaker, ‘Sonolysis of per- and poly fluoroalkyl substances (PFAS): A meta-analysis’, *Ultrasonics Sonochemistry*, vol. 87, p. 105944, Jun. 2022, doi: 10.1016/j.ultsonch.2022.105944.

[41] K. S. Suslick, D. A. Hammerton, and R. E. Cline, ‘Sonochemical hot spot’, *J. Am. Chem. Soc.*, vol. 108, no. 18, pp. 5641–5642, Sep. 1986, doi: 10.1021/ja00278a055.

[42] C. Devos *et al.*, ‘Ultrasound mechanisms and their effect on solid synthesis and processing: a review’, *Chem. Soc. Rev.*, vol. 54, no. 1, pp. 85–115, 2025, doi: 10.1039/D4CS00148F.

[43] T. Sidnell, R. J. Wood, J. Hurst, J. Lee, and M. J. Bussemaker, ‘Sonolysis of per- and poly fluoroalkyl substances (PFAS): A meta-analysis’, *Ultrasonics Sonochemistry*, vol. 87, p. 105944, Jun. 2022, doi: 10.1016/j.ultsonch.2022.105944.

[44] G. Tezcanli-Guyer and N. H. Ince, ‘Degradation and toxicity reduction of textile dyestuff by ultrasound’, *Ultrasonics Sonochemistry*, vol. 10, no. 4–5, pp. 235–240, Jul. 2003, doi: 10.1016/S1350-4177(03)00089-0.

[45] R. James Wood, T. Sidnell, I. Ross, J. McDonough, J. Lee, and M. J. Bussemaker, ‘Ultrasonic degradation of perfluorooctane sulfonic acid (PFOS) correlated with sonochemical and sonoluminescence characterisation’, *Ultrasonics Sonochemistry*, vol. 68, p. 105196, Nov. 2020, doi: 10.1016/j.ultsonch.2020.105196.

[46] J. H. Bang and K. S. Suslick, ‘Applications of Ultrasound to the Synthesis of Nanostructured Materials’, *Advanced Materials*, vol. 22, no. 10, pp. 1039–1059, Mar. 2010, doi: 10.1002/adma.200904093.

[47] J. H. Bang and K. S. Suslick, ‘Sonochemical Synthesis of Nanosized Hollow Hematite’, *J. Am. Chem. Soc.*, vol. 129, no. 8, pp. 2242–2243, Feb. 2007, doi: 10.1021/ja0676657.

[48] A. Kumar, T. Kumaresan, A. B. Pandit, and J. B. Joshi, 'Characterization of flow phenomena induced by ultrasonic horn', *Chemical Engineering Science*, vol. 61, no. 22, pp. 7410–7420, Nov. 2006, doi: 10.1016/j.ces.2006.08.038.

[49] P. Chavan, P. Sharma, S. R. Sharma, T. C. Mittal, and A. K. Jaiswal, 'Application of High-Intensity Ultrasound to Improve Food Processing Efficiency: A Review', *Foods*, vol. 11, no. 1, p. 122, Jan. 2022, doi: 10.3390/foods11010122.

[50] C. Li *et al.*, 'A review on ultrasound-enhanced heat transfer', *Ultrasonics Sonochemistry*, vol. 121, p. 107570, Oct. 2025, doi: 10.1016/j.ultsonch.2025.107570.

[51] A. Jalali, A. Amiri Delouei, M. R. Zaertaraghi, and S. Amiri Tavasoli, 'Experimental Investigation on Active Heat Transfer Improvement in Double-Pipe Heat Exchangers', *Processes*, vol. 12, no. 7, p. 1333, Jun. 2024, doi: 10.3390/pr12071333.

[52] J. S. Taurozzi, V. A. Hackley, and M. R. Wiesner, 'Ultrasonic dispersion of nanoparticles for environmental, health and safety assessment – issues and recommendations', *Nanotoxicology*, vol. 5, no. 4, pp. 711–729, Dec. 2011, doi: 10.3109/17435390.2010.528846.

[53] T. Leong, M. Ashokkumar, and S. Kentish, 'THE FUNDAMENTALS OF POWER ULTRASOUND – A REVIEW'.

[54] S. El-Hadad, M. E. Moussa, and M. Shoeib, 'Influence of Al11Ce3 Size and Distribution on the Electrochemical Properties of Sonoprocessed Al-10 wt.% Ce Alloy', *Inter Metalcast*, vol. 17, no. 3, Art. no. 3, Jul. 2023, doi: 10.1007/s40962-022-00870-1.

[55] X. Chen *et al.*, 'Understanding dual-frequency ultrasonic melt treatment on grain refinement and mechanical properties improvement of AZ80 magnesium alloy: experiment and simulation', *Journal of Materials Research and Technology*, vol. 15, pp. 4758–4767, Nov. 2021, doi: 10.1016/j.jmrt.2021.10.083.

[56] S. Yang, Y. Weng, Q. Zhao, G. Wu, Z. Deng, and L. Qin, 'Ultrasonic Melt Processing: Progress, Applications, and Future Directions', *Materials*, vol. 18, no. 3, p. 522, Jan. 2025, doi: 10.3390/ma18030522.

[57] T. J. Ashaolu, 'Nanoemulsions for health, food, and cosmetics: a review', *Environ Chem Lett*, vol. 19, no. 4, pp. 3381–3395, Aug. 2021, doi: 10.1007/s10311-021-01216-9.

[58] R. J. Wilson, Y. Li, G. Yang, and C.-X. Zhao, 'Nanoemulsions for drug delivery', *Particuology*, vol. 64, pp. 85–97, May 2022, doi: 10.1016/j.partic.2021.05.009.

[59] M. Laxmi, A. Bhardwaj, S. Mehta, and A. Mehta, 'Development and characterization of nanoemulsion as carrier for the enhancement of bioavailability of artemether',

Artificial Cells, Nanomedicine, and Biotechnology, vol. 43, no. 5, pp. 334–344, Sep. 2015, doi: 10.3109/21691401.2014.887018.

[60] D. G. Shchukin, E. Skorb, V. Belova, and H. Möhwald, 'Ultrasonic Cavitation at Solid Surfaces', *Advanced Materials*, vol. 23, no. 17, pp. 1922–1934, May 2011, doi: 10.1002/adma.201004494.

[61] T. J. Mason, 'Ultrasonic cleaning: An historical perspective', *Ultrasonics Sonochemistry*, vol. 29, pp. 519–523, Mar. 2016, doi: 10.1016/j.ultsonch.2015.05.004.

[62] F. J. Fuchs and J. D. Kramlick, 'Ultrasonic cleaning', in *Power Ultrasonics*, Elsevier, 2023, pp. 455–471. doi: 10.1016/B978-0-12-820254-8.00019-1.

[63] X. Huang *et al.*, 'Effects of cleaning protocols on surface roughness and optical properties of thermoplastic orthodontic retainers', *Clin Oral Invest*, vol. 30, no. 1, p. 21, Dec. 2025, doi: 10.1007/s00784-025-06711-9.

[64] F. Xie *et al.*, 'Recovery of Cu and Fe from Printed Circuit Board waste sludge by ultrasound: Evaluation of industrial application', *Journal of Cleaner Production*, vol. 17, no. 16, pp. 1494–1498, Nov. 2009, doi: 10.1016/j.jclepro.2009.06.012.

[65] T. J. Mason, D. Ghimpeteanu, I. Călinescu, M. Vinatoru, and A. Trifan, 'A simple new approach for mapping an ultrasonic tank for sonochemistry', *Ultrasonics Sonochemistry*, vol. 107, p. 106940, Jul. 2024, doi: 10.1016/j.ultsonch.2024.106940.

[66] A. Bampouli *et al.*, 'Understanding the ultrasound field of high viscosity mixtures: Experimental and numerical investigation of a lab scale batch reactor', *Ultrasonics Sonochemistry*, vol. 97, p. 106444, Jul. 2023, doi: 10.1016/j.ultsonch.2023.106444.

[67] M. Dular, O. C. Delgosha, and M. Petkovšek, 'Observations of cavitation erosion pit formation', *Ultrasonics Sonochemistry*, vol. 20, no. 4, pp. 1113–1120, Jul. 2013, doi: 10.1016/j.ultsonch.2013.01.011.

[68] M. Dular and A. Osterman, 'Pit clustering in cavitation erosion', *Wear*, vol. 265, no. 5–6, pp. 811–820, Aug. 2008, doi: 10.1016/j.wear.2008.01.005.

[69] F. J. Fuchs, 'Ultrasonic cleaning and washing of surfaces', in *Power Ultrasonics*, Elsevier, 2015, pp. 577–609. doi: 10.1016/B978-1-78242-028-6.00019-3.

[70] H. N. McMurray and B. P. Wilson, 'Mechanistic and Spatial Study of Ultrasonically Induced Luminol Chemiluminescence', *J. Phys. Chem. A*, vol. 103, no. 20, pp. 3955–3962, May 1999, doi: 10.1021/jp984503r.

[71] M. Dietrich, M. Franke, M. Stelter, and P. Braeutigam, 'Degradation of endocrine disruptor bisphenol A by ultrasound-assisted electrochemical oxidation in water', *Ultrasonics Sonochemistry*, vol. 39, pp. 741–749, Nov. 2017, doi: 10.1016/j.ultsonch.2017.05.038.

[72] C. Lei *et al.*, 'Effect of organic solvent additives on the enhancement of ultrasonic cavitation effects in water for lithium-ion battery electrode delamination', *Ultrasonics Sonochemistry*, vol. 110, p. 107049, Nov. 2024, doi: 10.1016/j.ultsonch.2024.107049.

[73] G. J. Price, N. K. Harris, and A. J. Stewart, 'Direct observation of cavitation fields at 23 and 515 kHz', *Ultrasonics Sonochemistry*, vol. 17, no. 1, pp. 30–33, Jan. 2010, doi: 10.1016/j.ultsonch.2009.04.009.

[74] B. E. Sarac, D. S. Stephens, J. Eisener, J. M. Rosselló, and R. Mettin, 'Cavitation bubble dynamics and sonochemiluminescence activity inside sonicated submerged flow tubes', *Chemical Engineering and Processing - Process Intensification*, vol. 150, p. 107872, Apr. 2020, doi: 10.1016/j.cep.2020.107872.

[75] M. Hodnett, 'Measurement techniques in power ultrasonics', in *Power Ultrasonics*, Elsevier, 2015, pp. 195–218. doi: 10.1016/B978-1-78242-028-6.00008-9.

[76] T. Kuroyama, 'Acoustic cavitation noise from ultrasonic horns: properties and applications as sound source', *Jpn. J. Appl. Phys.*, vol. 64, no. 5, p. 050803, May 2025, doi: 10.35848/1347-4065/adc744.

[77] M. Ashokkumar, M. Hodnett, B. Zeqiri, F. Grieser, and G. J. Price, 'Acoustic Emission Spectra from 515 kHz Cavitation in Aqueous Solutions Containing Surface-Active Solutes', *J. Am. Chem. Soc.*, vol. 129, no. 8, Art. no. 8, Feb. 2007, doi: 10.1021/ja067960r.

[78] M. Hodnett, R. Chow, and B. Zeqiri, 'High-frequency acoustic emissions generated by a 20 kHz sonochemical horn processor detected using a novel broadband acoustic sensor: a preliminary study', *Ultrasonics Sonochemistry*, vol. 11, no. 6, Art. no. 6, Sep. 2004, doi: 10.1016/j.ultsonch.2003.09.002.

[79] P. Wu, X. Wang, W. Lin, and L. Bai, 'Acoustic characterization of cavitation intensity: A review', *Ultrasonics Sonochemistry*, vol. 82, p. 105878, Jan. 2022, doi: 10.1016/j.ultsonch.2021.105878.

[80] I. E. Commission, *Measurement of Cavitation Noise in Ultrasonic Baths and Ultrasonic Reactors*. International Electrotechnical Commission: Geneva, Switzerland, 2019.

[81] C. Wang and S. Lin, 'The nonlinear standing wave inside the space of liquid', *Sci. China Phys. Mech. Astron.*, vol. 53, no. 3, pp. 496–503, Mar. 2010, doi: 10.1007/s11433-010-0105-2.

[82] K. Johansen, J. H. Song, K. Johnston, and P. Prentice, 'Deconvolution of acoustically detected bubble-collapse shock waves', *Ultrasonics*, vol. 73, pp. 144–153, Jan. 2017, doi: 10.1016/j.ultras.2016.09.007.

[83] E. A. Brujan, T. Ikeda, and Y. Matsumoto, ‘Shock wave emission from a cloud of bubbles’, *Soft Matter*, vol. 8, no. 21, p. 5777, 2012, doi: 10.1039/c2sm25379h.

[84] C. M. Schoellhammer *et al.*, ‘Ultrasound-mediated gastrointestinal drug delivery’, *Sci. Transl. Med.*, vol. 7, no. 310, Oct. 2015, doi: 10.1126/scitranslmed.aaa5937.

[85] S. Cochran, ‘Piezoelectricity and basic configurations for piezoelectric ultrasonic transducers’, in *Ultrasonic Transducers*, Elsevier, 2012, pp. 3–35. doi: 10.1533/9780857096302.1.3.

[86] J. Kim and J. Lee, ‘Parametric Study of Bolt Clamping Effect on Resonance Characteristics of Langevin Transducers with Lumped Circuit Models’, *Sensors*, vol. 20, no. 7, p. 1952, Mar. 2020, doi: 10.3390/s20071952.

[87] J. Kim, J. Kim, and J. Kang, ‘Advances in Langevin Piezoelectric Transducer Designs for Broadband Ultrasonic Transmitter Applications’, *Actuators*, vol. 14, no. 7, p. 355, Jul. 2025, doi: 10.3390/act14070355.

[88] A. Pérez-Sánchez, J. A. Segura, C. Rubio-Gonzalez, L. A. Baldenegro-Pérez, and J. A. Soto-Cajiga, ‘Numerical design and analysis of a langevin power ultrasonic transducer for acoustic cavitation generation’, *Sensors and Actuators A: Physical*, vol. 311, p. 112035, Aug. 2020, doi: 10.1016/j.sna.2020.112035.

[89] D. Meroni, R. Djellabi, M. Ashokkumar, C. L. Bianchi, and D. C. Boffito, ‘Sonoprocessing: From Concepts to Large-Scale Reactors’, *Chem. Rev.*, vol. 122, no. 3, Art. no. 3, Feb. 2022, doi: 10.1021/acs.chemrev.1c00438.

[90] Z. Dong, C. Delacour, K. Mc Carogher, A. P. Udepurkar, and S. Kuhn, ‘Continuous Ultrasonic Reactors: Design, Mechanism and Application’, *Materials*, vol. 13, no. 2, p. 344, Jan. 2020, doi: 10.3390/ma13020344.

[91] P. Adamou, E. Harkou, A. Villa, A. Constantinou, and N. Dimitratos, ‘Ultrasonic reactor set-ups and applications: A review’, *Ultrasonics Sonochemistry*, vol. 107, p. 106925, Jul. 2024, doi: 10.1016/j.ultsonch.2024.106925.

[92] X. M. Cheng, K. Yang, J. Wang, W. T. Xiao, and S. S. Huang, ‘Ultrasonic system and ultrasonic metal welding performance: A status review’, *Journal of Manufacturing Processes*, vol. 84, pp. 1196–1216, Dec. 2022, doi: 10.1016/j.jmapro.2022.10.067.

[93] A. Moussatov, C. Granger, and B. Dubus, ‘Cone-like bubble formation in ultrasonic cavitation field’, *Ultrasonics Sonochemistry*, vol. 10, no. 4–5, Art. no. 4–5, Jul. 2003, doi: 10.1016/S1350-4177(02)00152-9.

[94] I. Tzanakis, G. S. B. Lebon, D. G. Eskin, and K. A. Pericleous, ‘Characterizing the cavitation development and acoustic spectrum in various liquids’, *Ultrasonics Sonochemistry*, vol. 34, pp. 651–662, Jan. 2017, doi: 10.1016/j.ultsonch.2016.06.034.

[95] Y. Son, Y. No, and J. Kim, 'Geometric and operational optimization of 20-kHz probe-type sonoreactor for enhancing sonochemical activity', *Ultrasonics Sonochemistry*, vol. 65, p. 105065, Jul. 2020, doi: 10.1016/j.ultsonch.2020.105065.

[96] M. H. Dehghani *et al.*, 'Recent trends in the applications of sonochemical reactors as an advanced oxidation process for the remediation of microbial hazards associated with water and wastewater: A critical review', *Ultrasonics Sonochemistry*, vol. 94, p. 106302, Mar. 2023, doi: 10.1016/j.ultsonch.2023.106302.

[97] S. Doğruel and A. S. Özgen, 'Effect of ultrasonic and microwave disintegration on physico-chemical and biodegradation characteristics of waste-activated sludge', *Environmental Technology*, vol. 38, no. 7, pp. 844–859, Apr. 2017, doi: 10.1080/09593330.2016.1213771.

[98] S. Kentish and H. Feng, 'Applications of Power Ultrasound in Food Processing', *Annu. Rev. Food Sci. Technol.*, vol. 5, no. 1, Art. no. 1, Feb. 2014, doi: 10.1146/annurev-food-030212-182537.

[99] F. Dong, X. Li, L. Zhang, L. Ma, and R. Li, 'Cavitation erosion mechanism of titanium alloy radiation rods in aluminum melt', *Ultrasonics Sonochemistry*, vol. 31, pp. 150–156, Jul. 2016, doi: 10.1016/j.ultsonch.2015.12.009.

[100] J. Demaerel, S. Govaerts, R. R. Paul, T. Van Gerven, and W. M. De Borggraeve, 'Non-innocent probes in direct sonication: Metal assistance in oxidative radical C H functionalization', *Ultrasonics Sonochemistry*, vol. 41, pp. 134–142, Mar. 2018, doi: 10.1016/j.ultsonch.2017.09.027.

[101] D. C. Boffito, S. Mansi, J.-M. Leveque, C. Pirola, C. L. Bianchi, and G. S. Patience, 'Ultrafast Biodiesel Production Using Ultrasound in Batch and Continuous Reactors', *ACS Sustainable Chem. Eng.*, vol. 1, no. 11, pp. 1432–1439, Nov. 2013, doi: 10.1021/sc400161s.

[102] Z. Fang, R. L. Smith, and X. Qi, Eds, *Production of Biofuels and Chemicals with Ultrasound*, vol. 4. in Biofuels and Biorefineries, vol. 4. Dordrecht: Springer Netherlands, 2015. doi: 10.1007/978-94-017-9624-8.

[103] L. S. Teixeira, H. P. Vieira, C. C. Windmöller, and C. C. Nascentes, 'Fast determination of trace elements in organic fertilizers using a cup-horn reactor for ultrasound-assisted extraction and fast sequential flame atomic absorption spectrometry', *Talanta*, vol. 119, pp. 232–239, Feb. 2014, doi: 10.1016/j.talanta.2013.11.018.

[104] Y. Son, M. Lim, J. Khim, and M. Ashokkumar, 'Acoustic emission spectra and sonochemical activity in a 36 kHz sonoreactor', *Ultrasonics Sonochemistry*, vol. 19, no. 1, pp. 16–21, Jan. 2012, doi: 10.1016/j.ultsonch.2011.06.001.

[105] Y. Son, M. Lim, M. Ashokkumar, and J. Khim, 'Geometric Optimization of Sonoreactors for the Enhancement of Sonochemical Activity', *J. Phys. Chem. C*, vol. 115, no. 10, Art. no. 10, Mar. 2011, doi: 10.1021/jp110319y.

[106] K. C. Teo, Y. Xu, and C. Yang, 'Sonochemical degradation for toxic halogenated organic compounds', *Ultrasonics Sonochemistry*, vol. 8, no. 3, pp. 241–246, Jul. 2001, doi: 10.1016/S1350-4177(01)00083-9.

[107] D. Santos, U. F. Silva, F. A. Duarte, C. A. Bizzi, E. M. M. Flores, and P. A. Mello, 'Ultrasound-assisted acid hydrolysis of cellulose to chemical building blocks: Application to furfural synthesis', *Ultrasonics Sonochemistry*, vol. 40, pp. 81–88, Jan. 2018, doi: 10.1016/j.ultsonch.2017.04.034.

[108] M. Zargazi and M. H. Entezari, 'Sonochemical versus hydrothermal synthesis of bismuth tungstate nanostructures: Photocatalytic, sonocatalytic and sonophotocatalytic activities', *Ultrasonics Sonochemistry*, vol. 51, pp. 1–11, Mar. 2019, doi: 10.1016/j.ultsonch.2018.10.010.

[109] P. R. Gogate, A. B. Pandit, A. Wilhelm, B. Ratsimba, and H. Delmas, 'Destruction of formic acid using high frequency cup horn reactor', *Water Research*, vol. 40, no. 8, pp. 1697–1705, May 2006, doi: 10.1016/j.watres.2006.02.011.

[110] P. R. Gogate and P. N. Patil, 'Sonochemical Reactors', *Top Curr Chem (Z)*, vol. 374, no. 5, p. 61, Oct. 2016, doi: 10.1007/s41061-016-0064-9.

[111] G. Chatel and J. C. Colmenares, 'Sonochemistry: from Basic Principles to Innovative Applications', *Top Curr Chem (Z)*, vol. 375, no. 1, pp. 8, s41061-016-0096–1, Feb. 2017, doi: 10.1007/s41061-016-0096-1.

[112] W. Tangsopa and J. Thongsri, 'Development of an industrial ultrasonic cleaning tank based on harmonic response analysis', *Ultrasonics*, vol. 91, pp. 68–76, Jan. 2019, doi: 10.1016/j.ultras.2018.07.013.

[113] K.-V. Jenderka and C. Koch, 'Investigation of spatial distribution of sound field parameters in ultrasound cleaning baths under the influence of cavitation', *Ultrasonics*, vol. 44, pp. e401–e406, Dec. 2006, doi: 10.1016/j.ultras.2006.05.042.

[114] M. Hodnett, M. J. Choi, and B. Zeqiri, 'Towards a reference ultrasonic cavitation vessel. Part 1: Preliminary investigation of the acoustic field distribution in a 25kHz cylindrical cell', *Ultrasonics Sonochemistry*, vol. 14, no. 1, pp. 29–40, Jan. 2007, doi: 10.1016/j.ultsonch.2006.01.003.

[115] C. J. B. Vian, 'A Comparison of Measurement Techniques for Acoustic Cavitation'.

[116] M. Plattes, C. Koehler, and T. Gallé, 'Purely ultrasonic enzyme extraction from activated sludge in an ultrasonic cleaning bath', *MethodsX*, vol. 4, pp. 214–217, 2017, doi: 10.1016/j.mex.2017.07.003.

[117] L. M. Bryson, D. Fernandez Rivas, and C. Boutsioukis, ‘Cleaning of used rotary nickel-titanium files in an ultrasonic bath by locally intensified acoustic cavitation’, *Int Endodontic J*, vol. 51, no. 4, pp. 457–468, Apr. 2018, doi: 10.1111/iej.12866.

[118] J. M. Costa and A. F. D. Almeida Neto, ‘Ultrasound-assisted electrodeposition and synthesis of alloys and composite materials: A review’, *Ultrasonics Sonochemistry*, vol. 68, p. 105193, Nov. 2020, doi: 10.1016/j.ultsonch.2020.105193.

[119] Z. Zhou, Y. Yang, X. Li, Y. Zhang, and X. Guo, ‘Characterization of drinking water treatment sludge after ultrasound treatment’, *Ultrasonics Sonochemistry*, vol. 24, pp. 19–26, May 2015, doi: 10.1016/j.ultsonch.2014.11.007.

[120] J.-H. Lee, S. U. S. Choi, S. P. Jang, and S. Y. Lee, ‘Production of aqueous spherical gold nanoparticles using conventional ultrasonic bath’, *Nanoscale Res Lett*, vol. 7, no. 1, p. 420, Dec. 2012, doi: 10.1186/1556-276X-7-420.

[121] P. R. Gogate, S. Mujumdar, and A. B. Pandit, ‘Sonochemical reactors for waste water treatment: comparison using formic acid degradation as a model reaction’, *Advances in Environmental Research*, vol. 7, no. 2, Art. no. 2, Jan. 2003, doi: 10.1016/S1093-0191(01)00133-2.

[122] J. K. Chu, T. J. Tiong, S. Chong, U. A. Asli, and Y. H. Yap, ‘Multi-frequency sonoreactor characterisation in the frequency domain using a semi-empirical bubbly liquid model’, *Ultrasonics Sonochemistry*, vol. 80, p. 105818, Dec. 2021, doi: 10.1016/j.ultsonch.2021.105818.

[123] L. Paniwnyk, ‘Application of Ultrasound’, in *Emerging Technologies for Food Processing*, Elsevier, 2014, pp. 271–291. doi: 10.1016/B978-0-12-411479-1.00015-2.

[124] B. Zisu, M. Sciberras, V. Jayasena, M. Weeks, M. Palmer, and T. D. Dincer, ‘Sonocrystallisation of lactose in concentrated whey’, *Ultrasonics Sonochemistry*, vol. 21, no. 6, pp. 2117–2121, Nov. 2014, doi: 10.1016/j.ultsonch.2014.03.031.

[125] J.-L. Dion, ‘Contamination-free high capacity converging waves sonoreactors for the chemical industry’, *Ultrasonics Sonochemistry*, vol. 16, no. 2, pp. 212–220, Feb. 2009, doi: 10.1016/j.ultsonch.2008.07.009.

[126] C. P. Baldé *et al.*, ‘THE GLOBAL E-WASTE MONITOR 2024’, 2024.

[127] R. Hameed *et al.*, ‘A review on sustainable management strategies for navigating the piling e-waste crisis and associated environmental threats’, *Toxicology*, vol. 511, p. 154019, Feb. 2025, doi: 10.1016/j.tox.2024.154019.

[128] M. Jain, D. Kumar, J. Chaudhary, S. Kumar, S. Sharma, and A. Singh Verma, ‘Review on E-waste management and its impact on the environment and society’, *Waste Management Bulletin*, vol. 1, no. 3, pp. 34–44, Dec. 2023, doi: 10.1016/j.wmb.2023.06.004.

[129] S. M. Parvez *et al.*, 'Health consequences of exposure to e-waste: an updated systematic review', *The Lancet Planetary Health*, vol. 5, no. 12, pp. e905–e920, Dec. 2021, doi: 10.1016/S2542-5196(21)00263-1.

[130] V. Murthy and S. Ramakrishna, 'A Review on Global E-Waste Management: Urban Mining towards a Sustainable Future and Circular Economy', *Sustainability*, vol. 14, no. 2, p. 647, Jan. 2022, doi: 10.3390/su14020647.

[131] T. Ma *et al.*, 'Efficient Gold Recovery from E-Waste via a Chelate-Containing Porous Aromatic Framework', *ACS Appl. Mater. Interfaces*, vol. 12, no. 27, pp. 30474–30482, Jul. 2020, doi: 10.1021/acsami.0c08352.

[132] A. Priya and S. Hait, 'Comparative assessment of metallurgical recovery of metals from electronic waste with special emphasis on bioleaching', *Environ Sci Pollut Res*, vol. 24, no. 8, pp. 6989–7008, Mar. 2017, doi: 10.1007/s11356-016-8313-6.

[133] B. Ghosh, M. K. Ghosh, P. Parhi, P. S. Mukherjee, and B. K. Mishra, 'Waste Printed Circuit Boards recycling: an extensive assessment of current status', *Journal of Cleaner Production*, vol. 94, pp. 5–19, May 2015, doi: 10.1016/j.jclepro.2015.02.024.

[134] E. A. Oke and H. Potgieter, 'Discarded e-waste/printed circuit boards: a review of their recent methods of disassembly, sorting and environmental implications', *J Mater Cycles Waste Manag*, vol. 26, no. 3, pp. 1277–1293, May 2024, doi: 10.1007/s10163-024-01917-7.

[135] E. Y. L. Sum, 'The recovery of metals from electronic scrap', *JOM*, vol. 43, no. 4, pp. 53–61, Apr. 1991, doi: 10.1007/BF03220549.

[136] M. D. Rao, K. K. Singh, C. A. Morrison, and J. B. Love, 'Challenges and opportunities in the recovery of gold from electronic waste', *RSC Adv.*, vol. 10, no. 8, pp. 4300–4309, 2020, doi: 10.1039/C9RA07607G.

[137] J. Ruan and Z. Xu, 'Constructing environment-friendly return road of metals from e-waste: Combination of physical separation technologies', *Renewable and Sustainable Energy Reviews*, vol. 54, pp. 745–760, Feb. 2016, doi: 10.1016/j.rser.2015.10.114.

[138] S.-R. Shin, V. D. Mai, and D.-S. Lee, 'Chemical Recycling of Used Printed Circuit Board Scraps: Recovery and Utilization of Organic Products', *Processes*, vol. 7, no. 1, p. 22, Jan. 2019, doi: 10.3390/pr7010022.

[139] K. R. Ngoy *et al.*, 'Lithium-ion batteries and the future of sustainable energy: A comprehensive review', *Renewable and Sustainable Energy Reviews*, vol. 223, p. 115971, Nov. 2025, doi: 10.1016/j.rser.2025.115971.

[140] L. Feng *et al.*, 'Fundamental research on recycling spent lithium-ion batteries for environmental pollutant control', *Journal of Environmental Management*, vol. 394, p. 127620, Nov. 2025, doi: 10.1016/j.jenvman.2025.127620.

[141] K. Du, E. H. Ang, X. Wu, and Y. Liu, ‘Progresses in Sustainable Recycling Technology of Spent Lithium-Ion Batteries’, *Energy & Environ Materials*, vol. 5, no. 4, pp. 1012–1036, Oct. 2022, doi: 10.1002/eem2.12271.

[142] M. Kaya, ‘State-of-the-art lithium-ion battery recycling technologies’, *Circular Economy*, vol. 1, no. 2, p. 100015, Dec. 2022, doi: 10.1016/j.cec.2022.100015.

[143] C. Hendricks, N. Williard, S. Mathew, and M. Pecht, ‘A failure modes, mechanisms, and effects analysis (FMMEA) of lithium-ion batteries’, *Journal of Power Sources*, vol. 297, pp. 113–120, Nov. 2015, doi: 10.1016/j.jpowsour.2015.07.100.

[144] M. R. Palacín and A. De Guibert, ‘Why do batteries fail?’, *Science*, vol. 351, no. 6273, p. 1253292, Feb. 2016, doi: 10.1126/science.1253292.

[145] M. Bruno, L. L. Lassila, C. Francia, A. Santasalo-Aarnio, and S. Fiore, ‘Technical, economic and environmental analysis of production scraps direct recycling from lithium-ion battery manufacturing’, *Cleaner Environmental Systems*, vol. 20, p. 100386, Mar. 2026, doi: 10.1016/j.cesys.2025.100386.

[146] X. Xu *et al.*, ‘Challenges and opportunities toward long-life lithium-ion batteries’, *Journal of Power Sources*, vol. 603, p. 234445, May 2024, doi: 10.1016/j.jpowsour.2024.234445.

[147] J. Wen, D. Zhao, and C. Zhang, ‘An overview of electricity powered vehicles: Lithium-ion battery energy storage density and energy conversion efficiency’, *Renewable Energy*, vol. 162, pp. 1629–1648, Dec. 2020, doi: 10.1016/j.renene.2020.09.055.

[148] D. Yu, Z. Huang, B. Makuza, X. Guo, and Q. Tian, ‘Pretreatment options for the recycling of spent lithium-ion batteries: A comprehensive review’, *Minerals Engineering*, vol. 173, p. 107218, Nov. 2021, doi: 10.1016/j.mineng.2021.107218.

[149] P. Meshram, A. Mishra, Abhilash, and R. Sahu, ‘Environmental impact of spent lithium ion batteries and green recycling perspectives by organic acids – A review’, *Chemosphere*, vol. 242, p. 125291, Mar. 2020, doi: 10.1016/j.chemosphere.2019.125291.

[150] J. Y. Han and S. Jung, ‘Thermal Stability and the Effect of Water on Hydrogen Fluoride Generation in Lithium-Ion Battery Electrolytes Containing LiPF6’, *Batteries*, vol. 8, no. 7, p. 61, Jun. 2022, doi: 10.3390/batteries8070061.

[151] T. Rostami, B. Khoshandam, and S. Maroufi, ‘Recovery of lithium, cobalt, nickel, and manganese from spent lithium-ion batteries through a wet-thermal process’, *Materials Research Bulletin*, vol. 153, p. 111897, Sep. 2022, doi: 10.1016/j.materresbull.2022.111897.

[152] J. Liu *et al.*, 'Critical strategies for recycling process of graphite from spent lithium-ion batteries: A review', *Science of The Total Environment*, vol. 816, p. 151621, Apr. 2022, doi: 10.1016/j.scitotenv.2021.151621.

[153] M. C. Etude *et al.*, 'Recycling lithium-ion batteries: A review of current status and future directions', *Sustainable Chemistry One World*, vol. 4, p. 100027, Dec. 2024, doi: 10.1016/j.scowo.2024.100027.

[154] L. Gaines, Q. Dai, J. T. Vaughey, and S. Gillard, 'Direct Recycling R&D at the ReCell Center', *Recycling*, vol. 6, no. 2, p. 31, May 2021, doi: 10.3390/recycling6020031.

[155] H. Duan, K. Hou, J. Li, and X. Zhu, 'Examining the technology acceptance for dismantling of waste printed circuit boards in light of recycling and environmental concerns', *Journal of Environmental Management*, vol. 92, no. 3, pp. 392–399, Mar. 2011, doi: 10.1016/j.jenvman.2010.10.057.

[156] S. Mir and N. Dhawan, 'A comprehensive review on the recycling of discarded printed circuit boards for resource recovery', *Resources, Conservation and Recycling*, vol. 178, p. 106027, Mar. 2022, doi: 10.1016/j.resconrec.2021.106027.

[157] R. Seif, F. Z. Salem, and N. K. Allam, 'E-waste recycled materials as efficient catalysts for renewable energy technologies and better environmental sustainability', *Environ Dev Sustain*, vol. 26, no. 3, pp. 5473–5508, Jan. 2023, doi: 10.1007/s10668-023-02925-7.

[158] G. Harper *et al.*, 'Recycling lithium-ion batteries from electric vehicles', *Nature*, vol. 575, no. 7781, pp. 75–86, Nov. 2019, doi: 10.1038/s41586-019-1682-5.

[159] P. M. Tembo, C. Dyer, and V. Subramanian, 'Lithium-ion battery recycling—a review of the material supply and policy infrastructure', *NPG Asia Mater*, vol. 16, no. 1, Art. no. 1, Aug. 2024, doi: 10.1038/s41427-024-00562-8.

[160] M. Bhar, S. Ghosh, S. Krishnamurthy, Y. Kaliprasad, and S. K. Martha, 'A review on spent lithium-ion battery recycling: from collection to black mass recovery', *RSC Sustainability*, vol. 1, no. 5, pp. 1150–1167, 2023, doi: 10.1039/D3SU00086A.

[161] J. Hao, Y. Wang, Y. Wu, and F. Guo, 'Metal recovery from waste printed circuit boards: A review for current status and perspectives', *Resources, Conservation and Recycling*, vol. 157, p. 104787, Jun. 2020, doi: 10.1016/j.resconrec.2020.104787.

[162] R. Sommerville, P. Zhu, M. A. Rajaeifar, O. Heidrich, V. Goodship, and E. Kendrick, 'A qualitative assessment of lithium ion battery recycling processes', *Resources, Conservation and Recycling*, vol. 165, p. 105219, Feb. 2021, doi: 10.1016/j.resconrec.2020.105219.

[163] H. Wang, S. Zhang, B. Li, D. Pan, Y. Wu, and T. Zuo, 'Recovery of waste printed circuit boards through pyrometallurgical processing: A review', *Resources,*

Conservation and Recycling, vol. 126, pp. 209–218, Nov. 2017, doi: 10.1016/j.resconrec.2017.08.001.

[164] D. Latini *et al.*, 'A comprehensive review and classification of unit operations with assessment of outputs quality in lithium-ion battery recycling', *Journal of Power Sources*, vol. 546, p. 231979, Oct. 2022, doi: 10.1016/j.jpowsour.2022.231979.

[165] D. L. Thompson *et al.*, 'The importance of design in lithium ion battery recycling – a critical review', *Green Chem.*, vol. 22, no. 22, pp. 7585–7603, 2020, doi: 10.1039/D0GC02745F.

[166] H. Li, J. Eksteen, and E. Oraby, 'Hydrometallurgical recovery of metals from waste printed circuit boards (WPCBs): Current status and perspectives – A review', *Resources, Conservation and Recycling*, vol. 139, pp. 122–139, Dec. 2018, doi: 10.1016/j.resconrec.2018.08.007.

[167] J. Cui and L. Zhang, 'Metallurgical recovery of metals from electronic waste: A review', *Journal of Hazardous Materials*, vol. 158, no. 2–3, pp. 228–256, Oct. 2008, doi: 10.1016/j.jhazmat.2008.02.001.

[168] S. Udayakumar, M. I. B. A. Razak, and S. Ismail, 'Recovering valuable metals from Waste Printed Circuit Boards (WPCB): A short review', *Materials Today: Proceedings*, vol. 66, pp. 3062–3070, 2022, doi: 10.1016/j.matpr.2022.07.364.

[169] M. Gurung, B. B. Adhikari, H. Kawakita, K. Ohto, K. Inoue, and S. Alam, 'Recovery of gold and silver from spent mobile phones by means of acidothiourea leaching followed by adsorption using biosorbent prepared from persimmon tannin', *Hydrometallurgy*, vol. 133, pp. 84–93, Feb. 2013, doi: 10.1016/j.hydromet.2012.12.003.

[170] H. Deng *et al.*, 'A comprehensive review of whole process typical hydrometallurgical technologies for recycling waste lithium-ion batteries', *Separation and Purification Technology*, vol. 363, p. 132234, Aug. 2025, doi: 10.1016/j.seppur.2025.132234.

[171] Y. E. Milian, N. Jamett, C. Cruz, S. Herrera-León, and J. Chacana-Olivares, 'A comprehensive review of emerging technologies for recycling spent lithium-ion batteries', *Science of The Total Environment*, vol. 910, p. 168543, Feb. 2024, doi: 10.1016/j.scitotenv.2023.168543.

[172] J. Wu *et al.*, 'Recent advancements in hydrometallurgical recycling technologies of spent lithium-ion battery cathode materials', *Rare Metals*, vol. 43, no. 3, pp. 879–899, Mar. 2024, doi: 10.1007/s12598-023-02437-3.

[173] A. P. Abbott, D. Boothby, G. Capper, D. L. Davies, and R. K. Rasheed, 'Deep Eutectic Solvents Formed between Choline Chloride and Carboxylic Acids: Versatile

Alternatives to Ionic Liquids', *J. Am. Chem. Soc.*, vol. 126, no. 29, Art. no. 29, Jul. 2004, doi: 10.1021/ja048266j.

[174] E. L. Smith, A. P. Abbott, and K. S. Ryder, 'Deep Eutectic Solvents (DESs) and Their Applications', *Chem. Rev.*, vol. 114, no. 21, Art. no. 21, Nov. 2014, doi: 10.1021/cr300162p.

[175] T. El Achkar, H. Greige-Gerges, and S. Fourmentin, 'Basics and properties of deep eutectic solvents: a review', *Environ Chem Lett*, vol. 19, no. 4, pp. 3397–3408, Aug. 2021, doi: 10.1007/s10311-021-01225-8.

[176] Q. Zhang, K. De Oliveira Vigier, S. Royer, and F. Jérôme, 'Deep eutectic solvents: syntheses, properties and applications', *Chem. Soc. Rev.*, vol. 41, no. 21, p. 7108, 2012, doi: 10.1039/c2cs35178a.

[177] A. P. Abbott, G. Capper, D. L. Davies, R. K. Rasheed, and V. Tambyrajah, 'Novel solvent properties of choline chloride/urea mixturesElectronic supplementary information (ESI) available: spectroscopic data. See http://www.rsc.org/suppdata/cc/b2/b210714g/', *Chem. Commun.*, no. 1, pp. 70–71, Dec. 2003, doi: 10.1039/b210714g.

[178] A. T. H. Yeow *et al.*, 'A comprehensive review on the physicochemical properties of deep eutectic solvents', *Results in Chemistry*, vol. 7, p. 101378, Jan. 2024, doi: 10.1016/j.rechem.2024.101378.

[179] A. Azzouz and M. Hayyan, 'Potential applications of deep eutectic solvents in nanotechnology: Part II', *Chemical Engineering Journal*, vol. 468, p. 143563, Jul. 2023, doi: 10.1016/j.cej.2023.143563.

[180] O. S. Hammond, D. T. Bowron, and K. J. Edler, 'The Effect of Water upon Deep Eutectic Solvent Nanostructure: An Unusual Transition from Ionic Mixture to Aqueous Solution', *Angew Chem Int Ed*, vol. 56, no. 33, pp. 9782–9785, Aug. 2017, doi: 10.1002/anie.201702486.

[181] B. B. Hansen *et al.*, 'Deep Eutectic Solvents: A Review of Fundamentals and Applications', *Chem. Rev.*, vol. 121, no. 3, Art. no. 3, Feb. 2021, doi: 10.1021/acs.chemrev.0c00385.

[182] K. A. Omar and R. Sadeghi, 'Database of deep eutectic solvents and their physical properties: A review', *Journal of Molecular Liquids*, vol. 384, p. 121899, Aug. 2023, doi: 10.1016/j.molliq.2023.121899.

[183] K. A. Omar and R. Sadeghi, 'Physicochemical properties of deep eutectic solvents: A review', *Journal of Molecular Liquids*, vol. 360, p. 119524, Aug. 2022, doi: 10.1016/j.molliq.2022.119524.

[184] H. Ghaedi, M. Ayoub, S. Sufian, A. M. Shariff, and B. Lal, 'The study on temperature dependence of viscosity and surface tension of several Phosphonium-based deep eutectic solvents', *Journal of Molecular Liquids*, vol. 241, pp. 500–510, Sep. 2017, doi: 10.1016/j.molliq.2017.06.024.

[185] Y. Chen *et al.*, 'Surface Tension of 50 Deep Eutectic Solvents: Effect of Hydrogen-Bonding Donors, Hydrogen-Bonding Acceptors, Other Solvents, and Temperature', *Ind. Eng. Chem. Res.*, vol. 58, no. 28, pp. 12741–12750, Jul. 2019, doi: 10.1021/acs.iecr.9b00867.

[186] T. Lemaoui *et al.*, 'Predicting the Surface Tension of Deep Eutectic Solvents Using Artificial Neural Networks', *ACS Omega*, vol. 7, no. 36, pp. 32194–32207, Sep. 2022, doi: 10.1021/acsomega.2c03458.

[187] S. P. Ijardar, V. Singh, and R. L. Gardas, 'Revisiting the Physicochemical Properties and Applications of Deep Eutectic Solvents', *Molecules*, vol. 27, no. 4, p. 1368, Feb. 2022, doi: 10.3390/molecules27041368.

[188] M. Stanisz, B. J. Stanisz, and J. Cielecka-Piontek, 'A Comprehensive Review on Deep Eutectic Solvents: Their Current Status and Potential for Extracting Active Compounds from Adaptogenic Plants', *Molecules*, vol. 29, no. 19, p. 4767, Oct. 2024, doi: 10.3390/molecules29194767.

[189] H. A. Sabzkoohi and G. Kolliopoulos, 'Green Zero-Waste Metal Extraction and Recycling from Printed Circuit Boards', in *International Conference on Raw Materials and Circular Economy*, MDPI, Nov. 2021, p. 39. doi: 10.3390/materproc2021005039.

[190] S. Saffaj, D. Mantovani, and G. Kolliopoulos, 'Sustainable Leaching of Cu, Ni, and Au from Waste Printed Circuit Boards Using Choline Chloride-Based Deep Eutectic Solvents', *Metals*, vol. 15, no. 1, p. 82, Jan. 2025, doi: 10.3390/met15010082.

[191] R. Marin Rivera, G. Zante, J. M. Hartley, K. S. Ryder, and A. P. Abbott, 'Catalytic dissolution of metals from printed circuit boards using a calcium chloride–based deep eutectic solvent', *Green Chem.*, vol. 24, no. 7, Art. no. 7, 2022, doi: 10.1039/D1GC04694B.

[192] R. Marin Rivera *et al.*, 'Ultra-fast extraction of metals from a printed circuit board using high power ultrasound in a calcium chloride-based deep eutectic solvent', *RSC Sustainability*, vol. 2, no. 2, pp. 403–415, 2024, doi: 10.1039/D3SU00147D.

[193] J. J. Roy *et al.*, 'Direct recycling of Li-ion batteries from cell to pack level: Challenges and prospects on technology, scalability, sustainability, and economics', *Carbon Energy*, vol. 6, no. 6, p. e492, Jun. 2024, doi: 10.1002/cey2.492.

[194] S. Sloop *et al.*, 'A direct recycling case study from a lithium-ion battery recall', *Sustainable Materials and Technologies*, vol. 25, p. e00152, Sep. 2020, doi: 10.1016/j.susmat.2020.e00152.

[195] X. Ren *et al.*, 'Effects of Mechanical Stirring and Ultrasound Treatment on the Separation of Graphite Electrode Materials from Copper Foils of Spent LIBs: A Comparative Study', *Separations*, vol. 10, no. 4, p. 246, Apr. 2023, doi: 10.3390/separations10040246.

[196] W. Yang, Z. Tong, X. Bu, L. Dong, and S. Chehreh Chelgani, 'Mechanical and Ultrasonic Pretreatments for Efficient Peeling of Metal Foils from Spent Lithium-Ion Batteries', *ACS Omega*, vol. 10, no. 11, pp. 11214–11224, Mar. 2025, doi: 10.1021/acsomega.4c10547.

[197] P. Wiechers, A. Hermann, S. Koob, F. Glaum, and M. Gleiß, 'Development of a Process for Direct Recycling of Negative Electrode Scrap from Lithium-Ion Battery Production on a Technical Scale and Its Influence on the Material Quality', *Batteries*, vol. 10, no. 7, p. 218, Jun. 2024, doi: 10.3390/batteries10070218.

[198] E. Trebeck *et al.*, 'Investigation of Aqueous Delamination Processes for Lithium-Ion Battery Anodes', *Recycling*, vol. 10, no. 5, p. 189, Oct. 2025, doi: 10.3390/recycling10050189.

[199] Nikon company, *Digital camera Z8 reference guide*.

[200] H. E. J. Metzger, 'Cavitating bubbles in focused fields: the acoustic emission spectrum and broadband noise clearance upon synchronisation'.

[201] J. E. Stevenson, 'A Miniaturised Focussed Ultrasound Transducer for Soft Tissue Ablation'.

[202] Y. Marcus, *Deep Eutectic Solvents*. Cham: Springer International Publishing, 2019. doi: 10.1007/978-3-030-00608-2.

[203] W. Wang *et al.*, 'Ultrasound triggered organic mechanoluminescence materials', *Advanced Drug Delivery Reviews*, vol. 186, p. 114343, Jul. 2022, doi: 10.1016/j.addr.2022.114343.

[204] A. T. Sargent *et al.*, 'Reclamation and reuse of graphite from electric vehicle lithium-ion battery anodes *via* water delamination', *J. Mater. Chem. A*, vol. 11, no. 17, pp. 9579–9596, 2023, doi: 10.1039/D2TA09769A.

[205] S. Malmgren *et al.*, 'Consequences of air exposure on the lithiated graphite SEI', *Electrochimica Acta*, vol. 105, pp. 83–91, Aug. 2013, doi: 10.1016/j.electacta.2013.04.118.

[206] M. Kaya, ‘Recovery of metals and nonmetals from electronic waste by physical and chemical recycling processes’, *Waste Management*, vol. 57, pp. 64–90, Nov. 2016, doi: 10.1016/j.wasman.2016.08.004.

[207] H. A. Sabzkoohi and G. Kolliopoulos, ‘Green Zero-Waste Metal Extraction and Recycling from Printed Circuit Boards’, in *International Conference on Raw Materials and Circular Economy*, MDPI, Nov. 2021, p. 39. doi: 10.3390/materproc2021005039.

[208] G. Zante, R. Marin Rivera, J. M. Hartley, and A. P. Abbott, ‘Efficient recycling of metals from solar cells using catalytic etchants’, *Journal of Cleaner Production*, vol. 370, p. 133552, Oct. 2022, doi: 10.1016/j.jclepro.2022.133552.

[209] J. Jordens, B. Bamps, B. Gielen, L. Braeken, and T. Van Gerven, ‘The effects of ultrasound on micromixing’, *Ultrasonics Sonochemistry*, vol. 32, pp. 68–78, Sep. 2016, doi: 10.1016/j.ultsonch.2016.02.020.

[210] N. Masuda, A. Maruyama, T. Eguchi, T. Hirakawa, and Y. Murakami, ‘Influence of Microbubbles on Free Radical Generation by Ultrasound in Aqueous Solution: Dependence of Ultrasound Frequency’, *J. Phys. Chem. B*, vol. 119, no. 40, pp. 12887–12893, Oct. 2015, doi: 10.1021/acs.jpcb.5b05707.

[211] K. M. Swamy and K. L. Narayana, ‘Intensification of leaching process by dual-frequency ultrasound’.

[212] M.-L. Doche, A. Mandroyan, M. Mourad-Mahmoud, V. Moutarlier, and J.-Y. Hihn, ‘An ultrasonic-assisted process for copper recovery in a des solvent: Leaching and re-deposition’, *Chemical Engineering and Processing: Process Intensification*, vol. 121, pp. 90–96, Nov. 2017, doi: 10.1016/j.cep.2017.08.006.

[213] A. Mandroyan, M. Mourad-Mahmoud, M.-L. Doche, and J.-Y. Hihn, ‘Effects of ultrasound and temperature on copper electro reduction in Deep Eutectic Solvents (DES)’, *Ultrasonics Sonochemistry*, vol. 21, no. 6, pp. 2010–2019, Nov. 2014, doi: 10.1016/j.ultsonch.2014.02.019.

[214] N. C. Eddingsaas and K. S. Suslick, ‘Evidence for a Plasma Core during Multibubble Sonoluminescence in Sulfuric Acid’, *J. Am. Chem. Soc.*, vol. 129, no. 13, pp. 3838–3839, Apr. 2007, doi: 10.1021/ja070192z.

[215] A. Žnidarčič, R. Mettin, C. Cairós, and M. Dular, ‘Attached cavitation at a small diameter ultrasonic horn tip’, *Physics of Fluids*, vol. 26, no. 2, Art. no. 2, Feb. 2014, doi: 10.1063/1.4866270.

[216] M. Khavari *et al.*, ‘Cavitation-induced shock wave behaviour in different liquids’, *Ultrasonics Sonochemistry*, vol. 94, p. 106328, Mar. 2023, doi: 10.1016/j.ultsonch.2023.106328.

[217] B. Jacobson *et al.*, ‘Observation of cavitation dynamics in viscous deep eutectic solvents during power ultrasound sonication’, *Faraday Discuss.*, p. 10.1039.D4FD00031E, 2024, doi: 10.1039/D4FD00031E.

[218] J. Luo, W. Xu, Y. Zhai, and Q. Zhang, ‘Experimental study on the mesoscale causes of the influence of viscosity on material erosion in a cavitation field’, *Ultrasonics Sonochemistry*, vol. 59, p. 104699, Dec. 2019, doi: 10.1016/j.ultsonch.2019.104699.

[219] T. J. Tiong, T. Chandesa, and Y. H. Yap, ‘Comparison of sonochemiluminescence images using image analysis techniques and identification of acoustic pressure fields via simulation’, *Ultrasonics Sonochemistry*, vol. 36, pp. 78–87, May 2017, doi: 10.1016/j.ultsonch.2016.11.003.

[220] L. Bai, W. Xu, J. Deng, C. Li, D. Xu, and Y. Gao, ‘Generation and control of acoustic cavitation structure’, *Ultrasonics Sonochemistry*, vol. 21, no. 5, Art. no. 5, Sep. 2014, doi: 10.1016/j.ultsonch.2014.02.027.

[221] X. Ma, B. Huang, G. Wang, and M. Zhang, ‘Experimental investigation of conical bubble structure and acoustic flow structure in ultrasonic field’, *Ultrasonics Sonochemistry*, vol. 34, pp. 164–172, Jan. 2017, doi: 10.1016/j.ultsonch.2016.05.027.

[222] I. Garcia-Vargas, O. Louisnard, and L. Barthe, ‘Extensive investigation of geometric effects in sonoreactors: Analysis by luminol mapping and comparison with numerical predictions.’, *Ultrasonics Sonochemistry*, vol. 99, p. 106542, Oct. 2023, doi: 10.1016/j.ultsonch.2023.106542.

[223] A. Bampouli, Q. Goris, M. N. Hussain, O. Louisnard, G. D. Stefanidis, and T. Van Gerven, ‘Importance of design and operating parameters in a sonication system for viscous solutions: effects of input power, horn tip diameter and reactor capacity’, *Chemical Engineering and Processing - Process Intensification*, vol. 198, p. 109715, Apr. 2024, doi: 10.1016/j.cep.2024.109715.

[224] H. Metzger, Y. Zhang, A. Cammarano, and P. Prentice, ‘Revisiting the subharmonic route to acoustic chaos: broadband noise clearing via cavitation bubble synchronization’.

[225] O. Dahlem, J. Reisse, and V. Halloin, ‘The radially vibrating horn: A scaling-up possibility for sonochemical reactions’, *Chemical Engineering Science*, vol. 54, no. 13–14, pp. 2829–2838, Jul. 1999, doi: 10.1016/S0009-2509(98)00356-X.

[226] A. Priyadarshi *et al.*, ‘In-situ observations and acoustic measurements upon fragmentation of free-floating intermetallics under ultrasonic cavitation in water’, *Ultrasonics Sonochemistry*, vol. 80, p. 105820, Dec. 2021, doi: 10.1016/j.ultsonch.2021.105820.

[227] J. Kim and J. Lee, ‘Acoustic Power Measurement and Thermal Bioeffect Evaluation of Therapeutic Langevin Transducers’, *Sensors*, vol. 22, no. 2, p. 624, Jan. 2022, doi: 10.3390/s22020624.

[228] S. Freitas, G. Hielscher, H. P. Merkle, and B. Gander, ‘Continuous contact- and contamination-free ultrasonic emulsification—a useful tool for pharmaceutical development and production’, *Ultrasonics Sonochemistry*, vol. 13, no. 1, pp. 76–85, Jan. 2006, doi: 10.1016/j.ultsonch.2004.10.004.

[229] T. Tuziuti, K. Yasui, J. Lee, T. Kozuka, A. Towata, and Y. Iida, ‘Mechanism of Enhancement of Sonochemical-Reaction Efficiency by Pulsed Ultrasound’, *J. Phys. Chem. A*, vol. 112, no. 22, pp. 4875–4878, Jun. 2008, doi: 10.1021/jp802640x.

[230] S. Rarotra *et al.*, ‘Progress and Challenges on Battery Waste Management :A Critical Review’, *ChemistrySelect*, vol. 5, no. 20, pp. 6182–6193, May 2020, doi: 10.1002/slct.202000618.

[231] F. Larouche *et al.*, ‘Progress and Status of Hydrometallurgical and Direct Recycling of Li-Ion Batteries and Beyond’, *Materials*, vol. 13, no. 3, p. 801, Feb. 2020, doi: 10.3390/ma13030801.

[232] C. Lei *et al.*, ‘Lithium ion battery recycling using high-intensity ultrasonication’, *Green Chem.*, vol. 23, no. 13, Art. no. 13, 2021, doi: 10.1039/D1GC01623G.

[233] L. Gaines, ‘The future of automotive lithium-ion battery recycling: Charting a sustainable course’, *Sustainable Materials and Technologies*, vol. 1–2, pp. 2–7, Dec. 2014, doi: 10.1016/j.susmat.2014.10.001.

[234] A. Kosenko, K. Pushnitsa, A. A. Pavlovskii, P. Novikov, and A. A. Popovich, ‘The Review of Existing Strategies of End-of-Life Graphite Anode Processing Using 3Rs Approach: Recovery, Recycle, Reuse’, *Batteries*, vol. 9, no. 12, p. 579, Nov. 2023, doi: 10.3390/batteries9120579.

[235] S. Hatanaka, H. Mitome, K. Yasui, and S. Hayashi, ‘Multibubble sonoluminescence enhancement by fluid flow’, *Ultrasonics*, vol. 44, pp. e435–e438, Dec. 2006, doi: 10.1016/j.ultras.2006.05.022.

[236] R. J. Wood, J. Lee, and M. J. Bussemaker, ‘A parametric review of sonochemistry: Control and augmentation of sonochemical activity in aqueous solutions’, *Ultrasonics Sonochemistry*, vol. 38, pp. 351–370, Sep. 2017, doi: 10.1016/j.ultsonch.2017.03.030.

[237] B. Gielen *et al.*, ‘Characterization of stable and transient cavitation bubbles in a milliflow reactor using a multibubble sonoluminescence quenching technique’, *Ultrasonics Sonochemistry*, vol. 25, pp. 31–39, Jul. 2015, doi: 10.1016/j.ultsonch.2014.08.013.

[238] J. Bandelin, T. Lippert, J. E. Drewes, and K. Koch, ‘Impact of high flow rates and increased viscosity of digested sewage sludge on the cavitation intensity in ultrasonic tube reactors’, *Chemical Engineering and Processing - Process Intensification*, vol. 152, p. 107925, Jun. 2020, doi: 10.1016/j.cep.2020.107925.

[239] P. J. LaNasa and E. L. Upp, ‘Basic Flow Measurement Laws’, in *Fluid Flow Measurement*, Elsevier, 2014, pp. 19–29. doi: 10.1016/B978-0-12-409524-3.00002-2.

[240] C. Laguerie, M. Aubry, and J. P. Couderc, ‘Some physicochemical data on monohydrate citric acid solutions in water: solubility, density, viscosity, diffusivity, pH of standard solution, and refractive index’, *J. Chem. Eng. Data*, vol. 21, no. 1, pp. 85–87, Jan. 1976, doi: 10.1021/je60068a031.

[241] L. A. Yusuf *et al.*, ‘Toward decentralized nitrogen fixation using pulsed ultrasound’, *Cell Reports Physical Science*, vol. 6, no. 7, p. 102662, Jul. 2025, doi: 10.1016/j.xcrp.2025.102662.

[242] B. Jacobson *et al.*, ‘A mechanistic study identifying improved technology critical metal delamination from printed circuit boards at lower power sonications in a deep eutectic solvent’, *Ultrasonics Sonochemistry*, vol. 101, p. 106701, Dec. 2023, doi: 10.1016/j.ultsonch.2023.106701.

[243] F. Hossein and P. Angeli, ‘Advanced ultrasound vibration potential imaging’, *Chemical Physics Impact*, vol. 9, p. 100728, Dec. 2024, doi: 10.1016/j.chphi.2024.100728.

[244] D. J. Casadonte, M. Flores, and C. Petrier, ‘Enhancing sonochemical activity in aqueous media using power-modulated pulsed ultrasound: an initial study’, *Ultrasonics Sonochemistry*, vol. 12, no. 3, pp. 147–152, Feb. 2005, doi: 10.1016/j.ultsonch.2003.12.004.

[245] L. Li, J. Ge, F. Wu, R. Chen, S. Chen, and B. Wu, ‘Recovery of cobalt and lithium from spent lithium ion batteries using organic citric acid as leachant’, *Journal of Hazardous Materials*, vol. 176, no. 1–3, pp. 288–293, Apr. 2010, doi: 10.1016/j.jhazmat.2009.11.026.

[246] J. Marshall, D. Gastol, R. Sommerville, B. Middleton, V. Goodship, and E. Kendrick, ‘Disassembly of Li Ion Cells—Characterization and Safety Considerations of a Recycling Scheme’, *Metals*, vol. 10, no. 6, Art. no. 6, Jun. 2020, doi: 10.3390/met10060773.